Material properties of semiconducting nanostructures synthesized using the chemical bath deposition method.

by

Lehlohonolo Fortune Koao

(MS.c)

A dissertation presented in fulfillment of the requirements for the degree

PhD

in the

Faculty of Natural and Agricultural Sciences

Department of Physics

at the

University of the Free State, (QwaQwa Campus)

Republic of South Africa

Supervisor: Prof. B. F. Dejene

Co-supervisor: Prof. H. C. Swart

November 2013

This thesis is dedicated to my lovely daughter, my late mother and grand mother.

Acknowledgements

My sincere thanks and gratitude go to:

- Our *Almighty Creator* for opening my mind to pursue this project (*Psalms* 25:15).
- My principal supervisor, *Prof. B. F. Dejene,* who helped me shape my scientific outlook through his valuable guidance, suggestions and continuous encouragement, during the research work and the preparation of this manuscript. His patience at explaining different concepts and words of constant encouragement to explore deeper issues and to maintain a renaissance attitude towards education, kept me and my faith in the belief that education serves the educated on its own.
- My co-supervisor, *Prof. H. C. Swart*, for his useful comments and valuable suggestions during the progress of research work. I have learned quite a lot from his extensive knowledge in physics and many brilliant and creative ideas.
- The National Research Foundation (NRF) and the University of the Free State for financial support.
- To all members of staff, at the Department of Physics UFS (Qwa Qwa Campus) (Dr J. Dolo, Mr S. Motloung, Mr K. Tshabalala, Mr Ocaya, Mr J. Motloung and Miss Lemeko) and post graduate students (*Abdub Ali, Kewele Foka, Lephoto Mantwa, Dr Pontsho Mbule, Masetjhaba Tshabalala and Dr Daniel Bem*) for their assistance, support, interest and valuable hints.
- *Prof. J.R. Botha,* Physics department, University of Port Elizabeth, for allowing me to use their research facilities (PL measurement) at NMMU and for helping with the analysis of PL results. Extra thanks goes to *Mr K. Talla* for the PL measurements and for spending five sleepless nights with me during my visit at NMMU for doing PL experiments.
- *Dr P. Mushonga, Chemistry department, University of the Western Cape, for helping me with TEM measurements.*
- *Dr T. E. Motaung* and *Mr M. E. Mngomezulu* at Chemistry Department (Qwa Qwa campus) for their unwavering help by borrowing me the necessary materials and apparatus during the synthesis and preparation of the samples.

- My uncle (*Teboho Monkoe*), aunt *(Emily Monkoe*), two sisters (*Semakaleng and Relebohile*) and my brother (*Tshepo*) and lastly my girlfriend (*Mojabeng Tsholo*) for always supporting and advising me through the hard times.

- My father (*David*), I owe him an expression of my gratitude for his patience, understanding, support and encouragement during the completion of this research work.
- My daughter (*Boitelo*), who has been a constant source of encouragement and joy. I hope one day she will understand why I'm always running away from her and taking months without seeing her.
- Without any of these people, along with countless other friends and family, my education at UFS (Qwa Qwa Campus) would have been worse off. I have an immeasurable amount of gratitude for all those who have helped me in my education.

Abstract

The recent global research interest in wide band gap semiconductors has been focused on zinc oxide (ZnO) due to its excellent and unique properties as a semiconductor material. The high electron mobility, high thermal conductivity, good transparency, wide and direct band gap (3.37 eV), large exciton binding energy (60 meV) at room temperature and easiness of growing it in the nanostructure form, has made it suitable for wide range of applications in optoelectronics, piezoelectric devices, transparent and spin electronics, lasing and chemical sensing.

PbS nanostructures is a narrow energy gap material which have relevance for optical applications in the near-IR region of the electromagnetic spectrum such as telecommunications, photovoltaics and bioimaging. It has similar electron and hole effective masses hence the exciton, can be strongly confined which is not always feasible in other semiconductors. Thus the PbS system provides an ideal platform to investigate the exciton in the strong confinement regime.

In this thesis, structural and luminescence properties of undoped and doped ZnO and PbS nanostructures (nanorods, nanoflakes, nanoparticles, and nanoflowers) are investigated by different approaches for possible future application of these nanostructures as solar cells and light emitting diodes. Undoped and doped ZnO and PbS nanostructures were grown by chemical bath deposition process. Still it is a challenge for the researchers to produce a stable, reproducible high quality and homogeneously doped ZnO/PbS materials and this seriously hinders the progress of ZnO and PbS nanostructcures to be utilized in various applications.

The first part of the thesis includes synthesis of undoped ZnO nanostructures by controlling the growth parameters such as concentrations of precursors (zinc acetate) and synthesis time. Crystalline zinc oxide (ZnO) flower-like nanostructures were synthesized by the chemical bath deposition (CBD) method. The X-ray diffraction (XRD) pattern for the ZnO flower-like microstructures showed crystalline peaks corresponding to a hexagonal wurtzite ZnO structures. Scanning electron microscopy (SEM) observations showed the presence of microcrystallites forming microflower-like aggregates. In the case where a higher molar concentration of zinc acetate was used in the preparation process the microflower-like

structures were larger in size than that of the lower mol% used. The shape however did not change. The absorption edges red shifted slightly with an increase in the molar concentration of the zinc acetate and in synthesizing time. The band gap energies decreased slightly with an increase in the molar concentration of the zinc acetate and again in synthesizing time. PL showed that the maximum luminescence intensity was reached at the ZnO synthesized for 5 minutes, any further increase in the synthesizing time resulted into the luminescence intensity decrease. An increase in zinc acetate mol% resulted only in a decrease in luminescence intensity. Controlling growth parameters is important in the sense of controlling the physical, electronic, and chemical properties of materials. In order to understand how to tune these properties in the nanostructure, it is necessary to have an understanding of the growth mechanism that dictates the morphology, structure, and rate of growth of the nanomaterial. The ZnO nanostructures (flower-like rods) were later doped with rare-earth elements (e.g. Ce^{3+} and Eu^{3+}) and transition metal (e.g. Cu^{2+}). Flower-like hexagonal ZnO:Ce^{3+} nanostructures obtained for undoped and low mol% of Ce^{3+}. ZnO changed into mixed structure with emergence of pyramids for higher mol% Ce^{3+}. The absorption edges showed that as the molar concentration of Ce^{3+} ions increases the optical absorption edge shift to a higher. The band gap energies decreased linearly with Ce Concentration. The luminescence bands of undoped ZnO nanoflower-like was quenched and shifted from the yellow region to the blue region when ZnO flower-like was doped with different molar concentration of Ce^{3+}.

Eu^{3+} doped ZnO flower-like structures were synthesized. The XRD spectra of the undoped and low concentration Eu^{3+} doped ZnO nanostructures correspond to the various planes of a single hexagonal ZnO phase. In contrast with Ce^{3+} doping, the morphology of the ZnO flower-like rods totally changed to large blocks shape when doped with Eu^{3+} ions. The effective band gap energy of the ZnO decayed exponentially with the addition of Eu^{3+}. The maximum luminescence intensity was also measured for the same sample. Although weak luminescence was observed for excitation above the band gap at 300 nm the best results were obtained by exciting the Eu^{3+} directly through the $^7F_0 \rightarrow {}^5L_6$ absorption band at 395 nm. Excitation at a wavelength of 395 nm produced the highest Eu^{3+} luminescence intensity without any noticeable ZnO defect emissions.

In this work undoped and Cu^{2+}-doped ZnO nanostructures were prepared by the chemical bath deposition (CBD) method.

XRD analysis showed the sample prepared were hexagonal ZnO for undoped and Cu-doped. The presence of Cu^{2+} ions caused the particle size of ZnO flower-like structures to decrease. In the UV-Visible study the reflectance intensity decreased with an increase in the molar concentration of Cu^{2+} and there was no shift in the absorption edges. The luminescence intensity was found to be a maximum for the undoped ZnO flower-like structures and quenched after addition of Cu^{2+} ions.

In the last part of the thesis, the influence of synthesis temperature and molar concentration of lead acetate on the structure, morphology and optical properties of PbS nanoparticles were investigated. The X-ray diffraction (XRD) peaks correspond to the various planes of a single phase cubic PbS. The surface morphology study revealed nanorod structures at low synthesis temperatures but a particulate structure at the high synthesis temperatures. It was also observed that an increase in the molar concentration of lead acetate has no significant influence on the morphology of the PbS nanorods and the crystallite sizes. The reflectance spectra showed a shift of the absorption edge to a higher wavelength with an increase in the synthesis temperature and molar concentration of Pb acetate. The luminescence intensity was found to decrease with an increase in the synthesis temperature and molar concentration of Pb acetates.

The PbS nanoparticles were later doped with Tb^{3+} and co-doped with Ce^{3+} ions. When the Tb^{3+} concentration was increased to 2 mol%, the morphology of the PbS:Tb^{3+} changed to a mixture of spherical nanoparticles and nanorods. The absorption edges of these PbS nanoparticles slightly shifted to higher wavelength depending on the ionic strength of the precursors. The PL result show an increase in emission intensity with an increase in Tb^{3+} ions up to 0.3 mol% Tb^{3+} and decreased there after most probably due to luminescence concentration quenching. A new band at 433 nm was found to emerge as the Tb^{3+} ions increases. Co-doping PbS nanostructures with 0.3 mol% and 2 mol% Ce^{3+}, the spherical nanoparticles changed the morphology to the nanorods surrounded by the spherical nanoparticle. It was also observed that the size of the nanorods increased with an increase in the molar concentration of Ce^{3+} ions.

The nanoparticles showed good optical properties with high reflectance in the UV and visible regions. The absorption edges shifted to higher wavelength with the addition of Tb^{3+} and Ce^{3+}, respectively. The photoluminescence results displayed an optimum increase in luminescence intensity when the ratio of Ce:Tb was 1:10 and further increase in cerium content quenched the luminous intensity. It was observed that as the molar concentration of co-dopant (Ce^{3+}) increased the luminescence band at around 433 nm diminished.

Keywords: ZnO, PbS, Chemical bath deposition, Flower-like, Spherical, Nanorods, Absorption edges, Defects, Photoluminescence

DECLARATION

I (Koao Lehlohonolo Fortune) declare that the thesis hereby submitted by me for the *Philosophiae Doctor* degree at the University of the Free State is my own independent work and has not previously been submitted by me at another university/faculty. I furthermore, cede copyright of the thesis in favour of the University of the Free State.

Signature:…….. Date:……

TABLE OF CONTENTS

Title page i

Dedication ii

Acknowledgement iii

Abstract v

Declaration ix

List of figures xiv

Chapter 1

1. Introduction 1

2. Statement problem 3

3. Aim of this study 4

4. Research objectives 4

4. Thesis layout 5

References 6

Chapter 2: Background

2.1 Semiconductor nanocrystals/nanostructures 8

2.1.1 Shape control of semiconductor nanocrystals 9

2.1.1.1 3D Semiconductors 9

2.1.1.2 2D Semiconductors 10

2.1.1.3 1D Semiconductors 11

2.1.1.4 0D Semiconductors 13

2.1.2 Size control of semiconductor nanocrystals 14

2.1.2.1 Surface-area-to-volume ratio 14

2.1.2.2 The actual size of the particle 15

2.2 Confinement Regimes 16
2.2.1 The strong confinement regime 16
2.2.2 The intermediate confinement regime 17
2.2.3 The weak confinement regime 18
2.3 Luminescence 19
2.3.1 Mechanisms of luminescence 20
2.4 Energy transfer mechanisms 21
2.5 Basic properties of ZnO 24
2.5.1 Defects and luminescence in ZnO 25
2.6 Basic properties of PbS 27
2.9 Effects of doping semiconductors nanostructures 28
References 31

Chapter 3: Experimental Procedure and Overview of Research Techniques.

3.1 Experimental Procedure
3.1.1 Introduction 34
3.2 Synthesis
3.2.1 Synthesis of undoped ZnO, Ce^{3+}, Eu^{3+}, and Cu^{2+} doped ZnO nanostructures 34
3.2.2 Synthesis of undoped PbS, Tb^{3+} and Ce^{3+}-codoped PbS nanostructures 35
3.3 Sample Characterization
3.3.1 Introduction 36
3.3.2 Structural Analysis
3.3.2.1 X-Ray Diffraction 37
3.3.2.2 Scanning Electron Microscope 37
3.3.2.3 Energy Dispersive Spectroscopy 38
3.3.2.4 Tunnelling Electron Microscope 39
3.3.2.5 Auger Electron Spectroscopy 40
3.3.3 Optical Properties
3.3.3.1 Ultraviolet and visible (UV-Vis) Spectroscopy 41

3.3.3.2 Photoluminescence Spectroscopy 42
References 44

Chapter 4: Synthesis and characterization of ZnO flower-like microstructures using the chemical bath deposition method.

4.1 Introduction 46
4.2 Results and Discussions 46
References 56

Chapter 5: The effect of Ce^{3+} on structure, morphology and optical properties of flower-like ZnO synthesized using the chemical bath method.

5.1 Introduction 57
5.2 Results and Discussions 57
References 70

Chapter 6: Effect of Eu^{3+} on structure, morphology and optical properties of flower-like ZnO synthesized using the chemical bath method.

6.1 Introduction 72
6.2 Results and Discussions 73
References 82

Chapter 7: The effect of Cu^{2+} on structure, morphology and optical properties of flower-like ZnO synthesized using the chemical bath method

7.1 Introduction 84
7.2 Results and Discussions 84
References 90

Chapter 8: Synthesis of PbS nanostructures by chemical bath deposition method.

7.1 Introduction 91
7.2 Results and Discussions 91
References 100

Chapter 9: Effect of Tb molar concentration on optical properties of lead sulphide nanoparticles.

7.1 Introduction 102
7.2 Results and Discussions 102
References 112

Chapter 10: Optical properties of undoped, Tb^{3+} doped and Ce^{3+} co-doped nanoparticles synthesized using chemical.

7.1 Introduction 114
7.2 Results and Discussions 115
References 126

Chapter 11: Summary, Conclusion and future work.

Conclusion 128
Future work 133
Publications 134
Conferences 137

LIST OF FIGURES

1. Figure 2.1: Show the bulk density of states (DOS) in 3-D 10
2. Figure 2.2: Show the density of states (DOS) in 2-D 11
3. Figure 2.3: Show the density of states (DOS) in 1-D 12
4. Figure 2.4: Show the density of states (DOS) in 0-D 13
5. Figure 2.5: Excitation formation upon absorption of an incident photon 16
6. Figure 2.6: Illustration of the strong confinement regime 17
7. Figure 2.7: Illustration of the intermediate confinement regime 18
8. Figure 2.8: Illustration of the weak confinement regime 19
9. Figure 2.9: Show the electronic state singlet and triplet 20
10. Figure 2.10: A schematic diagram to illuminate the different ET processes 22
11. Figure 2.11: The hexagonal wurtzite structure of ZnO 24
12. Figure 2.12: The schematic representation of the position of various intrinsic defect levels emission within ZnO 26
13. Figure 2.13: The cubic structure of PbS 28
14. Figure 3.1: Illustration of the effect occurring during EDS 38
15. Figure 3.2: An example of an Auger process 40
16. Figure 4.1: XRD patterns for ZnO structures prepared different molar concentrations of zinc acetate at constant synthesizing time and annealed at ambient condition 47
17. Figure 4.2: XRD patterns for ZnO structures prepared different mol% of zinc acetate at constant synthesizing time and annealed at ambient condition 48
18. Figure 4.3: The dependence of average particle sizes of the ZnO on the zinc acetate concentration for different synthesis time 48
19. Figure 4.4: SEM images of ZnO microstructures for (a) 0.56M and (b) 0.86M Zinc acetate concentration synthesized at constant time 49
20. Figure 4.5: Representative of TEM image of the ZnO microflower-like structures prepared at 0.56 molar concentration of Zinc acetate for a constant time of 5 min 49

21. Figure 4.6: Representative EDS spectra of the ZnO microflower-like structures prepared at different mol% of Zinc acetate for a constant time of 5 min and the Zn peak of the two different mol% samples as inset 50
22. Figure 4.7: The reflectance spectra for ZnO structures prepared at different synthesizing times but constant mol% concentrations and annealed at ambient condition 51
23. Figure 4.8: The reflactance spectra for ZnO structures prepared different mol concentrations of zinc acetate at constant synthesizing time and annealed at ambient condition 51
24. Figure 4.9: Plot to determine the band gap energy of ZnO structures prepared at different synthesizing times but constant mol% concentrations and annealed at ambient condition 52
25. Figure 4.10: Plot to determine the band gap energy of ZnO structures prepared at prepared different mol% concentrations of zinc acetate at constant synthesizing time and annealed at ambient condition 53
26. Figure 4.11: The PL spectra of ZnO microstructures prepared at different synthesizing time but synthesized at constant mol% concentration of zinc acetate prepared by the CBD method 54
27. Figure 4.12: The PL spectra of ZnO microstructures prepared at different mol% concentrations of zinc acetate at constant synthesizing time and annealed at ambient condition 54
28. Figure 5.1: X-ray powder diffraction patterns for undoped and Ce-doped ZnO prepared by the CBD method 58
29. Figure 5.2: X-ray powder diffraction patterns for 10 mol % Ce-doped ZnO prepared by the CBD method and standard files of Zn- and Ce acetate 59
30. Figure 5.3: XRD patterns at (100) for undoped and Ce-doped ZnO prepared by CBD method 60
31. Figure 5.4: The graph of average grain size versus the molar concentrations of Ce^{3+} ions for undoped and Ce-doped ZnO 61
32. Figure 5.5: SEM images of (a) ZnO:0 mol % Ce^{3+}, (b) ZnO:3 mol % $Ce^{3+}$and (c) ZnO:10 mol % Ce^{3+}, illustrating the effect of different molar concentrations of Ce^{3+} on the ZnO structures 62

33. Figure 5.6: AES SEM images of (a) ZnO: 0 mol % Ce^{3+} and (b) ZnO: 10 mol % Ce^{3+}, illustrating the effect of different molar concentrations of Ce^{3+} and (c) one of the pyramids shape of ZnO:10 mol % Ce^{3+} ions 63
34. Figure 5.7: Auger spectra of the ZnO: 0 mol % Ce^{3+}, ZnO: 0.5 mol % Ce^{3+} and ZnO: 10 mol % Ce^{3+} ions prepared by the CBD method 64
35. Figure 5.8: Auger spectra and calculated concentrations of the ZnO: 10 mol% Ce^{3+} sample measured at the two areas as indicated on the SEM image 64
36. Figure 5.9: The absorbance spectra of undoped and Ce doped ZnO prepared by the CBD method 65
37. Figure 5.10: Plot to determine the band gap energy of undoped and Ce doped ZnO prepared by the CBD method 66
38. Figure 5.11: Dependence of band gap energies of the ZnO on the amount of Ce ion dopants 66
39. Figure 5.12: PL patterns for undoped and Ce-doped ZnO showing all the emissions within the visible and infrared range prepared at a different mol concentrations of cerium acetate with the inset PL spectra of the undoped and Ce^{3+} (0.1 mol %)-doped ZnO flower-like, with an excitation wavelength of 248 nm 67
40. Figure 5.13: PL fitted spectra of ZnO:0.3 mol % Ce^{3+} prepared by the CBD method 68
41. Figure 6.1: X-ray powder diffraction patterns for undoped and Eu-doped ZnO prepared by CBD method 73
42. Figure 6.2: X-ray powder diffraction patterns for 4 mol% Eu-doped ZnO prepared by the CBD method and standard files of Zn acetate and Eu nitrate 74
43. Figure 6.3: X-ray powder diffraction patterns at (101) for undoped and Eu-doped ZnO prepared by CBD method 75
44. Figure 6.4: Figure 4: SEM images of (a) 0 mol% Eu (b) 0.5 mol% Eu (c) 1mol% Eu and (d) 4 mol% Eu, illustrating the effect of different molar concentrations of Eu^{3+} 75
45. Figure 6.5: The reflectance spectra of undoped and doped ZnO nanostructures prepared by CBD method 77
46. Figure 6.6: Plot to determine the band gap energy of undoped and doped ZnO nanostructures prepared by CBD method 77

47. Figure 6.7: Dependence of band gap energies of the ZnO on the amount of Eu ion dopants 78

48. Figure 6.8 (a): PL emission spectra for undoped and Eu-doped ZnO nanostructures with different concentrations of Eu^{3+} with excitation wavelength of 395 nm with the inset the variation of the luminescence intensities as function of Eu dopant concentrations at 616 nm 79

49. Figure 6.8(b): PL emission spectra for undoped and Eu-doped ZnO nanostructures with different concentrations of Eu^{3+} with excitation wavelength of 300 nm 79

50. Figure 6.9: The deconvolution of the luminescence spectra taken from ZnO nanostructures doped with 3 mol% of Eu with the inset PL spectra of the undoped ZnO flower-like synthesized by the chemical bath method and both excited at 300 nm 81

51. Figure 7.1: X-ray powder diffraction patterns for undoped and Cu-doped ZnO prepared by CBD method 85

52. Figure 7.2: SEM images of (a) 0 mol% Cu (b) 0.1 mol% Cu (c) 0.5 mol% Cu and (d) 2 mol% Cu, illustrating the effect of different molar concentrations of Cu^{2+} 86

53. Figure 7.3: The reflectance spectra of undoped and doped flowers-like ZnO prepared by CBD method 87

54. Figure 7.4: Plot to determine the band gap energy of undoped and doped ZnO flower-like prepared by CBD method 87

55. Figure 7.5: PL emission spectra for undoped and Cu-doped ZnO flower-likes at different molar concentrations of Cu acetate, with excitation wavelength of 325 nm using He-Cd laser at room temperature 89

56. Figure 7.6: Dependence of emission intensity of the ZnO-Cu flower-like on the concentration of Cu and it was fitted with exponential decay first order 89

57. Figure 8.1: XRD patterns of PbS prepared at different synthesis temperatures but at constant molar concentration of lead acetate. 92

58. Figure 8.2: XRD patterns of the (111) planes of the PbS powders prepared by the CBD method. 92

59. Figure 8.3: The dependence of average grain sizes of the PbS on the the synthesis temperature of the CBD 93

60. Figure 8.4: XRD patterns of PbS samples prepared with different molar concentration of lead acetates and constant synthesis temperature using the CBD method 94
61. Figure 8.5: The SEM micrograph of PbS powders synthesized at the various temperatures: (a) 55 ºC, (b) 65 ºC, (c) 70 ºC and (d) 80 ºC but at constant molar concentration of lead acetate 95
62. Figure 8.6: The SEM micrograph of PbS powders synthesized at the various molar concentrations of Pb acetate: (a) 0.12 M, (b) 0.13 M and (d) 0.14 M and constant synthesis temperature 95
63. Figure 8.7: The absorbance spectra of PbS powders prepared at various temperature and at constant molar concentration of lead acetate 96
64. Figure 8.8: The absorbance spectra of PbS powders prepared at various molar concentration of lead acetates at constant synthesis temperature 97
65. Figure 8.9: PL emission spectra of PbS nanostructures in the visible region and for infrared region (as an inset) synthesized at various synthesis temperatures and with the deconvolution of the luminescence spectra taken from the 65 ºC of synthesis temperature 98
66. Figure 8.10: PL emission spectra of PbS nanostructures in the visible region and for the near infrared region (as an inset) synthesized at various lead acetate molar concentrations at constant synthesis temperature 99
67. Figure 9.1: X-ray powder diffraction patterns for undoped and Tb^{3+} doped PbS prepared by the CBD method 103
68. Figure 9.2: X-ray powder diffraction patterns at (111) for undoped and 2 mol% Tb^{3+}-doped PbS prepared by the CBD method 104
69. Figure 9.3: SEM images of (a) PbS: 0, (b) PbS: 0.3 (c) PbS: 1 and PbS: 2 mol% Tb^{3+} 105
70. Figure 9.4: TEM images of (a) PbS: 0, (b) PbS: 0.5 (c) PbS: 1 and (c) PbS: 2 mol% Tb^{3+} 105
71. Figure 9.5: A representative EDX spectrum of the 2 mol% Tb^{3+} doped PbS nanoparticles prepared by the CBD method 106
72. Figure 9.6: Auger spectra of the undoped PbS nanoparticles prepared by the CBD method 106
73. Figure 9.7: The reflectance spectra of undoped and Tb^{3+}-doped PbS nanoparticles 107

74. Figure 9.8: The variation of maximum absorption edges of the PbS on the amount of Tb^{3+} ion dopants 108
75. Figure 9.9: PL spectra of undoped PbS nanostructures showing the visible and the IR emissions as an inset 109
76. Figure 9.10: PL emission spectra in the visible and infrared region (shown as an inset) for undoped and Tb^{3+}-doped PbS nanostructures at different molar concentrations of Tb nitrate excited at a wavelength of 276 nm using a Xenon lamp 110
77. Figure 9.11: Maximum intensity of PbS nanoparticles at 376 nm and 433 nm (inset) as function of Tb^{3+} (mol%) 110
78. Figure 10.1: Represented XRD spectra of undoped, Tb-doped, Ce-doped and Tb-Ce co-doped PbS nanoparticles prepared by the CBD method 115
79. Figure 10.2: A representative of X-ray powder diffraction patterns at (111) for of undoped, Tb-doped, Ce-doped and Tb-Ce co-doped PbS nanoparticles prepared by the CBD method 116
80. Figure 10.3: SEM images of (a) PbS, (b) PbS: 1 mol% Tb^{3+}, (c) PbS: 1 mol% Ce^{3+} (d) PbS: 1 mol% Tb^{3+}: 0.3 mol% Ce^{3+} and (e) PbS: 1 mol% Tb^{3+}: 2 mol% Ce^{3+} illustrating the effect of dopant and co-dopant molar concentrations on PbS 117
81. Figure 10.4: TEM images of (a) PbS, (b) PbS: 1 mol% Tb^{3+} (c) PbS: 1 mol% $Tb^{3+:}$ 0.3 mol% Ce^{3+} and PbS: 1 mol% Tb^{3+}: 2 mol% Ce^{3+} illustrating the effect of dopant and co-dopant molar concentrations on PbS 118
82. Figure 10.5: A representative EDX spectrum of the PbS: 1 mol% Tb^{3+}: 2 mol% Ce^{3+} doped PbS nanoparticles prepared by the CBD method 119
83. Figure 10.6: Auger spectra of the undoped PbS nanoparticles prepared by the CBD method 119
84. Figure 10.7: The reflectance spectra of of undoped, Tb-doped, Ce-doped and Tb-Ce co-doped PbS nanostructures at different molar concentrations of Ce acetate and holding Tb nitrate constant 120
85. Figure 10.8: The dependence of maximum absorption edges of the PbS on the amount of Ce ion dopants 121

86. Figure 10.9: PL spectra of of undoped, Tb-doped and Ce-doped PbS nanostructures showing visible and with the inset IR (as an inset) emissions prepared by the CBD method and with the deconvolution of the luminescence spectra taken from undoped PbS 122
87. Figure 10.10: PL emission spectra for undoped, Tb-doped, Ce-doped and Tb-Ce co-doped PbS nanostructures at different molar concentrations of Ce acetate and holding Tb nitrate constant excited at wavelength of 276 nm using Xenon lamp 123
88. Figure 10.11: PL emission spectra for of undoped, Tb-doped, Ce-doped and Tb-Ce co-doped PbS nanostructures at different molar concentrations of Ce acetate and holding Tb nitrate constant showing emissions in the IR region 124
89. Figure 10.12: Maximum PL intensity of PbS nanoparticles at 376 nm and 433 nm (inset) prepared by the CBD method as function of Xmol% Ce/Tb (1 mol%) 125

Chapter 1: Definition of the research work

1. Introduction

Nanotechnology has developed a bridge among all the fields of science and technology. Materials and structures with low dimensions have excellent properties which enable them to play a crucial role in the rapid progress of the fields of science. With these amazing properties, one dimensional nanostructure has become the back bone of research in all the fields of natural sciences.

The investigation of materials at the nano-scale has gained a great deal of interest as it fills the gap between bulk and atoms or molecules, thus improving our understanding of fundamental properties and providing new physical effects. This has been one of the hottest areas of research in the last twenty years **[1, 2]**, fueled by the shrinking approach in device fabrication for optoelectronics and electronics. Up to date, many achievements have been reported in this field, which were a joint effort of physicists, chemists, biologists and material scientists. By controlling their size/shape and/or their chemical compositions, the electronic and optical properties of semiconductor nanocrystals, also called quantum dots (QDs), can be manipulated **[1, 3]**. Decreasing its dimensions to smaller pieces with 100 nm average lengths will not influence the band gap, but further decrease of its dimensions less than 10 nm will change its band gap and cause it to show some new properties such as visible light or enough catalytic activity for specification reaction. In particular, the confinement of the electron and hole in all spatial directions is responsible for atomic-like energy levels and physical properties.

Quantum dots can be produced by different techniques. Colloidal chemistry provides an attractive method of fabricating high quality nanocrystals. Being not attached to any surface, colloidal QDs are promising candidates to be used as building blocks for ordered structures, such as superlattices **[3, 4]**.

Semiconductors are materials that have intermediate conductivity between a conductor like aluminium and an insulator like a glass. Semiconductors are available as either elements or compound. Silicon and Germanium are the most common elemental semiconductors. Compound semiconductors include GaP, PbS and ZnO. Semiconductors are especially important because varying conditions like temperature and impurity (dopant) content can easily alter their conductivity. The semiconductors are important since they cover the

transition from the bulk to atomic regime, they are the perfect model system to observe, study size dependent and morphological dependent and physical properties that are governed by charge carrier motion.

Semiconductors are widely studies as photoactive material for optoelectronic devices such as photodetectors **[5]**, light emitting diodes **[6]** and solar cells **[7]**. Their attractions arises from their low synthetic cost, their solution processing ability and the dependence of their optoelectronic properties as a function of size, shape, doping and surface chemistry **[8-9]**. Recently there has been a growing interest in controllable synthesis of low-dimensional semiconductors nanoscale material with well-defined morphology due to their novel optical, electronic and potential applications in the fields of photonic and electronic devices **[6-13].** Many considerable efforts have been devoted to the development of synthesis methodologies for semiconducting nanostructures (nanocubes, nanorods, nanowires, nanobelts, nanotubes and nanostar) **[10-18]**. Most of the semiconductor nanostructure have been synthesized by traditional high temperature solid state method and again the final products were annealed at high temperatures which is energy consuming and difficult to control the particle size and morphology **[14-19]**.

The global research interest in wide band gap semiconductors has been significantly focused to zinc oxide (ZnO) due to its excellent properties as a semiconductor material. The high electron mobility, high thermal conductivity, good transparency, wide and direct band gap (3.37 eV), large exciton binding energy and easiness of growing it in the nanostructure form by many different methods make ZnO suitable for wide range of uses in optoelectronics, transparent electronics, lasing and sensing applications **[20-24]**. In last decade, the number of publications on ZnO has increased annually and in 2007 ZnO has became the second most popular semiconductor after Si and its popularity is still increasing with time [**25**].

Bulk Lead Chalcogenides are already employed in several applications, for instance, thermoelectronics, infrared (IR) lasers, IR-light emitting diodes, IR detectors, solar energy panels **[26]**. The ability to tune the photon emission of lead chalcogenide QDs in the near infrared region of the electromagnetic spectrum makes this type of QD suitable for several applications. PbS colloidal QDs belong to a class of IV-VI nanocrystals with narrow energy gaps to relevant for optical applications in the near-IR region of the electromagnetic spectrum such as long wavelength (1.3 and 1.55 μm) telecommunications [**26**], photovoltaics [**27**] and bioimaging in the spectroscopic window of low absorption of biological systems (1-1.2 μm) [**28**]. Bulk lead sulfide (PbS) has a small hole mass, which is almost equal to the mass of the electron. This leads to a large exciton Bohr radius R_{ex} ~ 18 nm. Owing to these properties,

electrons and holes, and hence the exciton, can be strongly confined. This is not always feasible in other semiconductors because of the different electron and hole effective masses [**29**]. Thus this system provides an ideal platform to investigate the exciton in the strong confinement regime.

In recent years, rare-earth (RE) and transition metal (TM) doped semiconductors nanostructured materials have attracted great attention in both fundamental studies and applications **[23-29]**. The rare earth elements (RE) have had and still have a unique and important impact on our lives. The unfilled 4f electronic structure of the rare earth elements makes them have special properties in luminescence, magnetism and electronics. Doping nanostructures with optically active luminescent materials manipulate the band structure of the nanocrystals by inducing radiative recombination of the excited electron-hole pair, which shifts the photoluminescence wavelengths and increases quantum efficiency. The doping also plays key roles in luminescence efficiency and show intense emissions in a wide range of wavelength depending on the dopant type, concentration and crystal dimensions, thus influencing their practical application. Lastly the doping of semiconductor nanoparticle with TM ions like Cu^{2+} are known to yield different nanostructures **[29-30]**, describe the importance roles of crystal structure and shape of the nanocrystals in optimizing the efficiency of TM-doped nanocrystals **[9].**

2. Statement of the problem.

Research on nanostructures is motivated by the exceptional properties that a material gains when its size is reduced to nanoscale lengths. Quantum dots are nano-sized semiconductors or metals that have diameter in the range between 1 and 100 nm, and contain a limited number of atoms. The trend in reducing the size of semiconductors is fueled by the (sub) micron-fabrication and computing industry. Thus studying the properties of these materials is crucial.

The nanotechnology has seen fast development in recent years. Companies are looking at beginning to research and develop products with nanotechnology in mind and their developments will be closely watched. Nanotechnology has begun to seep into the national (and international) consciousness and awareness and is being spoken about as revolutionizing technology that will change everything from basic building materials to computers to medicine. With all of this promise and frantic development, a simple, yet important, quantum dots (QD) with more effective and better physical and biological PL probes are yet to be

designed? Several synthesis method have been used to prepare semiconductor nanostructures, these can classified into five approaches: gas phase **[23-31]**, wet chemical (co-precipitation) **[24-32]**, sol-gel **[25-33]**, chemical bath method [**26-34]** and micro-emulsion **[27-35]**. Most of these methods are expensive, they need high temperature for synthesis and they take a lot of time for synthesis and very difficult to operate.

Previous attempts at doping CdSe, PbSe and ZnSe nanostructures frequently yielded inhomogeneously doped materials. The frequent failure of doping schemes was, until recently, attributed to the expulsion of dopant ions to the surface of nanocrystals by the intrinsic process of self-annealing or the ability of the ions to adsorb to the exposed surfaces of the nanocrystals. It appears; therefore, that successful doping of nanocrystals can be achieved by involving nanocrystals of the right size and morphology and choosing surfactants that do not bind too strongly to the dopant ions.

3. Aim of the study

- The project focuses on possibility of engineering band gap and influencing physical, chemical, and opto-electronic properties of ZnO(S) and PbS(S) by varying the dimensions of the system by changing the diameters and the composition of nanostructures. The ZnO(S) and PbS(S) nanostructures with various sizes, shapes and compositions will be studied with different techniques i.e. photoluminescence (PL) spectroscopic.
- Synthesis of undoped and doped semiconducting nanostructures by chemical bath deposition method due to its many advantages such as low cost, low temperature production, scalable and simplicity in instrumental operation. It is also easier to get homogeneous, smaller grain size and able to control the morphologies of nanomaterials due to low synthesis temperature (< 100 ºC).

4. Research objectives.

The general objective is to carry out the research and development to form foundation for future application of undoped and doped semiconducting (ZnO and PbS) nanostructures. The specific objectives to achieve:

- To investigate the dependence of morphological, compositional, structural, optical and photoluminescence properties of the synthesized ZnO nanostructures on the precursor constituents and the synthesis time.

- Synthesis and characterization of Ce^{3+} doped ZnO nanostructures, in order to study the effect of dopant (Ce^{3+}) on structure, morphology and optical properties.
- To investigate effect of Eu^{3+} molar concentration on the structure, morphology and optical properties of ZnO synthesized using the chemical bath method.
- To investigate the influence of Cu^{2+} ion concentration in the material properties on the ZnO nanostructures.
- To investigate the effect of synthesis temperature and molar concentration of lead acetate on the structure, morphology and optical properties of PbS nanoparticles prepared by chemical bath deposition method.
- Investigate effect of terbium molar concentration on optical properties of lead sulfide nanoparticles.
- To investigate the dependence of morphology, structure, optical and luminescence properties of Tb doped PbS on the amount of the co-dopant the Ce ions.

4. Thesis Layout.

This thesis is structured as follows: In Chapter 2, literature survey and background information is presented on the relevant theoretical aspects of present research on synthesis and characterization of undoped and doped semiconductors nanostructures. The shape control of semiconductor nanostructure is discussed. Attention is also focused on the luminescence properties, quenching mechanisms and the energy transfer mechanisms and the growth conditions of these nanostructures. The experimental procedures followed during the preparation of undoped and doped semiconductor nanostructures as well as the characterization techniques used are discussed in detail in chapter 3. A large number of structural, morphological and optical and luminescence characterization techniques were used in this study and these are thus discussed in this chapter. The experimental results that followed from the detailed study of the influence of growth parameters and the doping effects on the ultimate nanostructures material quality are presented and discussed in Chapter 4, 5, 6,7, 8, 9 and 10. These results take the form of SEM micrographs, PL, EDS and XRD measurements of composition as well as x-ray diffraction patterns to determine the presence of crystalline phases. Finally, in Chapter 11, the most significant results are summarized and conclusions are drawn, with suggestions for future research.

Reference

[1]. A. L. Rogach, A. Eychmuller, S. G. Hickey, and S. V. Kershaw, *Small*, **3(4)** (2007)536–557.

[2]. A. P. Alivisatos, *Sci*, **271(5251)** (1996) 933–937.

[3]. J. Hollingsworth, and V. Klimov, *Semiconductor and Metal Nanocrystals: synthesis and Electronic and Optical properties, chapter 'Soft' Chemical Synthesis and Manipulation of Semiconductor Nanocrystals*, New York: Marcel Dekker, Inc. (2004) 1–64.

[4]. A. Zrenner, *J. Chem. Phys.* **112 (18)** (2000) 7790–7798.

[5]. G. Konstantatos, J. Clifford, L. Levina, E. H. Sargent, *Nat. Photon*, **1** (2007) 531-534.

[6.] G. Konstantatos, C. Huang, L. Levina, Z. Lu, E. H. Sargent, *Adv. Funct. Mater*. **15** (2005) 1865-1869.

[7]. W. U. Huynh, J. J. Dittmer, A. P. Alivisatos, *Science*, **295** (2002) 2425-2427.

[8]. A. P. Alivisatos, *J. Phys. Chem*, **100** (1996) 13226-13239.

[9]. S. C. Erwin, L. Zu, M. I. Haftel, A. L. Efros, T. A. Kennedy, D. J. Norris, *Nature*, **43** (2005) 91-94.

[10]. S. A. Studenikin, N. Glego, M. Cocivera, *J. Appl. Phys*, **84** (1998) 2287-2294.

[11]. W. Wang, L. Wang, L. Liu, C. He, J. Tan, Y. Liang, *Cryst. Eng. Comm*, **14** (2012) 4997-5004.

[12]. Y. Jun, J. Jang, and J. Cheon, *Bull. Korean Chem. Soc*. **27 (7)** (2006) 961-971.

[13]. J. Kossanyi, D. Kouuyate, J. Pouliquen, J. C. Ronfard-Haret, P. Valat, *J. Lumin*, **46** (1990) 17-24.

[14]. H. Cao, G. Wang, S. Zhang, X. Zhang, *Nanotechnology*, **17** (2006) 3280-3287.

[15]. A. B. Djurišić, Y. H. Leung, K. H. Tam, *Appl. Phys. Lett*. **88** (2006) 103107-1 to 103107-4.

[16]. B. Cheng, Z. Zhang, H. Liu, Z. Han, Y. Xiao and S. Lei, *J. Mater. Chem*, **20** (2010) 7821-7826.

[17]. F. Ochanda, K. Cho , D. Andala , T.C. Keane , A. Atkinson , W. E. Jr Jones, *American Chemical Society*, **25 (13)** (2009) 7547-7552.

[18]. N. Zhao, L. Li, T. Huang, L. Qi, *The Royal Society of Chemistry*, **2** (2010) 2418-2423.

[19]. W. Q. Peng, S. C. Qu, G. W. Cong, Z. G. Wang, *Mater. Sci. Sem. Process*, **9** (2006) 156-159.

[20]. A. Janotti and C. G. Van de Walle, *Rep. Prog. Phys.* **72** (2009) 126501:1-126501:30

[21]. M. Willander, O. Nur, Q. X. Zhao, L. L. Yang, M. Lorenz, B. Q. Cao, J. Zúñiga Pèrez, C. Czekalla, G. Zimmermann, M. Grundmann, A. Bakin, A. Behrends, M. Al-Suleiman, A.

El-Shaer, A. Che Mofor, B. Postels, A. Waag, N. Boukos, A. Travlos, H. S. Kwack, J. Guinard and D. Le Si Dang, *Nanotechnology*, **20** (2009) 33200:1-332001:41

[22]. Z. L. Wang, *Materials Today*, **7** (2004) 26-33

[23]. Ü. Özgür, Ya. I. Alivov, C. Liu, A. Teke, M. A. Reshchikov, S. Doğan, V. Avrutin, S. -J. Cho and H. Morkoç, *J. Appl. Phys*. **98** (2005) 041301:1-041301:104

[24]. P. Klason, *Zinc oxide bulk and nanorods, A study of optical and mechanical properties*, PhD thesis, University of Gothenburg, (2008)

[25]. A. L. Rogach, A. Eychmuller, S. G. Hickey, S. V. Kershaw, *Small*, **3(4)** (2007) 536–557.

[26]. S. A. McDonald, G. Konstantatos, S. G. Zhang, P. W. Cyr, E. J. D. Klem, L. Levina, E. H. Sargent, *Nature Materials*, **4(2)** (2005) 138–142.

[27]. B. -R. Hyun, H. Chen, D. A. Rey, F. W. Wise, C. A. Batt, *J. Phys. Chem B*, **111(20)** (2007) 5726–5730.

[28]. X. S. Zhao, I. Gorelikov, S. Musikhin, S. Cauchi, V. Sukhovatkin, E. H. Sargent, E. Kumacheva, *Langmuir*, **21(3)** (2005) 1086–1090.

[29]. B. Bodo, P. K. Kalita, *AIP. Conf. Proc*. **1276** (2010) 31-35.

[30]. R. N. Bhargava, D. Gallagher, *Phys. Rev. Lett*. **72** (1994) 416-419.

[31]. C. Kaito, Y. Saito, K. Fujita, *Jpn. J. Appl. Phys*. **26** (1987) 1973-1975.

[32]. T. Saraidarov, R. Reisfeld, *J. Sol-Gel. Sci and Techn*, **26** (2003) 533–540.

[33]. T. Saraidarov, R. Reisfed, A. Sashchiuk, E. Lifshitz, *J. Sol-Gel. Sci and Techn*, **34 (**2005) 137-145.

[34]. L. F. Koao, F. B. Dejene, H. C. Swart, *SAIP'2011 Proceedings, the 56th Annual Conference of the South African Institute of Physics, edited by I. Basson and A.E. Botha (University of South Africa, Pretoria)*, ISBN: 978-1-86888-688-3 (2011) 151-155.

[35]. W. Xu, Y. Shen, A. Xie, F. Huang, *Russian. J. Physi. Chem A*, **83** (2009) 2297-2301.

Chapter 2: Background

2.1 Semiconductor nanocrystal/nanostructure

Nanocrystal or nanoparticle (not fully crystalline) is defined as a particle with size in range of 1 to 100 nm from zero (0D) to three dimensions (3D), which exhibits the unique physiochemical properties due to the quantum size effect that cannot be anticipated from bulk counterparts. Nanocrystals can be formed in a variety of shapes including dot, sphere, cube, rod, triangle, hexagon and many others. In this size range, they possess an immense surface area per unit volume, a very large percentage of atoms in the surface. As results, their unexpected properties can be obtained as compared to those of both individual atoms/molecules and bulk counterpart of the same chemical composition. The size and the shape of the semiconductor nanocrystals are crucial parameters for controlling nanocrystals properties. Semiconductor nanocrystals display unique optical, electronic and energetic properties that are dependent upon their size, shape and surface morphology **[1-3]**. One of the challenge or key elements for utilizing semiconductor nanocrystals in nanotechnology applications is the ability to control the crystal growth parameters in order to prepare anisotropic structures in the formation of nanocrystals.

Recently, the effects of nanocrystals shape have received great attention because unique behavior is expected in the evolution from zero-dimensional quantum dots to one dimensional (1D) quantum rods or quantum wires **[4]**. The early studies of anisotropic nanocrystals show that nanostructures of different shapes (e.g. QR and QW) can offer new possibilities for tailoring material properties and offer improved perfomance. Semiconductors with widely tunable energy band gap are considered to be materials for the next generation flat displays, photovoltanic, optoelectronics devices, lasers, sensors and photonic band gap devices **[5].**

The electronic band of the crystal is gradually quantized starting from the band edges as a function of size reduction resulting in an increase in the band gap energy. The following chapter provides the reader with a basic understanding of quantum size effects in semiconductor nanocrystals. We will also review the key issues that need to be carefully considered for the shape and size control of the semiconductor nanocrystals.

2.1.1 Shape control of semiconductor nanocrystals

When the shape of a semiconductors material is changed there is a dramatic change in their optical and electrical properties. There are different classifications of nanostructures in nanotechnology. Nanostructures are usually classified by their geometrical shape. Nanostructures usually consist of nanoparticles, nanopillars, nanopin films, nanorods, nanoshells, nanopowders, nanoclusters, nanowires, nanotubes, nanocrystallites, nanobelts, nanoneedles, nanofibers, nanoflakes, nanoflowers, nanofoams, nanomeshes, quantum dots, quantum heterostructures and sculptured thin films **[6, 7].** Nanostructures can be described as zero (0D), one (1D), two (2D), and three dimensional (3D) nanomaterials. Below we discuss different types of dimensional:

2.1.1.1 3-Dimenional semiconductors (3D)

The three dimensional nanomaterial are so named because they are not confined to the nanoscale in all three dimensions, i.e. if all three dimensions are not reduced, the material is called macro particles. In micro particles, the surface to volume ratio is small and surface effect does not dominate. Optical properties of the macro particles cannot be easily tuned with particle size. The band gap cannot be controlled with the change in size of the macro material, so the different colored emission cannot be observed from the same material. In bulk (Macro), the dimensions of the semiconductor crystal are much larger than theoretical exciton Bohr radius, allowing the exciton to extend to its natural limit. Figure 2.1 shows the dimensionality of a semiconductor system of 3D bulk semiconductor. In three dimensions (Bulk), the electron density of states is given by **[8]:**

$$g(E)_{3D} = \frac{1}{2\pi^2}\left(\frac{2m}{\hbar^2}\right)^{\frac{3}{2}} E^{\frac{1}{2}} \qquad (2.1)$$

It is clear from equation 2.1 that the density of state $\left(g(E)\right)$ is proportional to energy $E^{\frac{1}{2}}$. This gives the density of states per unit volume per at wave vector k, which is in terms of the parabolic equation, where $y = g(E)_{3D}\,dE$ and $x = E^{\frac{1}{2}}$. Density of states is essentially the number of different states at particular energy level that electrons are allowed to occupy, i.e. the number of electron states per unit volume per unit energy.

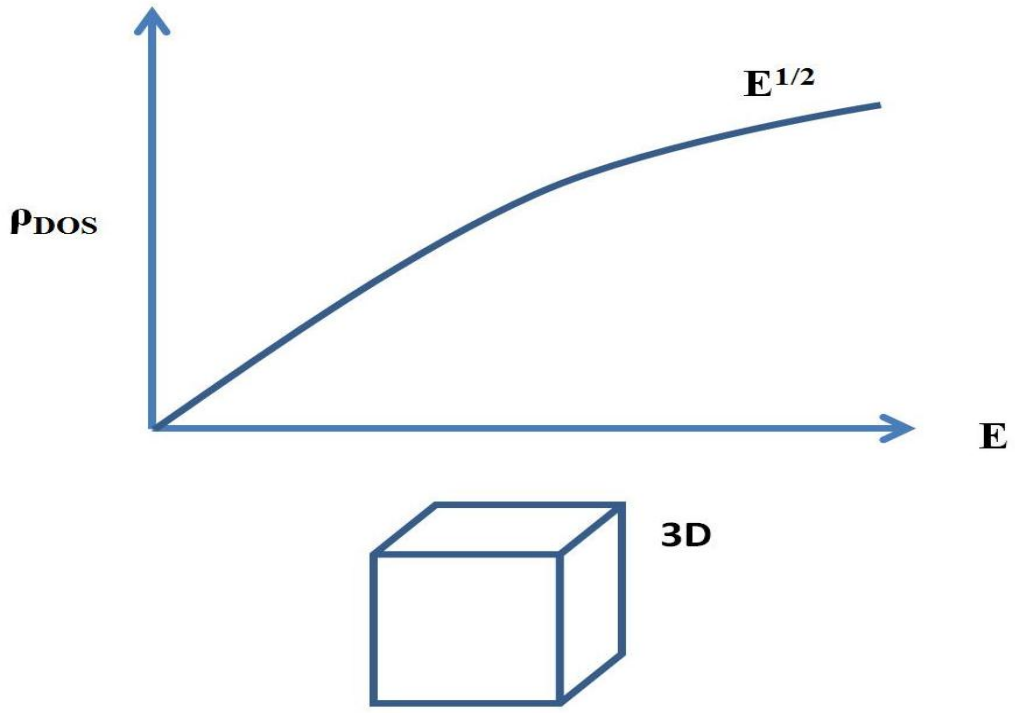

Figure 2.1: Show the bulk density of states (DOS) in 3D, which shows the smooth square-root function of energy [9].

2.1.1.2 2-Dimensional semiconductors (2D)

Two dimensional nanostructures have been studied and categorized as thin films. Thin films have been developed and used for significant amount of time in fields of electric devices and photovoltanic applications **[10]**. Thin film nanostructures are especially good for highly efficient conversion of light to electrical power in photovoltanic cell devices due to their large surface area **[11]**. The two dimensional nanomaterial's are so named because they have been confined to the nanoscale in only one dimension. The one dimension is reduced to nanometer range, so that the size is comparable to the de-Broglie wavelength of the exciton, while other two dimensions remain large, one obtains a structure known as quantum well (quantum film). In particular, when the thickness of the film is of the order of the de-Broglie wavelength of the electron, quantization of the electron levels due to the size of the film introduces new size effects. It is important that the film thickness approaches the atomic level. In two dimensions, the electronic density of the states is given by **[8]:**

$$g(E)_{2D} = \frac{m}{\pi\hbar^2} \qquad (2.2)$$

It is clear that the two dimensional density of states does not depend on energy. Immediately, as the top of the energy-gap is reached, a significant number of states are available. Figure 2.2 shows the reductions of the dimensionality of a semiconductors system from 3D to 2D, from a bulk semiconductor to a quantum films. The discrete energy level along the confined direction gives rise to a staircase-like density of states as a function of energy.

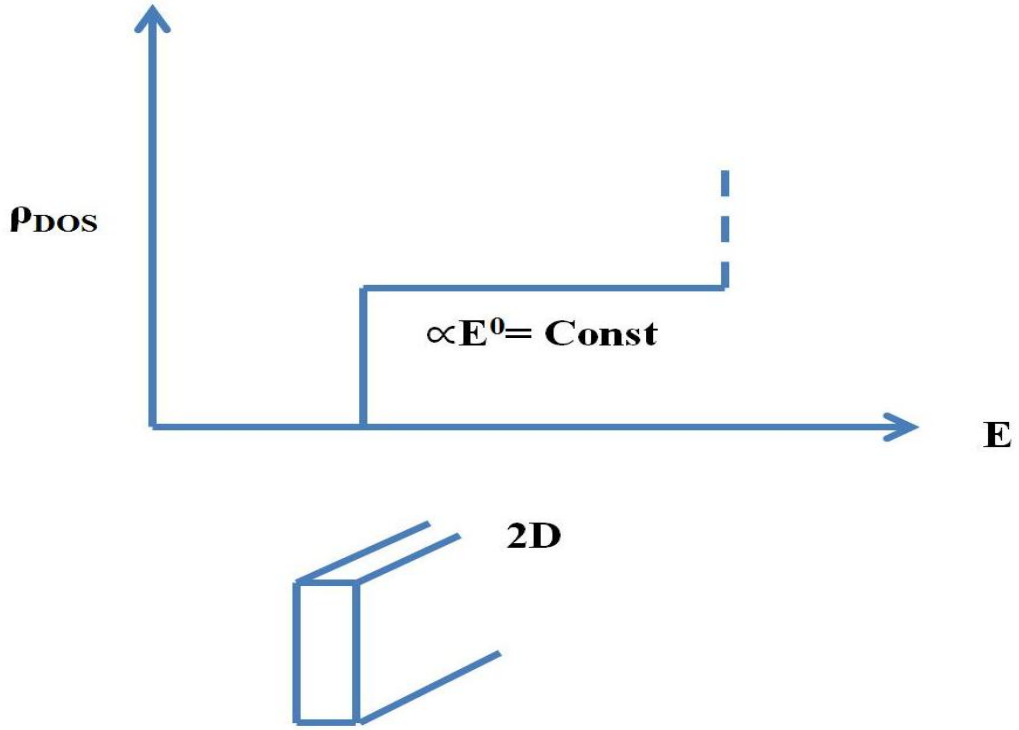

Figure 2.2: Show the density of states (DOS) in 2D confinement system. The function changes from the smooth square-root function of energy in a 3-Dimensional bulk system to a staircase like function in a quantum well [9].

2.1.1.3 1-Dimensional semiconductors (1D)

One dimensional nanostructure represents a group of nanomaterial with highly anisotropic morphologies. In one dimensional, if two dimensions are reduced and one remains large; the resulting structure is referred to a nanowire. But if two dimensions of nanowire become comparable to Bohr exciton radius, then this structure is known as quantum wire. Confinement in this structure is known as quantum confinement. The category of one dimensional nanostructure consists of a wide variety of morphologies. This includes

whiskers, nanowires, nanorods, fibers, nanotubes, nanocables and nanotubeles. Recently, one-dimensional have also become the focus of intensive research owing to their unique applications in mesoscopic physics and fabrication of nanoscale devices **[12-13]**. One dimensional also provides a good system to investigate the dependence of electrical and thermal transport properties on dimensionality and size reduction (or quantum confinement). And one dimensional crystalline nanostructure have little surface disorder and less deficiency, which will decrease the contribution of the surface related nonradiative recombination and are predicted high photoluminescence efficiency.

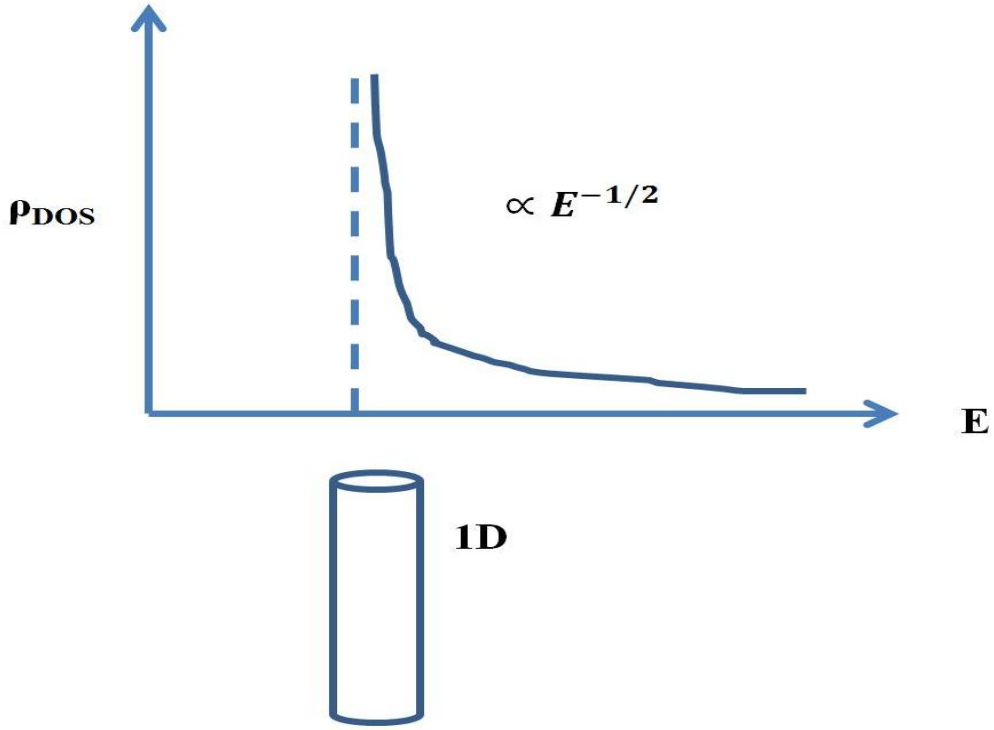

Figure 2.3: Show the density of states (DOS) in 1D confinement system. The function changes from the smooth square-root function of energy in a 3-Dimensional bulk system to a decay like function in a quantum wire [9].

In one dimension, the electronic density of states is given by **[8]:**

$$g(E)_{1D} = \frac{1}{\pi}\left(\frac{m}{\hbar^2}\right)^{\frac{1}{2}} E^{\frac{-1}{2}} \qquad (2.3)$$

Note that the density of states in a 1D system has a functional dependence on energy according to $E^{-\frac{1}{2}}$, respectively. Figure 2.3 shows the dimensionality of semiconductor system for 1D quantum wire.

2.1.1.4 0-Dimensional semiconductors (0D)

Zero dimensional nanomaterials are so named because they have been confined to the nanoscale in all three dimensions, i.e. if all three dimensions are reduced; the material is called quantum dot/nanoparticles. Consequently, such materials have electronic properties intermediate between those of bulk semiconductors and those of discrete molecules. All of the dimensions of 0D nanostructures are in the nanometric size range (such as nanoparticles or well-separated nanopowders). Nanoparticles also often possess unexpected optical properties as they are small enough to confine their electrons and produce quantum effects **[14]**. Nanoparticle research is currently an area of intense scientific due to a wide variety of potential applications in biomedical, optical and electronic fields.

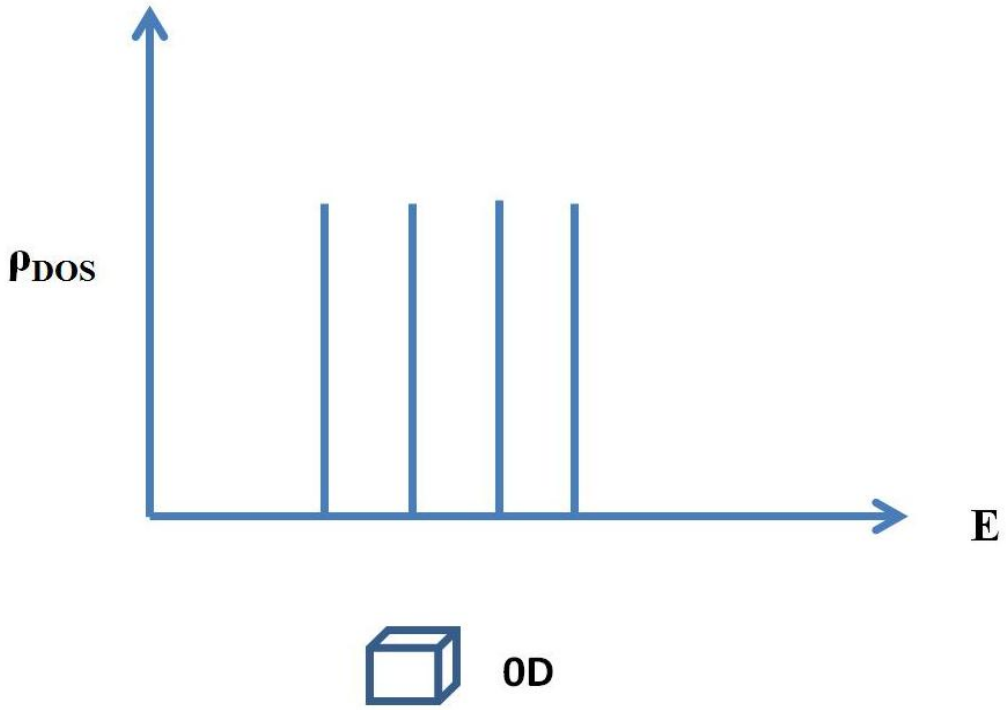

Figure 2.4: Show the density of states (DOS) in 0D confinement system. The function changes from the smooth square-root function of energy in a 3-Dimensional bulk system to a decay like function in a quantum wire to state of discrete energy in quantum dot [9].

The nanoparticles of the same material can be used for fabrication of LEDs having emission over the whole visible spectrum. In microparticles (bulk) the exciton extends to natural limit. However, if the size of a semiconductor micro crystal become small enough that it approaches the size of the material's exciton Bohr radius, then the electron energy levels can

no longer be treated as continuous, they must be treated as discrete, meaning there is a small and finite separation between energy levels as in Figure 2.4. In zero dimensions, all the available states exist only at discrete energy and can be represented by a Dirac delta function. The density of states for 0D can be represented with delta function **[8]**. Thus,

$$g(E)_{0D} = 2\delta(E - E_c) \tag{2.4}$$

2.1.2 Size control of semiconductor nanocrystals

One of the key elements for utilizing semiconductor nanocrystals in nanotechnology applications is the ability to control the particle sizes. It is of great importance to control the size of the semiconductor nanocrystal, since the band gap absorption and luminescence energy of the semiconductor nanocrystal depends on the size through quantum confinement. For each semiconductor particle there is a size threshold, the exciton Bohr diameter, below which the electronic properties of the semiconductor start to change. In this case, the exciton becomes confined within the dimension of the particles and quantum size effects are clearly noticed as a high energy shift of the optical band gap. Because of these size-dependent electronic properties, semiconductor nanocrystals have been intensely investigated in the last two decades as promising materials in the energy field of nanotechnology **[15]**. Two fundamental factors (large surface to volume ratio and the actual size of the particle (quantum confinement effects)), both related to the size of the individual nanocrystal, are responsible for these unique properties.

2.1.2.1 Surface-area-to-volume ratio

The surface-area-to-volume ratio, also called the surface-to-volume ratio and variously denoted sa/vol or SA:V, is the amount of surface area per unit volume of an object or collection of objects. The surface-area-to-volume ratio is measured in units of inverse distance. A characteristic feature of nanoscale materials is their surface to volume ratio R. This develops because the small of nanostructures means that a large fraction of their component atoms reside on the surface. There are both advantage and disadvantage consequences for the optical properties of such material. The advantage includes the development of more efficient catalysts. At the same time, disadvantages include lower emission quantum yields, stemming from the presence of surface defects, which leads to the

nonradiative recombination of carriers. As a particle become smaller the ratio of the number of surface atoms to those in the interior increases, with greater than a third of all atoms reading on the surface in very small particles. To understand this concept, consider a spherical material of radius "r" then,

$$R = \frac{Surface\ area\ of\ the\ sphere}{Volume\ of\ the\ sphere} = \frac{4\pi r^2}{\left(\frac{4}{3}\right)\pi r^3} = \frac{3}{r} \tag{2.5}$$

As the size of the sphere decreases, the above ratio increases. This leads to the surface playing an important role in the properties of the material.

2.1.2.2 The actual size of the particle (Quantum Confinement Effects)

In semiconductor nanoparticle, there is a change in the electronic properties of the material, as the size of the solid becomes smaller the band gap gradually becomes larger because of the quantum confinement effects. The quantum confinement effect can occur once the diameter of the particle is comparable to the wavelength of the electron, which could be either its De-Broglie wavelength or mean free path. The quantum confinement of nanocrystal as a particle in a sphere can occur when the size of the sphere is comparable to Excitonic Bohr radius, which is the length scale of an exciton. An exciton is a quasi-particle that forms when Coulomb-interacting electrons and holes in semiconductor bounded into pair states. They form upon the absorption of light, which promotes an electron from the semiconductor's valence band into its conduction band. This leaves behind a positively charged hole (i.e., the absence of an electron). Bohr exciton radius of such bound electron-hole pair is defined as **[16]**:

$$a_B = \frac{4\pi\varepsilon(\alpha)\hbar^2}{\mu e^2} \tag{2.6}$$

Where $\varepsilon(\alpha)$ is the optical frequency dielectric constant, e is electric charge, ħ is the reduced Plank's constant, $\mu = \left(\frac{m_e m_h}{m_e + m_h}\right)$ is reduced mass of electron-hole bound state, m_e and m_h are the effective mass of electron and hole, respectively. The a_B symbolize the characteristic length scale to observe quantum effects in nanomaterial. A stunning picture of exciton formation is as follows: A photon enters a semiconductor, exciting an electron from the valence band into a given level in the conduction band, and as consequence an empty level (a hole) is created in the valence band as shown in Figure 2.5.

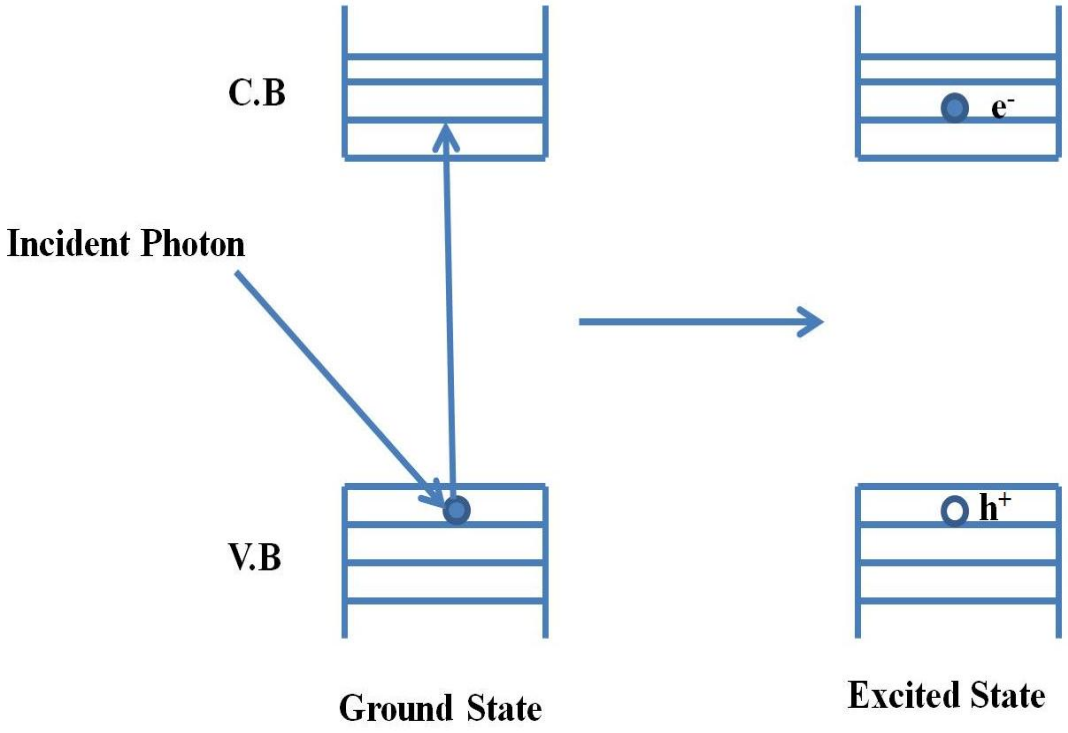

Figure 2.5: Excitation formation upon absorption of an incident photon. An electron (e^-) is excited from valence band (VB) to a given level in the conduction band (CB) creating a hole (h^+) in the valence band system.

2.2 Confinement regimes

It is therefore in this regime where the optical and electrical properties of materials become size and shape-dependent and where some of the most fascinating aspect of nano begins **[16].** Therefore, there are three confinement regimes that exist. They are referred to as the strong: ($a < a_e$, a_h), intermediate ($a_h < a < a_e$), and weak confinement regimes ($a > a_e$, a_h) **[16].** In all the cases, a is the critical dimension of the nanostructures. Below we describe these various confinement regimes in more details.

2.2.1 The strong Confinement Regime

For quantum dots one speaks of the strong confinement regime, where the individual motion of the electron and the hole are quantized. The strong confinement regime is often indirectly assumed when talking about nanoscale materials. The criterion is readily met in small nanomaterials, as well as in system where both electron and hole effective masses are small while the corresponding dielectric constants are large **[16].** Examples, lead chalcogenides such as PbS and PbSe, which have small electron and hole effective masses. This leads to

corresponding bulk exciton Bohr radii of $a_B \approx 18$ nm (PbS) and $a_B \approx 46$ nm (PbSe) **[16].** As a consequence, it is easy to achieve conditions where $a < a_e, a_h$ as shown Figure 2.6.

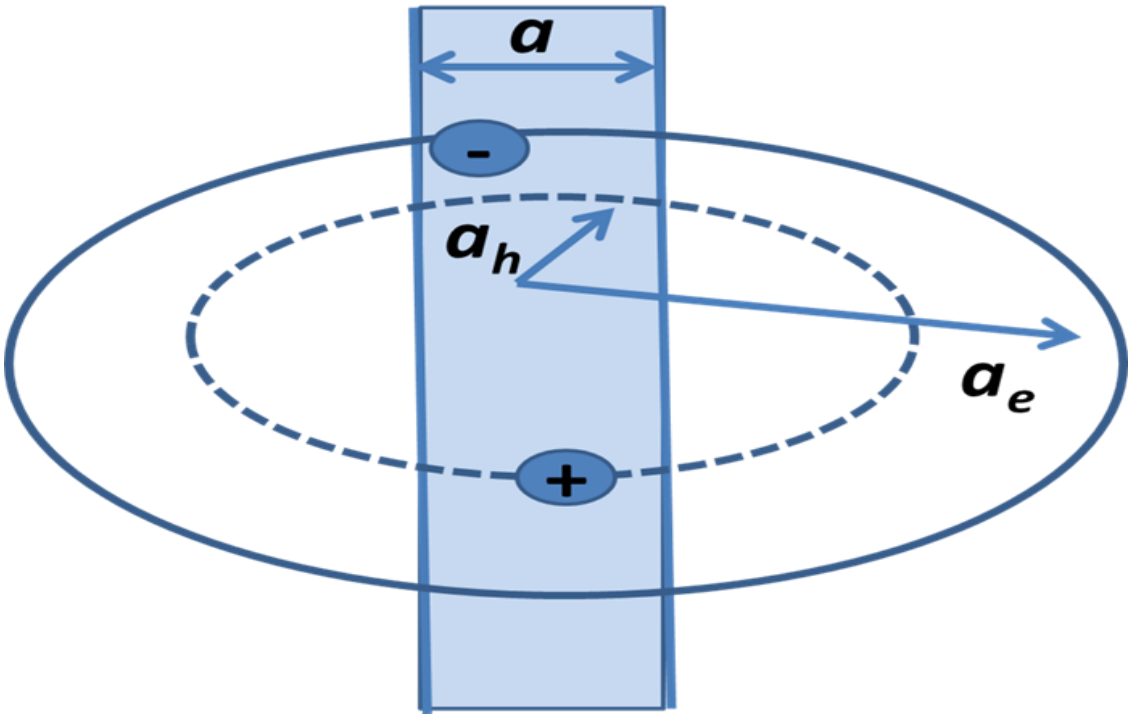

Figure 2.6: Illustration of the strong confinement regime, where $a < (a_e, a_h)$. The shaded region denotes the critical length scale a. For illustration purpose, a generic origin is used for both the electron and hole.

2.2.2 The intermediate Confinement Regime

For somewhat larger dots one can introduce an intermediate confinement regime if the effective mass of the holes is much bigger than that of the electron. In this case, the critical dimension of the material is smaller than one carrier's Bohr radius but larger than the other's. Since m_e is generally smaller than m_h, this criterion usually means that $a_h < a < a_e$ as shown in Figure 2.7 **[16]**. At this point, quantization effects should start to become apparent in the material.

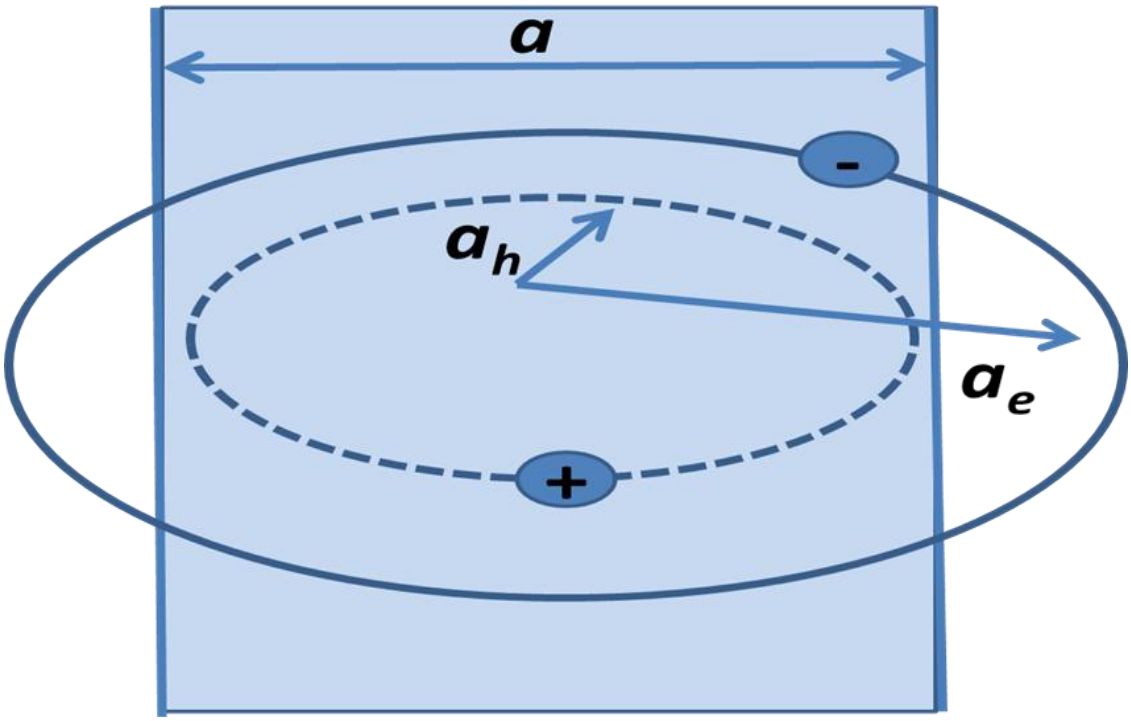

Figure 2.7: Illustration of the intermediate confinement regime, where $a_h < a < a_e$. The shaded region denotes the critical length scale *a*. For illustration purpose, a generic origin is used for both the electron and hole.

2.2.3 The Weak Confinement Regime

The Weak Confinement Regime is appropriate for relatively large quantum dots. In this scenario, $a > a_e$, a_h, the critical dimension of the nanostructure is larger than both the individual electron and hole Bohr radii as shown in Figure 2.8 **[16].** As consequence, the exciton binding energy is weak as in bulk systems. Furthermore, the optical and electrical properties of these nanostructures are essentially bulk-like. In our case we were able to observe nice optical properties where the critical dimension of the nanostructure is larger than both carriers **[17].**

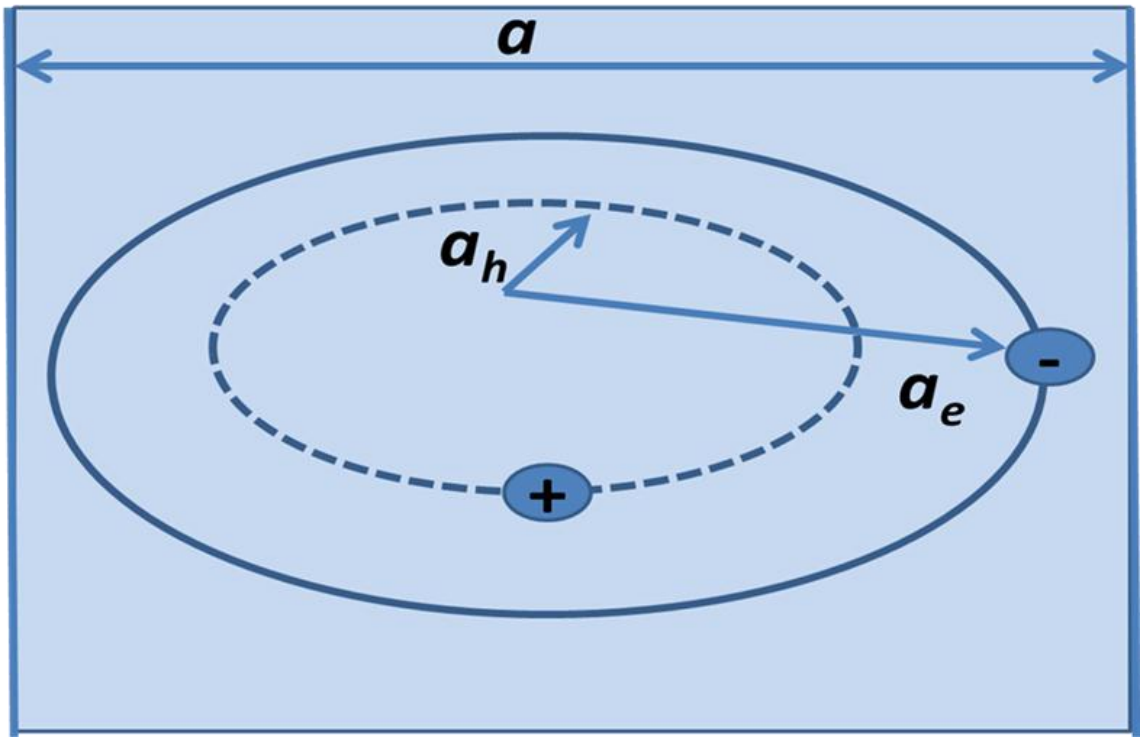

Figure 2.8: Illustration of the weak confinement regime, where, ($a > a_e, a_h$). The shaded region denotes the critical length scale *a*. For illustration purpose, a generic origin is used for both the electron and hole.

2.3 Luminescence

The term luminescence comes from a Latin root (Lumen= Light). It was first introduced to use as a luminescence by the German physicist and science historian Eilhard Wiedemann in 1888 for all phenomena of light that are not solely conditioned by the rise in temperature, that is, incandescence. Before considering the historical evolution of the understanding of luminescence, it should be noted that the present definition of luminescence is a spontaneous emission of radiation from an electronically excited species (or from a vibrationally excited species) not in thermal equilibrium with its environment **[18]**. There are various types of luminescence. They are classified according to the mode of excitation. Firstly: Photoluminescence (PL), is the emission of light arising from direct photon excitation of the emitting species **[18]**. PL is caused by moving electrons to energetically higher levels through the absorption of photons. Secondly: Cathodoluminescence (CL) is the emission of photons of characteristic wavelength from material that is under high-energy electron bombardment. In CL different materials exhibit fluorescent or phosphorescent kinetic behavior which can have an effect on the quality of the CL images, depending on the manner in which the image

is obtained. Thirdly: Thermoluminescence is any luminescence appearing in materials upon application of heat, caused by electron movement which increases as the temperature rises. Some materials such as strontium aluminate store energy when exposed to ultraviolet radiation.

2.3.1 Mechanism of Luminescence

Electronic states can be grouped into two broad categories, singlet states and triplet states. Electronic state is a combination of the wave functions of each of the electrons in each orbital's of the molecules. Absorption of an ultraviolet or visible photon promotes a valence electron from its ground state to an excited state with conservation of the electron's spin. Example, a pair of electrons occupying the same electronic ground state has opposite spins (unflipped and flipped electron) (Figure 2.9(a)). A singlet or a triplet can form when one electron (spin up) is excited to a higher energy level. In an excited singlet state, the electron is promoted in the same spin orientation as it was in the ground state (paired) as shown in Figure 2.9 (b). In a triplet excited stated, the electron that is promoted has the same spin orientation (parallel) to the other unpaired electron. However, in triplet states an electron in singlet excited state is transformed to a triplet excited state (Figure 2.9(c)) in which its spin is no longer paired with that of the ground state. The difference between the spins of ground singlet, excited singlet, and excited triplet is shown in Figure 2.9.

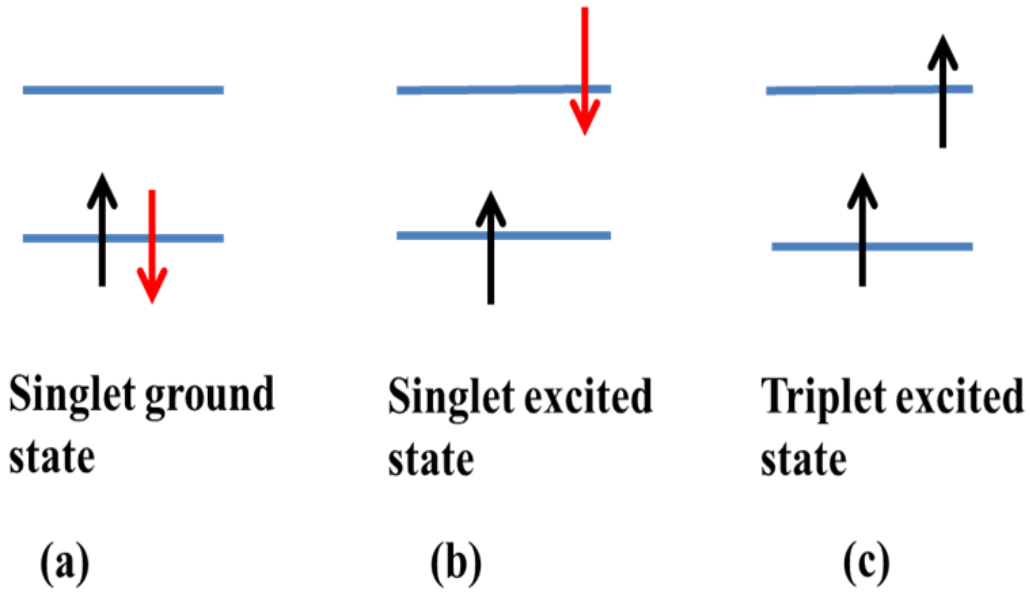

Figure 2.9: Show the electronic state singlet and triplet.

The main types of luminescence are consists of fluorescence and phosphorescence:

(a) Fluorescence

Fluorescence is the emission of a photon from a singlet excited state to a singlet ground state, or between any two energy levels with the same spin. In fluorescence the excited states are not stable and will not stay indefinitely. Fluorescence, therefore, decays rapidly after the excitation source is removed (ns time scale).

(b) Phosphorescence

Phosphorescence is a luminescence that delayed radiation of trapped photo-produced electrons or holes occurs in materials internal or exterior defect zones. In phosphorescence the emission is between a triplet excited and a singlet ground state or between any two energy levels that differ in their respective spin states. Phosphorescence may continue for some time (longer time scale, up to hours or even days) after removing the excitation source. Fluorescence differs from phosphorescence in that the electronic energy transition that is responsible for fluorescence does not change in electron spin, which results in short-live electrons ($<10^{-5}$ s) in the excited state of fluorescence. In phosphorescence, there is a change in electron spin, which results in a longer lifetime of the excited state (second to minutes).

2.4 Energy Transfer Mechanisms

The process in which the excitation of a certain ion migrates to another ion is called energy transfer. Generally the term energy transfer refers to movement of energy between different types of atoms or molecules **[19]**. It is a phenomenon which occurs in many different types of materials under a wide variety of physical conditions. The different fields of research have created some confusion in terminologies. Here the type of atom or molecule that absorbs the excitation energy is called sensitizer. The type of atom or molecule that emits the energy is called activator. If the sensitizer is a constituents of the host lattice, is called “host-sensitized” energy transfer and if the sensitizer is constituents of the impurity ion, is called “impurity-sensitized” energy transfer.

There are three basic mechanisms for energy transfer which are photoconductive, radiative reabsorption and non-radiative **[20]**. The photoconductive mechanism occurs when an absorbed photon creates free electron-hole pairs capable of migration. This mechanism is generally associated with studies of electrical conductivity. The second basic energy transfer mechanism is radiative reabsorption in which the sensitizer emits a real photon which is eventually absorbed by either another sensitizer or activator **[19-20]**. The third mechanism is non-radiative energy transfer in the absence of charge migration. In this case coulomb

interactions of the Van der Waals type allow energy to be transferred directly between the ions **[21]**. In some cases it is possible for non-radiative energy transfer to occur many times between sensitizers before transfer to an activator occurs. It is very important to understand the basic energy transfer mechanism in order to develop efficient luminescent material. In a schematic way, the different energy transfer processes between two ions can be represented as in Figure 2.10 **[22]**. From the schematic presented below, four processes following excitation of S can be distinguished: (a) S may luminescence (radiative transfer). When energy transfer is radiative, the photons are emitted by the sensitizer ions (S) and are then absorbed by any activator ions (A) within a photon travel distance, (b) S may decay non-radiatively producing heat. The nonradiative process are energy loss to the local vibrations of surrounding atoms (called phonons in solids) and to electronic states of atoms in the locality, such as energy transfer, which may be resonant (the migration between identical systems, which may ultimately emit radiation) or phonon assisted (the excess energy being dissipated as heat), (c) S may transfer energy to another S type ion which is called multiphonon-assisted energy transfer.

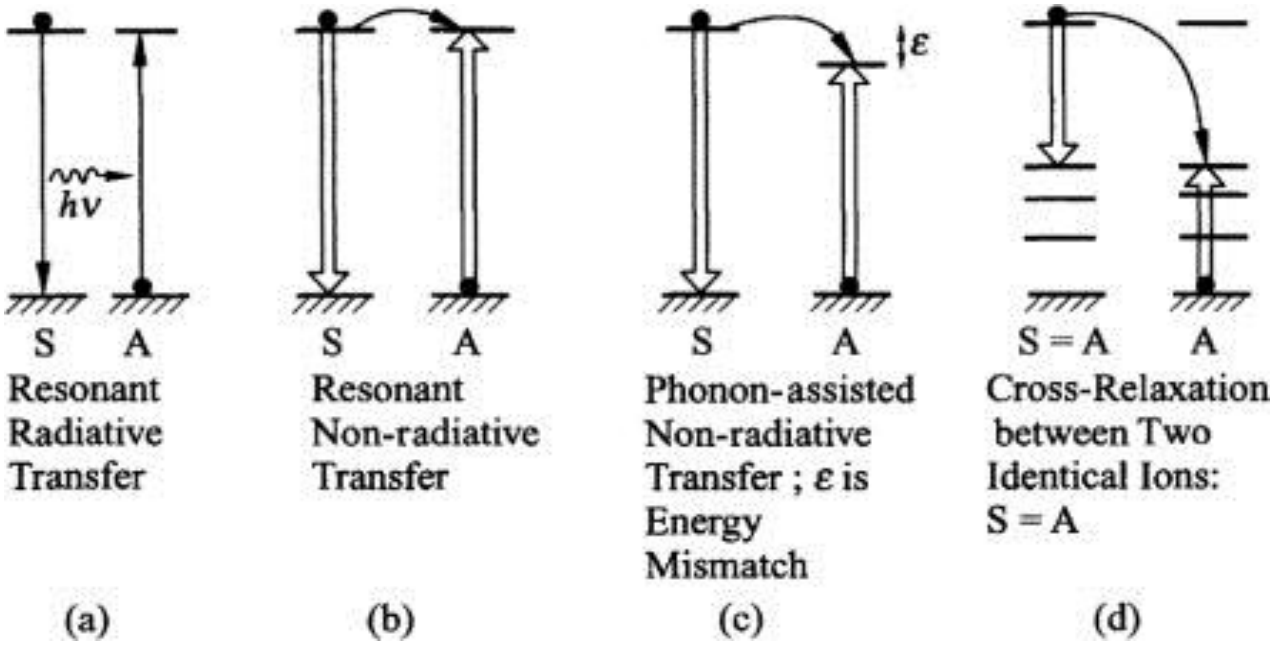

Figure 2.10: A schematic diagram to illuminate the different ET processes between two ions: (a) resonant radiative transfer through emission of sensitizer (S) and re-absorption by activator(A), (b) non-radiative transfer associated with resonance between absorber (sensitizer) and emitter (activator), (c) multiphonon-assisted ET, and (d) CR between two identical ions.

Excited electronic levels of rare earths in solids decay nonradiatively by exciting lattice vibrations (phonons). When the band gap energy between the excited level and the next lower electronic level is larger than the phonon energy, several lattice phonons are emitted in order to bridge the band gap energy and (d) S and A may also be identical ions, non-radiative transfer may give rise to self-quenching by cross-relaxation (CR) and is referred as a killer site **[23]**. Special cases of energy transfer are CR, where the original system loses the energy (E_5-E_4) by obtaining the lower state E_1 (which may also be the ground state E_0) and another system acquires the energy by going to a higher state $E_4^{'}$. CR may take place between the same rare earths (being a major mechanism for quenching at higher concentration in a given material) or between two differing elements, which happen to have two pairs of energy levels separated by the same amount. Theoretically, the CR rate for a dipole-dipole transfer probability is given by **[24-25]**:

$$P_{SA} = \frac{2\pi}{h}\left|\left\langle S^* A^0 \left| H_{SA} \right| S^0 A^* \right\rangle\right|^2 \rho_E \qquad (2.7)$$

Here, H_{AS} is electric dipole-dipole interaction Hamiltonian, proportional to the inverse third power of ion separation, ρ_E is the density of states provided by the vibrational motion contributing to the line broadening of the transition, and P_{SA} is proportional to the inverse sixth power of the ion separation. The wave function to be considered for the matrix element are describing an initial state of the system with the sensitizer in its excited state and the acceptor in its ground state, the final state having the sensitizer its ground state and the acceptor in its excited state. Therefore, the transfer probability can be written as [24-25]:

$$P_{SA}(R) = \frac{1}{\tau_s}\left(\frac{R_0}{R}\right)^6 \qquad (2.8)$$

Where τ_S is the actual lifetime of the sensitizer excited state and R_0 is the critical transfer distance for which excitation transfer and spontaneous deactivation of the sensitizer have equal probability. However, Dexter pointed out that this theory should be extended to include higher multipole and exchange interactions **[21]**. The energy transfer probability for electric multipolar interactions can be more generally written as:

$$P_{SA}(R) = \frac{1}{\tau_s}\left(\frac{R_0}{R}\right)^S \qquad (2.9)$$

Where S is appositive integer taking the following values, S= 6 for dipole-dipole interaction, S=8 for dipole-quadruple interactions, S= 10 for quadrupole-quadrupole interaction **[21]**. It

should be noted that for dipole-dipole interactions, the difference between radiative and non-radiative resonant transfer lies essentially in the fact that for radiative transfer there is no critical R_0 depending only upon concentration. Energy transfer between pairs of rare earth ions at dilution level below the self quenching limits has been known to take place generally through multipolar interaction like dipole-dipole interactions or dipole-quadruple interactions.

2.5 Basic properties of ZnO

Zinc oxide an inorganic compound with the formula ZnO. It is usually appears as a white powder, nearly insoluble in water. The powder is widely used as an additive into numerous materials and products including plastic, ceramics, glass, cement, rubber (e.g. car tires), lubricants, paints, food and fire retardants, etc. In material science, ZnO is often called a ii-vi semiconductor because zinc and oxygen belong to the 2nd and 6th groups of the periodic table, respectively. This semiconductor has several favorable properties: good transparency, high electron mobility, wide band gap, strong room temperature luminesces, high thermal conductivity. ZnO has additional advantages of being easy to grow especially at low temperatures and processing the richest known family of nanostructures **[26]**.

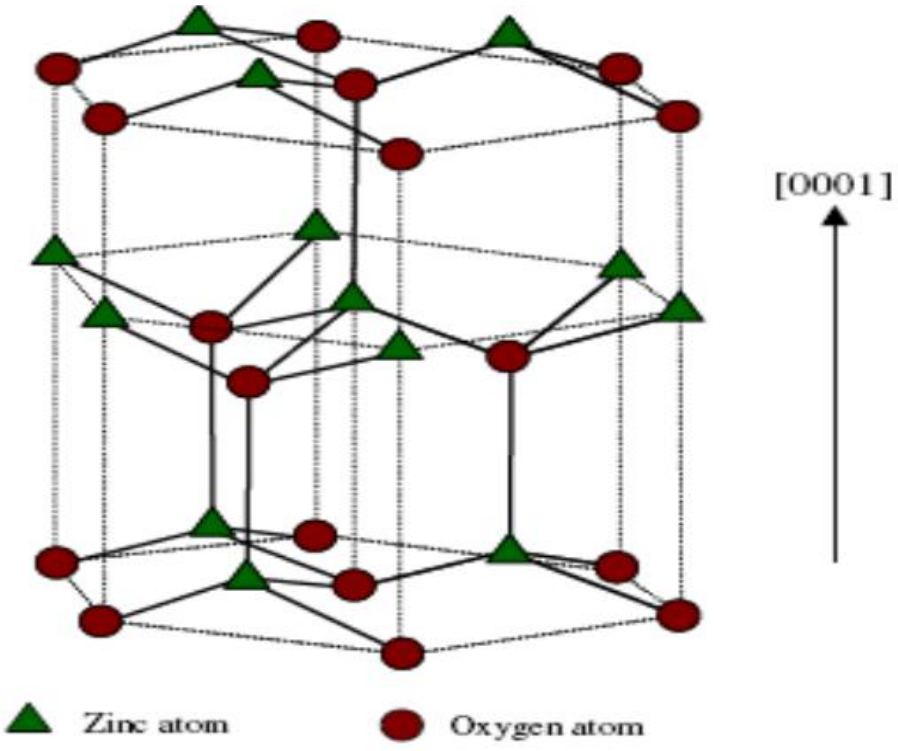

Figure 2.11: The hexagonal wurtzite structure of ZnO.

ZnO crystallize in three forms: hexagonal wurtzite, cubic zinc blende and the rarely observed cubic rock salt. The wurtzite structure is the most stable and thus the most common at ambient conditions. Hexagonal wurtzite structure has lattice parameters a= 3.296 nm and c= 0.520 nm. Its wurtzite structure is very simple to explain, where each oxygen ion is surrounded tetrahedral by four zinc ions, and vice versa, stacked alternatively along the c-axis as shown in Figure 2.11.

2.5.1 Defects and luminescence in ZnO

For any luminescent material, it is very important to investigate the origin of its luminescent centres and it is a key topic in optoelectronics. ZnO possesses a large number of extrinsic and intrinsic deep-level impurities and complexes (clusters) that emit light of different colours **[27]**, including violet, blue, green, yellow, orange and red, i.e., all constituents of white light **[28]**. Because of this, ZnO is considered to be attractive for applications requiring luminescent materials. The room temperature PL spectrum is normally characterized by near-band-edge (NBE) ultra-violet emission and at least one broad band emission due to the deep levels, called DLE. DLE refers to the broad band extending from just above 400 nm up to 750 nm, i.e., the whole visible spectrum. The broadness of the band results from the fact that it represents a superposition of many different deep levels emitting at the same time.

There are three common types of defects such as, line defects, point defects and complex defects. Line defects belong to the rows of atoms such as dislocations, while point defects belong to the isolated atoms in localized regions and the composition of more than one point defect form complex defects. These defects contribute to the luminescence properties in ZnO **[29-30]**. The extrinsic point defects are point defects involving foreign atoms such as impurities. If the defects only consist of host atom, then these defects are called intrinsic defects. Intrinsic optical recombinations take place between the electrons in the conduction band and holes in the valence band **[31]**. The deep level emission (DLE) band in ZnO are attributed to different intrinsic defects in the crystal structure of ZnO such as oxygen vacancies (V_o), zinc interstitial (Zn_i) **[32]** and oxygen anti-site (O_{zn}) and zinc anti-site **[33-34]** as shown in Figure 2.12. From this figure, the energy of the transition from conduction band to the Zinc vacancies (V_{Zn}) corresponds to the energy of 3.06 eV from the violet emission centred at 409 nm. The vacancy defects are formed when a host atom is missing in the crystal and it is denoted by V_c. In ZnO, oxygen vacancy (V_o) and zinc vacancy (V_{Zn}) are the two most common defects. The single ionized oxygen vacancy in ZnO is responsible for the green

emission. The oxygen vacancy has lower formation energy than the zinc interstitial and dominates in zinc rich growth conditions. The red luminescence from ZnO is attributed to doubly ionized oxygen vacancies **[35]**. Many researches have suggested oxygen vacancies as the source of green emission in ZnO **[36-37].**

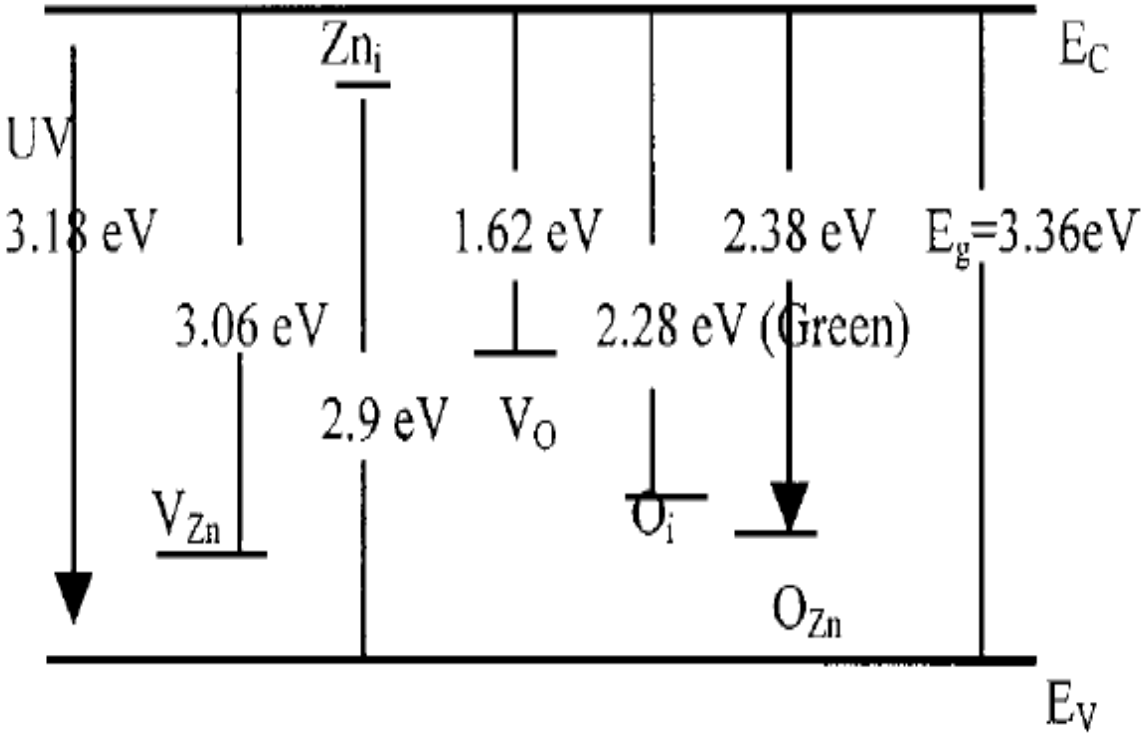

Figure 2.12: The schematic representation of the position of various intrinsic defect levels emission within ZnO.

Recently it has been observed that more than one deep level is involved in the green emission in ZnO. It is found that both V_0 and V_{Zn} contribute to the green emission **[38]**. The blue emission in ZnO belongs to zinc vacancies. The blue emission is attributed to the recombination between zinc interstitial (Zn_i) energy level to V_{Zn} energy level which is at approximately 2.9 eV (436 nm) above the valence band. In ZnO, oxygen interstitial (O_i) and zinc interstitial (Zn_i) are the two common intrinsic defects. The position of the Zn_i level is theoretically located at 0.22 eV below the conduction band **[39]** and is commonly produced in zinc-rich samples, which are expected to act as donor centres **[32]**. Oxygen interstitials defects are normally located at 2.28 eV below the conduction band which is responsible for the orange-red emissions in ZnO **[39]**.

The yellow emission in ZnO has also been attributed to oxygen interstitials **[40]** and was also observed metastable behaviour in undoped bulk ZnO **[41]**. Recently the yellow emission was observed in ZnO nanorods grown by low temperature (90^{o}C) chemical growth in different laboratories **[42]**. The origin of this band in these low temperature grown samples was attributed to O_i. The yellow emission in the chemically grown ZnO nanorods was also attributed to the presence of $Zn(OH)_2$ that is attracted to the surface of the nanorods **[43]**. Yellow emission has been observed in many different grown ZnO nanorods, and it was demonstrated that the emission can be replaced by the green and red bands upon post-growth annealing **[43]**. This was explained by the fact that upon proper post-growth annealing, the hydroxyl group can desorbs and hence modify the emission from that of the as grown ZnO nanorods.

Orange, orange-red and red emission bands have also been observed in ZnO **[43]**. The orange emission, which is not very common in ZnO, was proposed to be due to transitions related to oxygen interstitials **[44]**, recently the orange-red emission was attributed to transitions associated with zinc vacancy complexes **[45]**, and the red emission was proposed to be due to transitions associated with zinc interstitials **[46]**.

Extrinsic defects also play a vital role in the luminescence from ZnO. Mn, Na, Cu, Li, Fe, and OH are common extrinsic defects in ZnO that causes luminescence in ZnO. The ultra-violet (UV) emissions in ZnO at 3.35 eV are commonly related to the excitons bound to the extrinsic defects such as Li and Na accepters in ZnO **[41]**. The emission at 2.85 eV is due to copper impurities in ZnO **[47]**. The yellow emission at 2.2 eV was observed in Li doped ZnO thin film and Li related defects which are located at 2.4 eV below the conduction band **[48]**.

2.6 Basic properties of PbS

Lead (ii) sulfide is an inorganic compound with the formula PbS. PbS is an important IV-VI semiconductor with cubic rock salt structure with lattice parameter $a = 5.936$ Å. Pb^{++} and S^{--} ions occupy the lattice sites in the rock-salt crystal structure alternatively **[49]**. Each Pb atom is surrounded by 6 atoms of S, which are arranged at the corners of the surrounding octahedron and vice versa as shown in Figure. 2.13. PbS nanoparticles have applications in optical devices such as IR detectors, Pb^{2+} ion selective sensors and solar control coatings **[50]**. PbS nanoparticles can be used in electroluminescent devices such as optical switches due to their exceptional third order nonlinear optical properties **[51]**. PbS has attracted considerable attention in the field of material science due to its specially small direct band-

gap energy (0.41 eV at 300K) and a large exciton Bohr radius (18 nm) **[52]**. It also permits quantum size confinement effect to be clearly evident even for relatively larger structures **[53]**. PbS band-gap energy can be widened to visible region of about 5.2 eV forming nanoclusters **[54]**.

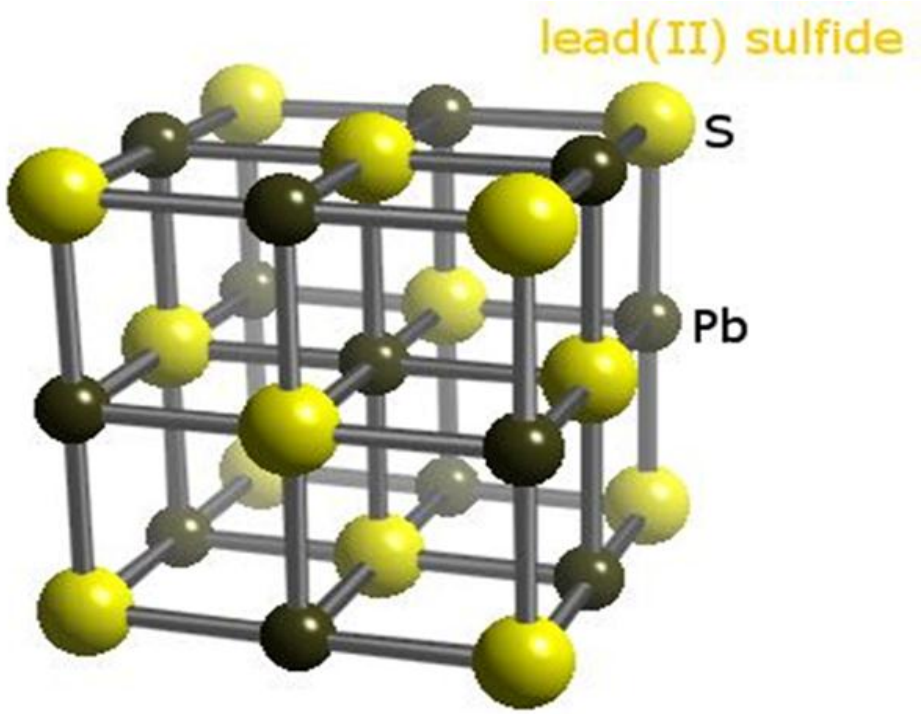

Figure 2.13: The cubic structure of PbS.

2.7 Effect of doping semiconductors

Doped semiconductors are semiconductors which contain impurities, foreign atoms which are incorporated into the crystal structure of the semiconductor. These impurities can either be unintentional due to lack of control during the growth of the semiconductor or are added on purpose to provide free carriers in the semiconductor. Doping is a widely used method to improve the electrical, magnetic, and optical properties of semiconductors, which are crucial for their practical applications **[55]**. Doping with transition metal (TM) and rare-earth (RE) ions materials manipulate the band structure of the nanocrystals, morphology and show intense emissions in a wide range of wavelength depending on the impurity type, concentration and crystal dimensions. It also plays key roles in luminescence efficiency thus influencing their practical applications. As we move towards nanotechnology, it is best to investigate the luminescence properties semiconducting nanostructures because of

nanoscopic interactions play key roles in controlling the excitation dynamics. Doping the semiconductor nanostructures with TM and RE ions has been subject of research in recent years to find out potential applications in photonic and biophotonic field **[56]**. Doped nanocrystals are worth of investigating in more details because band gap of nanocrystalline hosts can be adjusted by sizes and shapes to match the energy levels of luminescent centers and thus new luminescence is expected. Doping a semiconductor crystal introduces allowed energy states within the band gap but very close to the energy band that corresponds to the dopant type. In other words, donor impurities create states near the conduction band while acceptors create states near the valence band **[57]**. Dopants also have the important effect on shifting the material's Fermi level towards the energy band that corresponds with the dopant with the greatest concentration **[57]**. Several nanocrystalline particle systems have been studied as a free standing powder or in a matrix **[58]**.

The main goal of these studies has been to understand the physical properties of these powders nanostructures. The practical photonics applications of these nanostructures are still lacking due to the fact that the surface-related non-radiative recombination dominates in the weak confinement limit. To decrease the contribution of the surface-related nonradiative recombination, different dopants (impurities) in different powders (0D) were introduced. By incorporating the dopants in powders matrix, the dominant recombination direction can be transferred from the surface states to the dopant states. If the dopant induced transition can be localized as in case of the TM or RE elements, the radiative efficiency of the dopant-induced emission increases significantly. Researchers reported on remarkable optical properties of doped semiconductor nanoparticles and concluded that they form a new class of luminescent materials **[56]**. Erwin et al describe the inclusion of TM ions in semiconducting nanocrystals and described the important roles on crystal structure and shape of the nanocrystals in optimizing the efficiency of TM–doped nanocrystals **[59]**. The TMs are the elements found between the group IIA elements and the group IIB elements in the periodic table. They are the metals which make the transition to using the d-orbitals for their bonding. Hence they are sometimes called the d-block elements. The entire TM has certain properties in common. They have incompletely filled d shell, i.e. their electron configuration is d^n ($0 < n < 10$). They have several stable oxidation states or valences and many form compounds which are paramagnetic (have unpaired electrons). Nowadays, the applications of REs and in particular the application of RE doped bulk semiconductor materials have grown significantly. Actually

rare earth ions have been considered as the most important optical activators for luminescent devices.

The RE ions are characterized by a partially filled 4f shell that is well shielded by $5s^2$ and $5p^6$ orbitals **[26]**. The 4f shell remains unfilled, which means that the electrons in the 4f shell are optically active. The states arising from the various $4f^n$ configurations therefore tend to remain nearly invariant for a given ion. This shielding produces narrow spectral lines, long fluorescence lifetimes and energy level that are relatively insensitive to their host environment because the optically active electrons interact weakly with the ions environment **[28]**. The use of rare earth elements based phosphor, based on "line-type" f-f transitions, can narrow the emissions to the visible range, resulting in high efficiency and high lumen equivalence.

References

[1]. C. B. Murray, D. J. Norris, M. G. Bawendi, *J. Am. Chem. Soc*. **115** (1993) 8706-8715.

[2]. D. J. Milliron, S. M. Hughes, Y. Cui, L. Manna, J. Li, L. W. Wang, A. P. Alivisatos, *Nature*, **430** (2004) 190-195.

[3]. T. W. F. Chang, S. Musikhin, L. Bakueva, L. Levina, M. A. Hines, P. W. Cyr, E. H. Sargent, *Appl. Phys. Lett*. **84** (2004) 4295-4297.

[4]. X. Peng, L. Manna, W. Yang, J. Wickham, E. Scher, A. Kadavanich, A. P. Alivisatos, *Nature*, **404** (2000) 59-61.

[5]. W. U. Huynh, J. J. Dittmer, A. P. Alivisatos, *Science*, **295** (2002) 2425-2427.

[6]. U. Müller, *Nanostructures, in Inorganic Structural Chemistry*, 2nd edn, John Wiley & Sons, Ltd, Chichester, (2007) pp. 241–245.

[7]. M. Köhler, W. Fritzsche, *Characterization of nanostructures, in Nanotechnology*, 2nd edn, Wiley-VCH, Weinheim, (2008) pp. 211–224.

[8]. M. Kuno, *Introductory Nanoscience, physical and chemical concepts*, Garland Science, page 208-216.

[9]. M. Kuno, *Introductory Nanoscience, physical and chemical concepts*, Garland Science, page 229-230.

[10]. F. Xu, Z-Y. Yuan, G-H. Du, T-Z. Ren, C. Bouvy, M. Halasa, B-L. Su, *Nanotech*, **17** (2006) 588-594.

[11]. Q. Zhang, C. S. Dandeneau, X. Zhou, G. Cao, *Adv. Mater*, **21** (2009) 4087–4108.

[12]. Z. W. Pan, Z. R. Dai, Z. L. Wang, *Science*, **291** (2001) 1947-1949.

[13]. L. H. Dong, Y. Chu, Y. Liu, M. Y. Li, F. Y. Yang, L. L. Li, J. Coll. *Inter. Sci*. **301** (2006) 503-510.

[14]. S. Eustis, M. A. El-Sayed, *Chem. Soc. Rev*, **35** (2006) 209–217

[15]. A. P. Alivisatos, *J. Phys. Chem*, **100** (1996) 13226-13239.

[16]. M. Kuno, *Introductory Nanoscience, physical and chemical concepts*, Garland Science, page 32-42.

[17]. L. F. Koao, F. B. Dejene, H. C. Swart, J. R. Botha, *J. Lumin*. **143** (2013) 463–468.

[18]. S. E. Braslavsky, *Pure Appl. Chem*, **79** (2007) 293-465.

[19]. S. Speiser, *Chem. Rev*. **96** (1996) 1953-1976.

[20]. R. C. Powell, G. Blasse, *in luminescence and Energy transfer*, Ed, J. D. Dunits, Springer Verlag, **42** (1980) 43-46.

[21]. F. E. Auzel, *Proceedings of the IEEE*, **61** (1973) 758-788.

[22]. F. E. Auzel, *Chem. Rev*, **104** (2004) 139-173

[23]. G. Blasse, *Materials Chemistry and Physics.* **16** (1987) 201-298.

[24]. F. Auzel, *In: Radiationless Processes*, eds. B. Dibartolo and V. Goldberg (Plenum Publishing Co., New York, 1980) p: 213-216.

[25]. T. Forster, *Ann. Phys*, 2(1948) 55-75.

[26]. P. X. Gao, Y. Ding, Z. L. Wang *Nano. Lett.***3** (2003) 1315–1320.

[27]. M. Willander, O. Nur, Q. X. Yang, L. L. Yang, M. Lorenz, B. Q. Cao, J. Zuniga Perez, C. Czekalla, G. Zimmermann, M. Grundmann, A. Bakin, A. Behrends, M. Al-Suleiman, A. Al-Shaer, A. Che Mofor, B. Postels, A. Waag, N. Boukos, A. Travlos, H. S. Kwack, J. Guinard, D. Le Si Dang, *Nanotech*, **20** (2009) 332001:1-332001:5.

[28]. W. Liu, L. S. Gu, D. L. Ye, S. M. Zhu, S. M. Liu, X. Zhou, R. Zhang, Y. Shi, Y. Hang, C. L. Zhang, *Appl. Phys. Lett*. **88** (2006) 092101-1-4.

[29]. D. C. Look, *Mater. Sci. Eng. B*, **80** (2001) 383-387.

[30]. J. E. Jaffe, J. A. Snyder, Z. Lin, A. C. Hess, *Phys. Rev. B*, **62** (2000) 1660-1665.

[31]. U. Ozgur, Ya. I. Alivov, C. Liu, A. Take, M. A. Reshchikov, S. Dogan, V. Avrutin, S. J. Cho, H. Morkoc, *J. Appl. Phys*, **98** (2005) 041301:1-041301:104.

[32]. J. A. Garcia-Macedo, G. Valverde-Aguilar, J. L. Manriquez-Zepeda, *Nanophotonic Material V*, **7393** (2009) 73930Q:1-73930Q:11.

[33]. A. Janotti, C. G. van de Walle, *Phys. Rev. B*, **76** (2007**)**165202–165222.

[34]. F. Tuomisto, K. Saarinen, D. C. Look, G. C. Farlow, *Phys. Rev. B*, **72** (2005) 085206–085211.

[35]. Z. Fan, P. Chang, E. C. Walter, C. Lin, H. P. Lee, R. M. Penner, J. G. Lu, *Appl. Phys. Lett*, **85** (2004) 6128:1-6128:4.

[36]. F. A. Kroger, H. J. Vink, *J. Chem. Phys*. **22** (1954) 250-253.

[37]. S. A. Studenikin, N. Golego, M. Cocivera, *J. Appl. Phys*. **84** (1998) 2287-2294.

[38]. T. M. Borseth, B. G. Svensson, A. Y. Kuznetsov, P. Klason, Q. X. Zhao, M. Willander, *Appl. Phys. Lett*. **89** (2006) 262112:1-262112:3.

[39]. C. H. Ahn, Y. Y. Kim, D. C. Kim, S. K. Mohanta, H. K. Cho, *J. Appl. Phys*. **105** (2009) 013502:1-013502:6.

[40]. W. Q. Peng, S. C. Qu, G. W. Cong, Z .G. Wang, *Mater. Sci. Semic. Process*, **9** (2006) 156-159.

[41]. Ü. Özgür, Ya. I. Alivov, C. Liu, A. Teke, M. A. Reshchikov, S. Dogan, A. Avrutin,S-J. Cho, H. Morkoç, *J. Appl. Phys*, **98** (2005) 041301:1–041301:103.

[42]. D. Li, Y. H. Leung, A. B. Djurisic, Z. T. Liu, M. H. Xie, S. L. Shi, S. J. Xu, *Appl. Phys. Lett*, **85** (2004) 1601–1603.

[43]. K. H. Tam, C. K. Cheung, Y. H. Leung, A. B. Djurisic, C .C. Ling, C. D. Beling, S. Fung, W. M. Kwok, D. L. Phillips, L. Ding, W. K. Ge, *J. Phys. Chem*, **110** (2006) 20865–20871.

[44]. L. E. Greene, M. Law, J. Goldberger, F. Kim, J. Johnson, Y. Zhang, R. J. Saykally, P. Yang, *Angew. Chem. Int. Ed*, **42** (2003) 3031–3034.

[45]. M. Gomi, N. Oohira, K. Ozaki, M. Koyano, *Jpn. J. Appl. Phys*, **42** (2003) 481–485.

[46]. A. B. Djurisic, Y. H. Leung, K. H. Tam, Y. F. Hsu, L. Ding, W. K. Ge, C. Zhong, K. S.Wong, W. K. Chan, H. L. Tam, K. W. Cheah, W. M. Kwok, D. L. Phillips, *Nanotech*, **18** (2007) 095702:1-095702:8.

[47]. R. Dingle, *Phys. Rev. Lett*. **23** (1969) 579-581.

[48]. D. Zwingel, *J. Lumin*. **5** (1972) 385-405.

[49]. C. Kittel, *Introduction to Solid State Physics*. John Wiley and Sons Inc, 8th edition, (2005).

[50]. N. Choudhury, B. K. Sarma, *Thin. Solid. Films*, **519** (2011) 2132-2134.

[51]. A. Martucci, J. Fick, J. Schell, G. Battaglin, M. Guglielmi, *J. Appl. Phys.* **86** (1999) 79-87.

[52]. J. L. Machol, F. W. Wise, R. C. Patel, *Phys. Rev. B*, **48** (1993) 2819-2822.

[53]. A. K. Dutta, T. Ho, L. Zhang, P. Stroeve, *Chem. Mater*. **12** (2000) 1042-1048.

[54]. D. Kumar, G. Agarwal, B. Tripathi, D. Vyas, V. Kulshrestha, *J. Alloy. Comp*. **484** (2009) 463-466.

[55]. F. Ochanda, K. Cho, D. Andala, T. C. Keane, A. Atkinson, W. E. Jr Jones, *Langmuir*, **25(13)** (2009) 7547–7552.

[56]. R. N. Bhargava and D. Gallagher, *Phys. Rev. Lett*. **72** (1994) 416–419.

[57]. D. W. Snoeke, *Solid State Physics, Essential Concepts*, Addison-Wesley, (2009) page 85-97.

[58]. L. Brus, *J. Phys. Chem*, **90** (1986) 2555-2560.

[59]. S. C. Erwin, L. Zu, M. I. Haftel, A. L. Efros, T. A. Kennedy, D. J. Norris, *Nature*, **43** (2005) 91-94.

Chapter 3: Experimental

3.1 Experimental Procedure

3.1.1 Introduction

Different fabrication methods, such as vapour-phase transport **[1-3]**, pulsed laser deposition **[4]**, chemical vapour deposition **[5, 6]** and electrochemical deposition **[7]**, have been widely used to prepare semiconductors nanostructures. The complex processes, sophisticated equipment and high temperatures make them very difficult to up scale these processes for commercial application. Hence, an efficient, scalable and economical method for growing semiconductor nanostructures is required for a diverse range of applications. In recent years low-temperature wet chemical methods have received more attention and are already been commonly used to grow semiconductors nanostructures. There are mainly three common approaches in chemical growth at low temperature, i.e. the hydrothermal **[8, 9]**, chemical bath deposition (CBD) **[10, 11]**, and electrochemical deposition **[12-14]**. In this study the CBD method was used to grow samples. The CBD process is one of the useful solution methods for the preparation of compound semiconductors from aqueous solution. The CBD is a large area production process, simple in instrumental operation **[15]**, cheap and convenient process to prepare semiconducting materials. The more recent interest in all things 'nano' has provided a boost for CBD, since it is a low temperature, solution (almost always aqueous) technique, crystal size is often very small and it gives better homogeneity **[16].** The CBD process has been used extensively to synthesize semiconductor powders and thin films. Though CBD has many advantages, it suffers from some disadvantages. In case of a set CBD process, the heat needed for chemical reaction is supplied from the solution bath to the sample surface, resulting in both heterogeneous nucleations at the surface as well as homogeneous particle formation in the bath.

3.2 Synthesis

3.2.1 Synthesis of undoped ZnO, Ce^{3+}, Eu^{3+}, and Cu^{2+} doped ZnO nanostructures.

All the chemicals used for the preparation of the nano-powders were of analytical grade. It includes zinc acetate (Zn $(CH_3COO)_2.2H_2O$), thiourea ($(NH_2)_2CS$) and ammonia (25% NH_3). During the preparation of the nano-powders, ammonia was used as a complexing agent. The undoped ZnO precursors were prepared by dissolving 0.46 M of zinc acetate, 0.18 M of thiourea and 19.76 mL of ammonia in 80 mL of deionised water, separately. The chemical

bath solution was prepared as follows: 60 mL of a Zinc acetate, thiourea and ammonia solutions were mixed. The amount of solutions of zinc acetate, thiourea and ammonia was held constant at ratio of 1:1:1. Suspensions were formed immediately. Thereafter, the solutions was rapidly heated to 80ºC and kept for various time while continuously stirring. The resulted precipitates were left overnight and separated from the solvent by filtration. The ZnO particles were washed with 60 mL of acetone, ethanol and deionized water in that order. The obtained particles were dried at ambient conditions for 72 h and were ready to be characterized using various characterization technique.

The synthesis of ZnO nanostructures in the presence of Ce^{3+} cations was performed similarly, but adding different molar concentrations of $Ce(CHCOO)_3).6H_2O$ to the $Zn(CH_3COO)_2.2H_2O$ precursor. The varied amount of $Ce(CHCOO)_3.).6H_2O$ present in the precursor solution are in Ce mol%: 0.1, 0.3, 0.5, 0.7, 1, 3, 5, and 10.

Similar experimental procedure was followed during synthesis of the Eu^{3+}-doped of ZnO nanostructures, but adding different amounts of $Eu(NO_3)_3.6H_2O$ to the $Zn(CH_3COO)_2.2H_2O$ precursor, to obtain concentrations of 0.2, 0.5, 1, 2, 3, 4, and 5 mol% Eu.

Lastly, the synthesis of Cu^{2+}-doped ZnO nanostructures was also performed similarly, but adding different amounts of $Cu(CH_3COO)_2.2H_2O$ to the $Zn(CH_3COO)_2.2H_2O$ precursor, to obtain concentrations of 0.05, 0.1, 0.2, 0.4, 0.5, 0.6, 0.8, 1, 2 and 3 mol% Cu.

3.2.2 Synthesis of undoped PbS, Tb^{3+} doped and Ce^{3+}-codoped PbS nanoparticles.

All the chemicals used for the preparation of the nano-powders were of analytical grade. It includes lead acetate ($Pb(CH_3COO)_2.2H_2O$), Thiourea $(NH_2)_2CS$ and Ammonia (25% NH_3).

- The preparation of PbS powders were carried out using the following procedure: The PbS precursors were prepared by dissolving 0.13 M of lead acetate, 0.18 M of thiourea and 98.8 mL of ammonia in 400 mL of deionised water, separately. During the preparation of the nano-powders, ammonia was used as a complexing agent. The chemical bath solution was prepared as follows: 60 mL of a lead acetate, thiourea and ammonia solutions were mixed. The amount of solutions of lead acetate, thiourea and ammonia was held constant at ratio of 1:1:1. In order to investigate the growth conditions, the influence of dopant and ultimately prepare, various nanostructured of PbS the following experimental conditions are investigated.

- Different precursors were prepared at synthesis temperature of 55, 65, 70 and 80 ºC, while synthesizing time was kept constant at 10 minutes.
- The amount lead acetate (0.12M, 0.13M and 0.15M) in the precursor was varied while the bath temperature maintained 65 ºC for 10 minutes.
- For the preparation of Tb^{3+}-doped PbS samples, a solution of the rare earth nitrate in appropriate proportions in water is added to the precursor to obtain concentrations of 0.05, 0.1, 0.2, 0.3, 0.5, 1, 1.5 and 2 mol% Tb^{3+}.
- The synthesis of Ce^{3+}-codoped PbS nanoparticles were performed similarly, but holding the $Tb(NO_3)_3.6H_2O$ concentration constant at 1 mol% and adding different amounts of $Ce(NO_3)_3.6H_2O$ to the precursor, to obtain 0.1, 0.3, 0.5, 1 and 2 mol% Ce^{3+} concentrations. The precipitates formed were left overnight and then filtered. The obtained particles were dried at ambient conditions for 6 days and ready to be characterized using various characterization technique.

3.3 Sample Characterization

3.3.1 Introduction

In this study, a wide variety of characterization techniques were used to evaluate the material quality of the semiconductor nanostructures. The techniques broadly deal with the issues such as sample surface topography, morphology including grain size, shape, evidence of voids, the presence of crystalline phases and detection of shallow-level impurities. The presences of crystalline phases were determined by x-ray diffraction (XRD). The morphologies of the nanostructures were studied by scanning electron microscopy (SEM) and scanning auger electron microscopy (SAM). The morphologies and the grain sizes of semiconductor nanostructures were confirmed by Tunnelling electron microscopy (TEM). The stoichiometric ratios of pure, dopant and co-dopant semiconductor materials were determined by energy dispersive x-ray spectroscopy (EDS) and auger electron spectroscopy (AES). The optical properties of the nanostructures were evaluated by UV-vis spectroscopy. The luminescence properties were determined by photoluminescence (PL) measurements. The most important features of these characterization techniques are outlined in the following sections.

3.3.2 Structural Analysis

3.3.2.1 X-ray Diffraction (XRD)

Powder X - ray diffraction (XRD) is a rapid analytical technique, primarily used for phase identification of a crystalline material and can provide information on unit cell dimensions. The XRD patterns were conducted using a Bruker AXS Discover Model diffractometer with CuKα (1.5418Å) radiation. It is a common technique for the study of crystal structures, grain size and atomic spacing. The grain size can be obtained from the full width half maximum (FWHM) of the diffraction peaks using Debye formula **[17]**. X - Ray diffractometer consists of three basic elements: an X – ray tube, a sample holder and an X - ray detector. X - Rays are generated in a cathode ray tube by heating a filament to produce electrons, accelerating the electrons toward a target by applying a voltage, and bombarding the target material with electrons.

When electrons have sufficient energy to dislodge inner shell electrons of the target material, characteristic X - ray spectra are produced. Filtering, by crystal monochromators, is required to produce monochromatic X - rays needed for diffraction. Copper is the most common target material for single – crystal diffraction. These X - rays are collimated and directed onto the sample. As the sample and detector are rotated, the intensity of the reflected X - rays are recorded. When the geometry of the incident X - rays impinging the sample satisfies the Bragg Equation, constructive interference occurs and a peak in intensity occurs. A detector records and processes this X - ray signal and converts the signal to a count rate which is then output to a device such as a printer or computer monitor. The interaction of the incident rays with the sample produces constructive interference (and a diffracted ray) when condition satisfy Bragg's law **[18]**.

3.3.2.2 Scanning Electron Microscope (SEM)

The SEM is extremely useful for imaging surface and subsurface microstructure. Scanning electron microscopy was conducted using a SHIMADZU SSX-550 Superscan SEM Model operating in standard high vacuum mode and is equipped with energy dispersive spectroscope. By using it we can estimate the diameter, length, and shape. In a typical SEM, an electron beam is thermionically emitted from an electron gun fitted with a tungsten filament cathode and these emitted electrons are directed and focused on the sample by using an anode and various electromagnetic lenses between the electron gun and sample. Tungsten

has the highest melting point and lower vapour pressure of all metals. These projected electrons eject secondary and back scattered electrons after hitting the sample. The ejected secondary and back scattered electrons from the sample are detected by detectors and these detectors transfer these detected electrons into electronic signal which is sent to a computer to display the image. The electrons interact with the atoms that make up the sample producing signals that contain information about the sample's surface information.

3.3.2.3 Energy Dispersive Spectroscopy (EDS)

EDS analysis is useful in identifying materials and contaminants, as well as estimating their relative concentrations on the surface of the specimens. During EDS analysis, the specimen is bombarded with an electron beam inside the SEM. The bombarding electrons collide with the specimen atoms own electrons, knocking some of them off in the process. A position vacated by an ejected inner shell electron is eventually occupied by a higher - energy electron from an outer shell. Thus, by measuring the amounts of energy present in the X - rays being released by a specimen during electron beam bombardment, the identity of the atom from which the X - ray was emitted can be established.

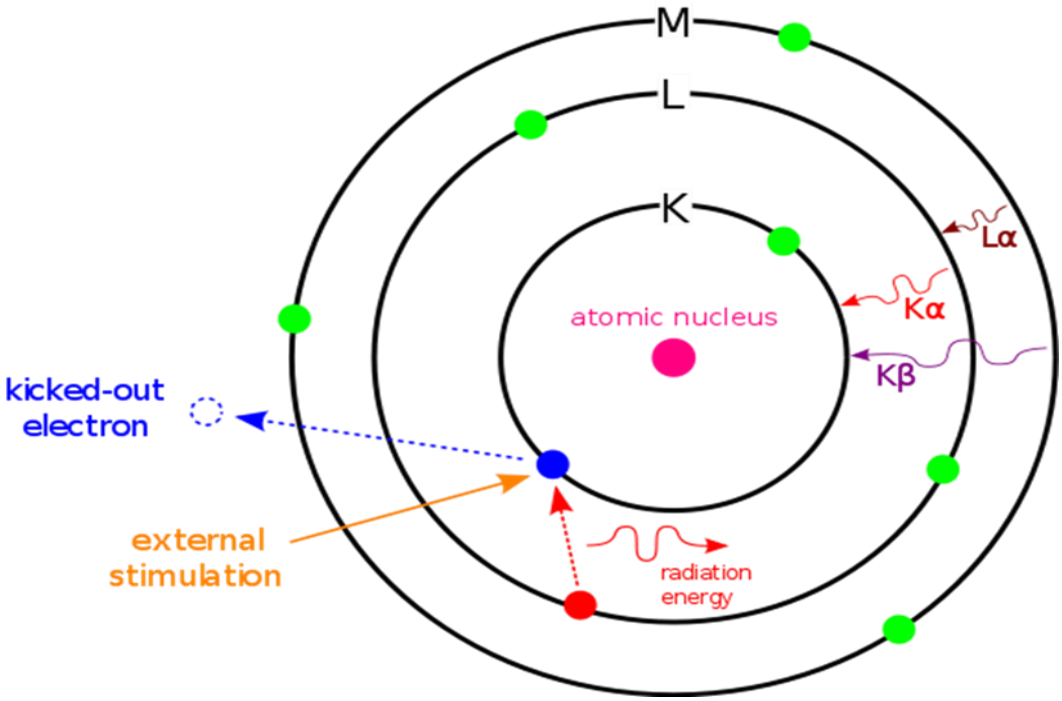

Figure 3.1: Illustration of the effect occurring during EDS.

Each of these peaks is unique to an atom and therefore corresponds to a single element. The higher a peak in a spectrum, the more concentrated the element is in the specimen. An EDX spectrum plot not only identifies the element corresponding to each of its peaks, but the type of X - ray to which it corresponds as well. An electron from one of the higher energy shells will drop down to fill this vacancy and in doing so an X-ray photon is released with an energy equal to the energy difference between the two levels involved, given by equation 3.2 where a L to K transition is considered.

$$E_{K-\alpha} = E_L - E_K \qquad 3.1$$

The same principle is valid for the calculation of other X-ray energies. Kα X-rays originate from an L shell electron filling the vacancy in the K shell, see Figure 3.1. The X-ray released by the electron is then detected and analyzed by the EDS. As the energy of the X-rays is characteristic of the difference in energy between the two shells, and of the atomic structure of the element from which they were emitted, this allows the elemental composition of the specimen to be measured.

3.3.2.4 Transmission Electron Microscopy (TEM)

Transmission Electron Microscopy (TEM) is a microscopy technique whereby a beam of highly-focused, mono-energetic beam of electrons is bombarded in vacuum on a very thin solid specimen (< 200 nm) and interacting with the sample as it passes through. The particle size and morphology of the synthesized powders were determined with TEM using Tecnai F20 coupled with an energy dispersive X-ray spectrometer (EDS). TEM works on the principle similar to that of an optical microscope with the key difference that it uses electrons and not photons as the source. In a TEM microscope, light is replaced by an electron beam and traditional lenses are replaced by electromagnetic lenses to produce an axial magnetic field that controls the focus of the electron beam. The electron beam is produced by an electron gun located at the top of the microscope. The beam is focused on the specimen using condenser lenses.

The output image is magnified over three stages. An objective lens works on magnifying the image. This image is then magnified further by the diffraction lens and finally by the projector lens before it is displayed on a fluorescent screen. An objective or a diffraction aperture can be used at the back focal plane or before the diffraction lens to improve the contrast of the final image **[19]**. TEM can be operated in a mode of imaging known as high resolution (HRTEM) or phase contrast. In this mode, it is possible to study the particle size,

morphology and crystal structure. Again analysis yields information about atomic structure and defects present in the material. The prepared powders samples were dispersed in ethanol 3 mm holey carbon copper grids were dipped into ethanol mixture and the grids were allowed to dry. After evaporation of the solvent the particles were observable in the microscope.

3.3.2.5 Auger electron spectroscopy (AES)

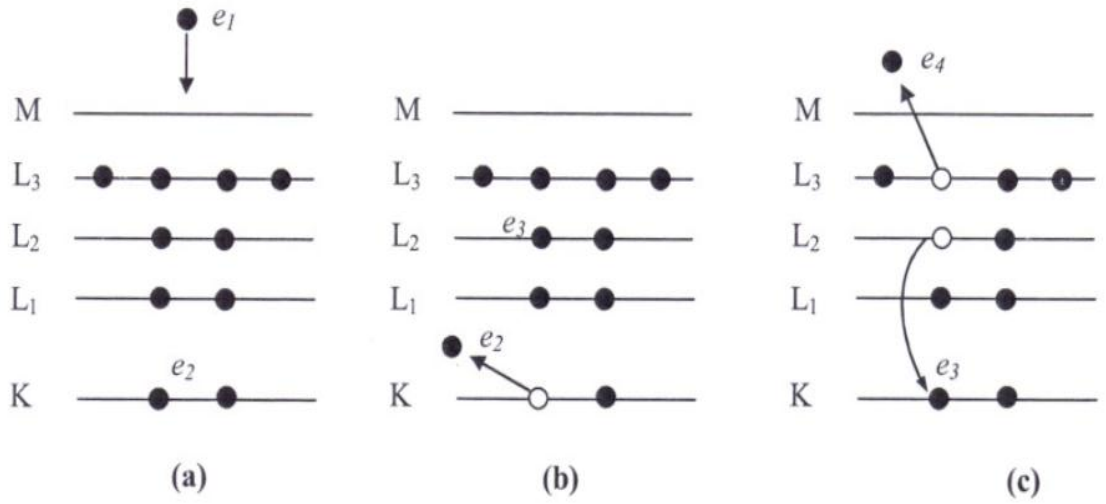

Figure 3.2: An example of an Auger process (a) a primary incident electron (e_1) on atom with energy levels K, L_1, L_2, L_3 and M. (b) the electron e_2 is removed from the K shell (c) the vacancy is filled by e_3 from energy level L_2 and the excess energy is transferred to electron e_4 which is ejected from the atom.

AES is a common analytical technique used specifically in the study of surfaces and, more generally, in the area of materials science. The morphology of the prepared nanoparticles and the elemental analysis were determined by Scanning Auger electron microscopy (SAM) and Auger electron spectroscopy (AES) using a PHI 700 Scanning Auger Nanoprobe. The Auger process is illustrated in Figure 3.2. In this example an incident primary electron (e_1) removes an electron (e_2) from the K shell of the atom. An electron (e_3) from an outer level (L_2) moves into the vacancy and the energy released is used to eject another electron (e_4) from the L_3 energy level in the atom, leaving vacancies in two shells. The final electron (e_4) is called the Auger electron and is denoted by the three energy levels involved in the process. In this case the electron is called the K_{L2L3} Auger electron. The energy of the ejected Auger electron in the example is:

$$E_{KL2L3} = E_K - E_{L2} - E^*_{L3} \qquad 3.2$$

Where E_K and E_{L2} are the binding energies of those levels and E^*_{L3} is starred because it is the binding energy of the L_3 level because of the doubly ionized state.

The analysis of Auger energies immediately leads to elemental identification. In AES process, the primary beam energy must be between 5 and 10 keV. On entering a solid the electron beam is scattered, elastically and inelastically, until it either escapes back through the surface or reaches the thermal energies. In the process the primary electrons produces ionizations in the solid and excite secondary electrons, most with a few eV energy but some with energies up to 1 keV or higher. Both the major components of the secondary electron spectrum, the backscattered primaries and the low energy secondary may be used to form the image in a scanning electron microscope (SEM) although they carry rather different information.

3.3.3 Optical Properties

3.3.3.1 UV-VIS-NIR Spectroscopy/ Diffuse Reflectance spectroscopy

Spectroscopy is the study of light (including the non-visible wavelengths) emitted, reflected, or scattered from a sample. The optical measurements were carried out in the 200 to 800 nm wavelength range using a Perkin Elmer UV/Vis Lambda 20 Spectrophotometer. Reflectance spectroscopy is very closely related to Uv/Vis spectroscopy, in that both of these techniques use visible light to excite valence electrons to empty orbitals. The difference in these techniques is that in UV/Vis spectroscopy one measures the relative change of absorption of light as it passes through a solution, whereas in diffuse reflectance, one measures the relative change in the amount of reflected light off of a surface. Absorption and reflection of light by solution and powder, respectively, is one of the oldest and still one of the most useful instrumental methods.

Diffuse reflectance relies upon the focused projection of the spectrometer beam into the sample where it is reflected, scattered and transmitted through the sample material. The back reflected, diffusely scattered light (some of which is absorbed by the sample) is then collected by the accessory and directed to the detector optics. Only the part of the beam that is scattered within a sample and returned to the surface is considered to be diffuse reflection. Diffuse reflection is the radiation that penetrates into the sample and then emerges at all angles after suffering multiple reflections and refractions by the sample particles. Diffuse Reflectance

spectroscopy is based on relationship known as Kubelka-Mulk function, which is a linear relation between analyte concentration and reflectance for diffuse reflectance spectroscopy **[20]**:

$$f(R) = K = \frac{(1-R)^2}{2R} = \frac{k}{s} \qquad 3.3$$

Where: R is absolute reflectance of sample layer, k is the molar absorption coefficient and s is the scattering coefficient. There are two factors affecting diffuse reflectance data, firstly: particle size is a major consideration when performing diffuse reflection measurements. The bandwidths decrease and relative intensities are dramatically altered as particle size decreases. To acquire a high quality diffuse reflection spectrum, it is necessary to uniformly grind the sample to less than 50 μm in size. Secondly: sample homogeneity, the Kubelka-Munk model for diffuse reflection is derived for homogeneous sample of infinite depth. To avid peak intensity variations, it is necessary to distribute the analyte as uniformly as possible.

1.3.3.2 Photoluminescence Spectroscopy (PL)

Photoluminescence (PL) is a non-destructive, contactless method of probing the electron structure of materials. When light of sufficient energy is illuminated a material, photons are absorbed and excitations are created. In this study photoluminescence measurements were done on a Carry Eclipse Fluorescence Spectrophotometer system, equipped with a 150 W xenon lamp and a SPEX 1870, 0.5M Spectrometer, equipped with a He-Cd laser lamp as the excitation sources. In order to understand the concept of a gap in energy, first consider that some of the electrons in a solid are not firmly attached to the atoms, as they are for single atoms, but can step from one atom to another. These loosely attached electrons are bound in the solid by differing amounts and thus have much different energy. Electrons having energies above a certain value are referred to as conduction electrons, while electrons having energies below a certain value are referred to as valence electrons.

Furthermore, there is an energy gap between the conduction and valence electron states. Under normal conditions electrons are forbidden to have energies between the valence and conduction bands. If a light particle (photon) has energy greater than the band gap energy, then it can be absorbed and thereby raise an electron from the valence band up to the

conduction band across the forbidden energy gap. In this process of photo excitation, the electron generally has excess energy which it loses before coming to rest at the lowest energy in the conduction band. At this point the electron eventually falls back down to the valence band. As it falls down, the energy it loses is converted back into a luminescent photon which is emitted from the material. Thus the energy of the emitted photon is a direct measure of the band gap energy, e.g., the process of photon excitation followed by photon emission is called photoluminescence. Through PL measurement, we can obtain a variety of material parameters, which are: band gap determination, Impurity levels and defect detection, recombination mechanisms **[21].**

References

[1]. J. S. Lee, K. Park, M. I. Kang, I. W. Park, S. W. Kim, W. K. Chom, H. S. Han

and S. Kim, *J. Cryst. Growth*, **254** (2003) 423-431.

[2]. Q. X. Zhao, P. Klason and M. Willander, *Appl. Phys. A*, **88** (2007) 27-30.

[3]. M. H. Huang, Y. Wu, H. Feick, N. Tran, E .Weber and P. Yang, *Adv. Mater*. **13** (2001) 113-116.

[4]. Y. Sun, G. M. Fuge and M. N. R. Ashfold, *Chem. Phys. Lett*. **396**

(2004) 21-26.

[5]. J .Wu and S. C. Liu, *Adv .Mater*. **14** (2002) 215-218.

[6]. W. I. Park, D. H. Kim, S.W. Jung and G. C. Yi, *Appl. Phys. Lett*. **80** (2002) 4232-4234.

[7]. H. D. Yu, Z. P. Zhang, M. Y. Han, X. T. Hao, and F. R. Zhu, *J. Am. Chem. Soc*. **127** (2005) 2378-2379.

[8]. M. Guo, P. Diao, S. M. Cai, *Appl. Surf. Sci.* **249** (2005) 71-75.

[9]. H. Q. Le, S. J.Chua, K. P Loh, E. A. Fitzgerald, Y. W. Koh, *Nanotechnology*, **17** (2006) 483-488.

[10]. L. Vayssieres, *Adv. Mater*. **15** (2003) 464-466.

[11]. L. Vayssieres, K. Keis, S. E. Lindquist and A. Hagfeldt, *J.Phys. Chem. B*. **105** (2001) 3350-3352.

[12]. J. H. Yang, G. M. Liu, J. Lu, Y. F. Qiu, S. H. Yang, *Appl. Phys. Lett*. **90** (2007) 103109-1-3.

[13]. H. H. Guo, J. Z. Zhou, Z. H. Lin, *Electrochemistry Communications*, **10** (2008)

146-150.

[14]. Y. Hames, Z. Alpaslan, A. Ko¨semen, S. E. San, Y. Yerli, *Solar Energy*, **84** (2010) 426-431.

[15]. T. P. Niesen, M. R. De Guire, *J. Electroceram*. **6** (2001) 169-207.

[16]. L. F. Koao, F. B. Dejene, H .C. Swart, J. R. Botha, *J. Lumin*. **143** (2013) 463–468.

[17]. B. D. Cullity 1978, *Elements of X-ray Diffraction (2nd Ed)*, (Addison Wesley) p 285-284.

[18]. E. J. A. Pope, M. Asami, J. D. Mackenzie, *J. Mater. Res.* 4 (**1989)** 1018-1026.

[19]. P. Champness, *Microscopy Handbooks. Electron diffraction in the transmission electron microscope*, i–xiv, (2001) 1–170.

[20]. G. RangaRao, H. RanjanSahu, Proc. *Indian Acad. Sci. (Chem. Sci)*, **113** (2001) 651-658.

[21]. http://www.itst.ucsb.edu/~vinhnguyen/Time-Frequency_Spectroscopy.htm

CHAPTER 4

Synthesis and characterization of ZnO flower-like microstructures using the chemical bath deposition method

4.1. Introduction

Zinc oxide (ZnO) a wide, direct band gap (3.37 eV) semiconductor has been intensively studied in the past decade. It crystallizes in both the cubic and hexagonal form. It is commercially used as a phosphor for cathode ray tubes in flat panel displays **[1]** and photovoltaic devices **[2].** ZnO has attracted much attention because of different properties it displays in nano forms in comparison with those of the bulk materials. Size dependence on optical properties of nanocrystalline semiconductors makes them an interesting candidate for phosphor applications **[3].** Numerous attempts of synthesizing one dimensional ZnO nanostructures have been reported **[4-6].** To the best of our knowledge no work has been done on synthesis of ZnO nanostructures for shorter time and higher zinc acetate concentration in the precursors that resulted into single phase ZnO. Therefore in this work a single phase flower-like ZnO nanostructures synthesised for shorter period of time (< 10 min) and higher precursor concentrations prepared by CBD are presented.

4.2 Results and discussions

4.2.1 Structural and compositional analyses.

Figure 4.1: shows the XRD patterns of the ZnO microstructures synthesised at constant molar concentration (mol %) of zinc acetate of 0.56M but for different synthesizing times. The average calculated values of the cell constants of *a* and *c* were 3.257 and 5.215 Å, respectively, which matched perfectly with standard data available in JCPDS card no. (36-1451, a = 3.24982 and c= 5.20661 Å). The formation of ZnO phase within 1 min shows the advantage of CBD method over other conventional methods. Figure 4.2: shows the XRD patterns of the ZnO microstructures synthesised at various mol% of zinc acetate but for constant synthesizing times. The average calculated values of the cell constants of *a* and *c* were 3.267 and 5.219 Å, respectively. The results indicate single hexagonal wurtzite nanocrystallites. No structural dependence on the synthesis time and molar concentration of

zinc acetate was observed. The average size of the as-prepared crystals can be calculated from the Full Width Half Maximum (FWHM) of the diffraction peaks using the Debye formula **[7].** The average grain sizes were found to be 48 ± 1, 45 ± 1 and 42 ± 1 nm for particles synthesized for 10 minutes, 5 minutes and 1 minute, respectively.

Figure 4.3 depict the dependence of average grain sizes on the amount of zinc acetate mol% for samples synthesized for 10 and 5 minutes. It is clear that the calculated average grain size increases with an increase in the synthesis time and the zinc acetate mol%. It is also observed that the samples synthesised for longer period depict improved crystallinity and larger grain sizes.

Figure 4.4 (a) and (b) show SEM images of the as prepared ZnO microstructures prepared at different mol% of zinc acetate but synthesized for a constant time of 5 min. All the SEM imaging was taken at 0.05 nm field of view. The surface aspects of all the SEM images are composed of flower-like structures. It is clear that the flower-like structures are clustered with some nearly spherical nanoparticles superimposed on them. An increase in zinc acetate concentrations results into larger flower-like structures.

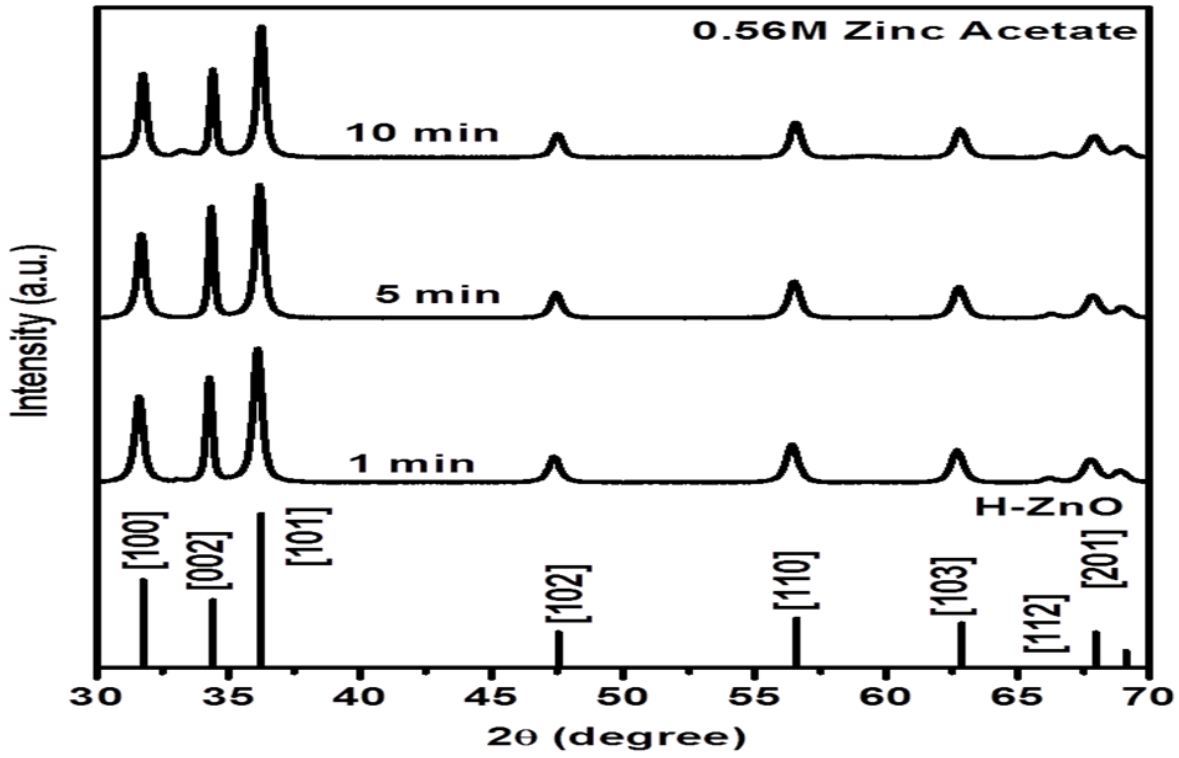

Figure 4.1: X-ray powder diffraction patterns for ZnO structures prepared at different synthesizing times but constant mol% and annealed at ambient condition.

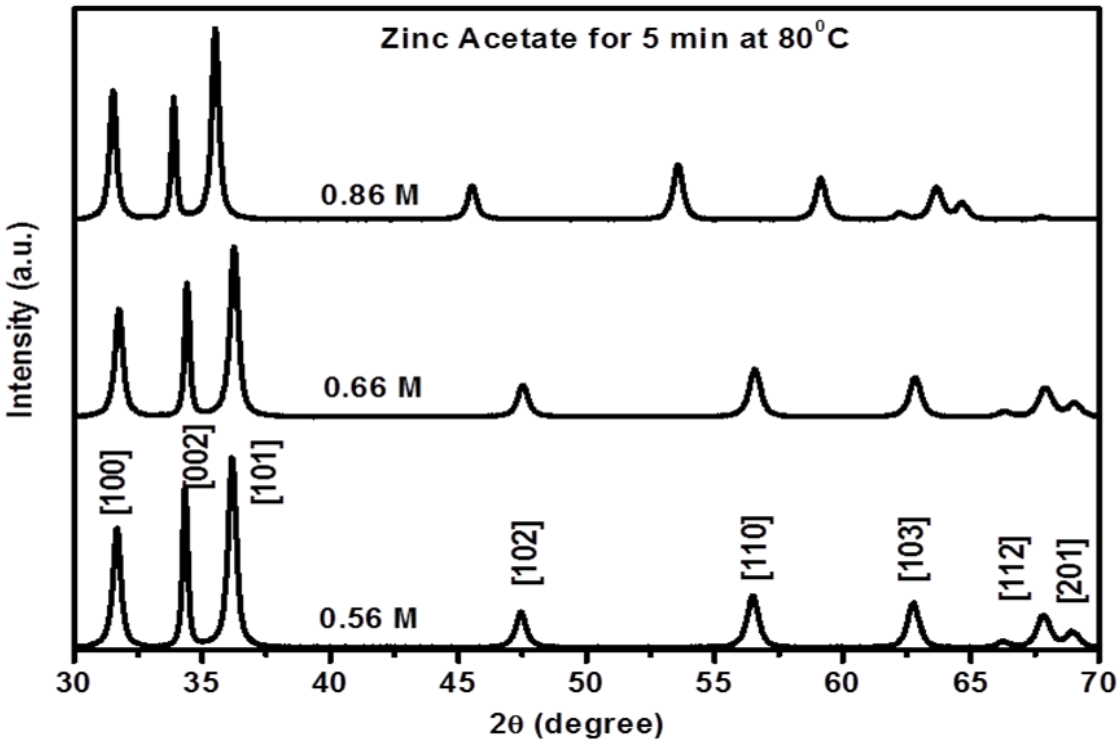

Figure 4.2: X-ray powder diffraction patterns for ZnO structures prepared different mol% of zinc acetate at constant synthesizing time and annealed at ambient condition.

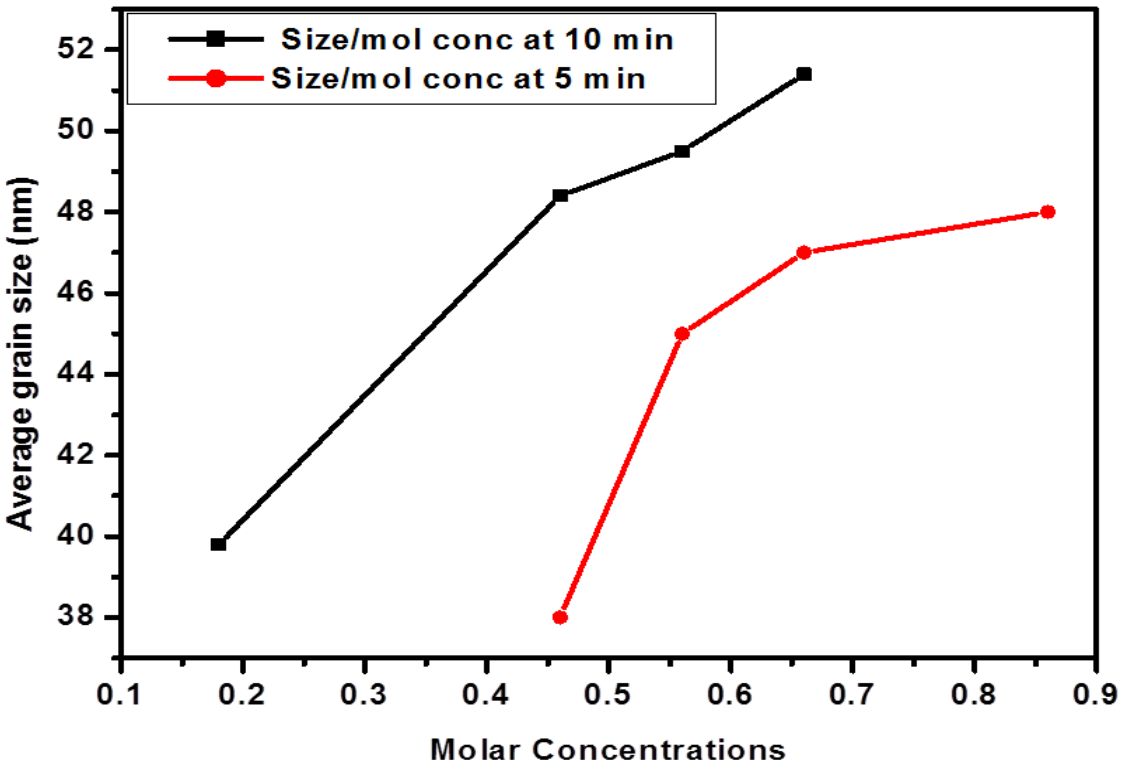

Figure 4.3: The dependence of average particle sizes of the ZnO on the zinc acetate mol% for different synthesis time.

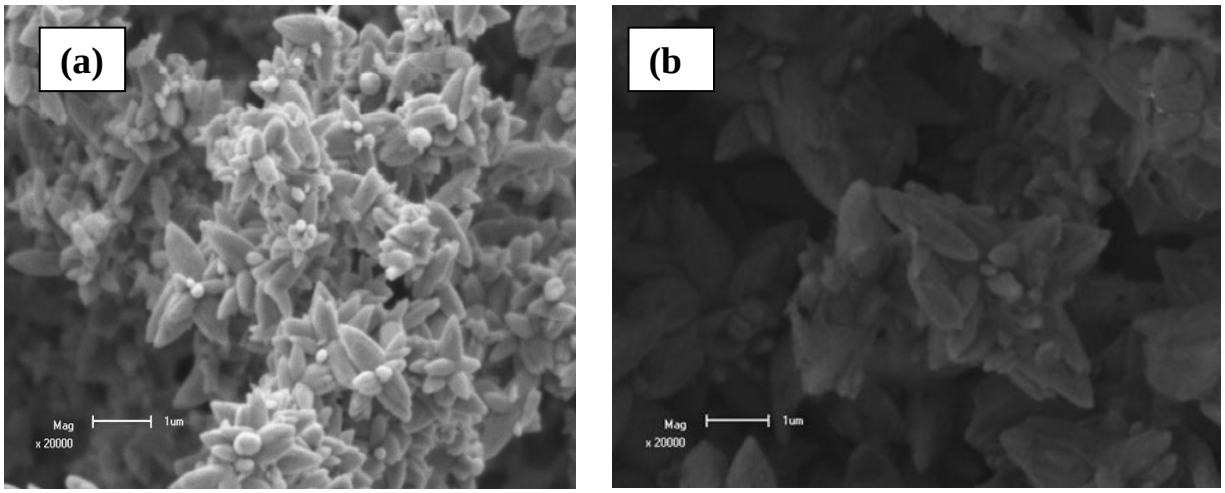

Figure 4.4: SEM images of ZnO microstructures for (a) 0.56M and (b) 0.86M Zinc acetate mol% synthesized at constant time of 5 min.

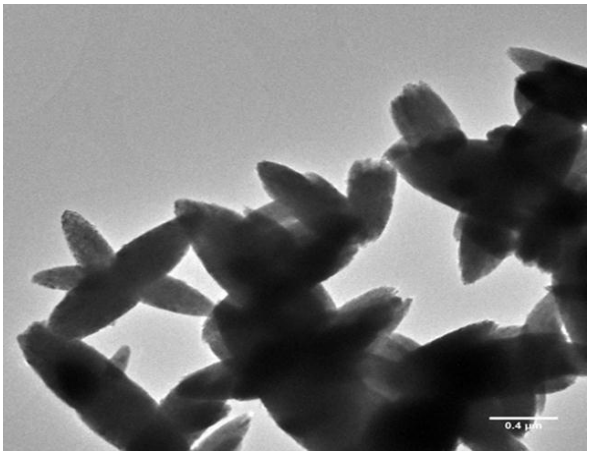

Figure 4.5: Representative of TEM image of the ZnO microflower-like structures prepared at 0.56 molar concentration of Zinc acetate for a constant time of 5 min.

The TEM micrograph of ZnO synthesized for 5 minutes using 0.56M zinc acetate is shown in Figure 4.5. The presences of ZnO flower-like microstructures are clearly visible in the TEM images. The microstructures are aggregated. The elemental composition of the ZnO samples were analysed using EDS. Figure 4.6 show the elemental analysis of the ZnO flower-like microstructures which suggests the existence of Zn and O (from the cores and the outside shell) and C (from the C double sided tape). It is clear that the amount of Zn and O increased with an increase in the concentration of the precursor (as shown in an inset).

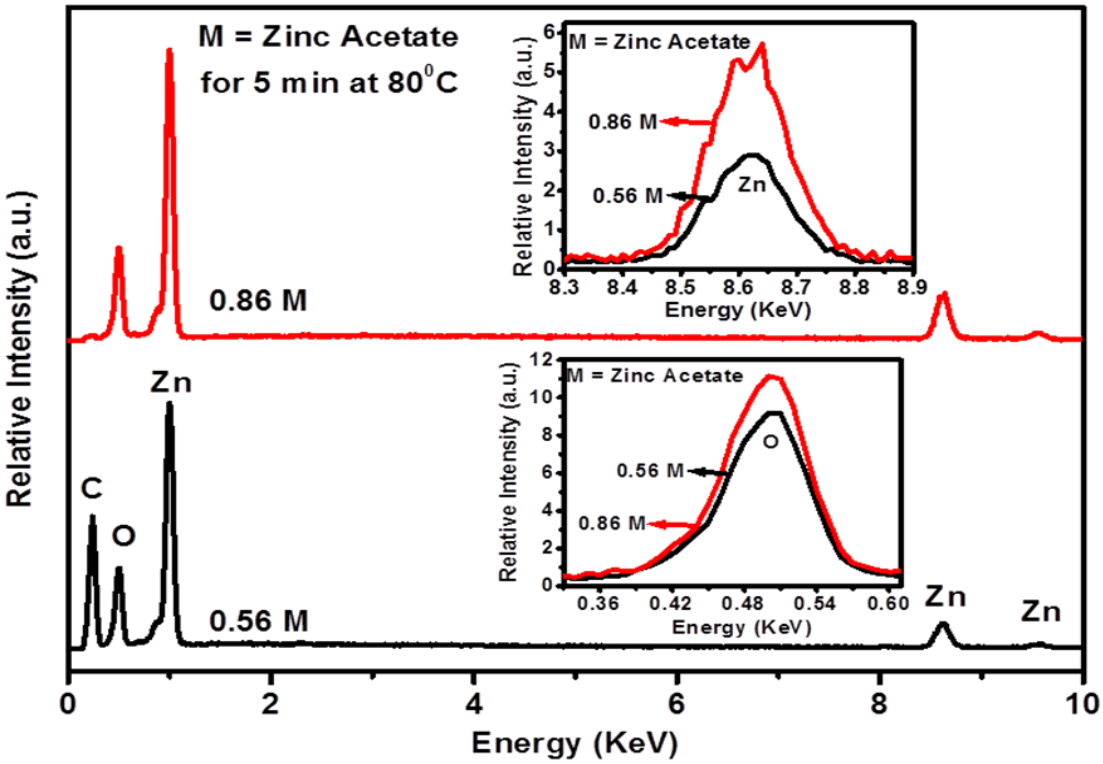

Figure 4.6: Representative EDS spectra of the ZnO microflower-like structures prepared at different mol% of Zinc acetate for a constant time of 5 min and the Zn peak of the two different mol% samples as inset.

4.3 Optical properties

The UV-visible reflectance spectra of the as prepared samples are illustrated in Figure 4.7 and 4.8, respectively. The spectra of all the samples show good optical quality in the visible range due to the complete reflectance in the 500-800 nm range. Diffuse reflectance spectral studies in the UV-Vis-NIR region were carried out to estimate the optical band gap of the synthesized flower-like rods. It clearly indicates that, the zinc acetate molar concentration and the synthesizing time shifted the optical reflection edge to a higher wavelength while the reflectance intensity decreased slightly. The ZnO is a direct band gap material. The energy band gap of these materials was estimated using the Kubelka-Munk function remission function **[8]**,

$$K=\frac{(1-R)^2}{2R} \qquad 4.1$$

Where *K* is reflectance transformed according to Kubelka Munk, R is reflectancy (%), $\boldsymbol{hv}$ is the photon energy.

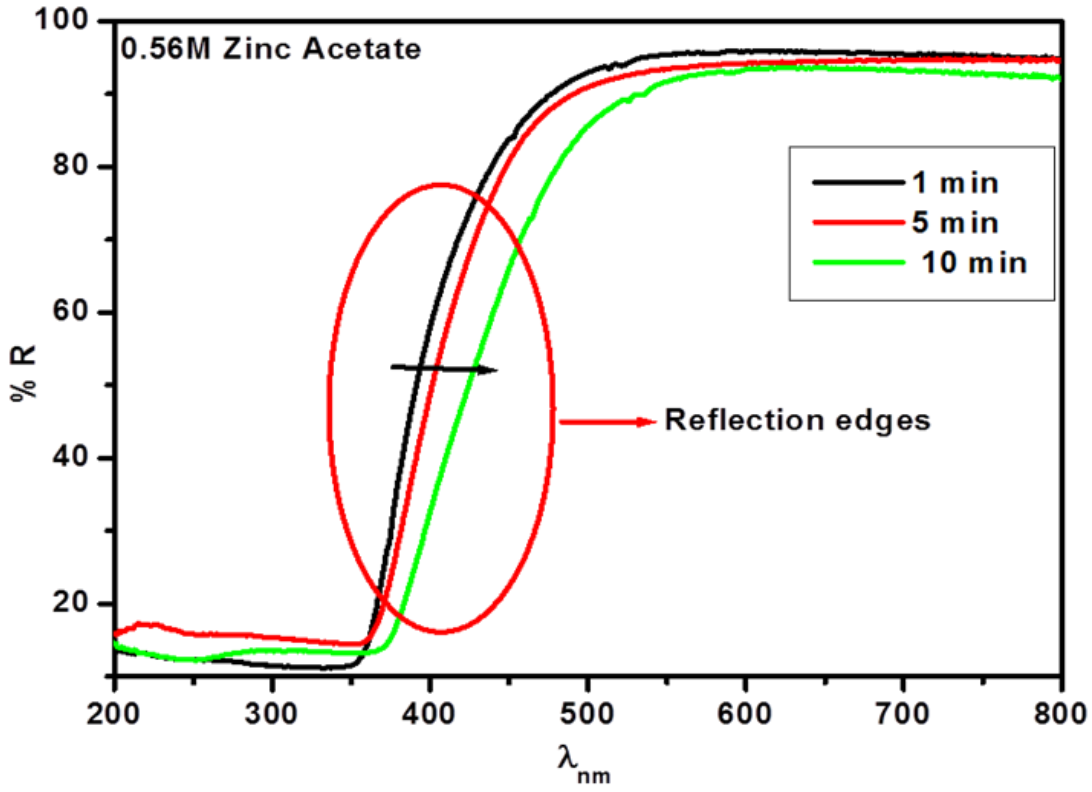

Figure 4.7: The reflectance spectra for ZnO structures prepared at different synthesizing times but constant mol% and annealed at ambient condition.

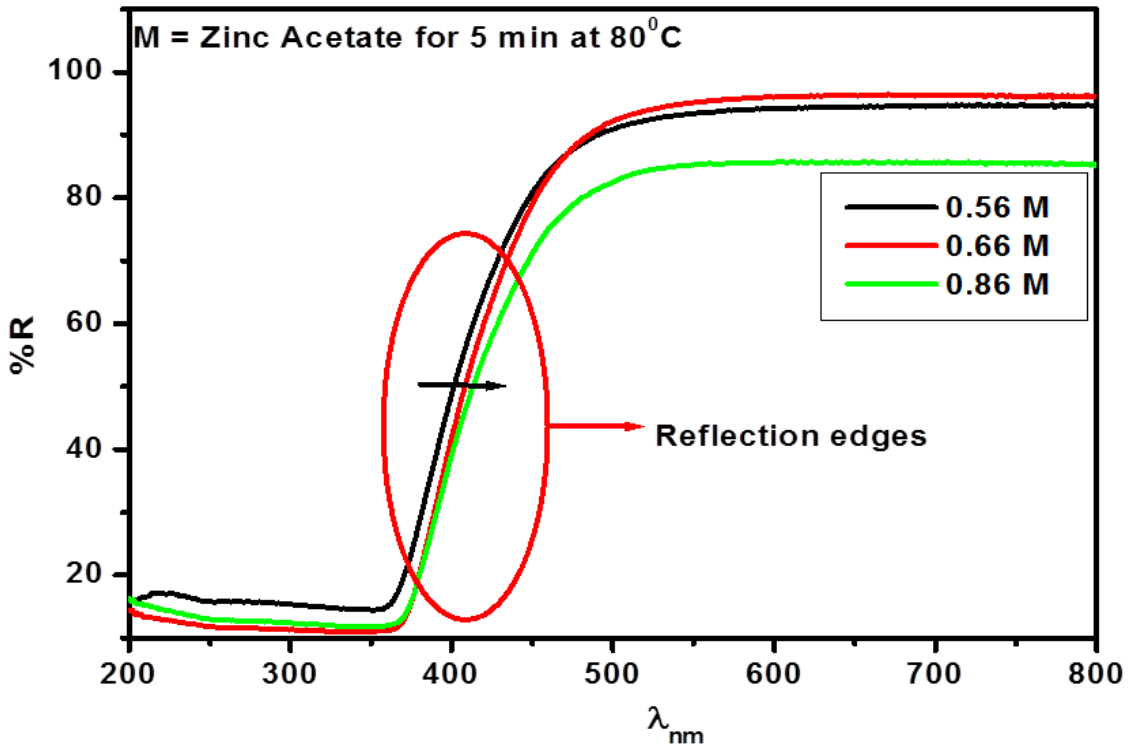

Figure 4.8: The reflactance spectra for ZnO structures prepared with different mol% of zinc acetate at constant synthesizing time and annealed at ambient condition.

In Figure 4.9 and 4.10 the energy band gaps were measured with the help of reflectance spectra plotting graphs of $(K^{*}\boldsymbol{hv})^{n}$ versus f($\boldsymbol{hv}$) **[9]**. E_g is the band gap and n=2 for direct transitions. It can be seen clearly that the band gap energy of the ZnO microstructures decreases slightly with an increase in the synthesizing time and zinc acetate concentration. The estimated band gap energy for the synthesis time were 3.36 ± 0.01, 3.28 ± 0.01 and 3.05 ± 0.01 eV for ZnO flower-like rod synthesized for 1 minute, 5 minutes and 10 minutes, respectively. The estimated band gap energy for the various mol% of zinc acetate were 3.28 ± 0.01, 3.22 ± 0.01 and 3.15 ± 0.01 eV for ZnO flower-like rod synthesized at 0.56, 0.66 and 0.86 M, respectively. All the calculated band gap energies were below the theoretical band gap value of 3.37 eV. The red shift of reflection edge and the reduction of band-gap energy may be due to an increase in grain size as confirmed by SEM and XRD analyses. It is known that as the grain size increases, the electronic states are not discrete and results in reducing of the band gap and decreases the oscillator strength **[10]**.

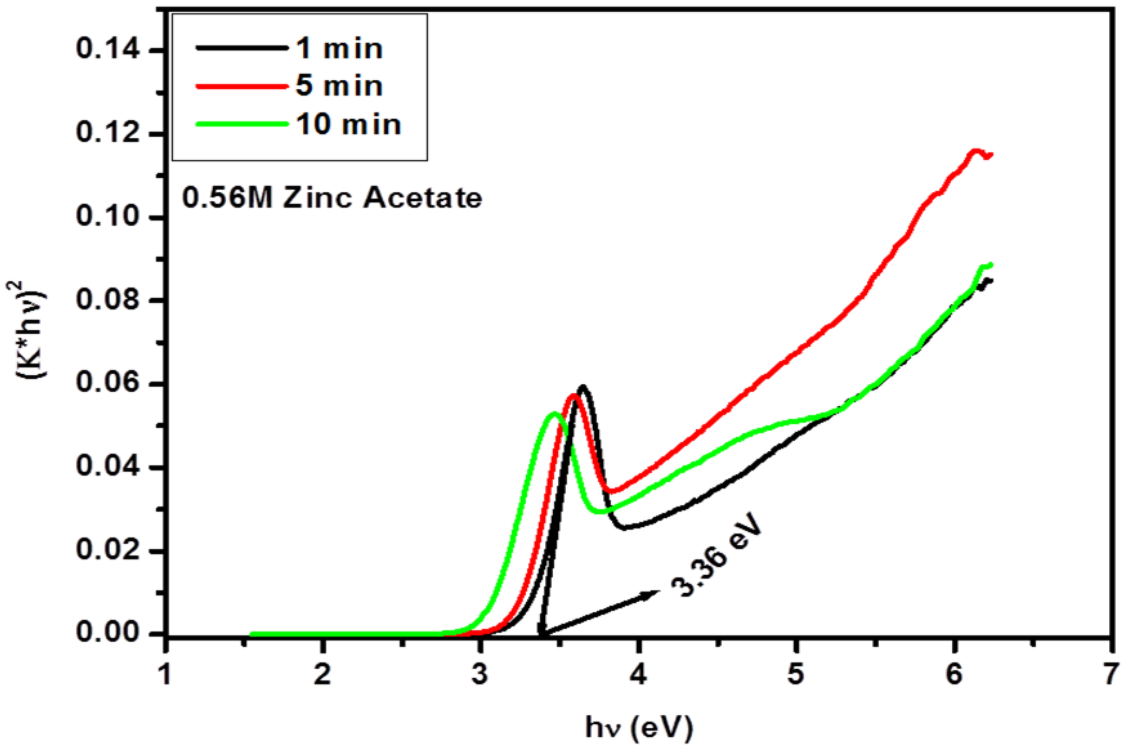

Figure 4.9: Plot to determine the band gap energy of ZnO structures prepared at different synthesizing times but constant mol% and annealed at ambient condition.

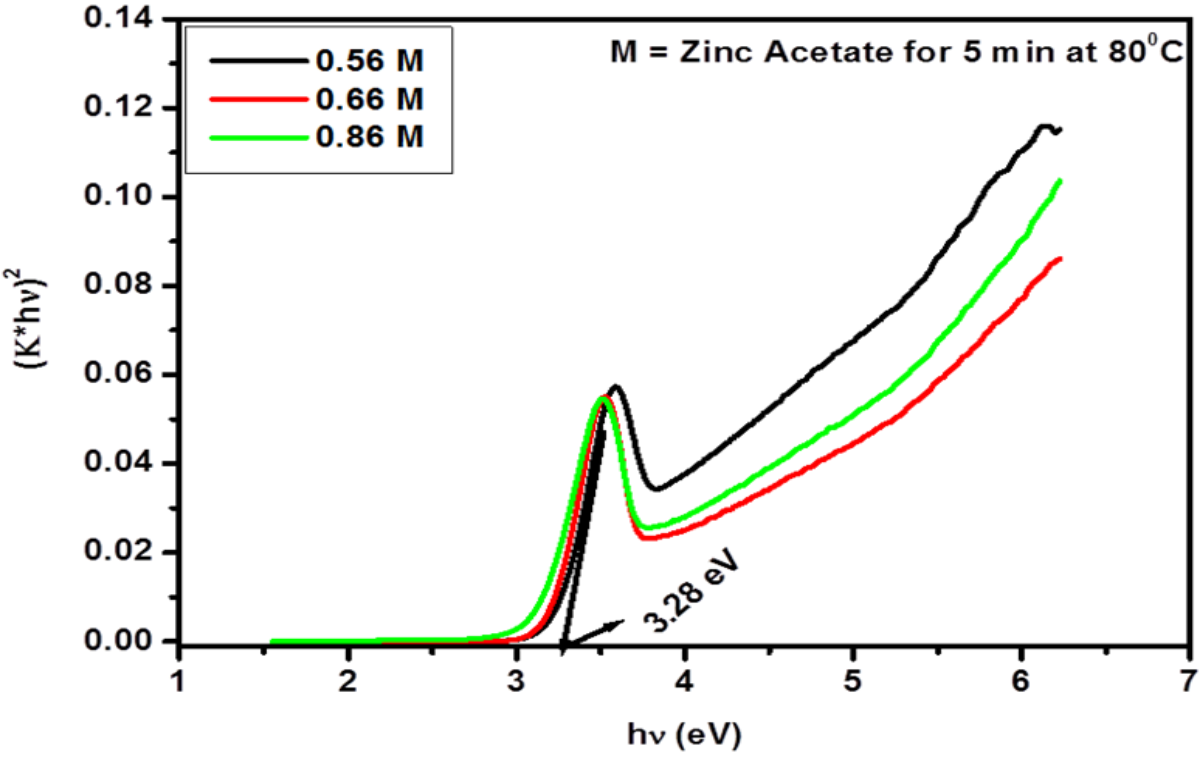

Figure 4.10: Plot to determine the band gap energy of ZnO structures prepared at prepared different mol% of zinc acetate at constant synthesizing time.

4.4 Photoluminescence

The PL measurement of the ZnO flower-like structure was carried out at room temperature with 325 nm excitation. Figure 4.11 shows strong and broad emission spectra, which were mainly located in the orange region with its maximum luminescence intensity at around 606 nm. To our results, the orange band emission may be due to the excess oxygen and zinc as was confirmed by the EDS analysis indicating that with the increase in the mol% zinc acetate the amount of Zn and O increased. Kumar et al. **[11]** have observed orange-red coupled emission from ZnO nanoparticles due to the interstitial and vacancies of oxygen as confirmed by their X-ray photoelectron spectroscopy data. Peng et al. **[12]** found a yellow emission in the as-prepared ZnO sample and a green emission in the annealed sample. The change of the visible emission is related to oxygen defects. Comparing the three patterns, the maximum luminescence intensity was reached at the ZnO synthesized for 5 minutes, any further increase in the synthesizing time resulted into the luminescence intensity decrease. An increase in zinc acetate mol% resulted only in a decrease in luminescence intensity as shown in Figure 4.12.

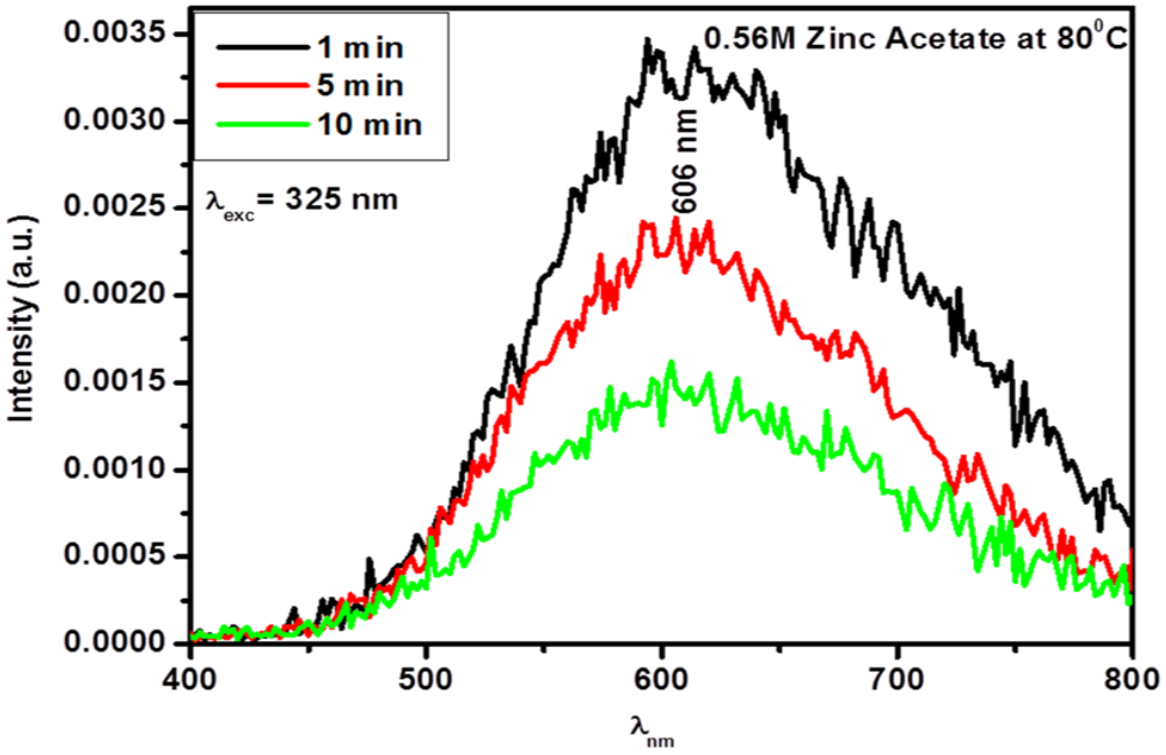

Figure 4.11: The PL spectra of ZnO microstructures prepared at different synthesizing time but synthesized at constant mol% of zinc acetate prepared by the CBD method.

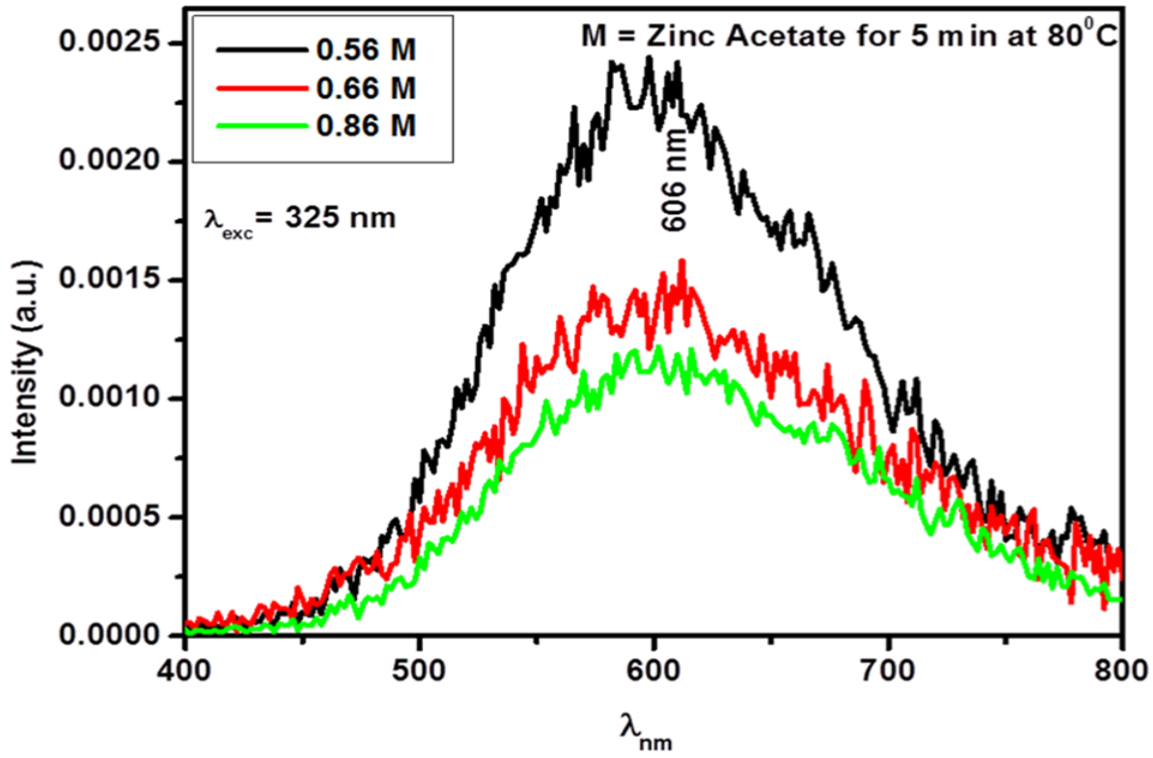

Figure 4.12: The PL spectra of ZnO microstructures prepared at different mol% of zinc acetate at constant synthesizing time and annealed at ambient condition.

The relative decrease of the PL intensity with the increase in the zinc acetate mol% suggested the increase of the grains size played a major role in decreasing the defect densities **[13]**. In other words, their gradual decrease of PL emission intensities reveals a significant decrease in the surface/volume ratio **[10]**. This decrease in luminescence intensity may be due to the increase in particle size as confirmed by the SEM and XRD analysis. There was no shift in the luminescence band of ZnO samples prepared at different synthesizing times and constant mol% of zinc acetate; which may be due to the uniform particle sizes as observed with the SEM. Therefore, it is well understood that the non-radiative recombination's increases with increasing particle size resulting into the luminescence intensity decrease **[14]**.

References

[1]. T. V. Prevenslik, *J. Lumin*, **1210 (**2000) 87-89.

[2]. P. K. Ghosh, M. K. Mitra, K. K. Chattopadhyay, *Nanotech*, **16** (2005) 107–112.

[3]. O. M. Ntwaeabora, R. E. Kroon, V. Kumar, J-P. Ahn, J-K. Park, H.C. Swart, *J. of Phys and Chem. of Solids*. **70 (**2009) 1438-1442.

[4]. G. Shen, J. Hee Cho, S. I. Juang, C. J. Lee, *Chem. Phys. Lett*, **401 (**2005) 529-533.

[5]. Y. Sun, G. M. Fuge, M. N. R. Ashfold, *Chem. Phys. Lett*, **396** (2005) 21-26.

[6]. J. Q. Hu, Q. Li, X. M. Meng, C. S. Lee, S. T. Lee, *Chem. Mater*, **15 (**2003) 305-308.

[7]. B. D. Cullity1978, 1956 *Elements of X-ray Diffraction (2nd Ed),* (Addison Wesley) 285-284.

[8]. L. F. Koao, F. B. Dejene, H. C. Swart, J. R. Botha, *J. Lumin*, **143** (2013) 463-468.

[9]. J. Tauc, R. Grigorovici, A. Vancu Sharma, *Phys. Status Solidi*, **15** (1966) 627-629.

[10] S. N. Sahu, K. K, Nanda, *PINSA*, **67 (A)** (2001) 103-130.

[11]. V. Kumar, H. C. Swart, O. M. Ntwaeaborwa, R. E. Kroon, J. J. Terblans, S. K. K. Shaat, A. Yousif and M. M. Duvenhage, *Mater. Lett.* **110(15)** (2013) 57-60.

[12]. W. Q. Peng S. C. Qu, G. W. Cong, Z. G. Wang, *Materials Science in Semiconductor Processing*, **9** (2006) 156‑159.

[13]. M. Cheraghizade, R. Yousefi, F. Jamali-Sheini, A. Sa'aedi, *J. Telecommunication Devices*, 1**(3)** (2012) 79-82.

[14]. S. Sadhu, P. Saha Chowdhury, A. Patra, *J. Lumin*. **126 (**2007) 387-392.

CHAPTER 5

The effect of Ce^{3+} on structure, morphology and optical properties of flower-like ZnO synthesized using the chemical bath method

5.1. Introduction

ZnO is one of the important semiconductor materials and has received a wide range of research interest because of its potential applications in various fields such as UV light-emitting diodes and laser diodes **[1]**, solar cell **[2]**, gas sensors **[3]**, field emission display [4], and infrared windows. Currently, much effort on research has been focused on one-dimensional nanostructures that show interesting optical, electrical, and magnetic properties resulting from low dimensionality **[5]**. These one dimensional nanostructures provide new opportunities for studying low-dimensional physics, such as dimensionally confined transport phenomena, since they represent the smallest dimension for efficient transport of electrons and excitons at room temperature **[6]**. One dimensional nanostructure is advantageous for the fabrication of nanodevices, such as nano-sized sensors and field-effect transistors **[7-8]**. Doping the semiconductor nanocrystals with transition metal (TM) and rare-earth (RE) has been the subject of the research in recent years to find out the potential applications in photonic and biophotonic field **[9]**. Ce^{3+} ions were widely used as activators in various oxides materials for its allowed optical transitions of 4f-5d. Many researchers have mentioned two main luminescent bands of Ce^{3+} doped glasses and crystals at 357 and 450 nm **[10]**, but in other samples luminescence bands at 448 nm are observed **[11]**. Numerous methods for fabricating the ZnO nanostructures have been investigated; including sol-gel method **[12-13]**, hydrothermally method **[14]**, wet chemical synthesis **[15]**, thermal evaporation **[16]**, and chemical bath deposition **[17]**. However, most preparation methods need high temperature (900-1200°C), complex process and vacuum systems. Hence, an efficient and economical method for growing ZnO nanorods is required for a diverse range of applications.

5.2 Results and discussions

5.2.1 Structural and compositional analyses.

Figure 5.1 shows the XRD patterns from the ZnO particles produced with 0, 0.1 mol %, 0.3 mol % and 10 mol % Ce-doping.

Koao L F et al J. of Lumin 143 (2013) 463-468

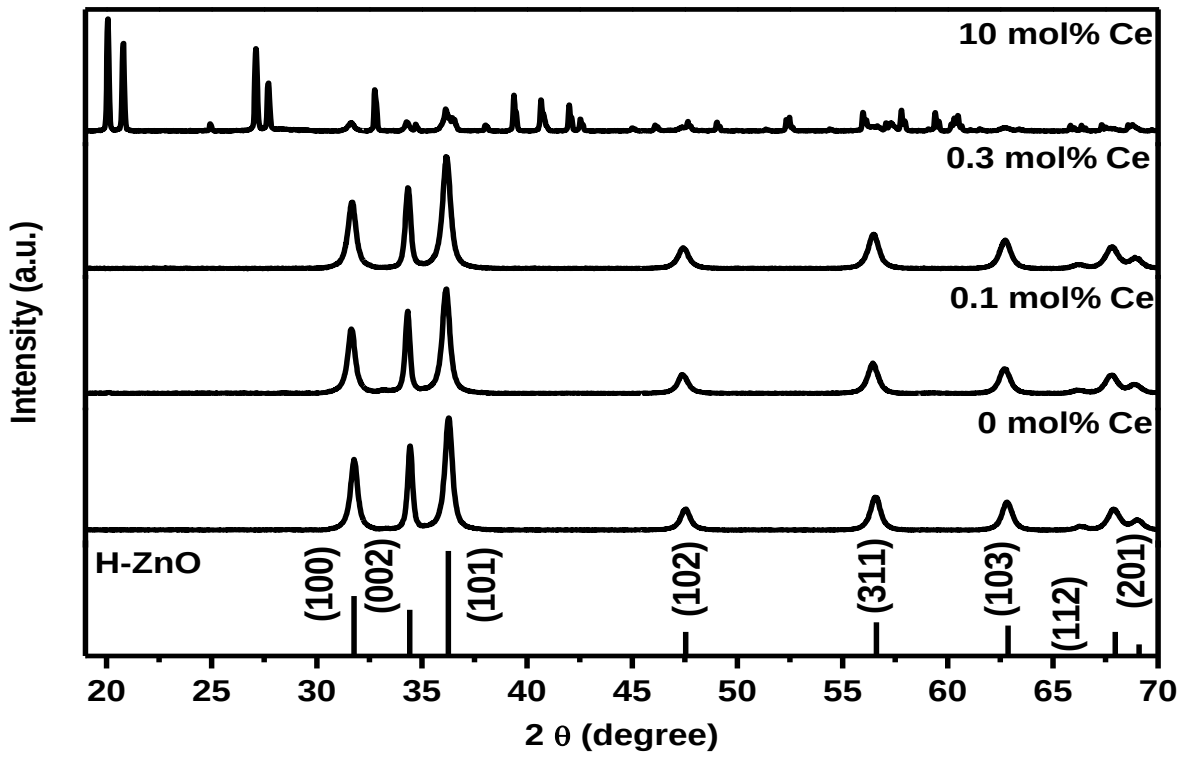

Figure 5.1: X-ray powder diffraction patterns for undoped and Ce-doped ZnO prepared by the CBD method.

The ZnO has seven peaks at 31.8, 34.5, 36.4, 47.5, 56.5, 62.8, 67.8 and 69.1 belonging to the (100), (002), (101), (102), (311), (103), (112) and (201) lattice planes. All the peaks were consistent with the hexagonal wurtzite ZnO crystal structure (JCPDS36-1451 with *a* = 3.24982 and *c*= 5.20661 Å). No peaks of impurity phases were observed at the low mol % Ce concentrations. The higher Ce concentration (10%) XRD pattern, Figure 5.2, however, clearly shows that extra impurity peaks are present. The peaks belong to Zinc (-) and Cerium (*) acetate as well as ZnO (+) according to the 33-1464, 48-1151 and 36-1451 files, respectively, as indicated. It is therefore clear that not all the dopants were incorporated in the ZnO at higher Ce concentrations. The ZnO peaks are, however, still visible in the XRD spectrum. The diffraction peaks shift slightly toward lower angles with an increase in the dopant ions as shown in Figure 5.3, indicating that the lattice parameters are slightly larger than those of undoped ZnO, which is mainly due to larger radius of Ce^{3+} (1.03 Å) than that of Zn^{2+} (0.74Å). This indicating that the dopant ions are well incorporated into the lattice sites of Zn^{2+} and lead to the increase in inter atomic distance **[18-19]**. Luo et al. **[20]** showed the successful incorporation of Ce^{3+} ions into the core of ZnO nanocrystals. The calculated average values of the ZnO cell constant of *a* and *c* are 3.25468 and 5.21157Å, respectively which matched perfectly with the standard data available in JCPDS. No significant changes

were observed for lattice parameters with the variations of the Ce ions concentrations for the lower doping concentration of the Ce ions.

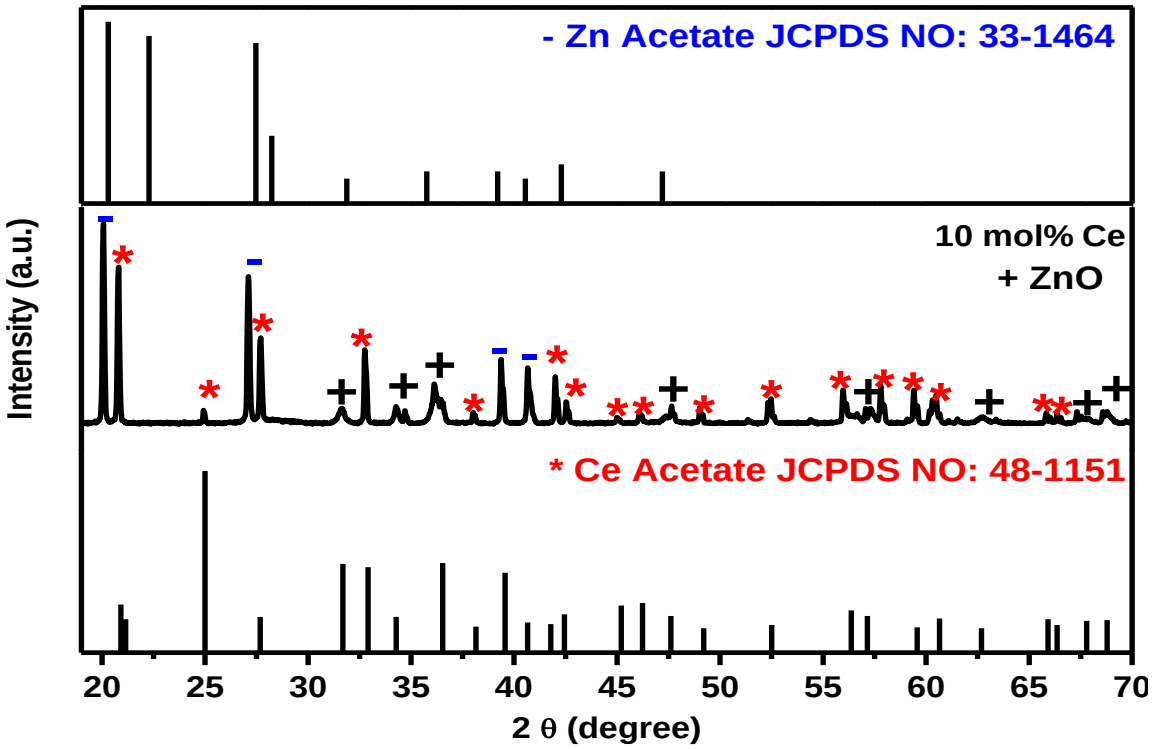

Figure 5.2: X-ray powder diffraction patterns for 10 mol % Ce-doped ZnO prepared by the CBD method and standard files of Zn- and Ce acetate.

The average grain size of the as-prepared nanocrystals can be calculated from the Full Width Half Maximum (FWHM) of the diffraction peaks using the Debye formula **[21]**. All major diffraction peaks for all samples were chosen to estimate the average size of the nanograins by the least square method. The average grain size of the as prepared samples was estimated to be 42 nm ± 2 nm. From Figure 5.4 it is clear that the estimated average particle size was in the same order for all the Ce^{3+} ion concentrations for Ce doping concentration up to 3 mol %. The estimated average crystallite grain size for the ZnO structure with some cerium acetate impurities was about 135 ± 3 nm. Figure 5.5 (a-c) show SEM micrographs of the as prepared undoped, 3 mol % and 10 mol % Ce doped ZnO nanostructures. The surface aspects of the SEM images of the un-doped ZnO are composed of uniform flower-like structures. Although the grain sizes were in the same order the particle sizes of the flower-like structures, however, have increased with an increase in the amount of the Ce dopant.

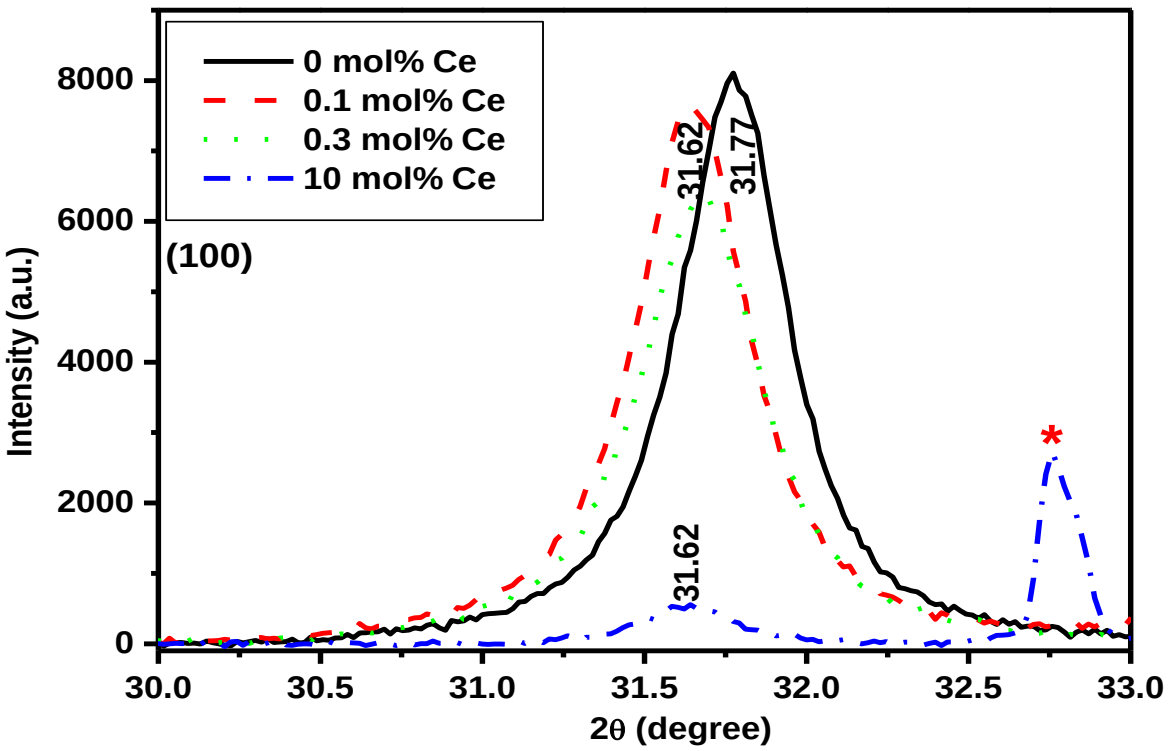

Figure 5.3: X-ray powder diffraction patterns at (100) for undoped and Ce-doped ZnO prepared by CBD method.

With the incorporation of the Ce ions into the ZnO, the flower-like structure broke up in mixed structures with the emergence of pyramid shapes. When the Ce concentration was increased to 10 mol %, the morphology of the ZnO:Ce was totally changed with large pyramid shapes with small quantities of other material attached to the main structures. The particle size of the pyramid structures from the ZnO 10 mol% of Ce^{3+} ions was large, in the order of about 10 μm. Figure 5.6 (a) and (b) show enlarged SEM micrographs with a 5 nm field of view of the undoped and 10 mol % Ce doped ZnO nanostructures. Figure 5.6(c) is a SAM image of the 10 mol % doped particle. The Ce^{3+} ions are shown in red colour. The presences and the effect of Ce^{3+} ions are clearly visible in the SAM image at higher molar concentration where the material containing the Ce^{3+} ions are adsorbed at the surface of the pyramids due to the low solubility of Ce into the ZnO. Ce is, however, also incorporated into the pyramid structures but extra material with a high concentration of Ce is present outside the particles as indicated.

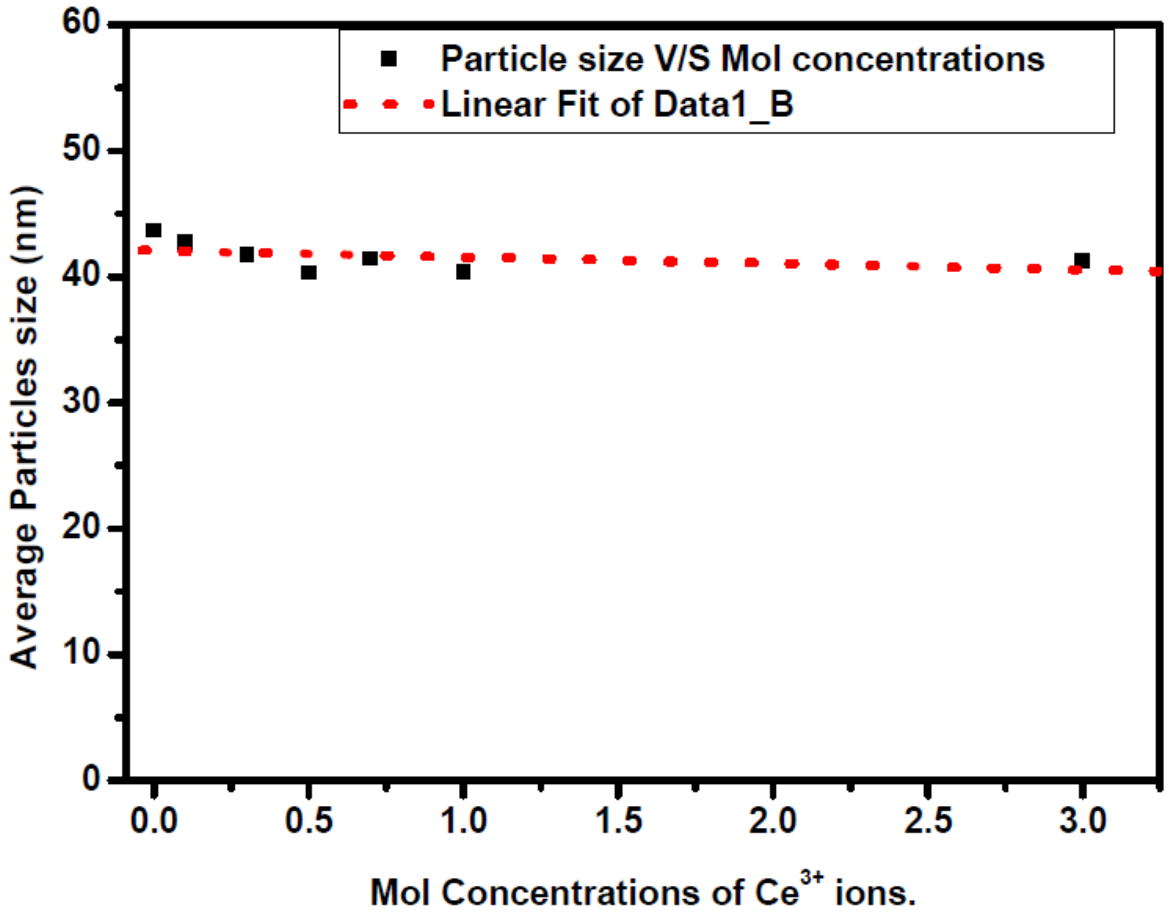

Figure 5.4: The graph of average grain size versus the molar concentrations of Ce^{3+} ions for undoped and Ce-doped ZnO.

AES measurements were carried out to check the elements and to evaluate their purity. The Auger spectrum of the undoped and Ce^{3+}-doped ZnO are shown in Figure 5.7. The typical spectrum of the nano flowers confirms the presence of Zn and O. The signals at energy of 276 eV are ascribed to the presence of adventitious carbon, which come from the atmosphere and due to handling. Ce peaks were clearly visible for the low mol% samples as indicated by the example of the ZnO:0.5 mol % Ce^{3+}sample. A high concentration of Ce was detected on the material adsorbed on the surface of the ZnO:10 mol % Ce^{3+} sample. The Zn concentration was relatively very low compared to the bulk sample. Moreover, no other impurities were found on the surface of the ZnO, suggesting that the as-synthesized ZnO are relatively pure with agglomerated Ce enrich adsorbed material on the surface thereof.

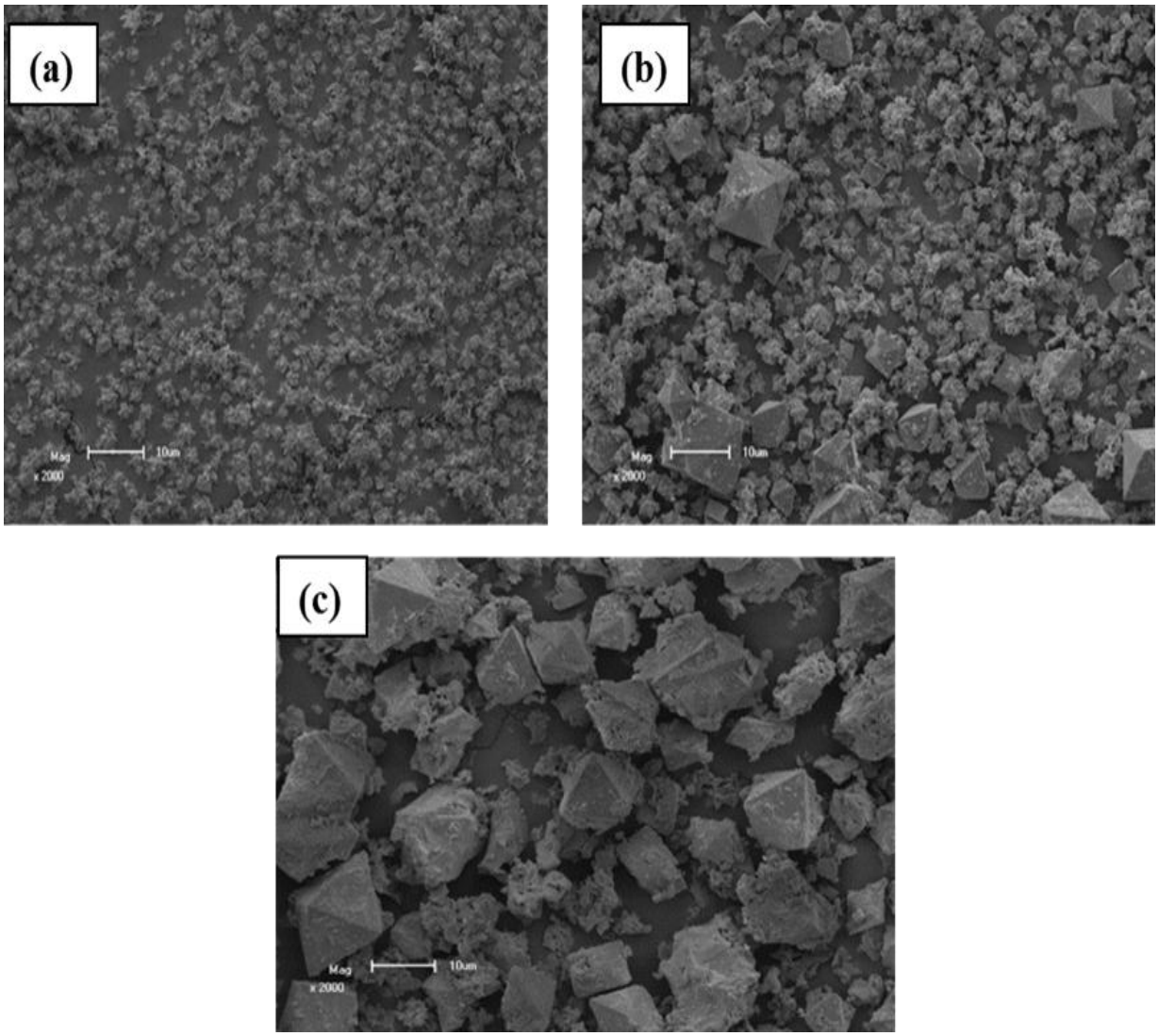

Figure 5.5: SEM images of (a) ZnO:0 mol % Ce^{3+}, (b) ZnO:3 mol % $Ce^{3+}$and (c) ZnO:10 mol % Ce^{3+}, illustrating the effect of different molar concentrations of Ce^{3+} on the ZnO structures.

Figure 5.8 shows AES spectra and the concentration values at two different positions on the 10% sample. The AES spectra were measured on (1) the ZnO crystals itself and (2) on the material with extra undissolved material with a high concentration of Ce present outside the particles. The atomic concentration on the ZnO itself was close to 10%, but on the other areas the Ce concentration was about 30% which clearly shows that not all the cerium acetate was dissolved in the ZnO. It must be pointed out that the samples were not sputtered clean and therefore extra adventitious C was present on the surface and although sensitivity factors and matrix effects were taken into account during the concentration calculations the limitation of concentration calculations with AES must be kept in mind.

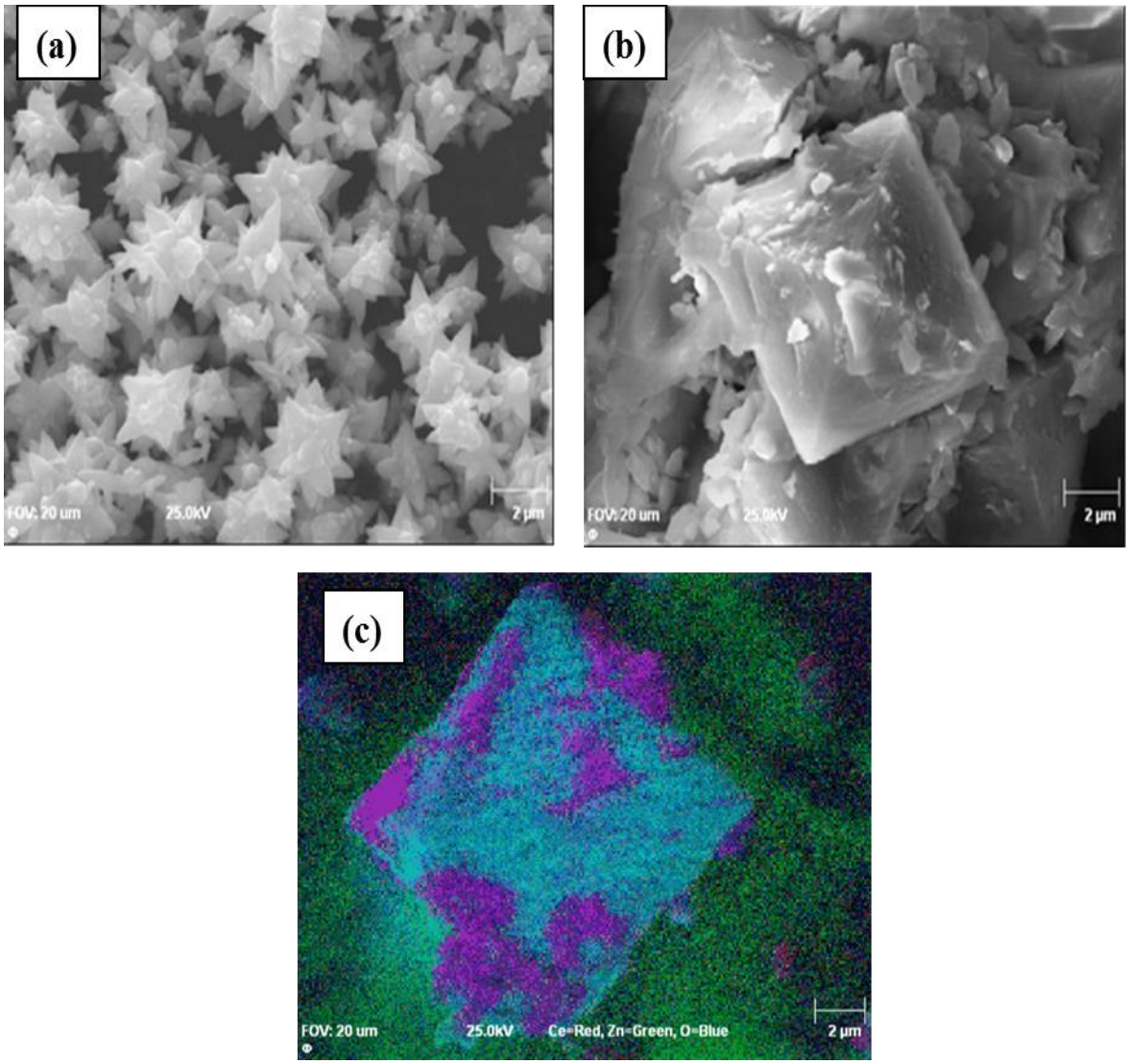

Figure 5.6: AES SEM images of (a) ZnO: 0 mol % Ce^{3+} and (b) ZnO: 10 mol % Ce^{3+}, illustrating the effect of different molar concentrations of Ce^{3+} and (c) one of the pyramids shape of ZnO:10 mol % Ce^{3+} ions.

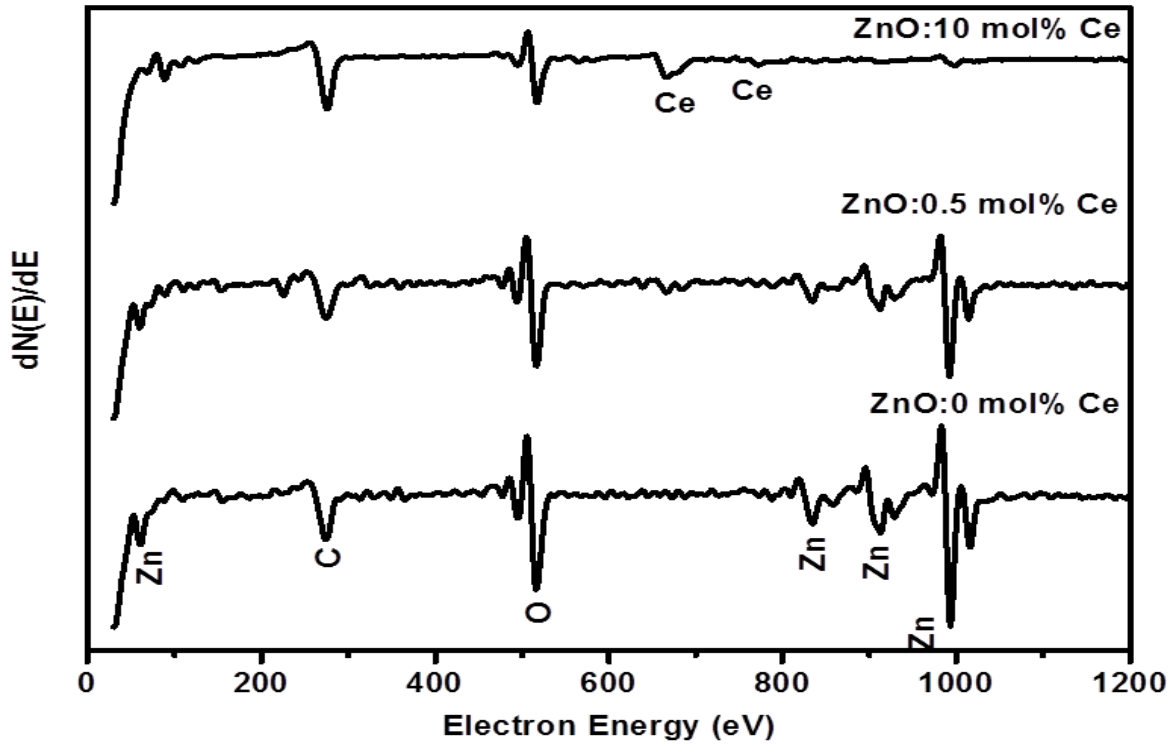

Figure 5.7: Auger spectra of the ZnO: 0 mol % Ce^{3+}, ZnO: 0.5 mol % Ce^{3+} and ZnO: 10 mol % Ce^{3+} ions prepared by the CBD method.

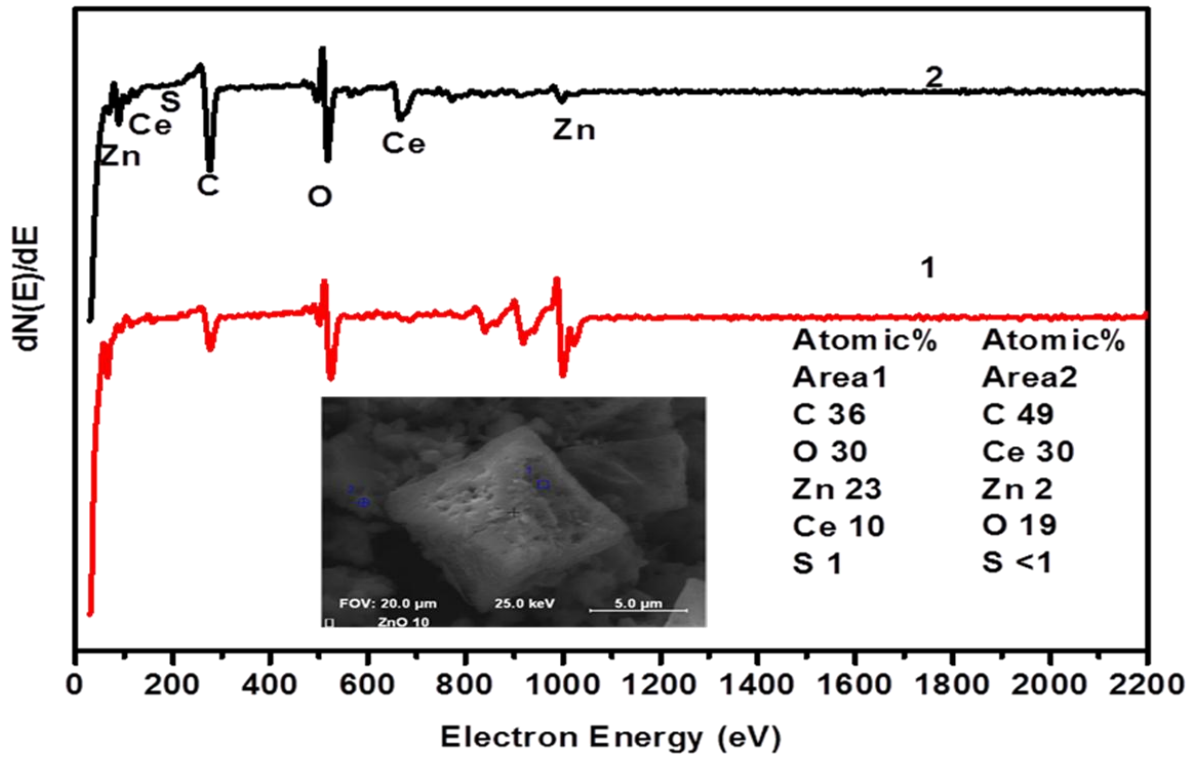

Figure 5.8: Auger spectra and calculated concentrations of the ZnO: 10 mol% Ce^{3+} sample measured at the two areas as indicated on the SEM image.

5.3 Optical properties

The UV-visible reflectance spectra of the as prepared samples are illustrated in Figure 5.9. The spectra of all the samples (at low molar concentrations of Ce^{3+}) show good optical quality in the visible range due to the complete reflectance in the 400-800 nm range. It clearly indicates that, firstly as the molar concentration of Ce^{3+} ions increases the optical absorption edge shift to a higher wavelength while the reflectance intensity decreases **[22]**. Furthermore, absorption bands corresponding to the forbidden 4f-4f transitions are usually weak and therefore not detected. The dependence of the band gap energy of the ZnO on the amount of Ce incorporated is illustrated in Figure 5.11. It can be seen clearly that the band gap energy of the ZnO decreases linearly with the addition of Ce content. The highest band gap energy is obtained at undoped ZnO flower-like structures, with its estimated band gap energy of 3.0 ± 0.1 eV. The decrease in band gap of ZnO may be due to the presence of defect states and disorder **[23-24]**.

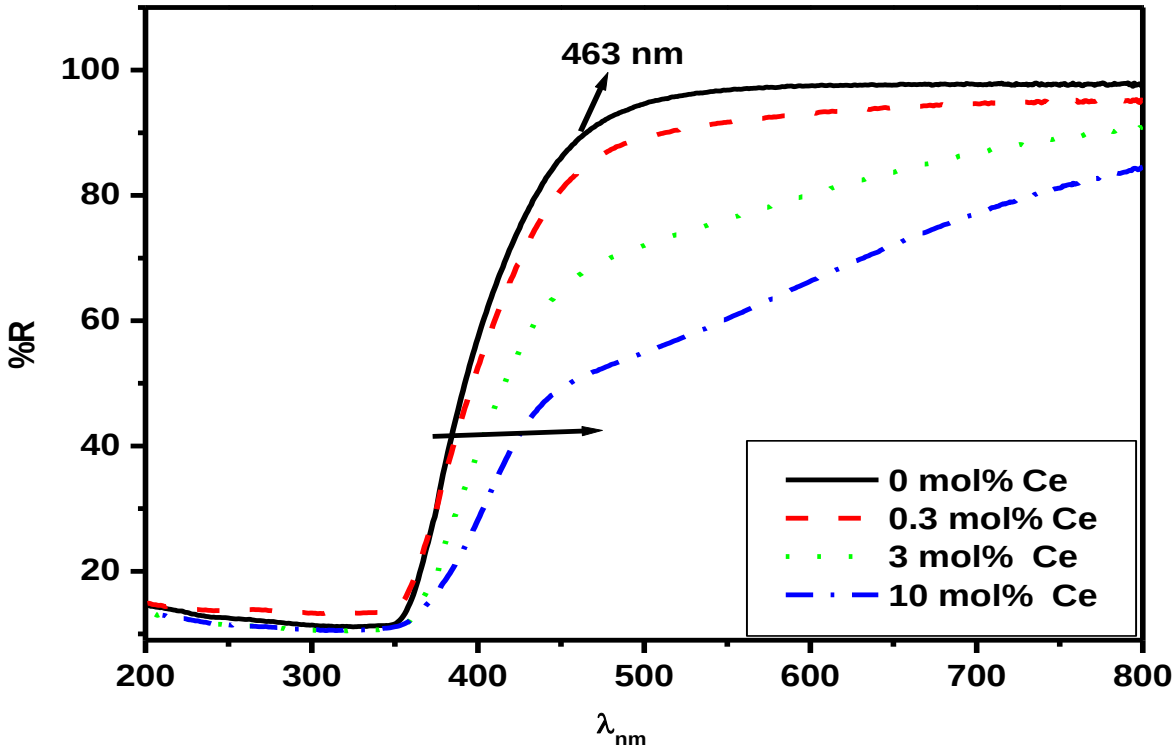

Figure 5.9: The absorbance spectra of undoped and Ce doped ZnO prepared by the CBD method.

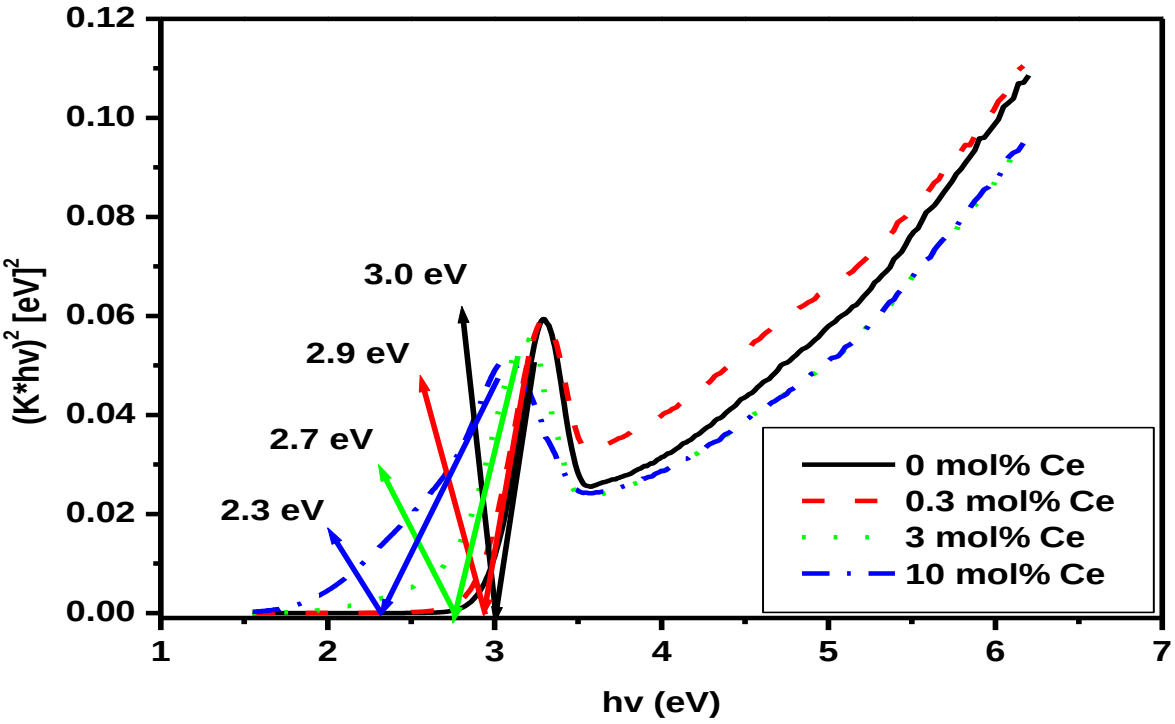

Figure 5.10: Plot to determine the band gap energy of undoped and Ce doped ZnO prepared by the CBD method.

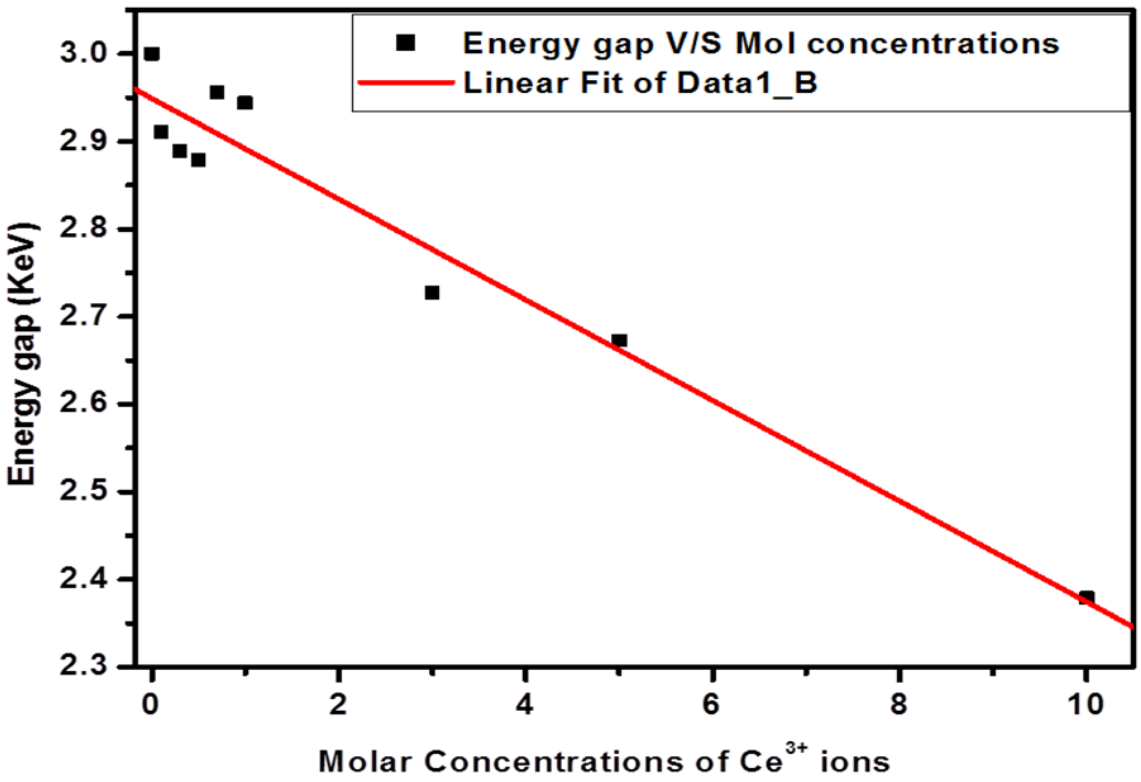

Figure 5.11: Dependence of band gap energies of the ZnO on the amount of Ce ion dopants.

However, such defects will produce a tail in the reflectance spectra which are clearly observed in the present study (Figure 5.9). Ce 4f electrons introduce new states close to the conduction band of ZnO. A newer conduction band is therefore formed which leads to a reduction of the band gap **[24]**. Although the structures obtained with the high Ce doping were not pure ZnO the values are added for completeness.

5.4 Photoluminescence

The PL emission spectra of ZnO nanostructures in the presence of different concentration of Ce^{3+} excited with 248 nm at ambient temperature are shown in Figure 5.12. The undoped and Ce^{3+} (0.1) mol %-doped ZnO sample when excited with 248 nm wavelength is shown in the inset of Figure 5.12.

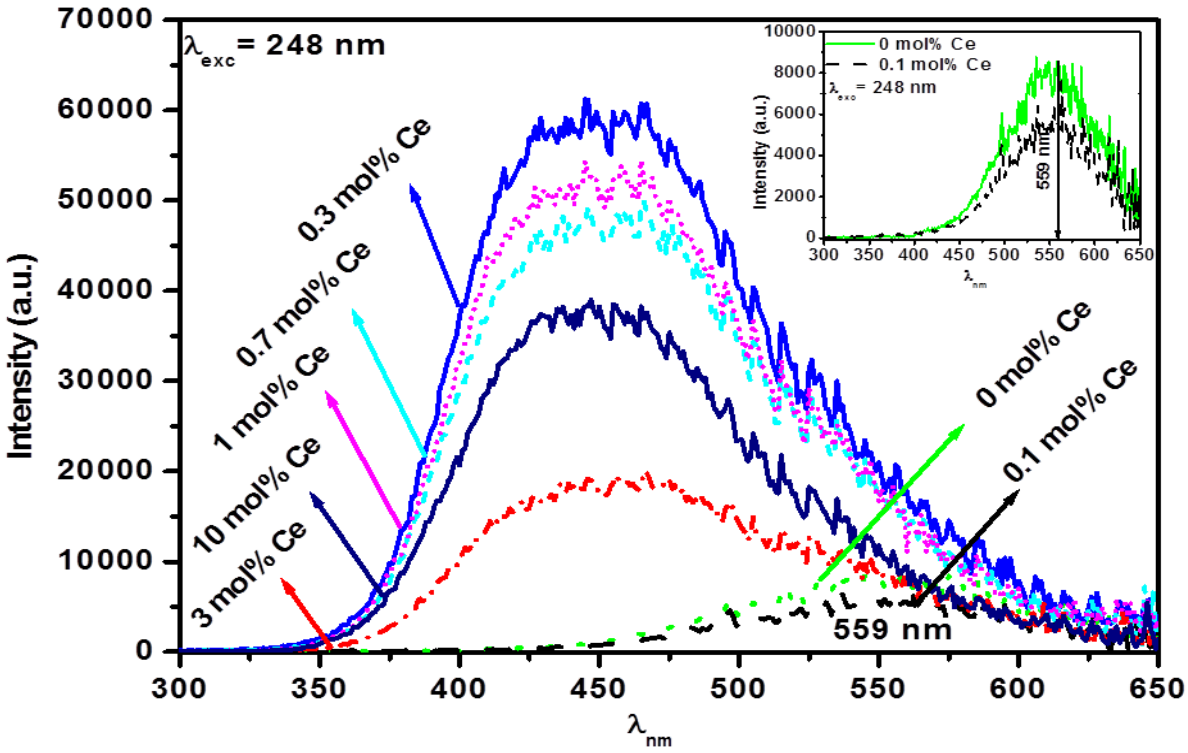

Figure 5.12: PL patterns for undoped and Ce-doped ZnO showing all the emissions within the visible and infrared range prepared at a different mol concentrations of cerium acetate with the inset PL spectra of the undoped and Ce^{3+} (0.1 mol %)-doped ZnO flower-like, with an excitation wavelength of 248 nm.

The emission spectra of the undoped ZnO depict a weak broad peak at around 559 nm. The PL peak at around 559 nm is associated with the oxygen vacancy-related green emission of ZnO **[25]**. It was observed that the presence of Ce^{3+} ions affect the luminescence intensity

and luminescence wavelength. The highest fluorescence intensity yield of the particles was obtained at the cerium concentration of 0.3 mol % and lower or higher Ce contents results in a substantial decrease in emission intensity. As the dopant concentration increase, a shift toward lower wavelength is observed (from green to the blue region). The shift of luminescence band from green to blue region may be due to the nanostructures that are changing in shape from flower-like to pyramids shape as confirmed by SEM analysis. Lang et al **[26]** and other researchers **[27]** have reported that by doping ZnO nanostructures with Ce^{3+} the luminescence intensity increases with an increase in the molar concentration of Ce^{3+}. On the contrary we observed the highest luminescence intensity to be at 0.3 mol % and a decrease at higher concentrations. Lastly there was a shift in the luminescence band from a higher to a lower wavelength. According to the reported values in literature **[22]**, the transitions in a Ce^{3+} doped ZnO lattice may be attributed to (i) 399–404 nm–exciton emission (ii) 417 nm–$^5D_0$–^4F (charac- teristic emission of Ce^{3+}) (iii) 426–428 nm–$^5D_4$–$^4F_1$ (iv) 448–452 nm–$^5D_0$–$^7F_1$ (v) 468 nm–$^5D_2$–$^7F_0$ (vi) 553–566 nm–$^5D_4$–F_j (vii) 601 nm–$^5D_0$–$^7F_1$ (viii) 629 nm–$^5D_0$–$^7F_2$.

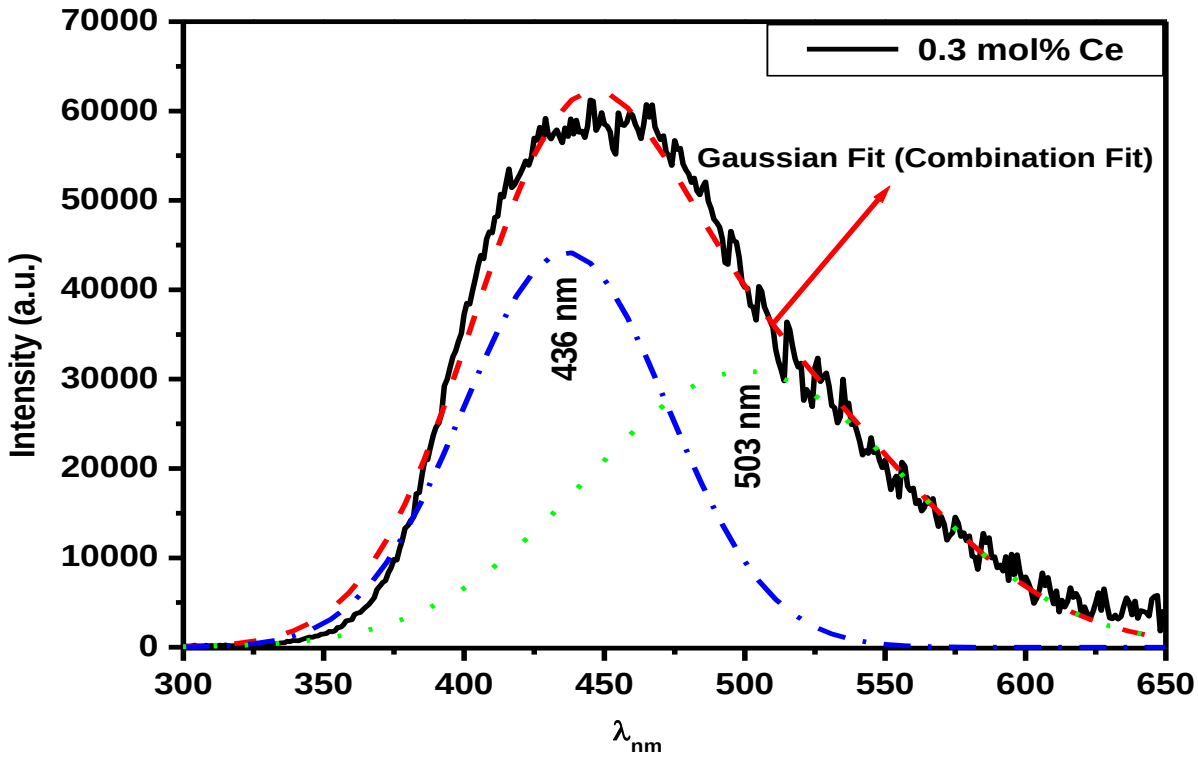

Figure 5.13: PL fitted spectra of ZnO: 0.3 mol % Ce^{3+} prepared by the CBD method.

Kumar et al**. [27, 28]** have been reported on the defect emission in ZnO from the UV region up to the red emission region. Deconvolution of the 0.3 mol % Ce doped ZnO spectrum in

Figure 5.13 reveals very wide band widths. The Guassian-multi curve fits of the broad peak at around 436 (blue fit) and other peak 503 nm (green fit) fits very well with the experimental curve of the Ce (0.3 mol %)-doped ZnO. The two peaks are due to the Ce^{3+} ions [**29**]. They originate from the transitions from the lower 5d (^2D) excited state to the split $^2F_{5/2}$ (436 nm) and $^2F_{7/2}$ (503 nm) energy levels **[30].** The increase in luminescence intensity may be due to the energy transfer from the ZnO to the Ce^{3+} ions because of different valences between Ce^{3+} and Zn^{2+} which produces defects **[29].** The enhancement of the intensity of Ce^{3+} and the suppression of the green emission from ZnO suggest that the energy from the excitation source was absorbed by ZnO and transferred non-radiatively to the Ce^{3+} ions. At higher Ce concentrations the crystal structures changed and the energy transfer was less effective and no trend in the intensity as function of Ce concentration could be monitored. This may be due to the incorporation of large amounts of rare earth (e.g. Ce, Eu and Tb) may enhance the phase separation tendency resulting from the limit of solid solubility, leading to strong composition modulations of alloys, and thus, potential fluctuations induced in the band edge results in strong carrier localization, which significantly affects the PL characteristics **[30].** In this case it might bean interplay between the ZnO:Ce doped material and the undissolved, cerium acetate, with the effect of no clear trend in the intensity.

References

[1]. M. H. Huang, S. Mao, H. Feick, H. Yan, Y. Wu, H. Kind, E. Weber, R. Russo, P. Yang, *Science*, **292** (2001) 1897-1899.

[2]. Z. S. Wang, C. H. Huang, Y. Y. Huang, Y. J. Hou, P. H. Xie, B. W. Zhang, H. M. Cheng, *Chem. Mater*. **13** (2001) 678-682.

[3]. X. F. Chu, D. L. Jiang, A. B. Djurisic, H. L. Yu, Chem. *Phys. Lett*. **401** (2005) 426-429.

[4]. C. J. Lee, T. J. Lee, S. C. Lyu, Y. Zhang, H. Ruh, H .J. Lee, *Appl. Phys. Lett*. **81** (2002) 3648-3650.

[5]. J. C. Johnson, H. Yan, R. D. Schaller, P. B. Petersen, P. Yang, R. J. Saykally, *Nano. Lett*, **2** (2002) 279-283.

[6]. Y. Huang, X. Duan, Q. Wei, C. M. Lieber, **291** (2001) 630-633.

[7]. M. H. Huang, S. Mao, H. Feick, H. Yan, Y. Wu, H. Kind, E. Weber, R. Russo, P. Yang, *Science*, **292** (2001) 1897-1899.

[8]. M. Arnold, P. Avouris, Z. W. Pan, Z. L. Wang, *J. Phys. Chem. B*, **107** (2003) 659-663.

[9]. J. H. Chung, C. S. Ah, D. -J. Jang, *J. Phys. Chem. B*, **105** (2001) 4128-4132.

[10]. L. F. Koao, H. C. Swart, F. B. Dejene, *J. Rare Earths*, **28**(2010) 206-210.

[11]. L. F. Koao, H. C. Swart, R. I. Obed, F. B. Dejene, *J. of Lumin*, **131**(2011) 1249-1254.

[12]. E. Ohshima, H. Ogino, I. Niikura, K. Maeda, M. Sato, M. Ito, T. Fukuda, *J. Cryst. Growth*, **260** (2004) 166-170.

[13]. P. Veradi, N. Nastase, C. Gherasim, C. Ghica, M. Dinescu, R. Dinu, C. Flueraru, *J. Cryst. Growth*, **197** (1999) 523-528.

[14]. J. Deenathayalan, M. Saroja, M. Venkatachalami, P. Gowthaman, T. S. Senthil, *Chalcogenide Lett*, **8** (2011) 549-554.

[15]. N. Y. Lee, M. S. Kim, *J. Mater. Sci*, **26** (1991) 1126-1130.

[16]. Q. Wan, K. Yu, T. H. Wang, *Appl. Phys. Lett*. **83** (2003) 2253-2255.

[17]. P. Gowthaman, M. Saroja, M. Venkatachalam, J. Deenathayalan, T. S. Senthil, *Aust. J. Basic and Appl Sci*. **11** (2011) 1379-1382.

[**18**]**.** C. Cheng, Z. Jiang, C. Liu, *J. Photochem and Photobio A: Chem*. **195** (2008) 151-155.

[**19**]**.** M. Zhong, G. Shan, Y. Li, G. Wang, Y. Liu, *Mater. Chem and Phys*, **106** (2007) 305-309.

[20]. Q. Luo, L. S. Wang, H. Z. Guo, K. Q. Lin, Y. Chen, G. H. Yue, D. L. Peng, *Appl. Phys A*, **108** (2012) 239-245.

[21]. B. D. Cullity 1978, *Elements of X-ray Diffraction (2nd Ed)*, (Addison Wesley) p 285-284.

[22]. N. R. Panda, B. S. Aecharya, T. B. Singh, R. K. Gartia, *J. Lumin*. **136** (2013) 369-377.

[**23**]**.** M. Saleem, L. Fang, H. B. Ruan, F. Wu, Q. L. Huang, C. L. Xu, C.Y. Kong, *International. J. Phys. Sci*, **7** (2012) 2971-2979.

[**24**]**.** A. Douayar, P. Prieto, G. Schmerber, K. Nouneh, R. Diaz, I. Chaki, S. Colis, A. El Fakir, N. Hassanain, A. Belayachi, Z. Sekkat, A. Slaoui, A. Dinia, and M. Abd-Lefdil, *Eur. Phys. J. Appl. Phys*. **61** (2013) 10304-1-10304-5.

[25]. S. Bayan, U. Das, D. Mohanta, *Phys. Status Solidi A*, **8** (2010) 1859-1863.

[**26**]. J. Lang, Q. Han, J. Yang, C. Li, X. Li, L. Yang, Y. Zhang, M. Gao, D. Wang, J. Cao, *J. Appl. Phys*, **107** (2010) 1-4.

[27]. V. Kumar, H. C. Swart, O. M. Ntwaeaborwa, R. E. Kroon, J. J. Terblans, S. K. K. Shaat, A. Yousif, M. M. Duvenhage, *Materials Letters*, **110 (15)** (2013) 57-60.

[28]. V. Kumar, F. Singh, O. M. Ntwaeaborwa, H. C. Swart, *Appl.Surf. Sci*. **279** (2013) 472-478.

[**29**]. Y. Jung, B. Y. Noh, Y. S. Lee, S. H. Baek, J. H. Kim, K. Park, *Nanoscale Research Letters*, 7:43 (2012) 1-5.

[30]. B. Cheng, Z. Zhang, H. Liu, Z. Han, Y. Xiao, S. Lei, *J. Mater. Chem*. **20** (2010) 7821-7826.

CHAPTER 6

Effect of Eu^{3+} on the structure, morphology and optical properties of flower-like ZnO synthesized using chemical bath deposition

6.1 Introduction

ZnO is a common host material and has attracted much attention due to its special properties **[1]** and potential applications. Since ZnO has a wide bandgap energy of 3.37 eV at room temperature, its nanocrystals are suitable host materials for doping elements such as rare-earth (RE) and transition metal (TM) ions which are optically and magnetically active **[2].** RE doped ZnO nanocrystals are a potential candidate material for flat panel display phosphors due to efficient emission in the visible range **[3]**, and different activators can be used to modify the colour of luminescence. The PL properties of nanocrystalline group II-VI semiconductors doped with TM and RE ions have attracted much attention in both basic and applied research fields during the past decade **[4, 5]**. The introduction of impurities can modulate the structure of semiconductors and cause dramatic change of the photoelectric and optical properties **[6]**. Thus, doping impurities into one-dimensional ZnO nanostructure to improve the optical and PL properties needs to be explored. Much work has been done to investigate the optical properties of TM or RE doped semiconductor nanoparticles **[7]**.

However, the study on the optical properties of RE doped one-dimensional ZnO nanostructures is rarely available, probably due to the limited solubility of RE ions as a result of the large difference in ionic radii between Zn^{2+} and the RE ions (R_{Zn}^{2+} = 0.06nm, R_{RE}^{3+}= 0.10-0.12 nm) **[7]**, which makes penetration of the rare earth ions into the ZnO crystal lattice very difficult. It has been reported that RE ions can be doped into bulk semiconductors as efficient activators, producing luminescence via $4f^n$-$4f^n$ transitions **[8]**. The PL of the ZnO doped with RE ions is disappointing **[7]** at this stage.

Until now, different synthesis methods have been developed for the preparation of RE doped ZnO nanostructures such as solvothermal **[9]**, magnetron sputtering **[10]**, chemical vapour reaction **[11]** and hydrothermal reaction **[12]**.

Koao L F et al J. of Lumin 147 (2014) 85-89

6.2 Results and discussions

6.2.1 Structural and compositional analyses.

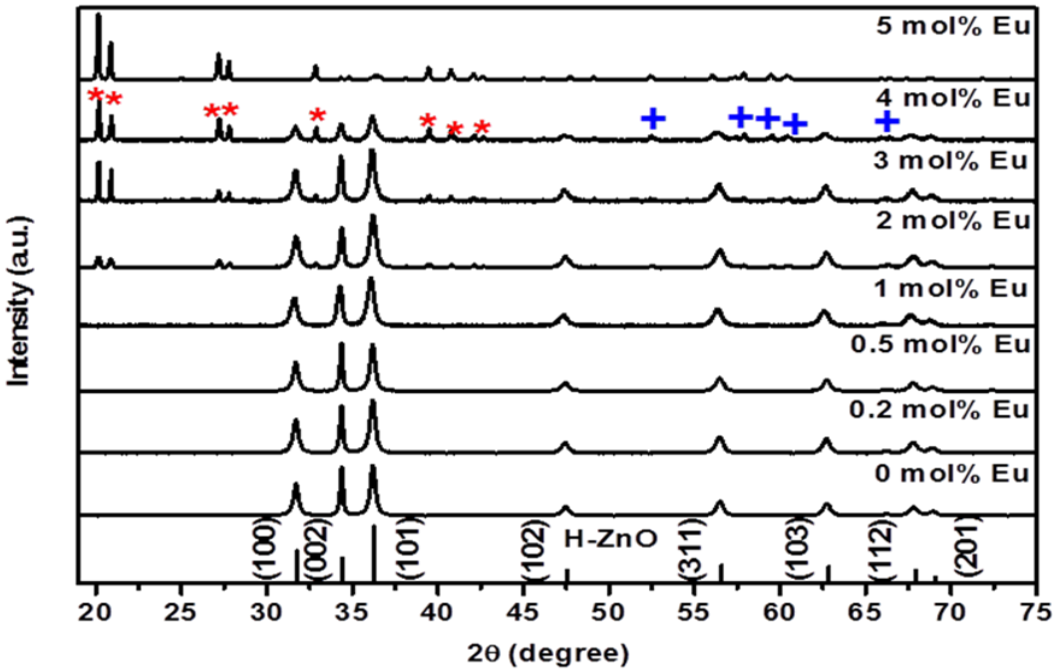

Figure 6.1: X-ray powder diffraction patterns for undoped and Eu-doped ZnO.

Figure 6.1 shows the XRD pattern of undoped and Eu doped ZnO with different molar concentrations of Eu^{3+}. For the undoped sample the diffraction peaks can be indexed to hexagonal wurtzite ZnO crystal structure with JCPDS No: 36-1451 and the calculated average values of the cell constants *a* and *c*, using all the peaks, were 0.3257 and 0.5216 nm. The measured average lattice parameters are slightly larger than those of bulk ZnO, a = 0.3249 and c = 0.5206 nm. No impurity peaks were observed for the low Eu doping concentration of 1 mol%, but for higher doping levels extra impurity peaks start to emerge. The impurity related peaks (indicated by asterisks and addition in Figure 6.1) may be due to incomplete reaction at higher molar concentration of Eu^{3+}. Additional impurities occur when the doping concentration was increased to as high as 4 mol% as shown in Figure 6.2. The peaks belong to europium nitrate (*) and europium oxide according to the files no 78-0377 and 71-0154, respectively. The diffraction peaks shift slightly toward lower angles with an increase in the dopant ions as shown in Figure 6.3, indicating that the lattice parameters are slightly larger than those of undoped ZnO, which is mainly due to larger radius of Eu^{3+} (0.095 nm) than that of Zn^{2+} (0.074 nm). This indicating that the dopant ions are well

incorporated into the lattice sites of Zn^{2+} and lead to the increase in inter atomic distance **[10]**. This observation does not hold for samples doped above 2 mol% of Eu. It is clear that not all the Eu^{3+} ions were incorporated in the ZnO lattice at higher dopant concentrations.

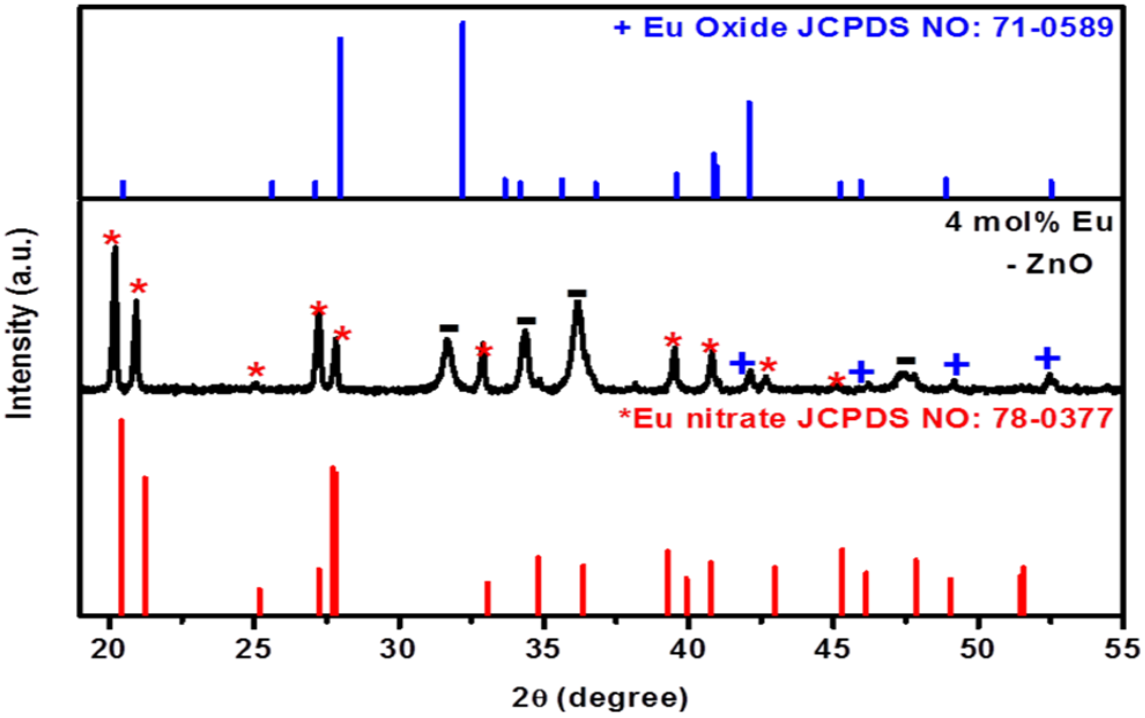

Figure 6.2: X-ray powder diffraction patterns for 4 mol% Eu-doped ZnO and standard files of Zn acetate and Eu nitrate.

The incorporation of major amounts of Eu may enhance the phase separation tendency resulting from the limit of solid solubility, leading to a strong composition variation of alloys **[13]**. ZnO peaks however were still seen up to 4 mol% Eu^{3+}. The average size of the as-prepared grain size can be calculated using the Debye formula **[14]**. All major reflection peaks ((100), (002), (101), (102), (311), (103), (112) and (201)) and for all samples were chosen to estimate the average size of the nanocrystallites by the least square method. The average grain size of the undoped and low Eu doping up to 4 mol% samples was estimated as 47 ± 5 nm. The estimated average crystallite size for the changed Eu acetate structure was about 105 ± 1 nm. Figure 6.4 shows SEM micrographs of the undoped and doped ZnO nanostructures. The morphology of un-doped ZnO consists of flower-like structures, which changed in size and shape with an increase in the amount of Eu dopant. When the Eu^{3+} ions were incorporated into ZnO, the flower-like structure changed to mixed structures including the emergence of block-like shapes, causing a complete change of the surface aspect to large

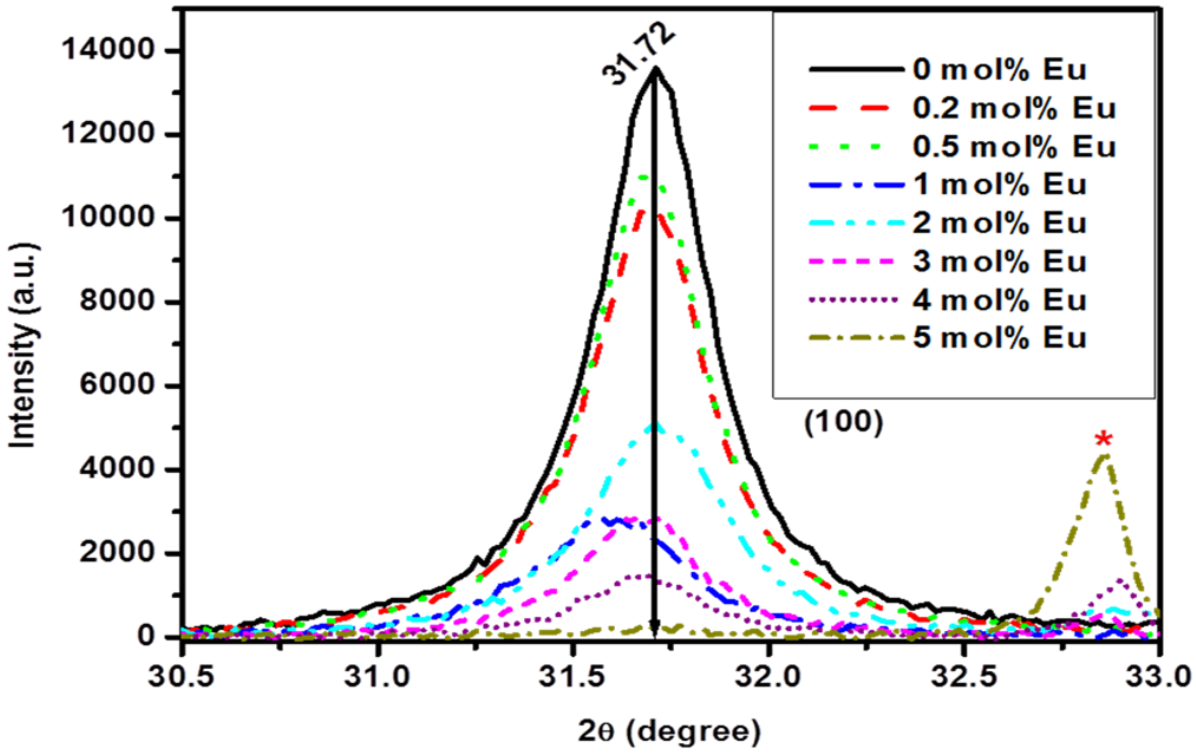

Figure 6.3: X-ray powder diffraction patterns at (101) for undoped and Eu-doped ZnO.

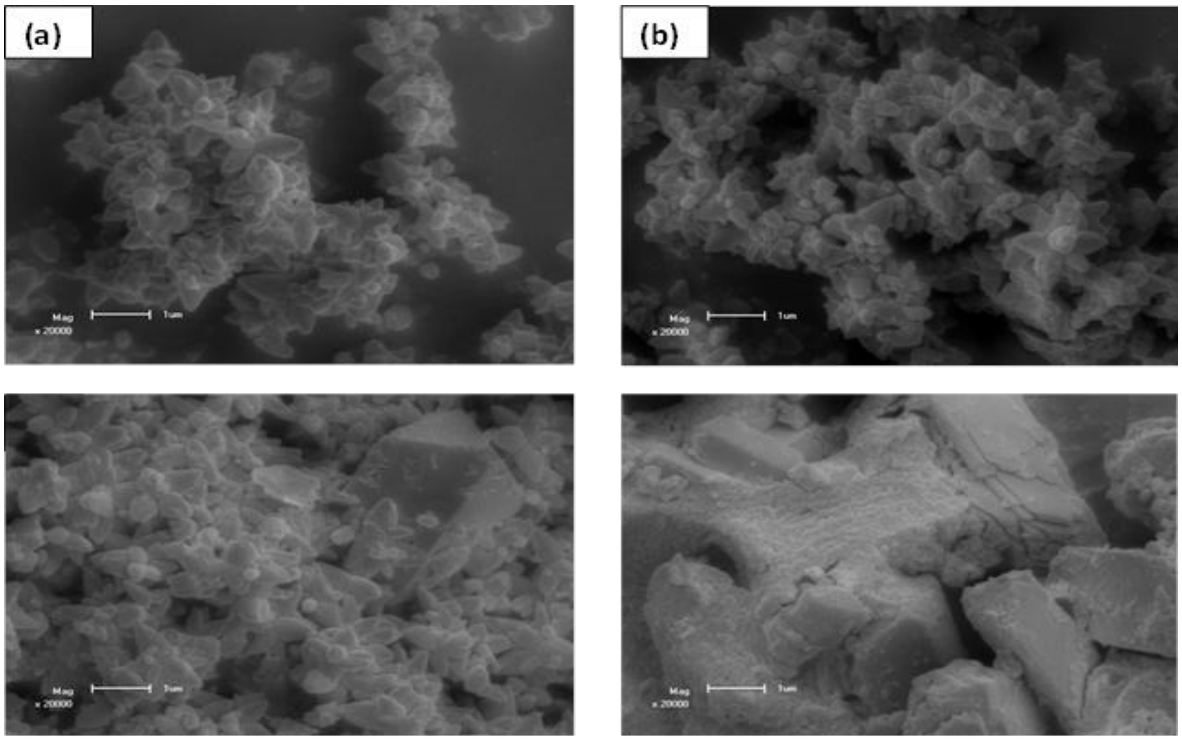

Figure 6.4: SEM images of (a) 0 mol% Eu (b) 0.5 mol% Eu (c) 1mol% Eu and (d) 4 mol% Eu, illustrating the effect of different molar concentrations of Eu^{3+}.

blocks at 4 mol% of Eu. The particle sizes of the block-like structures were about 10 μm. Similar results were obtained for ZnO doped with Ce^{3+} that after doping the flower-like structure became clustered and changed in shape, especially for Ce concentration higher than 3 mol % **[15].**

6.3 Optical properties

The UV-visible reflectance spectra of the samples are given in Figure 6.5. The sharp absorption edge is characteristic of a homogeneous structure **[16]**. The figure shows clearly that the absorption edge shifted to higher wavelength for Eu concentration up to 4 mol% and then reduced to lower wavelength for higher concentration. This shift in the onset of absorption edge to higher wavelength is due to change in the new crystal band gap. Furthermore, absorption bands corresponding to the forbidden Eu^{3+} 4f-4f transitions (around 395, 465, 527, 535 and 589 nm) were detected for higher molar concentration of Eu. The band at around 344 nm is attributed to the exciton absorption, which is blue-shift compared with bulk ZnO **[17]**. The absorption peaks at around 395, 465, 527, 535 and 589 nm are assigned to $^7F_0 \rightarrow {}^5L_6$, $^5D_2$, $^5D_1$, $^5D_1$ and $^5D_0$ transitions of Eu^{3+} ions, respectively **[18]**.

From Figure 6.6, the estimated band gap energy obtained at undoped ZnO flower-like structures is around 3.27 ± 0.03 eV. The dependence of the band gap energy of the ZnO on the amount of Eu incorporated is illustrated in Figure 6.7. It can be seen from this graph that the band gap of the ZnO nanostructures decay nearly exponential with Eu^{3+} content. This suggests that the band gap of ZnO actually decreases with increasing Eu^{3+} doping concentration. The decrease in band gap energy and the shift of the absorption edges to higher wavelengths might be due to the presence of defect states and disorder due to the Eu^{3+} doping **[19-20]**.

The Eu^{3+} 4f electrons introduce new states close to the conduction band of the ZnO. A new defect band is therefore formed below the conductions which lead to reduction in the effective band gap **[19]**. It is clear that at ZnO doped with 5 mol% of Eu^{3+} the estimated band gap increases up to 3.35 eV. At the higher Eu(5mol%) molar concentration almost no ZnOwas observed in the XRD pattern and the structure mainly consist of Eu nitrate which shows a much higher band gap of about 3.35eV. Due to this full change in structure, this point was not added to the trend of the band gap as function of Eu^{3+} concentration graph. This change in structure may be due to the fact that the Eu^{3+} ions were not fully incorporated in the ZnO lattice at higher dopant concentrations.

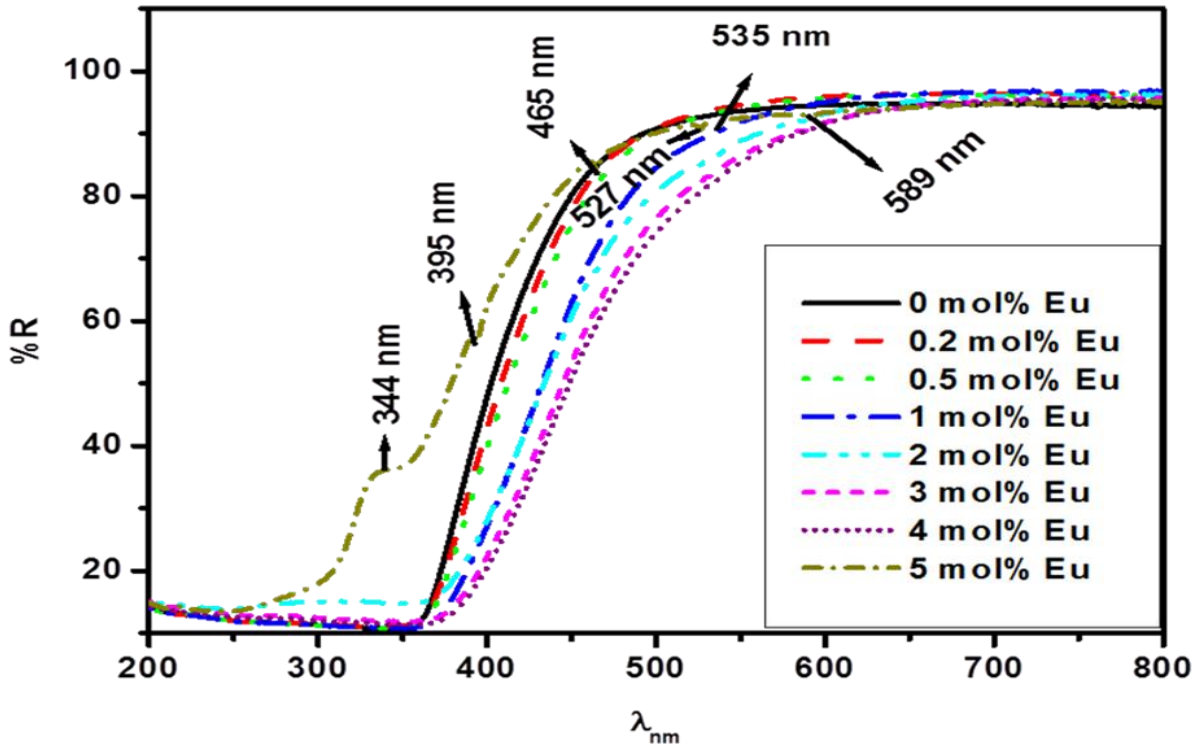

Figure 6.5: The reflectance spectra of undoped and doped ZnO nanostructures prepared by CBD method.

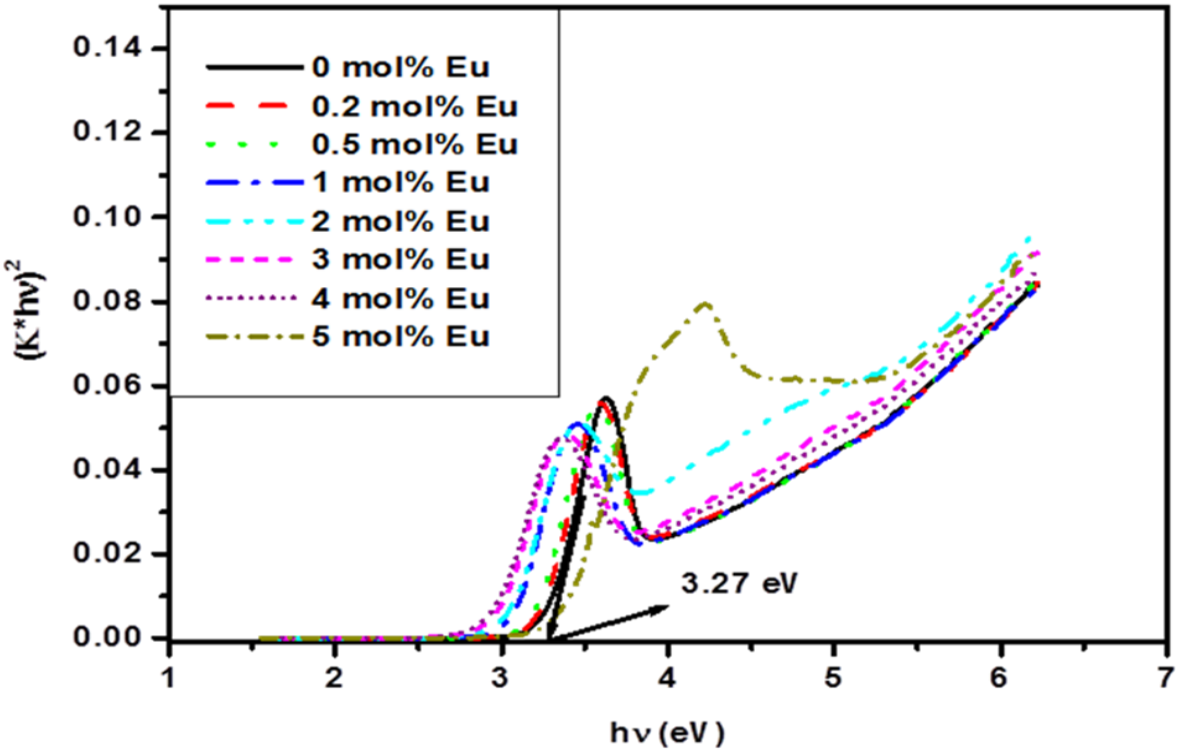

Figure 6.6: Plot to determine the band gap energy of undoped and doped ZnO nanostructures prepared by CBD method.

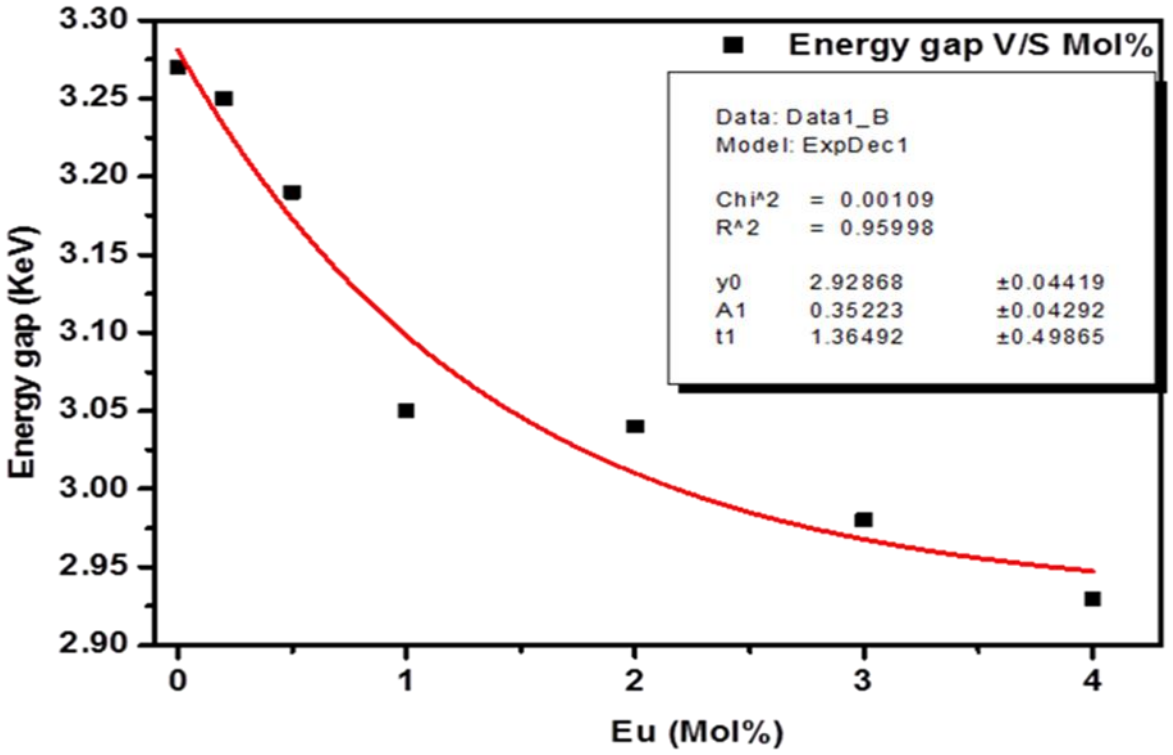

Figure 6.7: Dependence of band gap energies of the ZnO on the amount of Eu ion dopants.

The incorporation of major amounts of Eu may enhance the phase separation tendency resulting from the limit of solid solubility, leading to a strong composition difference of alloys and thus, potential fluctuations induced in the band edge results in strong carrier localization, which significantly affects the optical characteristics **[13].**

6.4 Photoluminescence

The PL emission spectra of Eu-doped ZnO nanostructures excited at 395 nm (corresponding to the $^7F_0 \rightarrow {}^5L_6$ absorption line of Eu^{3+} found in the reflection measurements) and 300 nm (above the ZnO bandgap) are shown in Figure 6.8 (a) and (b), respectively. The emissions in Figure 6.8(a) at 591, 616 and 696 nm may be attributed to Eu^{3+} ion transitions, namely $^5D_0$-$^7F_1$, $^5D_0$-$^7F_2$, and $^5D_0$-$^7F_4$, respectively. The emission intensity as a function of Eu^{3+} mol% is presented in an inset of Fig. 6.8 (a). The Gaussian fit suggests that the optimum dopant concentration of these nanoparticles must be at 3 mol% Eu^{3+}. Above this optimum concentration, the concentration quenching effect on the emission intensity is observed. This further increase in the Eu^{3+} ions above 3 mol% resulted in luminescence quenching caused by non-radiative interactions between ions as the resonant energy transfer became stronger **[21-22]**.

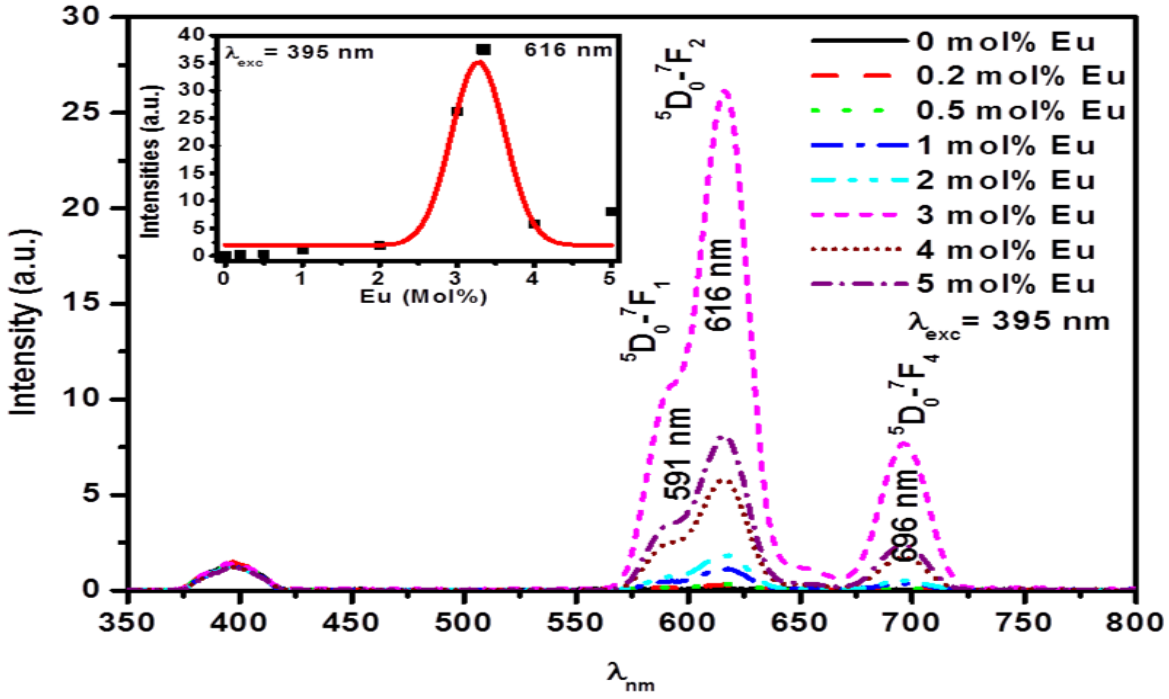

Figure 6.8(a): PL emission spectra for undoped and Eu-doped ZnO with different concentrations of Eu^{3+} with excitation of 395 nm with the inset the variation of the emission intensities as function of Eu dopant concentrations at 616 nm and (b) with an excitation wavelength of 300 nm.

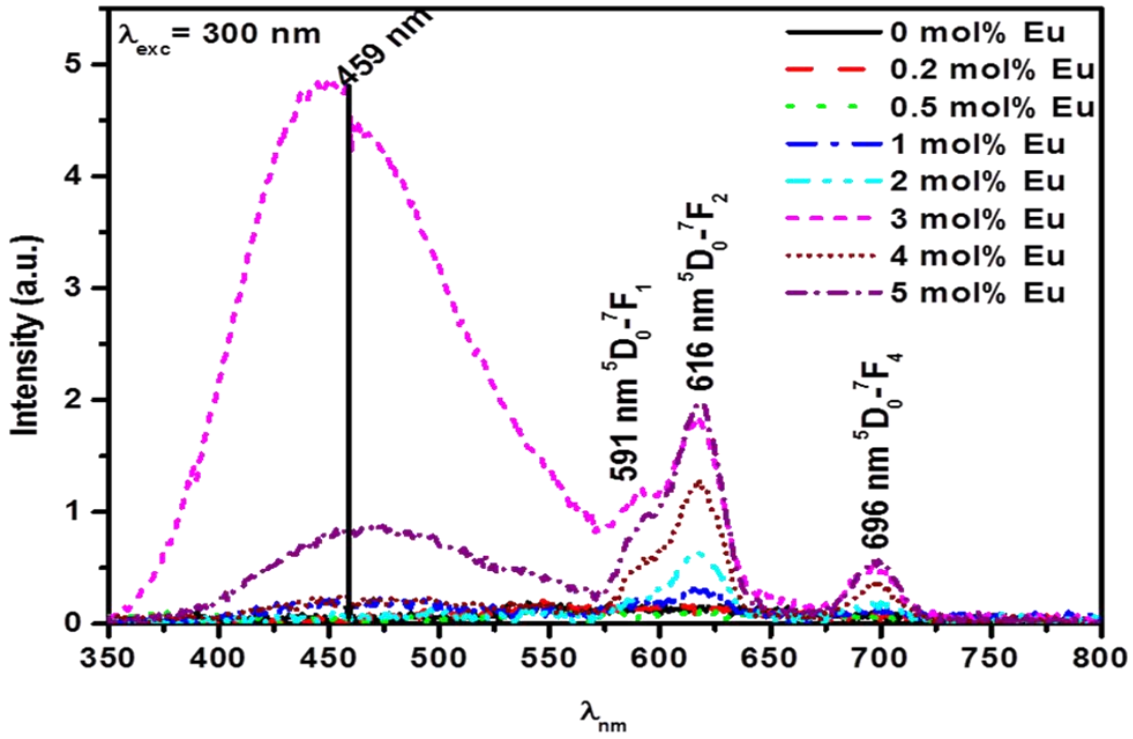

Figure 6.8(b): PL emission spectra for undoped and Eu-doped ZnO nanostructures with different concentrations of Eu^{3+} with excitation wavelength of 300 nm.

Eu^{3+}, like other rare earths, at higher molar concentrations has a low solubility in the ZnO, therefore, Eu^{3+} ions tend to migrate to the ZnO surface. Zhong et al **[23]** and other researchers **[12, 24]** have reported that when exciting Eu^{3+}-doped ZnO at lower wavelengths than 385 nm no emission from Eu^{3+} could be observed. On the contrary, we observed Eu^{3+} emission by exciting ZnO:Eu^{3+}samples with 300 nm wavelength (Figure 6.8(b)), although the emission intensity of ZnO doped with 3 mol% Eu excited at 395 nm is 13 times than the one excited at 300 nm by using the luminescence band at around 616 nm for both excitations. In both figures the PL intensity was found to be a maximum for ZnO:3 mol% Eu^{3+} with excitation wavelength of 337 and 395 nm, respectively. In addition, when exciting at this shorter wavelength we also observed blue emission near 445 nm which did not occur when exciting the Eu directly at 395 nm. We attribute this to defect emission of ZnO **[25]**. The group of Lang et al **[26]** observed that the luminescence band of green emission of ZnO increased in luminous intensity with an increase in the molar concentration of Ce^{3+} ions. The improved intensity of the green emission confirmed increases in the density of defects, which could be due to the oxygen vacancy introduced by the existence of Ce impurities in ZnO nanorods **[26]**. Similarly in our study the enhanced blue emission of ZnO may be due to increase in density of defects as the Eu^{3+} ions increases. Figure 6.9 shows the deconvolution of the PL spectrum of the ZnO nanostructures doped with 3 mol% Eu doped using Gaussian peaks, revealing very wide band widths. The emissions at around 435 and 488 nm are related to the intrinsic defects emission within the ZnO host **[23]**. The luminescence of the undoped ZnO samples when excited at 300 and 395 nm wavelength are shown in the inset of Figure 6.9. The yellowish emission at around 601 nm for undoped ZnO may be attributed from double ionized oxygen vacancies **[27-29]**. The presence of the Eu^{3+} ions decreases the yellow emission of undoped ZnO. The decreasing of the self-activated yellowish emission band in undoped ZnO nanoplates suggests a marked increase in surface defect states as a result of doping. A point of interest which needs to be pointed out is the need to find a phosphor that can full the efficient emission gap (yellow gap) around 560 nm, which fairly seriously extends into the amber range of 590 nm to 600 nm in the ranges of wavelengths covered by reasonably efficient diodes made from either III-nitrides or III-phosphides. It is possible to vary the emission wavelength of GaN-based blue LED's between 370 nm (band- gap of pure GaN), and 470 nm by increasing the In content in InGaN devices **[30]**.

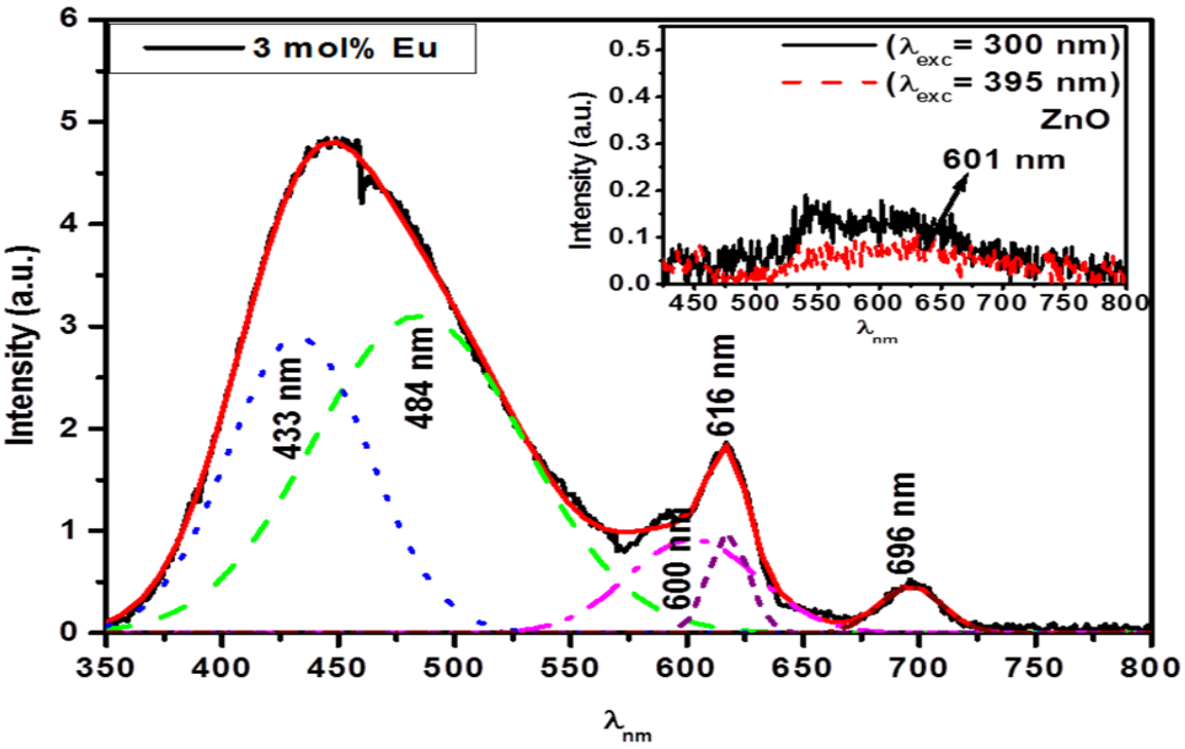

Figure 6.9: The deconvolution of the luminescence spectra taken from ZnO nanostructures doped with 3 mol% of Eu with the inset PL spectra of the undoped ZnO flower-like both excited at 300 nm.

References

[1]. V. Kumar, H. C. Swart, O. M. Ntwaeaborwa, R. E. Kroon, J. J. Terblans, S. K. Shaat, A. Yousif, M. M. Duvenhage, *Mater. Lett.* **110 (15)** (2013) 57-60.

[2]. H. Liu, J. Yang, Y. Wang, M. Wei, *Mater. Chem. Phys*. **112** (2008) 1021-1023.

[3]. T. Toyama, H. Takeuchi, D. Yamaguchi, H. Kawasaki, K. Itatani, H. Okamoto, *J. Appl. Phys.* **108** (2010) 084302-1-084302-6.

[4]. L. Chen, J. Zhang, Y. Luo, S. Lu, X. Wang, *Appl. Phys. Lett*. **84** (2004) 112-114.

[5]. R. N. Bhargava, *J. Lumin*. **70** (1996) 85-94.

[6]. K. J. Kim, Y. R. Park, *Appl. Phys. Lett*.**7 8** (2001) 475-477.

[7]. S. Bachir, K. Azuma, J. Kossanyi, P. Valat, J. C. Ronfard-Haret, *J. Lumin*. **75** (1997) 35-49.

[8]. A. Bol, R. Beek, A. Meijerink. *Chem. Mater*. **14** (2002) 1121-1126.

[9]. C. Cheng, Z. Jiang, C. Liu, *J. Photochem. and Photobio. A: Chem*. **195** (2008) 151-155.

[10]. Q. Luo, L. S. Wang, H. Z. Guo, K. Q. Lin, Y. Chen, *Appl. Phys*. **A108** (2012) 239-245.

[11]. B. C. Cheng, Y. H. Xiao, G. S. Wu, L. D. Zhang, *Adv. Funct. Mater*.**14** (2004) 913-919.

[12]. P. M. Aneesh, M. K. Jayaraj, *Bull. Mater. Sci*, **33** (2010) 227-231.

[13]. B. Cheng, Z. Zhang, H. Liu, Z. Han, Y. Xiao, S. Lei, *J. Mater. Chem*, **20** (2010) 7821-7826.

[14]. B. D. Cullity 1978, *Elements of X-ray Diffraction (2nd Ed)*, (Addison Wesley) p 285-284.

[15]. L. F. Koao, F. B. Dejene, H. C. Swart, J. R. Botha, *J. Lumin*. **143** (2013) 463–468.

[16]. N. R. Panda, B. S. Aecharya, T. B. Singh, R. K. Gartia, *J. Lumin*. **136** (2013) 369-377.

[17]. Y. Hu, H. J. Chen, *J. Nanopart. Res*. **10** (2008) 401-407.

[18]. S. Yan, J. Zhang, X. Zhang, S. Lu, X. Ren, Z. Nie, X. Wang. *J. Phys. Chem. C*, **111** (2007)13256-13260.

[19]. A. Douayar, P. Prieto, G. Schmerber, K. Nouneh, R. Diaz, I. Chaki, S. Colis, A. El Fakir, N. Hassanain, A. Belayachi, Z. Sekkat, A. Slaoui, A. Dinia, M. Abd-Lefdil, *Eur. Phys. J. Appl. Phys*. **61** (2013) 10304-1-10304-5.

[20]. M. Saleem, L. Fang, H. B. Ruan, F. Wu, Q. L. Huang, C. L. Xu, C. Y. Kong, *Int. J. Phys. Sci.* **7** (2012) 2971-2979.

[21]. L. F. Koao, H. C. Swart, R. I. Obed, F. B. Dejene, *J. Lumin.* **131** (2011) 1249-1254.

[22]. J. G. Sole, L. E. Bausa, D. Jaque, *An introduction to the Optical Spectroscopy of inorganic Solids*, John Willey & Sons Ltd. (2005) 200-202.

[23]. M. Zhong, G. Shan, Y. Li, G. Wang, Y. Liu, *Mater. Chem and Phys*, **106** (2007) 305-309.

[24]. C. C. Yang, S. Y. Cheng, H. Y. Lee, S. Y. Chen, *Ceram. Int*. **32** (2006) 37-41.

[25]. F. S. V. Kumar, O. M. Ntwaeaborwa, H. C. Swart, *Appl. Surf. Sci.* **279** (2013) 472-478.

[26]. J. Lang, Q. Han, J. Yang, C. Li, X. Li, L. Yang, Y. Zhang, M. Gao, D. Wang, J. Cao, *J. Appl. Phys*. **107** (2010) 1-4.

[27]. V. A. Dijken, E. A. Meulenkamp, D. Vanmaekelbergh, A. Meijerink, *J. Lumin*. **87** (2000) 454-456.

[28]. A. Janotti, C. G. Van de Walle, *Phys. Rev. B,* **76** (2007) 165202-1-165202-22.

[29]. H. He, Q. Yang, C. Liu, L. Sun, Z. Ye, *J. Phys. Chem. C*, **115** (2011) 58-64.

[30]. A. K. Bedyal, V. Kumar, S. S. Pitale, E. Coetsee, M. M. Duvenhage, O. M. Ntwaeaborwa and H. C. Swart, *J. of Mat. Sci*., **48 (9)** (2013) 3327-3333.

CHAPTER 7

The effect of Cu^{2+} on structure, morphology and optical properties of flower-like ZnO synthesized using the chemical bath deposition method

7.1 Introduction

One-dimension (1D) nanostructures represent a group of nanomaterial with highly anisotropic morphologies, the smallest dimension falling in the range of 1-100 nm. Nowadays most of researchers focused on controlling the morphology of the ZnO for different applications **[1].** It has been proven that as the particles become smaller in size, changes in the morphology and size distribution, may take on different chemical and physical properties **[2].** For nanoparticles, both the size and the surface effects are very important. Doping nanoparticles play key roles in luminescence efficiency and the positions of the emission bands, thus influencing their practical application. Secondly, doping semiconductor nanoparticle with transitional metal ions like Mn^{2+} and Cu^{2+} yield different nanostructures **[3-4].** Semiconductor nanoparticles are currently an active subject of research in nanoscience and nanotechnology **[5].** ZnO is one of the most important semiconductor compounds in group II-VI. It has gained more attention in material science because of its excellent optical, electronic and other physical and chemical properties **[6].** It has been widely used in near-UV emission, gas sensors, transparent conductor and piezoelectric application **[7-9].** Most of the ZnO nanostructure doped with rare earth and transition metal have been synthesized by traditional high temperature solid state method and again the final products were annealed at high temperatures which is energy consuming and difficult to control the particle size and morphology properties. In the present study the ZnO powders were prepared by chemical bath deposition (CBD) method at a bath temperature of 80^0C. The final yields were annealed at ambient conditions.

7.2 Results and discussions

7.2.1 Structural and compositional analyses.

Figure 7.1 shows XRD patterns of undoped and Cu doped ZnO with different molar concentrations of Cu^{2+}. Results of some intermediate doping percentage have been omitted to avoid clustering. All the diffraction peaks can be indexed to the hexagonal wurtzite ZnO crystal structure (JCPDS36-1451 with a = 3.24982 and c = 5.20661 Å).

Koao L F et al Physica B 439 (2013) 173-176

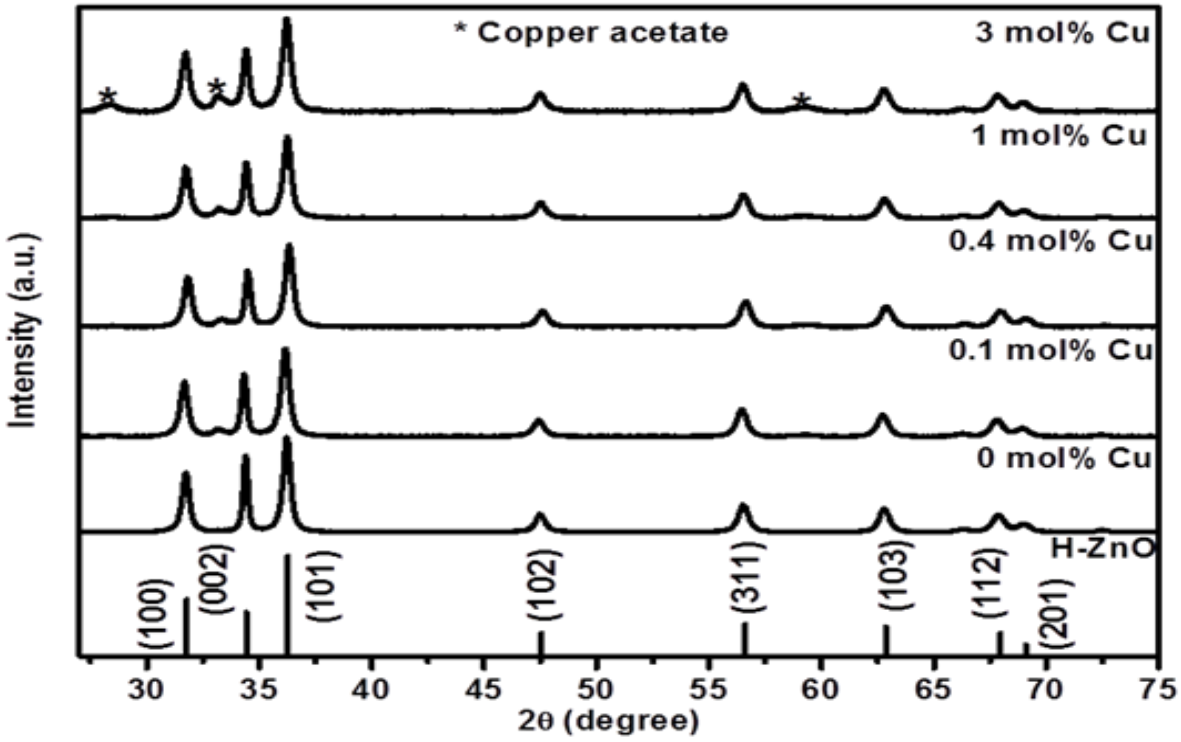

Figure 7.1: X-ray powder diffraction patterns for undoped and Cu-doped ZnO prepared by CBD method.

The calculated average values of the lattice constants of *a* and *c* of 3.2531 nm and 5.2078 nm matched perfectly with the standard data available in JCPDS. All the XRD peaks were used to estimate the lattice parameters. No significant changes were observed for the lattice parameters with the variations in Cu^{2+} ions concentration. It is expected that the Cu^{2+} ions were well incorporated into the ZnO lattices at low and higher molar concentration due to the small difference in the ionic radius of the Zn^{2+} ion (0.74 Å) and the Cu^{2+} ion (0.73 Å). Additional peaks marked with asterisk (*) observed from the higher Cu^{2+} ion concentration XRD patterns are attributed to the monoclinic cupper acetate with JCPDS NO: 27-0145. This may be due to the low solubility of copper acetate at high molar concentration. It is clear that at higher molar concentration of Cu^{2+} ions the crystallinity of the ZnO did not change.

The average grain size of the as-prepared nanocrystals was calculated using the Debye formula **[10].** All major diffraction peaks for all samples were chosen to estimate the average grain sizes of the nanocrystals by the least square method. The average grain-sizes of the as prepared samples were estimated to be 46 ± 1 nm. Using this method for grain-size estimation the inclusion of Cu^{2+} ions in the ZnO nanostructures did not have an effect.

Figure 7.2 (a), (b), (c) and (d) show SEM micrographs of the as prepared undoped and doped ZnO nanostructures prepared at different molar concentrations of Cu^{2+} ions. The surface aspects of the SEM image of un-doped ZnO are composed of flower-like structures. The flower-like structures changed in shape with an increase in the amount of Cu dopant. With the incorporation of the Cu^{2+} ions into the ZnO, the flower-like structure changed to a mixed structure with the emergence of irregular shapes. When the Cu concentration was increased to 2 mol%, the morphology of the ZnO:Cu has totally changed with clustered irregular shapes with small quantities of other material attached to the main structures.

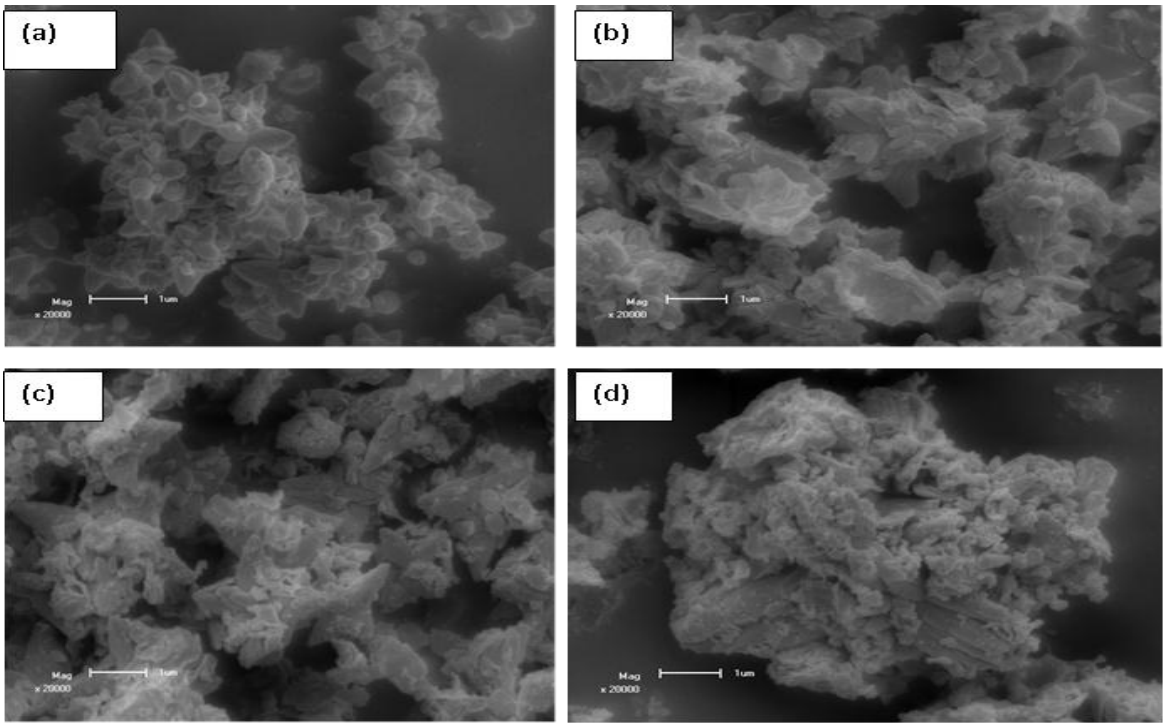

Figure 7.2: SEM images of (a) 0 mol% Cu (b) 0.1 mol% Cu (c) 0.5 mol% Cu and (d) 2 mol% Cu, illustrating the effect of different molar concentrations of Cu^{2+}.

7.3 Optical properties

Figure 7.3 shows the reflectance measurements in the UV-visible region of the as prepared samples. It clearly indicates that, firstly the reflectance intensity in the visible region decreased while the absorption increased with an increase in the molar concentration of Cu^{2+}. Secondly, there was no shift on the absorption edge. Furthermore, no additional band for Cu was detected from the spectra extended to longer wavelengths, indicating the phase purity of the doped flower-like ZnO. Meaning that the Cu^{2+} ions were well incorporated into the ZnO lattices at low and higher molar concentration.

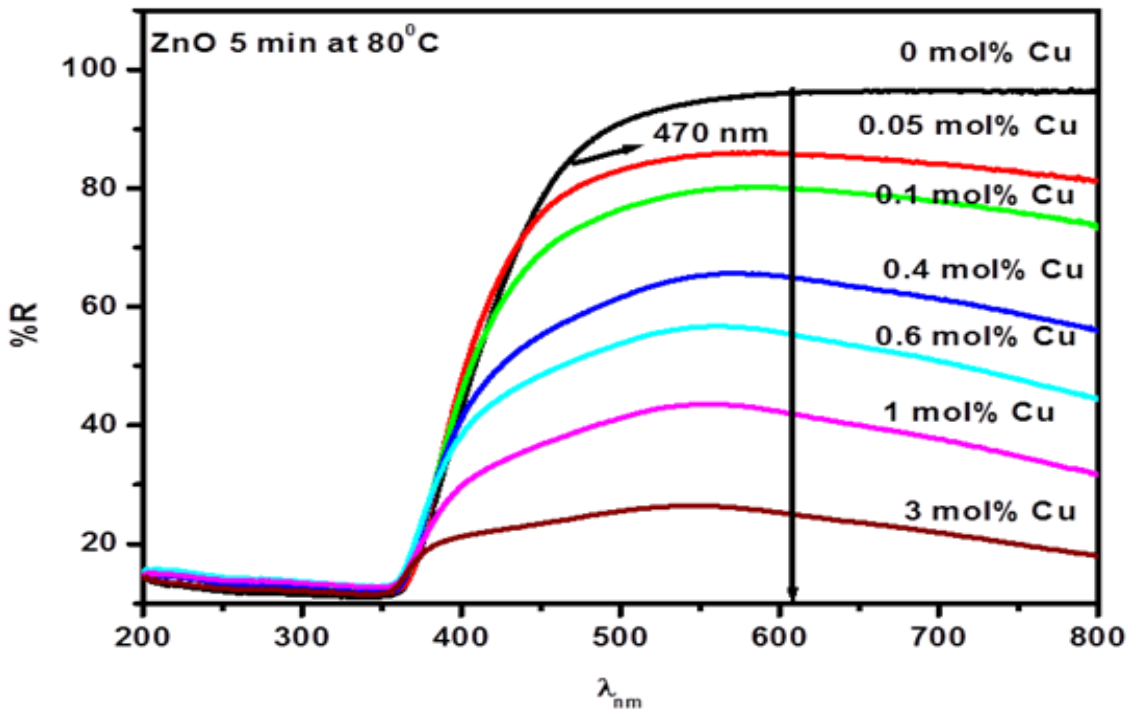

Figure 7.3: The reflectance spectra of undoped and doped flowers-like ZnO prepared by CBD method.

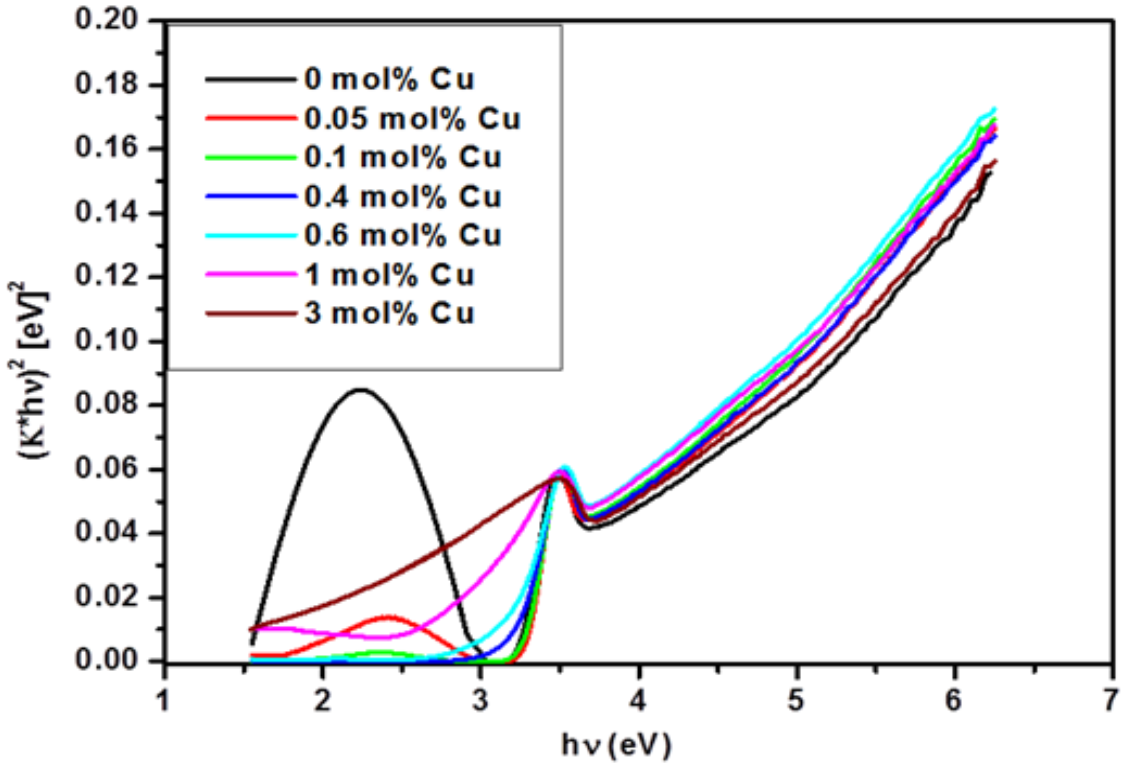

Figure 7.4: Plot to determine the band gap energy of undoped and doped ZnO flower-like prepared by CBD method.

Koao L F et al Physica B 439 (2013) 173-176

In Figure 7.4, the estimated band gap energy of undoped ZnO was estimated as 3.26 ± 0.12 eV. The estimated band gap energy is lower than that of bulk ZnO (3.37 eV). This band gap reduction may be due to surface defects density of undoped ZnO **[11].** It can be observed that there was no significant change in the band gap of Cu doped ZnO. This is confirmed by absence of any shift in absorption edge as shown in Figure 7.3. The onset of absorption edge also show non shifting characteristic in Figure 7.4. The variation in slope of different energy curve could be attributed to the non uniformity in particle sizes as confirmed by SEM analysis.

7.4 Photoluminescence

The PL emission spectrums of undoped and Cu-doped ZnO flower-likes when excited with 325 nm at ambient temperature are shown in Figure 7.5. There are two emission bands on the spectrum of undoped ZnO flower-likes. One is a weak sharp blue emission centering at around 373 nm, which is attributed to the recombination of free excitons of ZnO **[11]** and the other a strong and broad green emission band centered at around 552 nm. The PL peak at around 552 nm is associated with the oxygen vacancy-related green emission of ZnO **[12].** It was observed that the presence of Cu^{2+} ions only affected the luminescence intensity. The highest luminescence intensity yield of the particles was obtained for the undoped ZnO and higher Cu contents results in a substantial decrease in emission intensity **[13].** The dependence of the luminescence intensity of the ZnO on the concentration of Cu^{2+} ions is illustrated in Figure 7.6. It can be seen clearly that the luminescence intensity of the ZnO in the visible region decay nearly exponential with the Cu^{2+} content. The Cu-doped ZnO nanostructures still need further studies for lower concentration of Cu. The group of Aravind *et al* managed to get the highest luminescent intensity at 0.01 mol% of Cu doped ZnO and further increase in the Cu molar concentration lead to luminescent quenching **[14].** Other researchers **[13, 15]** managed to get the highest luminescence intensity for undoped ZnO and doping ZnO with Cu also caused a decrease in luminescence intensity, similar then us. The decreasing of the self-activated green emission band in Cu-doped ZnO nanostructures suggests a marked reduction in surface defects states as a result of the doping and increasing the non-radiative recombination, the decrease in luminescence intensity may be due to the Cu-Cu clustering in the ZnO lattice. With increase in doping concentration, more and more Cu luminescent centres are introduced in the structure and clustering occurred above a certain concentration.

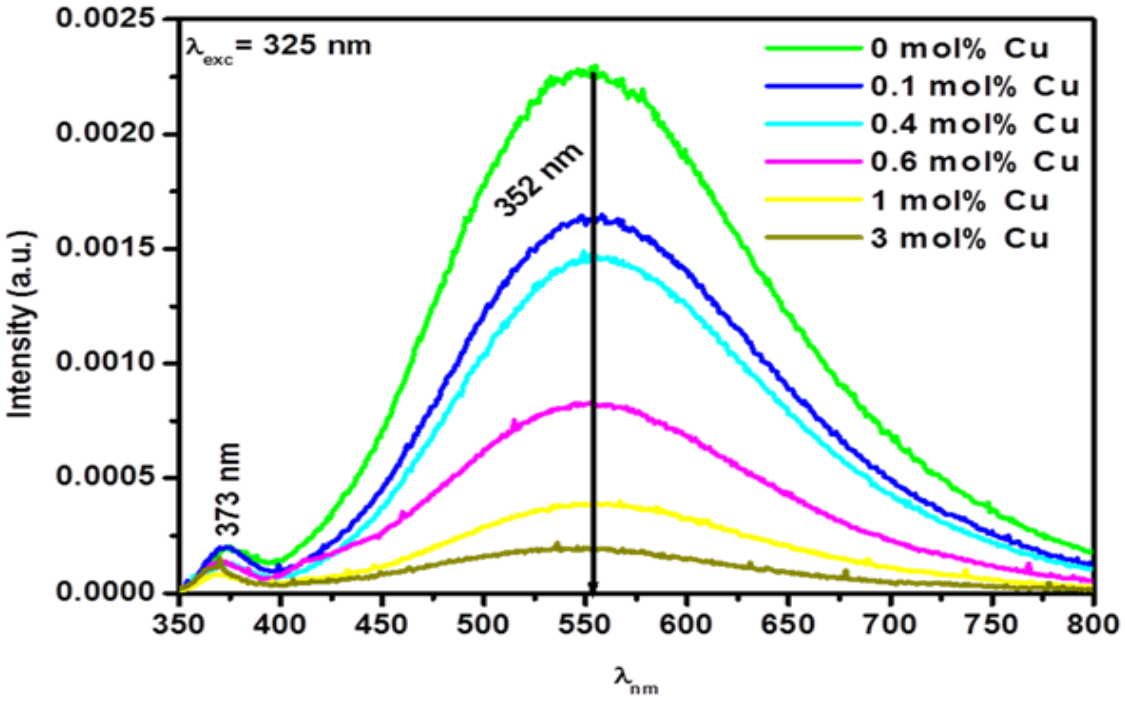

Figure 7.5: PL emission spectra for undoped and Cu-doped ZnO flower-likes at different molar concentrations of Cu acetate, with excitation wavelength of 325 nm using He-Cd laser at room temperature.

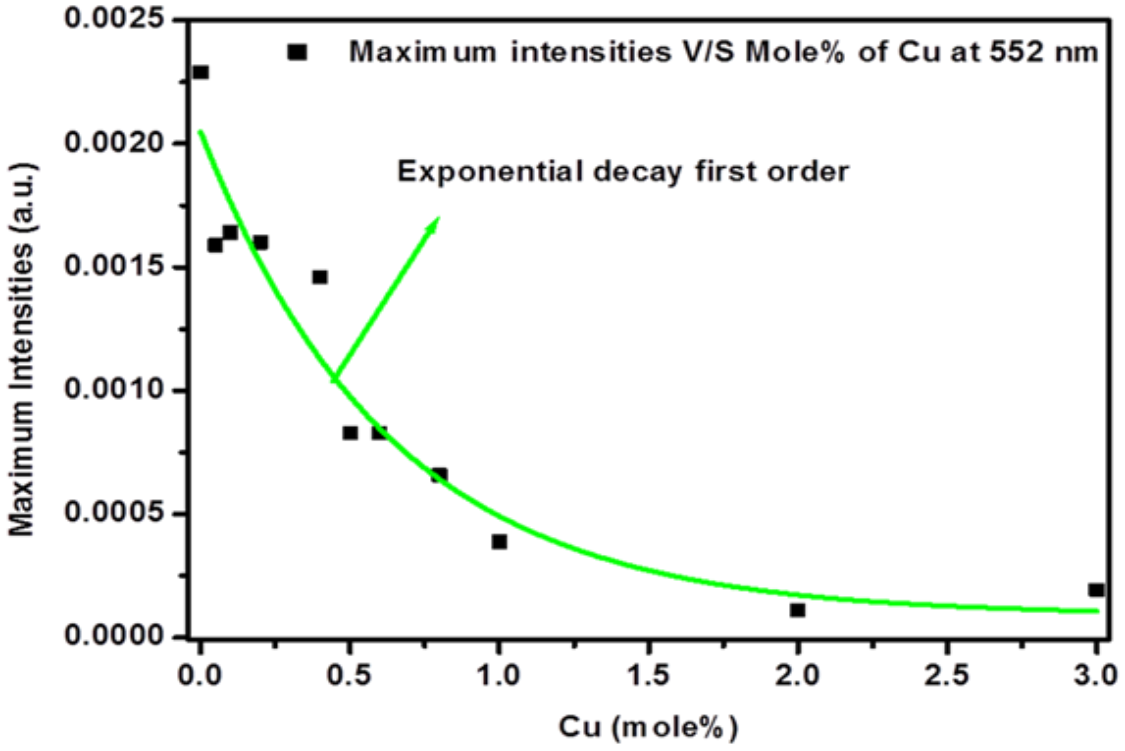

Figure 7.6: Dependence of emission intensity of the ZnO-Cu flower-like on the concentration of Cu and it was fitted with exponential decay first order.

References

[1]. A. B. Djurišić, Y. H. Leung, K. H. Tam, *Appl. Phys. Lett.* **88** (2006) 103107-1-103107-3.

[2]. L. Wischmeier, T. Voss, I. Rückmann, J. Gutowski, *Phys. Rev. B.* **74** (2006) 195333-1-195333-9.

[3]. W. Q. Peng, S. C. Qu, G. W. Cong, Z. G. Wang, *J. Cryst. Growth*. **279** (2005) 454-460.

[4]. B. Bodo, P. K. Kalita, *AIP. Conf. Proc*. **1276** (2010) 31-35.

[5]. C. Burda, X. Chen, R. Narayanan, M. A. E1-sayed. *Chem. Rev*. **105** (2005) 1025-1102.

[6]. J. Huang, Y. Wu, C. Gu, M. Zhai, K. Yu, *Sensors and Actuators B: Chemica*. **146** (2010) 206-212.

[7]. L. Yuzhen, G. Lin, X. Huibin, D. Lu, Y. Chunlei, W. Jiannong, G. Weikun, Y. Shihe, W. Ziyu, *J. Appl. Phys*. **99** (2006) 114302-1-114302-4.

[8]. A. Hachigo, H. Nakahata, K. Higaki, S. Fujii, S-I. Shikata, *Appl. Phys. Lett*. **65** (1994) 2556-2558.

[9]. L. Spanhel, M. A. Anderson, *J. Am. Chem. Soc*. **113** (1991) 2826-2833.

[10]. B. D. Cullity, *Elements of X-ray Diffraction (2nd Ed)*, Addison Wesley, 1978, pp 284-285.

[11]. J. Lee, M. Yoon, *J. Phys. Chem. C.* **113** (2009) 11952-11958.

[12]. S. Bayan, U. Das, D. Mohanta, *Phys. Status Solidi A.* **8** (2010) 1859-1863.

[13]. R. Elilarassi, G. Chandrasekaran, *J Mater Sci: Mater Electron*. **21** (2010) 1168–1173.

[14]. A. Aravind, M. K. Jayaraj, M. Kumar, R. Chandra, *J. Mater. Sci: Mater Electron*. **24** (2013)106–112.

[15]. Z. A. Khan, A. Rai, S. R. Barman, S. Ghosh, *App. Phys. Lett.* **102** (2013) 022105-1–022105-3.

CHAPTER 8

Synthesis of PbS nanostructures by chemical bath deposition method

8.1 Introduction

In recent years, interest in the development of the semiconductor nanostructured materials has grown rapidly owing to their unique physical and chemical properties **[1]**. This is due to their potential application in the area of solar cells, optoelectronic devices, photoconductors, sensor and infrared detector devices **[2].** Their attractiveness arises from their low synthetic cost, their solution processing ability and the dependence of their optoelectronic properties as a function of size, shape, doping and surface chemistry **[3-4]**. PbS nanocrystals are attractive for infrared-related applications because the energy of their first excitonic transition can be easily tuned from the visible to the infrared **[5]**. As its large exciton Bohr radius (18 nm) **[6-7]**, the effects of strong quantum confinement can be achieved even for relatively large structures **[8]**. The band gap energy of PbS can changed from 0.41 eV to the values up to 5.2 eV by varying the shape and size from the bulk materials to nanocrystal structures **[9]**.The preparation of PbS has been explored by a number of methods including sonochemical synthesis **[6]**, liquid phase synthesis **[10]**, chemical bath deposition (CBD) [**11]** and gas phase synthesis **[12]**.

8.2 Results and discussions

8.2.1 Structural and compositional analyses.

Figure 8.1(a) shows X-ray diffraction (XRD) patterns of the PbS powders synthesized at various bath temperatures as indicated (55, 65, 70 and 80 ºC). All XRD patterns show four intense peaks at around 2θ = 25.99, 30.11, 43.09 and 51.03º. All these peaks corresponding to the cubic phase of PbS which matched well with the standard JCPDS card no. (05-0592, a = 5.936 Å). The estimated average value of the cell constant *a* was 5.934 Å which match perfectly with the standard data. No significant changes were observed for the lattice parameter with the variations of the synthesis temperature. This is confirmed by the JCPDS card no: 18-1740. However, as the bath temperature was increased from 65 to 80 ºC the extra peaks disappeared and the intensity of the peaks attributed to PbS improved as shown in Figure 8.2.

Koao L F et al Int. J. Electrochem 9 (2014) 1747-1757

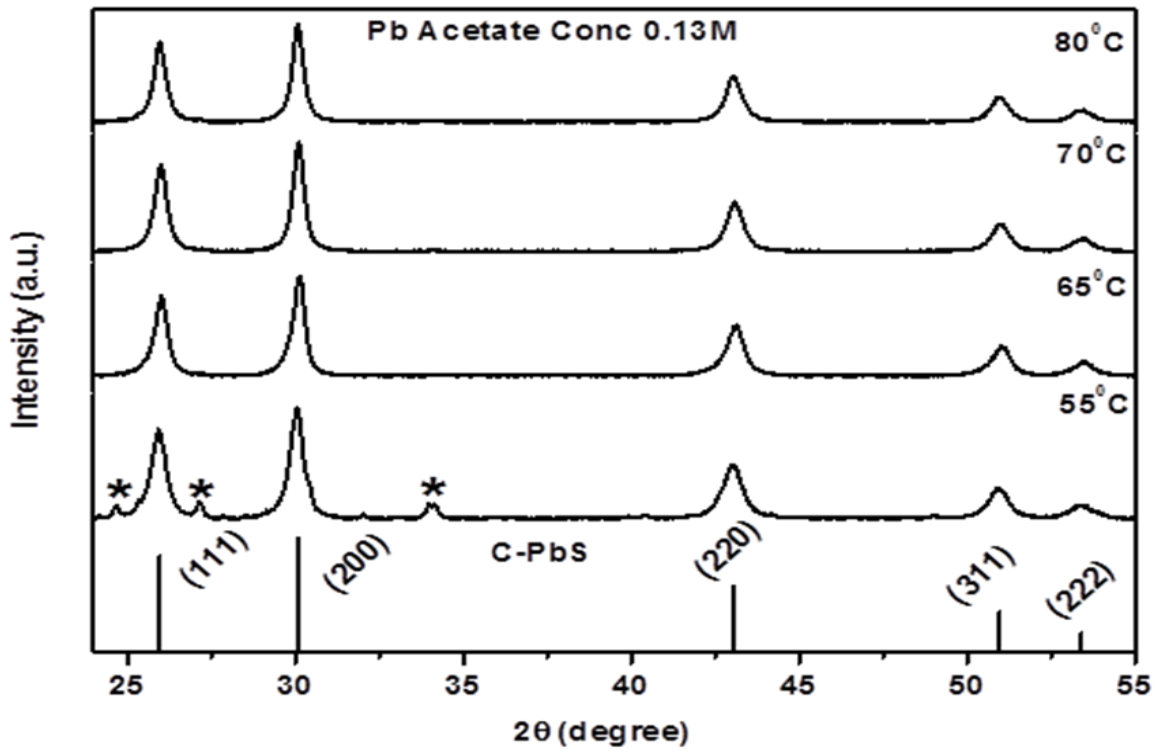

Figure 8.1: XRD patterns of PbS prepared at different synthesis temperatures but at constant molar concentration of lead acetate.

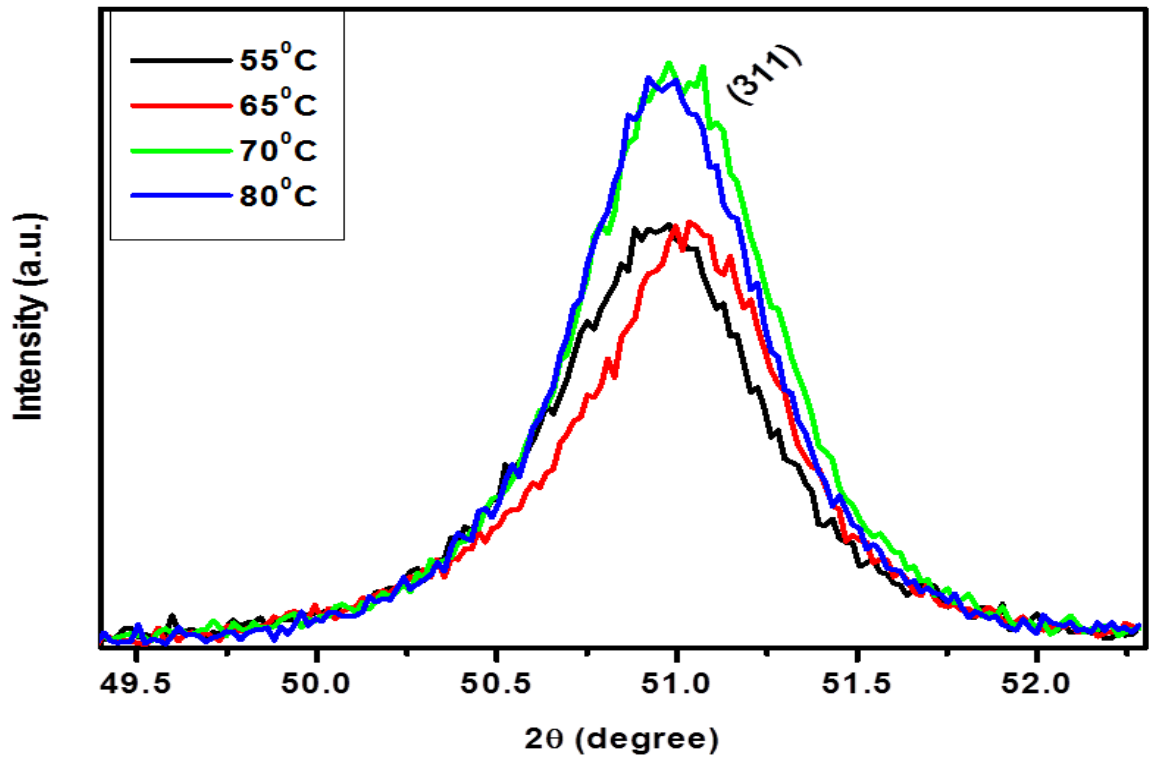

Figure 8.2: XRD patterns of the (111) planes of the PbS powders prepared by the CBD method.

This improved intensity with well-defined sharper peaks indicates a higher crystallinity of the prepared material. The average grain size of the as-prepared nanocrystals was calculated from the Full Width Half Maximum (FWHM) of the diffraction peaks using the Debye formula **[13]**. All major diffraction peaks for all samples were chosen to estimate the average size of the nano crystallites by the least square method. It is clear from Figure 8.3 that the estimated average grain size increased slightly with an increase in the synthesis temperature. Figure 8.4 shows the XRD patterns of the PbS nanostructures synthesized by varying the concentration of the precursors (Pb acetate). All the peaks match well with the standard cubic structure of PbS.

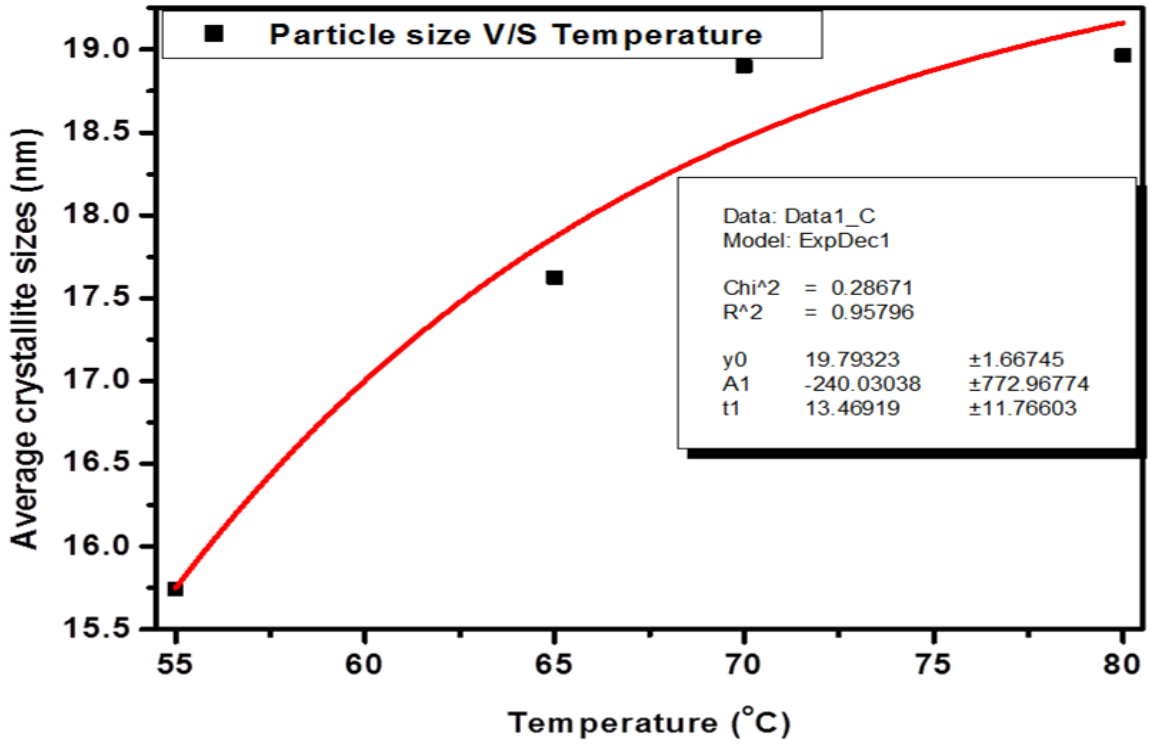

Figure 8.3: The dependence of average crystallite sizes of the PbS on the synthesis temperature of the CBD.

It is clear that at the low molar concentration (0.12 M) and the highest molar concentration (0.14) there are extra peaks marked with star (*) which were due to unreacted lead acetate oxide hydrate. It is observed that the best crystallite structure was obtained for PbS samples synthesized at 0.13 M of lead acetate. The estimated crystallite sizes from the Debye formula were 30 ± 1, 35 ± 1 and 31 ± 1 nm for 0.12, 0.13 and 0.14 mol% of lead acetate, respectively. No clear trend in the estimated crystallite sizes with an increase in lead was observed.

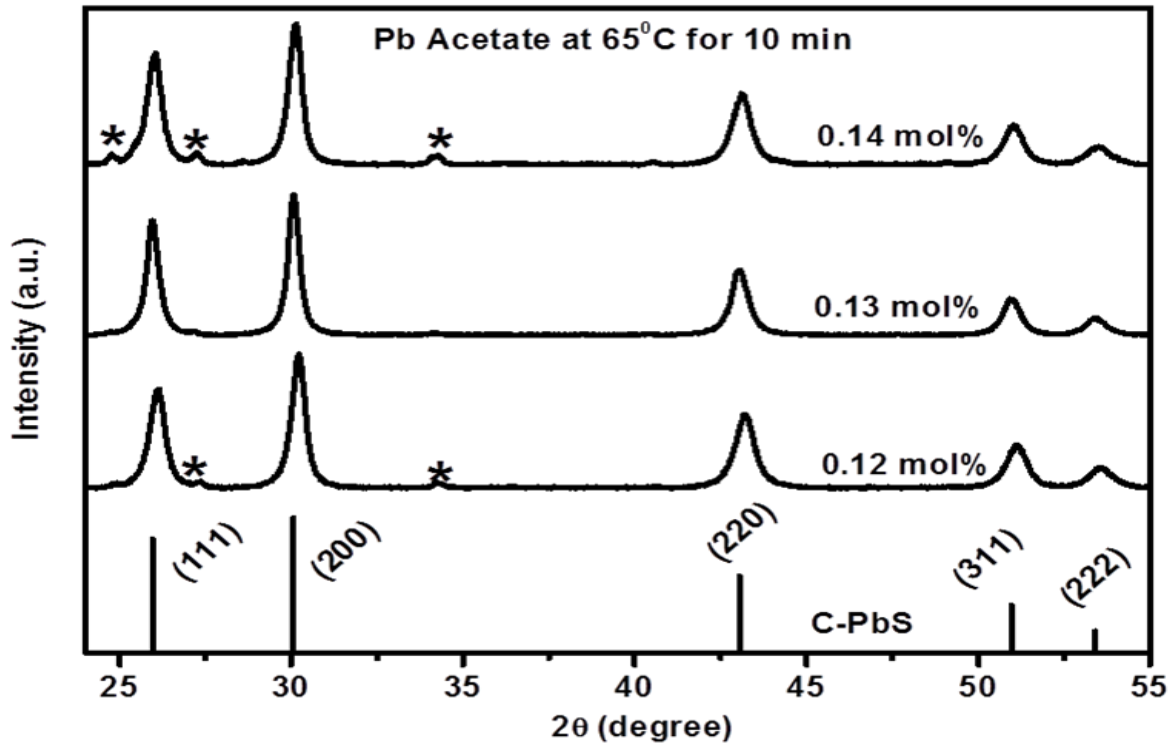

Figure 8.4: XRD patterns of PbS samples prepared with different molar concentration of lead acetates and constant synthesis temperature using the CBD method.

Figure 8.5 (a), (b), (c) and (d) show surface morphologies of the PbS powders synthesized at various temperatures ranging from 55 to 80 ºC. All the samples were taken at 10 keV with a 0.05 nm field of view. Karami et al **[2]** have reported that by increasing the synthesis temperature there was no influence on particle sizes and morphology. On the contrary we observed that the surface aspects of the SEM images of the PbS powders were composed of uniform nanorods structures for the synthesis temperature of 55 to 70 ºC, however, the nanorods size increased slightly with an increase in the synthesis temperature. With a further increase in the synthesis temperature to 80 ºC, the nanorods structure broke up in mixed structures with the emergence of spherical nanoparticle and plate-like shapes. Figure 8.6 (a), (b) and (c) show surface morphologies of the PbS powders synthesized at various molar concentrations of lead acetates. The surface morphologies consisted of agglomerated nanorods structures. The nanorods also increased slightly in size with an increase in the molar concentration of lead acetate.

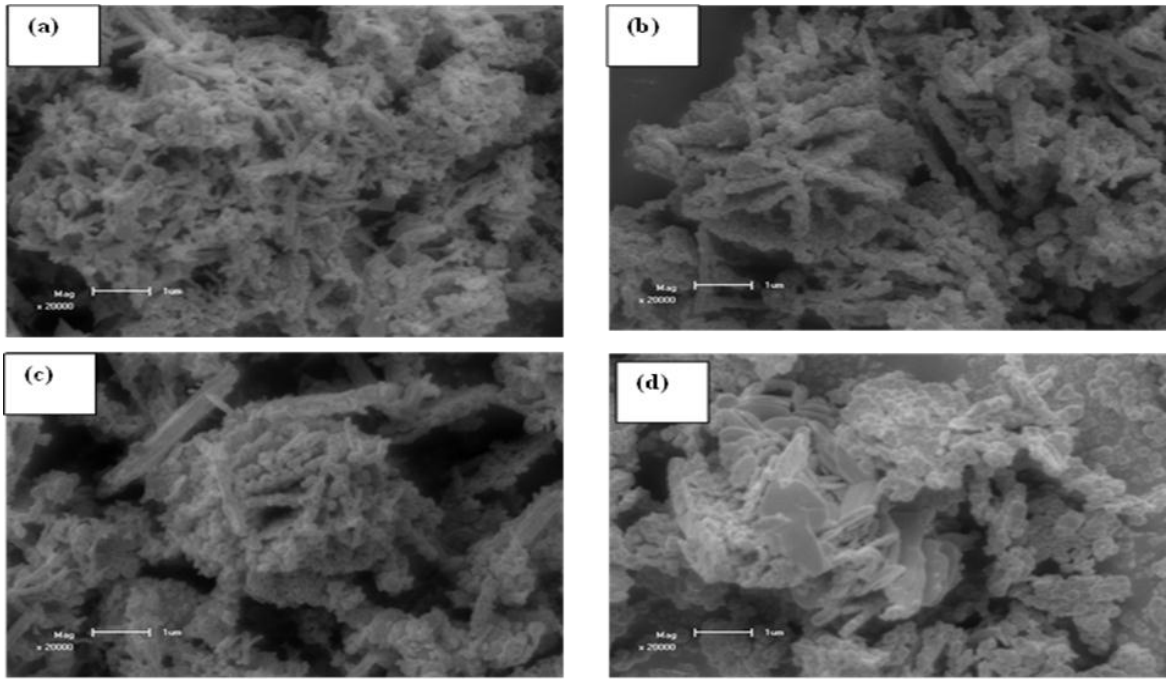

Figure 8.5: The SEM micrograph of PbS powders synthesized at the various temperatures: (a) 55 ºC, (b) 65 ºC, (c) 70 ºC and (d) 80 ºC but at constant molar concentration of lead acetate.

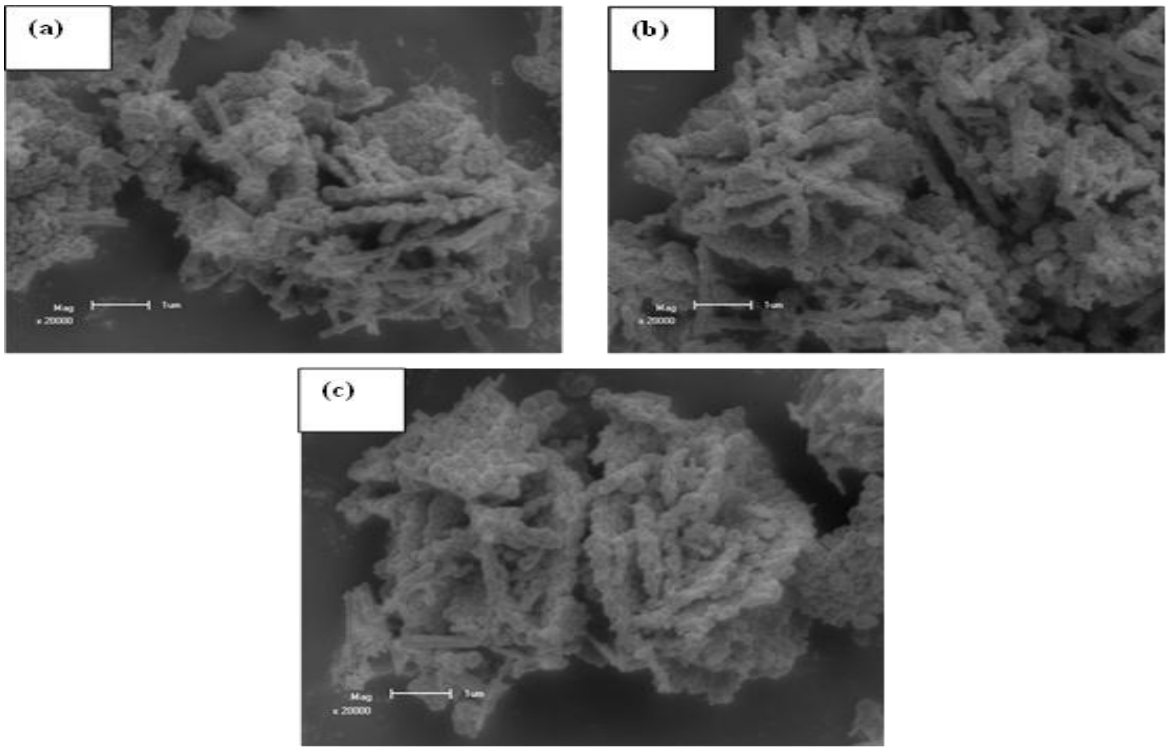

Figure 8.6: The SEM micrograph of PbS powders synthesized at the various molar concentrations of Pb acetate: (a) 0.12 M, (b) 0.13 M and (d) 0.14 M and constant synthesis temperature.

8.3 Optical properties

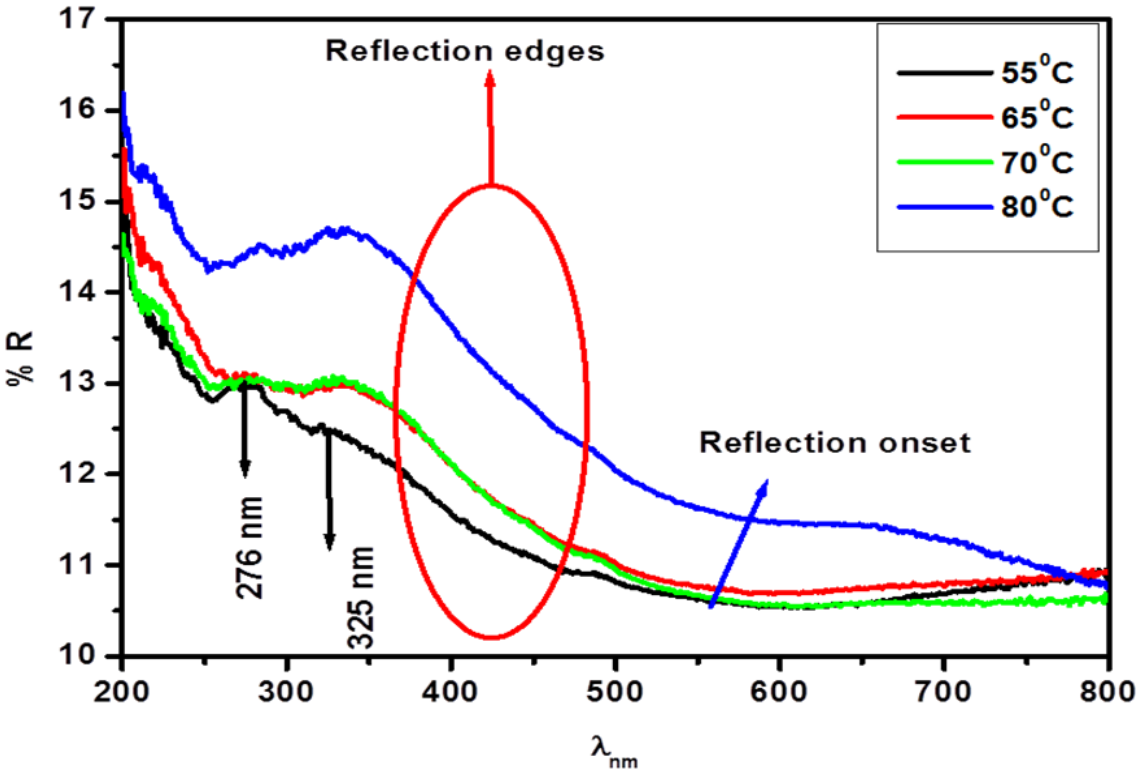

Figure 8.7: The absorbance spectra of PbS powders prepared at various temperature and at constant molar concentration of lead acetate.

The UV-visible reflectance spectra of the as prepared samples are illustrated in Figure 8.7. The optical spectra of the samples prepared at 55, 65, 70 and 80 ºC have reflection onset at about 550 nm. The reflection edge is strongly shifted to higher wavelengths. In addition, the three optical spectra at temperatures between 55 and 70 ºC display one well-defined absorption band with a maximum at about 325 nm.

Figure 8.8 shows the diffuse reflectance spectra of the PbS nanostructure synthesised at different molar concentration of lead acetate. On increasing the molar concentration of lead acetate, the absorption edges shifted slightly to higher wavelength. We can ascribe the origin of the absorption bands at 335 and 647 nm to $1s_e$-$1s_h$ and $1p_e$-$1p_h$ transitions in PbS nanoparticles, respectively **[14-15]**. The shift of absorption edges to higher wavelengths can be attributed to the increase in grain size with an increase in synthesis temperature. While the small variation in crystallite size for the molar concentration of precursor (lead acetate) is reflected in the small variation in absorption edges. This result correlates well with the data obtained from the XRD and SEM analysis.

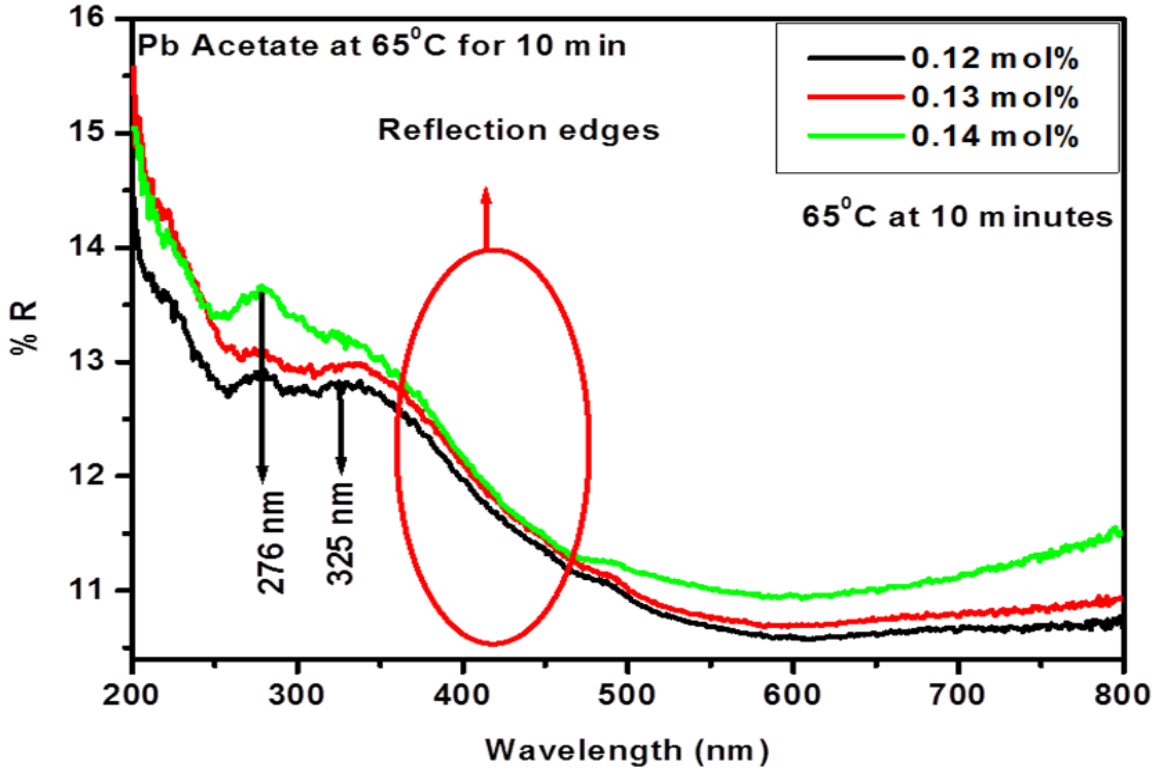

Figure 8.8: The absorbance spectra of PbS powders prepared at various molar concentration of lead acetates at constant synthesis temperature.

8.4 Photoluminescence

The PL emission spectra of the samples when excited at 277 nm are shown in Figure 8.9. The excitation wavelength which correspond to the $1d_h \rightarrow 1d_e$ transition of PbS was confirmed by the UV analysis. Deconvolution of the PbS (0.13 M lead acetate) emission spectra revealed two bands in the visible region. The bands are associated with the electronic transitions from the $1p_e \rightarrow 1p_h$ (336 nm) and $1s_e \rightarrow 1p_h$ (379 nm) energy levels **[14]**. The emissions in the UV region (336 and 379 nm) arose from the recombination of excitons and/or shallowly trapped electron-hole pairs **[16-17]**. An extra PL emission was observed in the infrared region, with a maximum of the broad emission at 725 nm and a shoulder at 825 nm. These emissions were due to deep level defects. Figure 8.10 shows the PL emission spectra of the PbS nanostructures excited at 277 nm. It is clear that the emission bands of the PbS nanostructures did not change, only the emission intensity changed as the synthesis temperature increased. The relative decrease of the PL intensity with the increase in the synthesis temperature suggested that the increase of the crystallite size played a major role in decreasing the defect densities **[16]**. In other words, the gradual decrease of PL emission intensities reveals a significant decrease in the surface/volume ratio for high temperature grown samples **[18]**.

This decrease in luminescence intensity can be due to slightly increasing grain size as the synthesis temperature increased as confirmed by the SEM and XRD analysis. Therefore, it is well understood that the non-radiative recombination's increased with increasing particle size and as a result the luminescence intensity decreased **[19]**. In this work it was very interesting to find that the grain sizes, morphology, optical and luminescence properties of PbS nanostructures depend on the synthesis temperatures and the molar concentration of lead acetate.

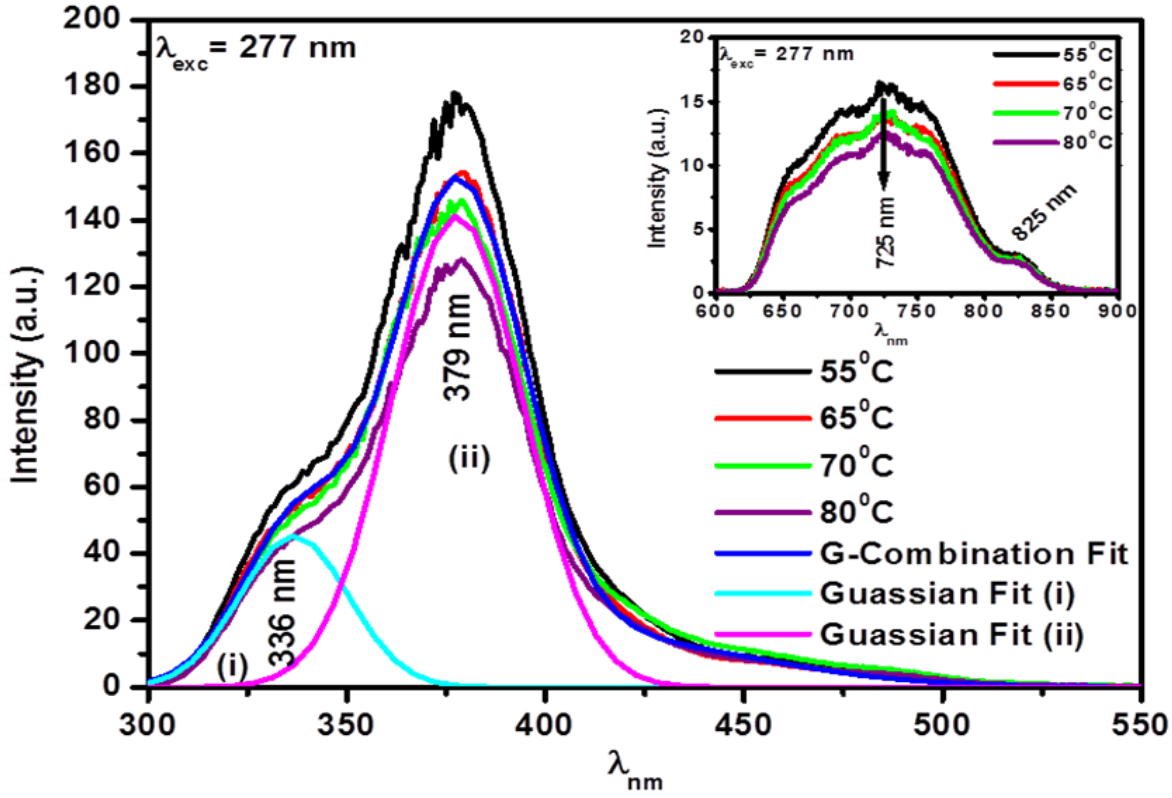

Figure 8.9: PL emission spectra of PbS nanostructures in the visible region and for infrared region (as an inset) synthesized at various synthesis temperatures but at constant molar concentration of lead acetate and with the deconvolution of the luminescence spectra taken from the 65 °C of synthesis temperature.

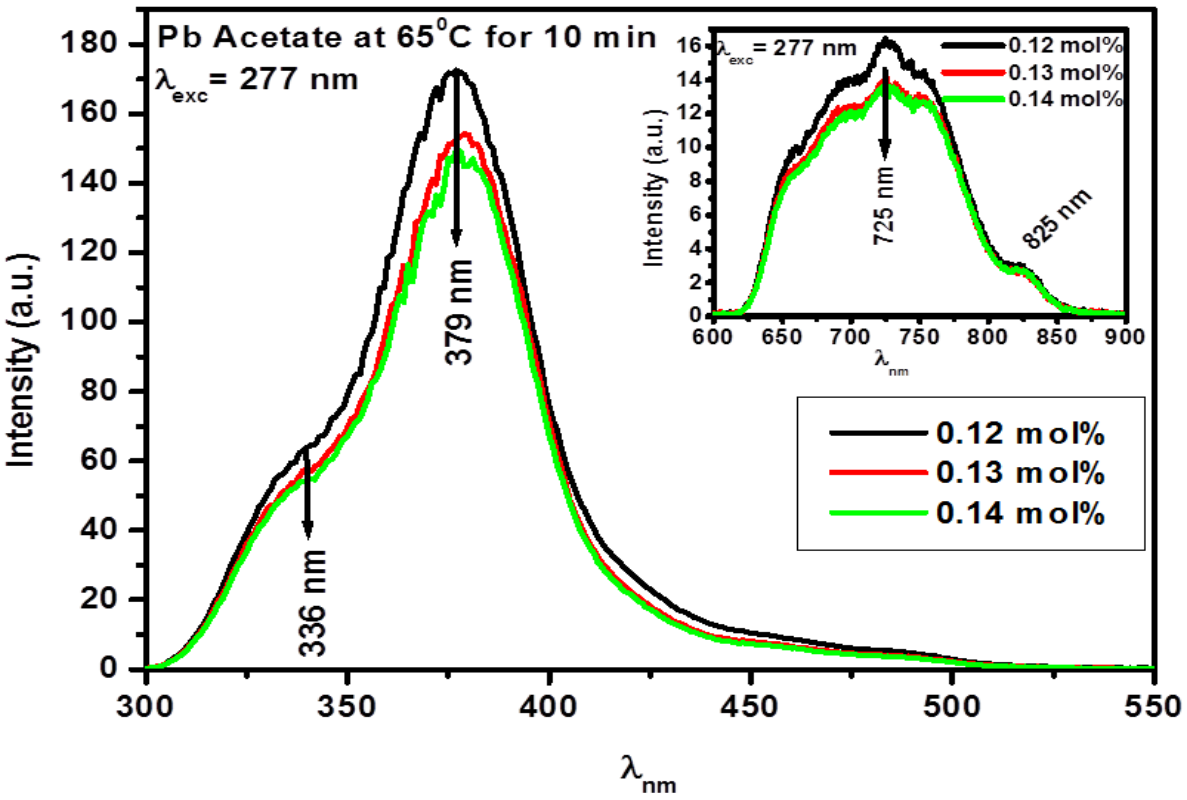

Figure 8.10: PL emission spectra of PbS nanostructures in the visible region and for the near infrared region (as an inset) synthesized at various lead acetate molar concentrations at constant synthesis temperature.

Reference

[1]. Y. N. Xia, P. D. Yang, Y. G. Sun, Y. Y. Wu, B. Mayers, B. Gates, Y. D. Yin, F. Kim, Y. Q. Yan, A*dv. Mater*. **15 (**2003) 353-389.

[2]. H. Karami, M. Ghasemi, S. Matini, *Int. J. Electrochem. Sci*., **8** (2013) 11661-11679.

[3]. A. P. Alivisatos, *J. Phys. Chem*. **100** (1996) 13226-13239.

[4]. S. C. Erwin, L. Zu, M. I. Haftel, A. L. Efros, T. A. Kennedy, D. J. Norris, *Nature*. **436 (**2005) 91-94.

[5]. S. A. McDonald, G. Konstantatos, S. Zhang, P. W. Cyr, J. D. E. Klem, L. Levina, E. H. Sargent, *Nat. Mater*. **4** (2005) 138-142.

[6]. S. M. Zhou, X. H. Zhang, X. M. Meng, X. Fan, S. T. Lee, S. K. Wu, *J. Solid State Chem*. **178** (2005) 399–403.

[7]. J. Zhu, S. Liu, O. Palchik, Y. Koltypin, A. Gedanken, *J. Solid State Chem*. **153** (2000) 342-348.

[8]. A. K. Dutta, T. Ho, L. Zhang, P. Stroeve, *Chem. Mater.* **12** (2000) 1042-1048.

[9]. D. Kumar, G. Agarwal, B. Tripathi, D. Vyas, V. Kulshrestha, *J. of Alloys and Comp.* **484** (2009) 463-466.

[10]. C. Wang, W. X. Zhang, X. F. Qian, X. M. Zhang, Y. Xie, Y. T. Qian, *Mater. Lett.* **40** (1999) 255-304.

[11]. L. F. Koao, F. B. Dejene, H. C. Swart, *SAIP'2011 Proceedings, the 56th Annual Conference of the South African Institute of Physics, edited by I. Basson and A.E. Botha (University of South Africa, Pretoria),* ISBN: 978-1-86888-688-3 (2011) 151-155.

[12]. C. Kaito, Y. Saito, K. Fujita, *Jpn. J. Appl. Phys*. **26** (1987) 1973-1975.

[13]. B. D. Cullity, *Elements of X-ray Diffraction (2nd Ed),* Addison Wesley (1956) 284-285.

[14]. X. Ai, L. Guo, Y. Zou, Q. Li, H. Zhu, *Mater. Lett.* **38** (1999) 131-135.

[15]. K. S. Babu, C. Vijayan, P. Haridoss, *Mater. Sci. Eng C*. **27** (2007) 922-927.

[16]. M. Cheraghizade, R. Yousefi, F. Jamali-Sheini, A. Sa'aedi, J. *Telecom. Dev*, **1(3)** (2012) 79-82.

[14]. M. Navaneethan, K. D. Nisha, S. Ponnusamy, C. Muthamizhchelvan, *Rev. Adv. mater. Sci*, **21** (2009) 217-224.

[18]. S. N. Sahu, K, K, Nanda, *PINSA*, **67 (A)** (2001) 103-130.

[19]. S. Sadhu, P. Saha Chowdhury, A. Patra, *J. Lumin*. **126** (2007) 387-392.

CHAPTER 9

Effect of Tb molar concentration on optical properties of PbS nanoparticles

9.1 Introduction

Semiconductor phosphor nanocrystal structures have been extensively studied for the last two decades because of their unusual structural, electronic, and optical properties **[1]**. Doping with optically active luminescent materials control the band structure of the nanocrystal structures and show intense emissions in a wide range of wavelength depending on the impurity type, concentration and crystal dimensions, and also play key roles in luminescence efficiency and the positions of emission bands, thus influencing their practical applications.

PbS nanocrystals and nanowires are potentially useful in electroluminescent devices such as light-emitting diodes, lasers, solar cells and biological systems **[2-3]**. This PbS nanoparticles can be easily incorporated into polymer, glassy matrices where they can be applicable in fiber optics telecommunication **[3]** and again can be incorporated in semiconductor nanoparticles (e.g. ZnO and ZnS) where they can be applied in light emitting diodes, laser diodes and ultraviolet photodetectors **[3]**. PbS nanoparticles embedded in an amorphous silica (SiO_2) host was also investigated **[4].** Studies of the effect of Tb^{3+} concentration on the luminescence of PbS nanoparticles are very limited and will remain a subject of great interest.

9.2 Results and discussions

9.2.1 Structural and compositional analyses.

Figure 9.1 show the XRD patterns of the undoped and Tb^{3+}-doped PbS. All the peaks of undoped PbS were assigned by using the JCPDS file (No. 78-1897), with lattice constant a=5.914 Å. All the peaks matched perfectly with the standard data. No diffraction peaks from any other chemical species such as terbium nitrate were detectable when the doping molar concentration of Tb was lower than 2 mol%. It is expected that the Tb^{3+} were easily incorporated into the PbS lattice due to the smaller ionic radius of the Tb^{3+} ion (0.10 nm) as compared to that of Pb^{2+} (0.123 nm) **[5]**.

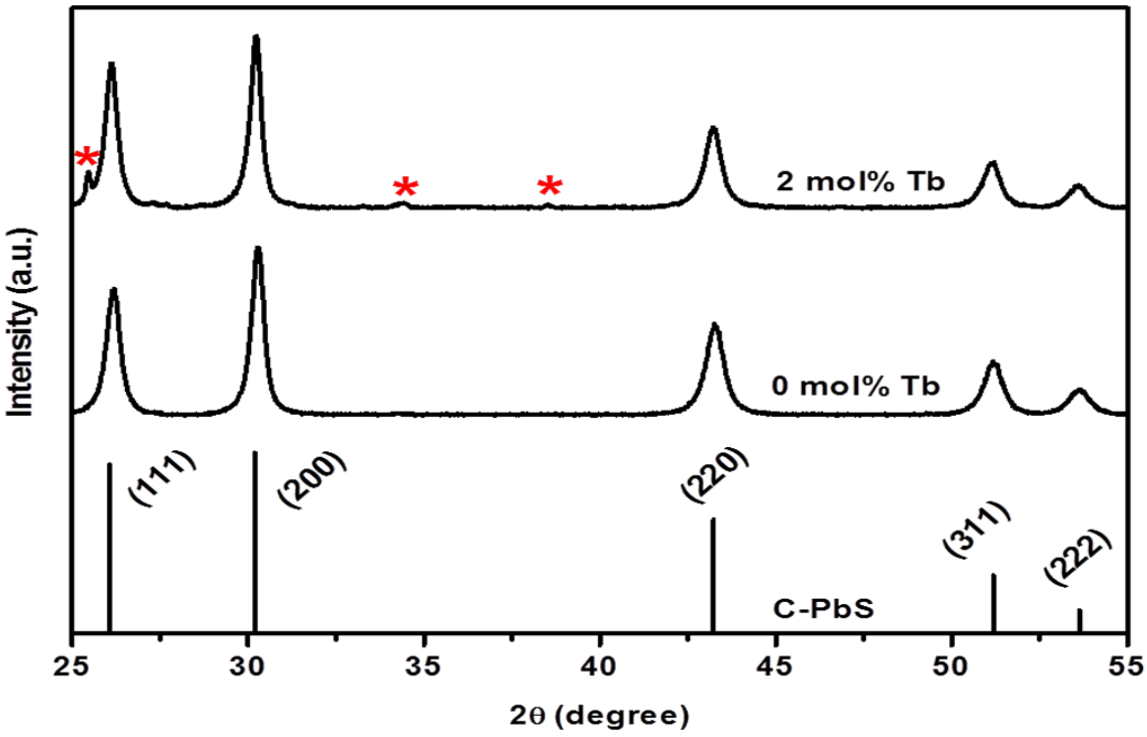

Figure 9.1: X-ray powder diffraction patterns for undoped and Tb^{3+} doped PbS prepared by the CBD method.

As the Tb^{3+} ions increased to 2 mol%, the XRD pattern shows the emergence of additional peaks at 2θ = 25.42, 34.29 and 38.56 which are marked with a star (*), specifically associated with the Tb^{3+} nitrate (JCPDS card no. 80-1318). This might be due to the insolubility of Tb^{3+} at the higher molar concentrations. Furthermore, as can be seen in Figure 9.2, the positions of the (111) diffraction peaks evidently shifted to the lower angle side and the diffraction peaks become more intense with the increasing Tb^{3+} content. This shift may indicating that the estimated lattice parameters were a little larger than those of undoped PbS (the estimated experimental value of the cell constants are a = 5.9094 and 5.9322 Å for 0 mol% and 2 mol% of Tb^{3+}, respectively) **[6-8].** It was observed that the lattice parameters increased with an increase in the mol% of Tb^{3+} ions. The increase in lattice parameters might be due to the lattice distortion as Tb^{3+} ions occupied the lattice sites of Pb^{2+}. Lattice parameter increased with an increase in the crystalline size **[9]**. The average grain size of the as-prepared nanocrystals can be calculated from the Full Width Half Maximum (FWHM) of the diffraction peaks using the Debye formula **[10]**. All major diffraction peaks were chosen to estimate the average size of the nanocrystals by the least square method. The estimated grain size was 34± 2 and 36± 2 nm, for the 0 mol% and 2 mol% Tb^{3+} respectively.

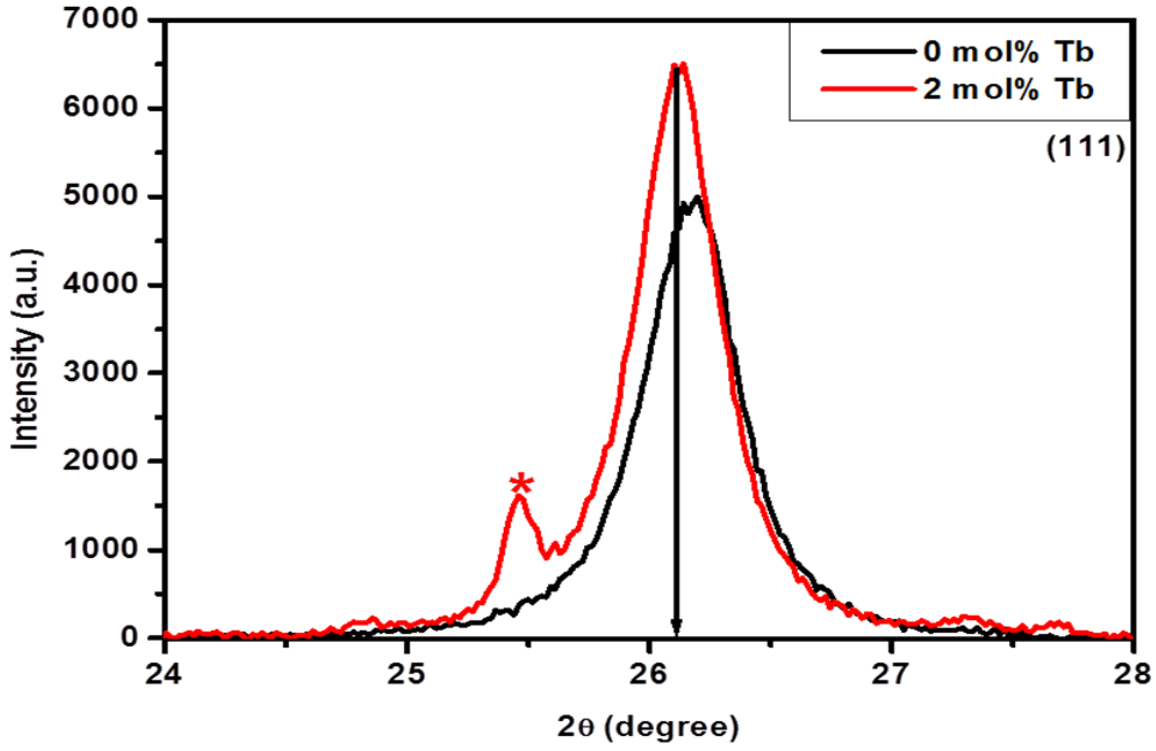

Figure 9.2: X-ray powder diffraction patterns at (111) for undoped and 2 mol% Tb^{3+}-doped PbS prepared by the CBD method.

The estimated average grain was about 35± 2 nm. Figure 9.3 (a), (b), (c) and (d) show SEM micrographs of the undoped and doped PbS nanostructures prepared at different molar concentrations of the Tb^{3+} ions. The surface aspects of undoped PbS is composed of nearly spherical nanoparticles. It is clear that all nanoparticles are clustered and non-homogeneous. When the Tb^{3+} concentration was increased to 2 mol%, the morphology of the PbS:Tb^{3+} changed to a mixture of spherical nanoparticles and nanorods. A representative TEM image of undoped PbS and Tb^{3+}-doped PbS is displayed in Figure 9.4. The image shows that the undoped crystallites have an almost agglomerated spherical (marked with red arrows) morphology. In the TEM images (0.5 and 2 mol% of Tb^{3+}), lattice fringes (indicated by blue arrow) can clearly be observed, which indicate that the particles were crystalline.

All the TEM images of the undoped and Tb^{3+}-doped) PbS shows similar morphology. The average diameters were estimated to be 36 ± 1 nm, which is consistent with the results calculated using Debye's formula. TEM-EDX spectrum of the nanostructures suggests the existence of Pb, S, Tb, O and C in addition to the copper signal from a TEM Cu grid (see Figure 9.5). From the spectra it is clear that the Tb became visible for the higher Tb^{3+} doped concentration of PbS as shown for the PbS doped with 2 mol% Tb^{3+} ions.

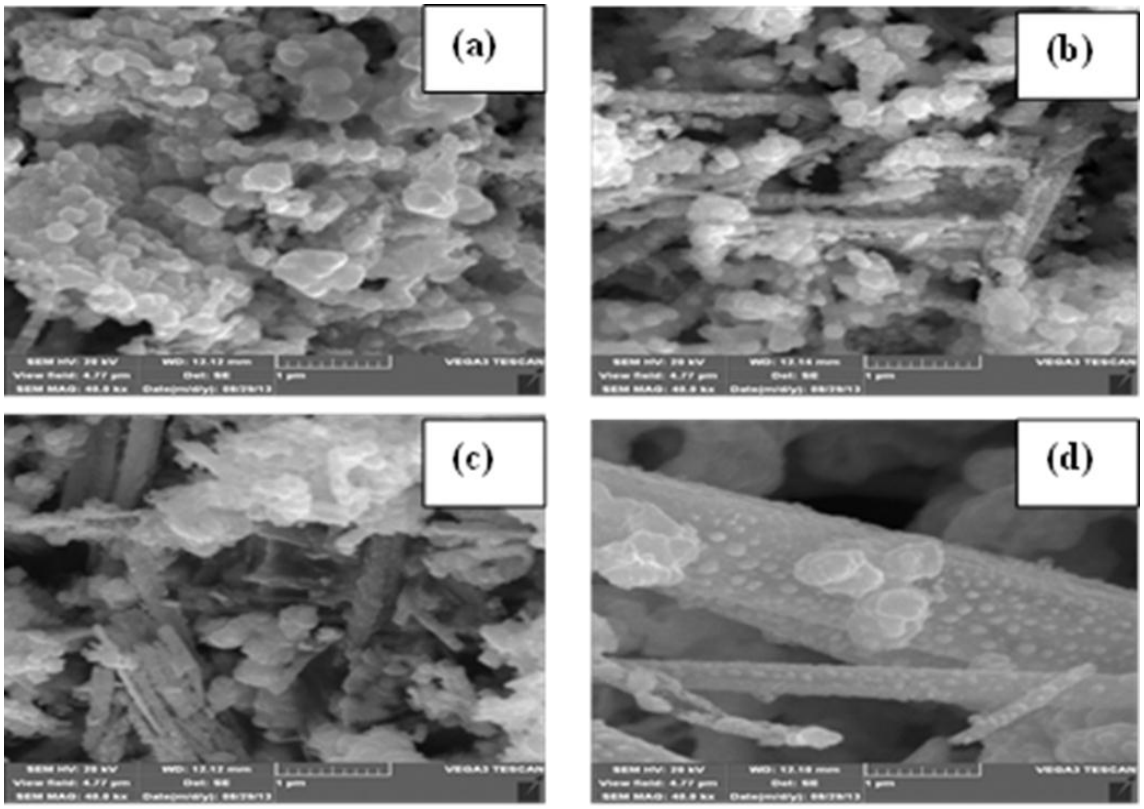

Figure 9.3: SEM images of (a) PbS: 0, (b) PbS: 0.3 (c) PbS: 1 and PbS: 2 mol% Tb^{3+}.

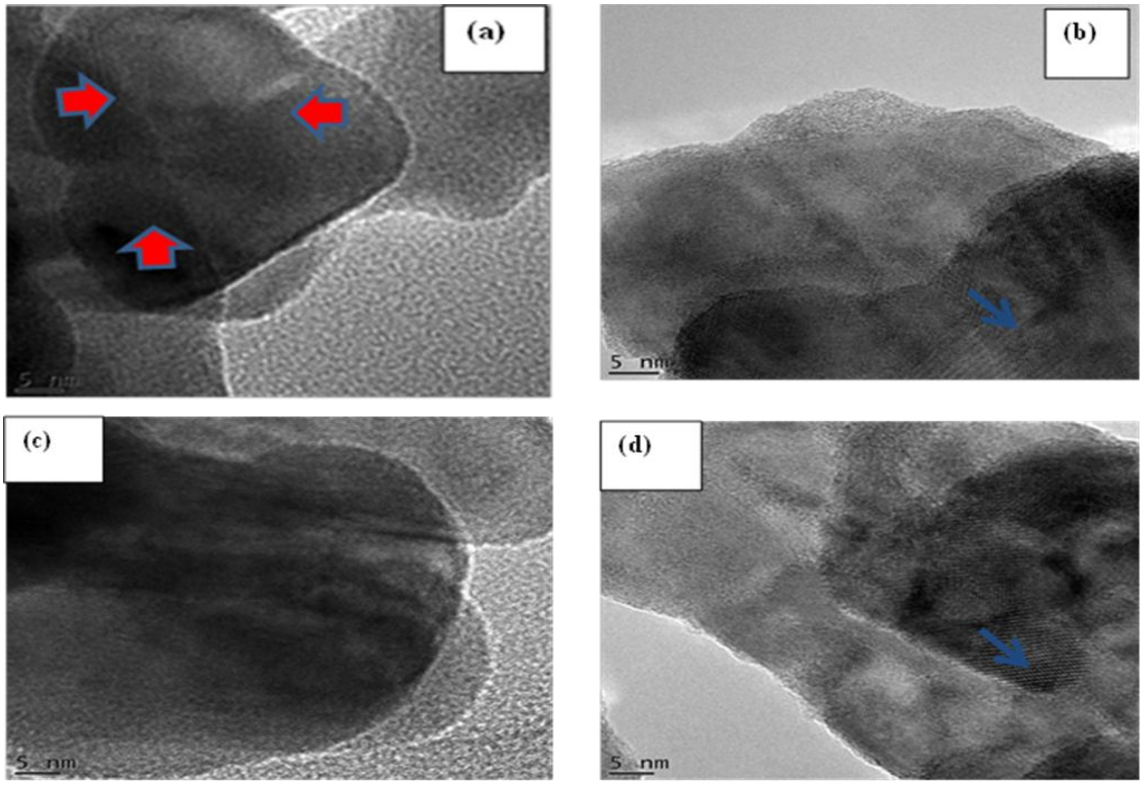

Figure 9.4: TEM images of (a) PbS: 0, (b) PbS: 0.5 (c) PbS: 1 and (c) PbS: 2 mol% Tb^{3+}.

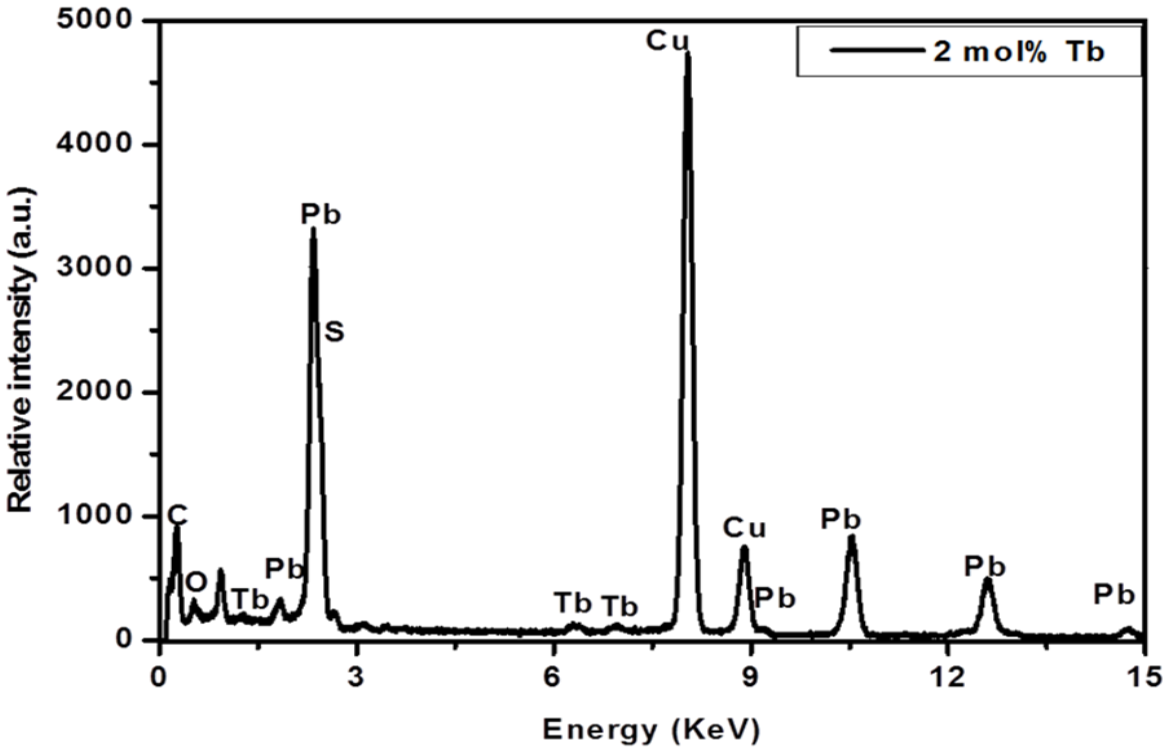

Figure 9.5: A representative EDX spectrum of the 2 mol% Tb^{3+} doped PbS nanoparticles prepared by the CBD method.

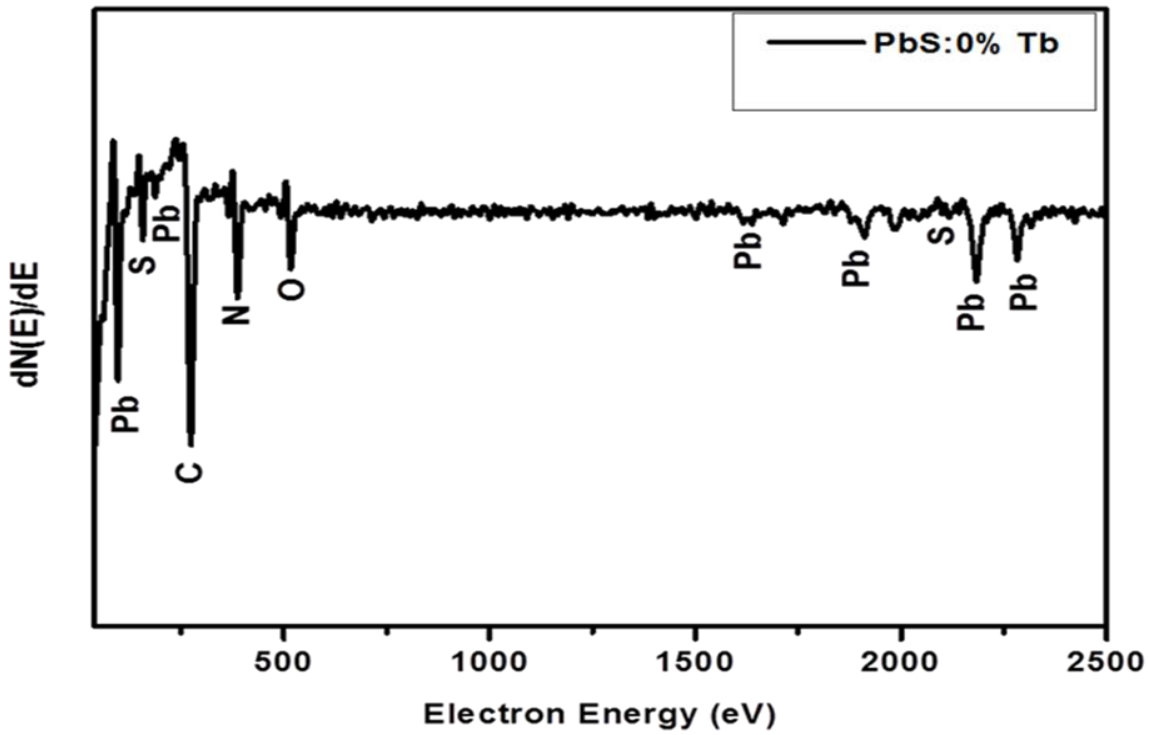

Figure 9.6: Auger spectra of the undoped PbS nanoparticles prepared by the CBD method.

No Tb^{3+} was measured for the lower (0.5 mol% Tb^{3+}) concentration of Tb^{3+} doped sample. From the spectra there is no clear evidence of S except for a small shoulder to the right of the Pb peak. Due to the overlapping between the Pb and the S signal in the EDX spectra, AES measurements were carried out to double check the elements and to evaluate their purity. The Auger spectrum of the undoped PbS nanoparticles is shown in Figure 9.6. The typical spectrum of the spherical nanoparticles confirms the presence of Pb and S. The signals at kinetic energies of 517, 387 and 276 eV are ascribed to the presence of adventitious O, N and C, respectively, which come from atmospheric adsorbed gases. Moreover, no other impurities were found on the surface of the PbS nanoparticles.

9.3 Optical properties

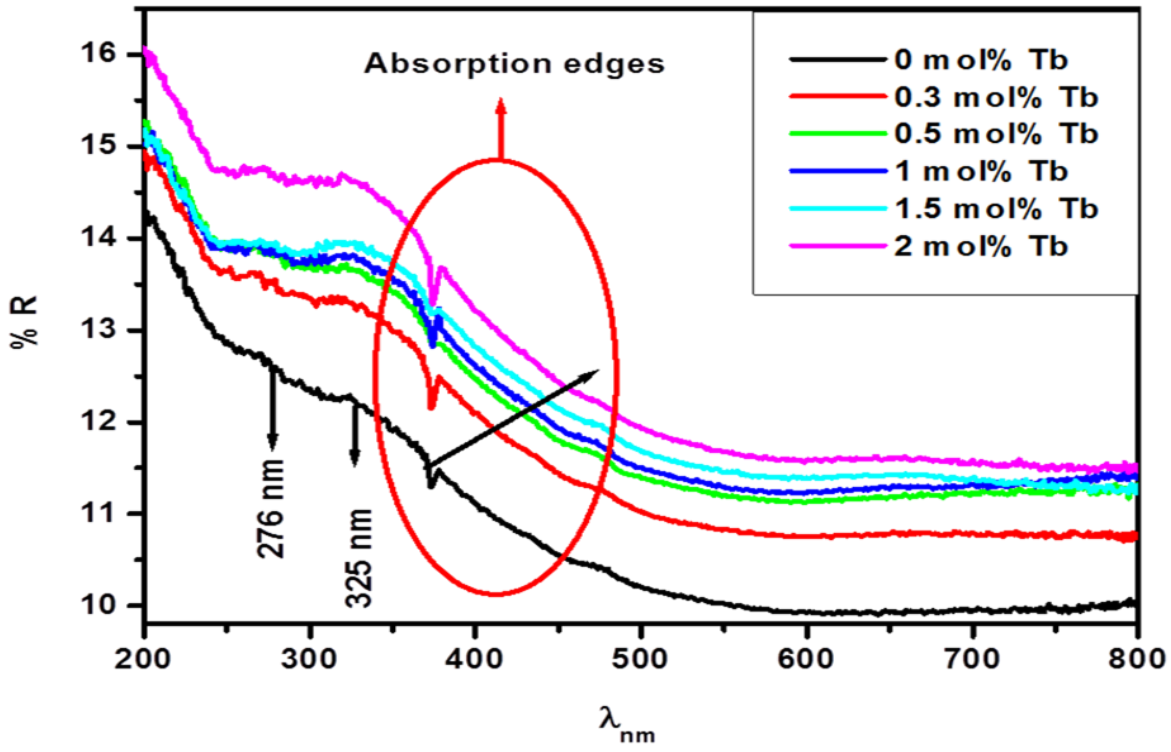

Figure 9.7: The reflectance spectra of undoped and Tb^{3+}-doped PbS nanoparticles.

Figure 9.7 shows the UV-visible reflectance spectra of the as prepared samples. The spectra of all the samples show good optical quality in the visible range due to the complete reflectance in the 250-500 nm range. It clearly indicates that as the molar concentration of Tb^{3+} ions increased the optical absorption edge shift to a higher wavelength while the reflectance intensity increased. Although the percentage absorption changed, the absorption edge onset at around 580 nm did not change noticable. The dependence of the absorption edges of the PbS on the amount of Tb^{3+} incorporated is illustrated in Figure 9.8. It can be

seen clearly that the absorption edges of the PbS exponentially decay with the Tb^{3+} content. Optical spectra of the undoped and Tb^{3+}-doped PbS powders exhibit reflectance peaks at around 335 and 276 nm. The peaks are attributed to the electronic transitions between the split energy levels of PbS nanoparticles: 1sh→1se and 1dh→1de, respectively **[11-13]**. The shift of the absorption edges to higher wavelengths might be due to the presence of defect states and disorder **[14, 15]**. Secondly, might be due to the estimated grain sizes using Debye's equation that were slightly increasing as the molar concentration of Tb^{3+} increased as confirmed by XRD **[13].**

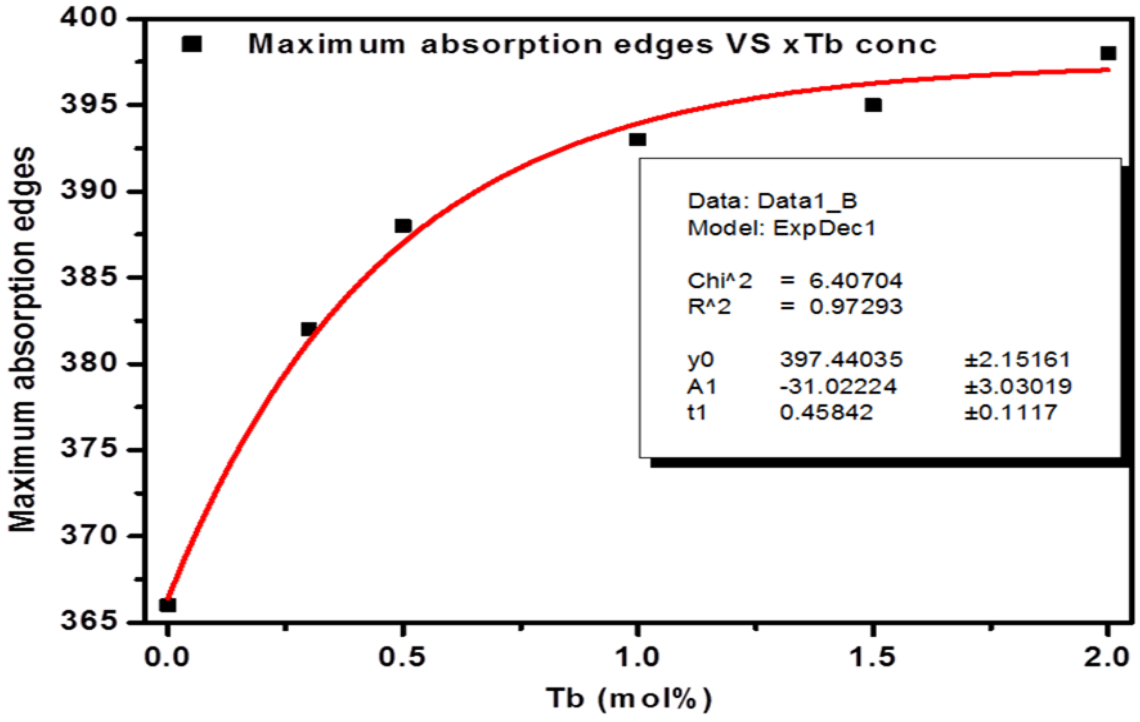

Figure 9.8: The variation of maximum absorption edges of the PbS on the amount of Tb^{3+} ion dopants.

9.4 Photoluminescence

The PL emission spectra of the samples when excited at 276 nm are shown in Figure 9.9. The excitation wavelength which correspond to the $1d_h \rightarrow 1d_e$ transition of PbS was confirmed by UV analysis. Deconvolution of the undoped PbS emission spectra reveals two bands in the visible region. The bands are associated with the electronic transitions from the $1p_e \rightarrow 1p_h$ (338 nm) and $1s_e \rightarrow 1p_h$ (376 nm) energy levels **[11]**. The emissions in the UV region (338 and 376 nm) arise from the recombination of excitons and/or shallowly trapped electron-hole pairs **[16-17]**.

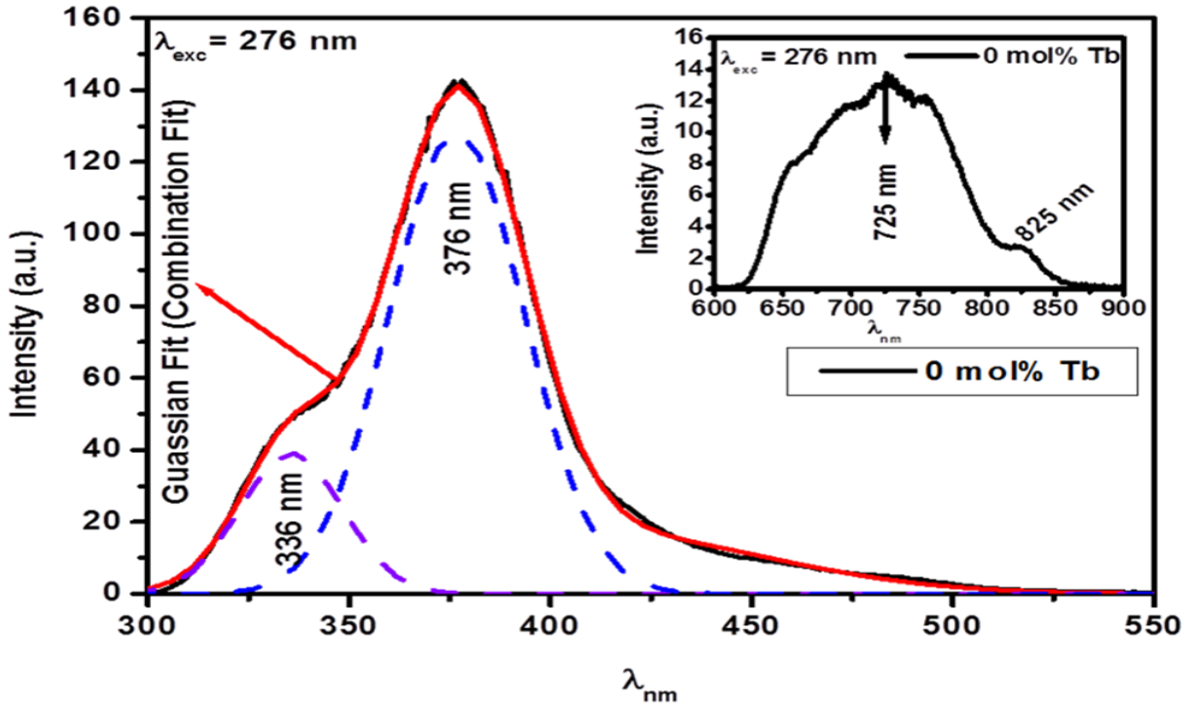

Figure 9.9: PL spectra of undoped PbS nanostructures showing the visible and the IR emissions as an inset.

An extra PL emission is observed in the infrared region, with a maximum of broad emission at 725 nm and a shoulder at 825 nm. These emissions are due to deep level defects. Figure 9.10 with its inset shows the PL emission spectra of PbS samples nanostructures excited at 276 nm. The Tb^{3+}-doped samples show similar emissions as undoped once at around 336, 376, 725 and 825 nm. An increase in emission intensity was observed with an increase in Tb^{3+} ions up to 0.3 mol% Tb^{3+} and decreased there after most probably due to luminescence quenching. A band at 433 nm was found to emerge as the Tb^{3+} ions increases. The PL peak at around 433 nm is usually related to the transition of electrons from conduction band edge to holes, trapped at interstitial Pb^{2+} sites **[16-19].** An increase in Tb^{3+} concentrations up to 0.3 mol% Tb^{3+} ions caused an increase in the luminescence intensity (see Figure 9.11). This might be due to the different in valencies between Tb^{3+} and Pb^{2+} ions due to charge compensation requirements, resulting in oxygen defects. The energy of the excitation source was absorbed by Tb^{3+} ions (donor) and then transferred non-radiatively to the PbS nanoparticles (acceptor). This implies that there is a possibility of dopant (Tb^{3+}) transferring energy to the host (PbS) just as it was observed in SiO_2:Ce **[20]**, where Ce transfers energy to SiO_2. A further increase in the Tb^{3+} ions above 0.3 mol% resulted in luminescence quenching.

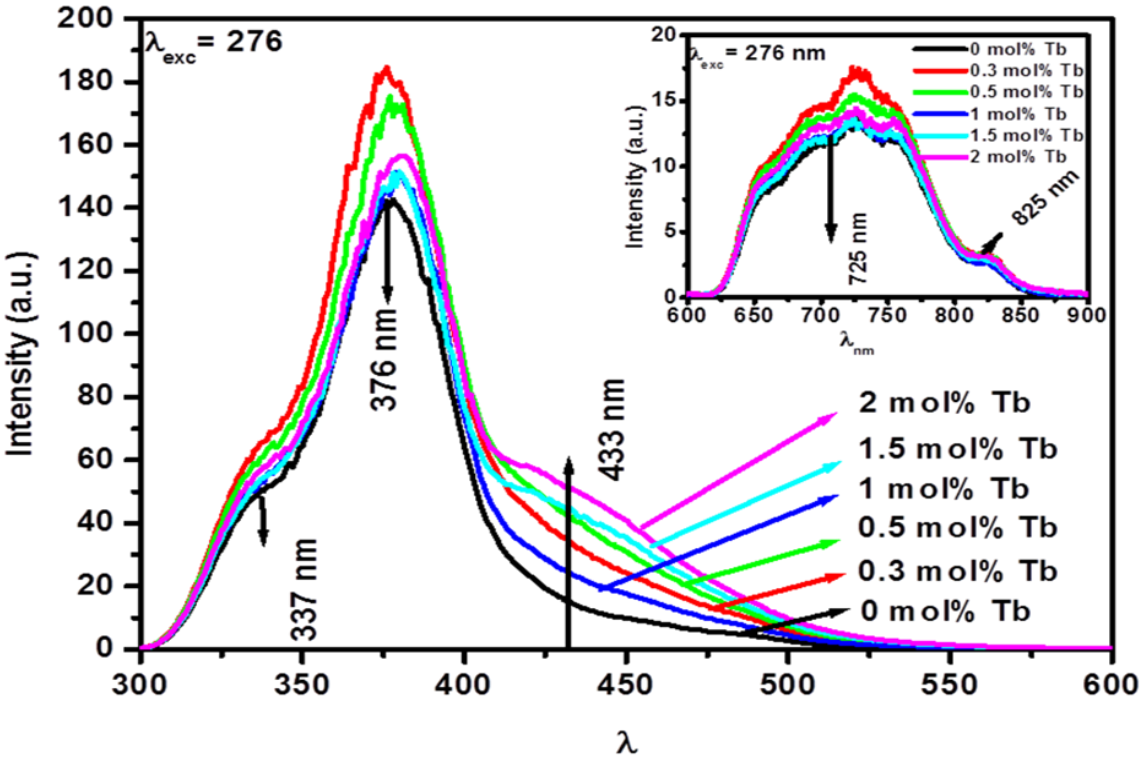

Figure 9.10: PL emission spectra in the visible and infrared region (shown as an inset) for undoped and Tb^{3+}-doped PbS nanostructures at different molar concentrations of Tb nitrate excited at a wavelength of 276 nm using a Xenon lamp.

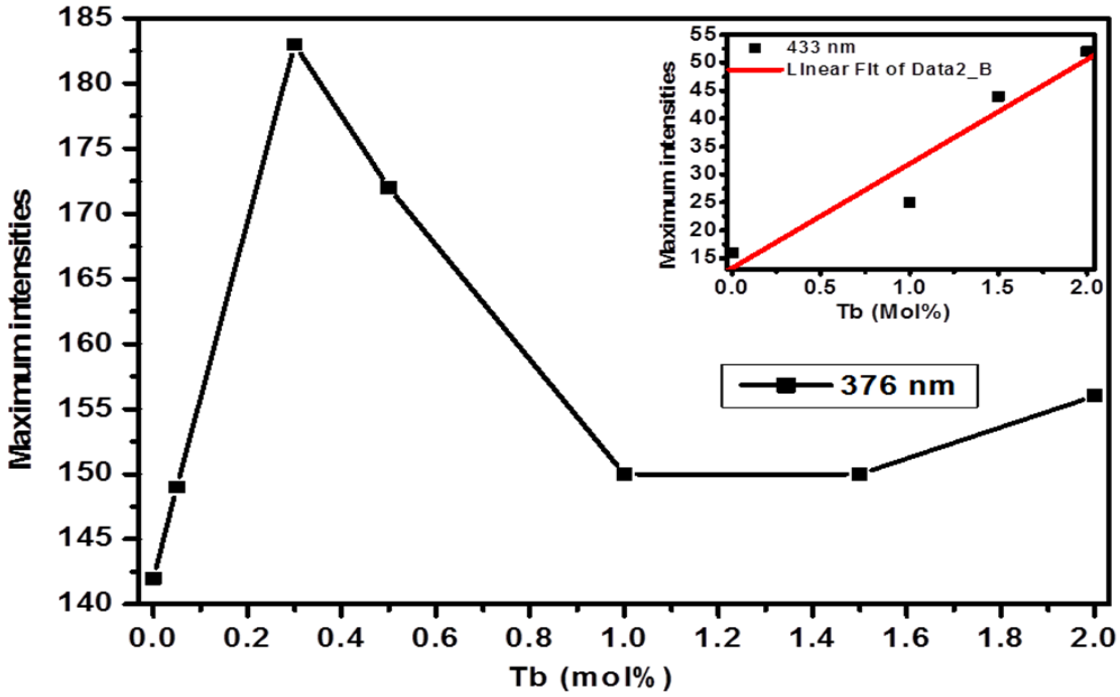

Figure 9.11: Maximum intensity of PbS nanoparticles at 376 nm and 433 nm (inset) as function of Tb^{3+} (mol%).

Firstly, the decrease in luminescence intensity might be due to a slightly increase in the estimated grain size with an increase in the Tb^{3+} ion molar concentration, as confirmed by the XRD analysis. It is well understood that the non-radiative recombination increased with increasing particle size which resulted in the luminescence intensity decrease **[5].** Secondly, the quenching might be due to the Tb ions either tends to locate on the crystal surface, causing an undesired Tb-Tb interaction, or formed terbium nitrate aggregates, which act as a quenching site, resulting in a drastic decrease in the luminescent intensity **[21]**. The increase in luminescence intensity band at around 433 nm might be attributed to lattice defects increase caused by Tb^{3+} doping into PbS lattice.

References

[1]. S. Acharya, U. K. Gautam, T. Sasaki, Y. Bando, Y. Golan, K. Ariga, *J. American. Chem. Soc*, **130** (2008) 4594-4595.

[2]. D. Kumar, G. Agarwal, B. Tripathi, D. Vyas, V. Kulshrestha, *J. of Alloys and Comp.* **484** (2009) 463-466.

[3]. O. M. Ntwaeabora, R. E. Kroon, V. Kumar, T. Dubroca, J –K. Ahn Park, H. C. Swart, *J. Phys. Chem. Solids*, **70 (**2009) **1438-**1442.

[4]. M. S. Dhlamini, J. J. Terblans, O. M. Ntwaeaborwa, J. M. Ngaruiya, K. T. Hillie , J. R. Botha and H. C. Swart, *J. Lumin*, **128 (12)** (2008) 1997-2003.

[5]. S. Sadhu, P. Saha Chowdhury, A. Patra, *J. Lumin*, **126 (**2007)387-392.

[6]. J. Lang, Q. Han, J. Yang, C. Li, X. Li, L. Yang, Y. Zhang, M. Gao, D. Wang, J. Cao, *J. App. Phys*, **107 (**2010) 074302:1-074302:4.

[7]. P. P. Partha, J. Manam, *Nanosystems: Phys. Chem. Mathem.* **4(3)** (2013) 395-404.

[8]. L. Saravanan, A. Pandurangan. R. Jayavel, *J. Nanopart. Research*, **13 (**2011)1621-1628.

[9]. S. N. Sahu, K. K. Nanda, *PINSA*, **67A (1)** (2001)103-130.

[10]. B. D. Cullity. *Elements of X-ray Diffraction*, 2nd ed, Addison Wesley, 1978. 284-285.

[11]. X. Ai, L. Guo, Y. Zou, Q. Li, H. Zhu, *Mater. Lett*, **38 (**1999) 131-135.

[12]. K. S. Babu, C. Vijayan, P. Haridoss, *Mater. Sci. Engin C*, **27 (**2007) 922-927.

[13]. S. Lu, U. Sohling, T. Krajewski, M. Menning, H. Schmidt, *J. Mater Scie. Lett.* **17 (**1998) 2071-2073.

[14]. L. F. Koao, F. B. Dejene, H. C. Swart, J. R. Botha, *J. Lumin*, **143 (**2013) 463-468.

[15]. M. Saleem, L. Fang, H. B. Ruan, F. Wu, Q. L. Huang, C. L. Xu, C. Y. Kong, *Intern. J. Phys. Scie*, **7(23)** (2012) 2971-2979.

[16]. M. Cheraghizade, R. Yousefi, F. Jamali-Sheini, A. Sa'aedi, *J. Telecomm. Devices*, **1(3)** (2012) 79-82.

[17]. M. Navaneethan, K. D. Nisha, S. Ponnusamy, C. Muthamizhchelvan, *Rev. Advan. Mater. Scie*, **21 (**2009) 217-224.

[18]. H. Cao, G. Wang, S. Zhang, X. Hang, *Nanotech*, **17 (**2006) 3280-3287.

[19]. S. Z. Liu, S. L. Xiong, K. Y. Bao, J. Cao, Y. T. Qiang, *J. Phys .Chem C,* **113 (**2009)13002-13007.

[20]. L. F. Koao, H. C. Swart, R. I. Obed, F. B. Dejene, *J. Lumin*, **131 (**2011)1249- 1254.

[21]. M. Pal, U. Pal, J. M. G. Y. Jiménez, F. Pérez-Rodriguez, *Nanoscale. Research. Lett.* 7 **(**2012) 1-12.

CHAPTER 10

Optical properties of undoped, Tb^{3+} doped and Ce^{3+} co-doped PbS nanoparticles synthesized using chemical bath deposition method

10.1 Introduction

Due to fundamental interest, as well as their potential technological applications, such as information processing and storage, electronics and optoelectronics nanodevices, and biological fluorescent labelling, much attention has been focused on the synthesis and properties of low-dimensional nanocrystalline semiconductors **[1-2]**. PbS belong to a class of IV-VI nanocrystals with narrow energy gaps of relevance optical applications in the near-IR region of the electromagnetic spectrum such as long wavelength (1.3 and 155 μm) telecommunications **[3]**, photovoltanics **[4]** and bio-imaging in the spectroscopic window of low absorption of biological systems [1-1.2 μm] **[5]**. As its large exciton Bohr radius (18 nm) **[6]**, the effects of strong quantum confinement can be achieved even for relatively large structures **[7]**. PbS nanostructures may be used in optical devices such as light-emitting diodes and optical switches due to its third order nonlinear optical properties **[6, 8]**. PbS nanoparticles exhibit stronger quantum size effect and larger third order non-linear susceptibility than other semiconductors **[9-10]**. PbS nanocrystals have band gaps that are turnable over wide spectrum **[11]**. Compared with the bulk counterpart, the band gaps of PbS nanocrystals are significantly blue shifted from the near-IR into the visible and near-UV (ultraviolet) region with decreasing particle size **[12]**. This kind of nanomaterial's exhibits unusual physical and chemical properties in comparison with their bulk materials, such as size-dependent variation of the band gap energy. Furthermore, impurity ions doped into these nanocrystals can influence the electronic structure and transition probabilities.

Studies of the effect of Tb^{3+} concentration on the luminescence of PbS nanoparticles are very limited and will remain a subject of great interest. No report has been found on the effects of Ce^{3+} co-doping on the structure, optical and luminescence properties of Tb^{3+} doped PbS nanoparticles synthesized using the chemical bath deposition method.

10.2 Results and discussions

10.2.1 Structural and compositional analyses.

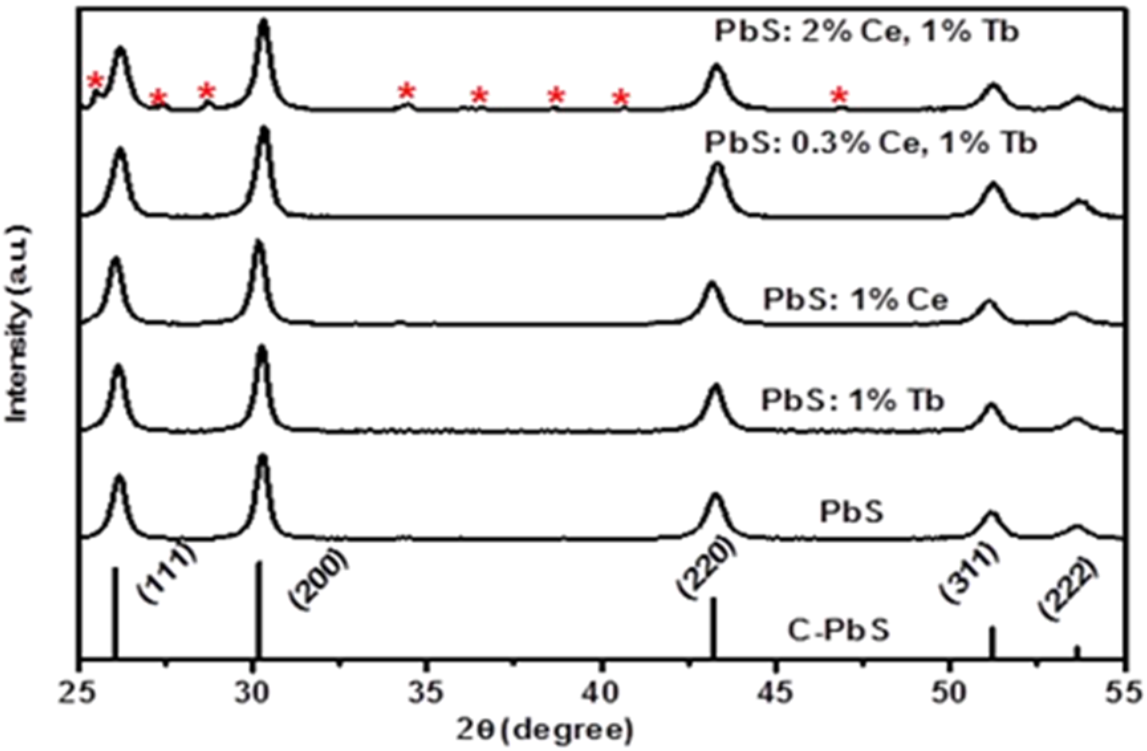

Figure 10.1: Represented XRD spectra of undoped, Tb-doped, Ce-doped and Tb-Ce co-doped PbS nanoparticles prepared by the CBD method.

Figure 10.1 shows the XRD patterns of the undoped, Tb^{3+}-doped, Ce^{3+}-doped and Ce^{3+} co-doped PbS samples. All the observed diffraction peaks can be indexed to the cubic structure of PbS with JCPDS file (No. 78-1897), with lattice constant a=5.914 Å. No diffraction peaks from any other chemical species such as cerium acetate and terbium nitrate are detectable when the Ce^{3+} co-doping is lower than 2 mol%. It is expected that the Tb^{3+} and Ce^{3+} are easily incorporated into the PbS lattice due to the smaller ionic radius of the Tb^{3+} and Ce^{3+} ions (0.10 and 0.103 nm, respectively) compared to that of Pb^{2+} (0.123 nm) **[13]**. By carefully analysing the XRD patterns, we find that, when Ce^{3+} co-doped is higher than 1 mol% the additional peaks appear which are marked with star (*), specifically associated with the Ce acetate (JCPDS card no. 48-1151). This may be due to insolubility of Ce at high molar concentrations. Furthermore, as can be seen in Figure 10.2, the positions of the main diffraction peaks (111) evidently shift to the smaller angle side and the diffraction peaks

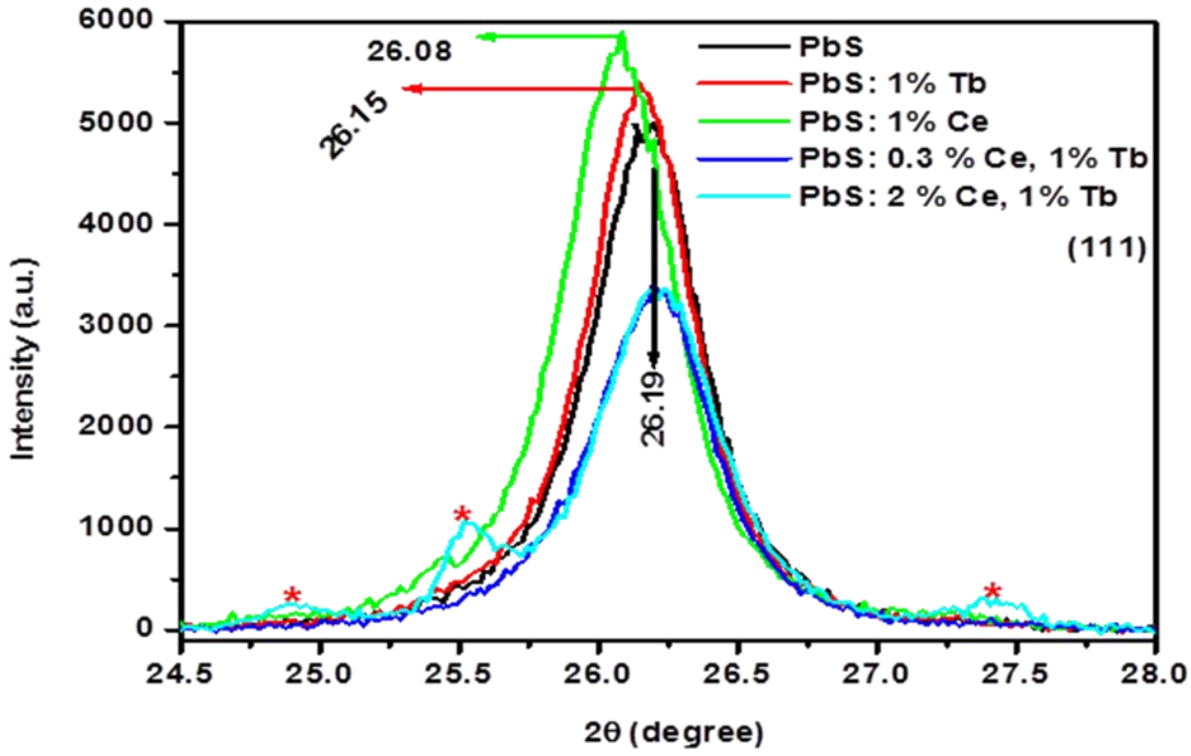

Figure 10.2: A representative of X-ray powder diffraction patterns at (111) for of undoped, Tb-doped, Ce-doped and Tb-Ce co-doped PbS nanoparticles prepared by the CBD method.

intensities increases signifying improvement in crystallinity with the addition of Tb and Ce content, respectively. This shift may indicating that the estimated lattice parameters are slightly larger than those of undoped PbS (the estimated experimental value of the cell constants are a = 5.9094, 5.9276Å and 5.9322 Å for 0 mol%, 1 mol% Tb^{3+} and 1 mol% of Ce^{3+}, respectively) **[14-16].** It was observed that the lattice parameters increase with an increase in the mol% of Tb^{3+} and Ce^{3+} ions. The increase in lattice parameters may be due to the lattice distortion as Tb^{3+} and Ce^{3+} ions occupy the Pb^{2+} lattice sites **[17]**. The co-doped samples show the diffraction peaks shift at slightly higher angle with significant decrease in intensity. The estimated lattice parameters are 5.9336 and 5.9414 Å for 0.3 and 2 mol% Ce^{3+} co-doped PbS, respectively.

The decreases in intensity of diffraction peaks indicate the loss of crystallinity due to lattice distortion **[18]**. When Ce^{3+} ions as a co-dopent are incorporated into the periodic crystal lattice of PbS, a strain is induced into the system, resulting in the alteration of the lattice periodicity and decrease in the crystal symmetry. The average grain size of the as-prepared nanocrystals can be calculated from the Full Width Half Maximum (FWHM) of the

diffraction peaks using the Debye formula **[19]**. All major diffraction peaks are chosen to estimate the average size of the nanocrystals by the least square method. The estimated grain size are 34 ± 2, 36 ± 2, 37 ± 2, 33 ± 1 and 32 ± 1 nm for undoped, 1 mol% Tb^{3+}-doped, 1 mol% Ce^{3+}-doped, 0.3mol% Ce: 1 mol% Tb co-doped and 2 mol% Ce: 1 mol% Tb co-doped PbS samples. It is clear that the estimated grain size increases for doped samples but decreases for Ce co-dopant when compared to undoped PbS.

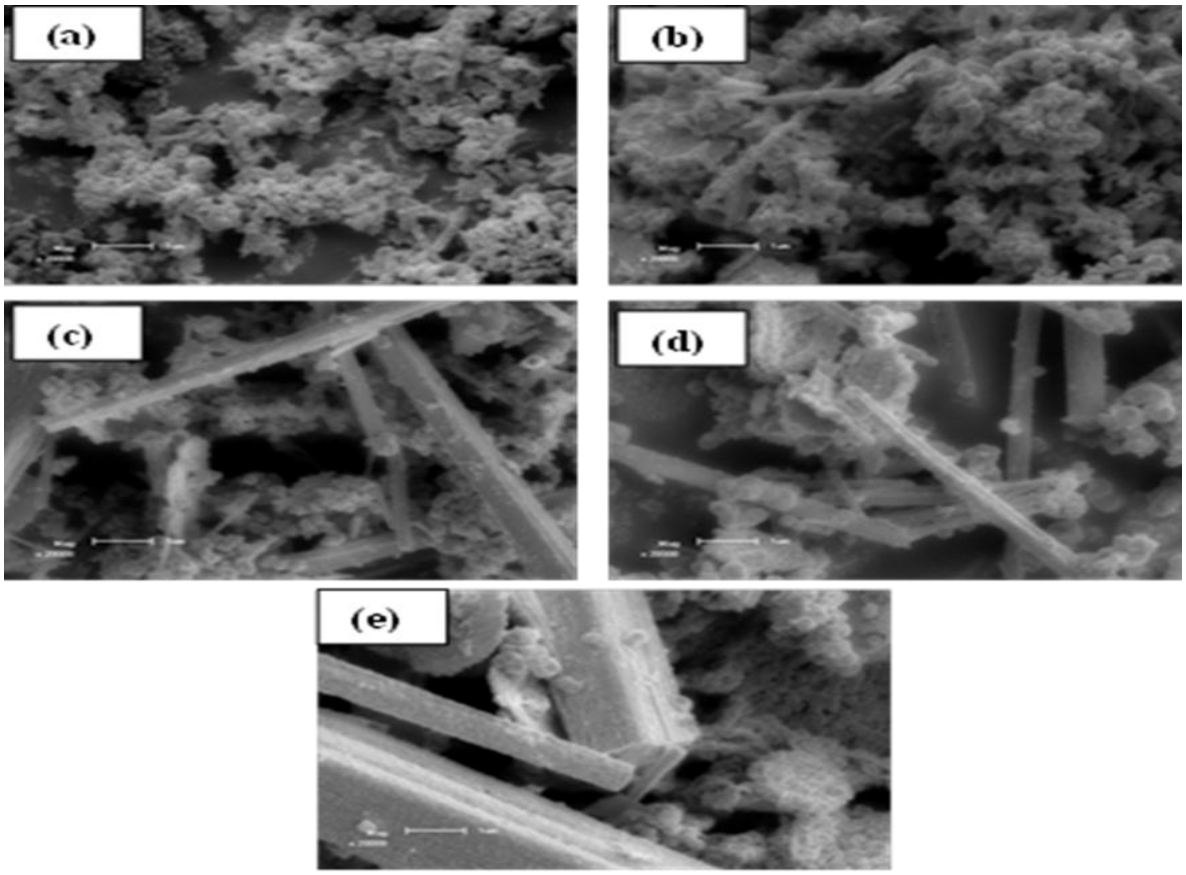

Figure 10.3: SEM images of (a) PbS, (b) PbS: 1 mol% Tb^{3+}, (c) PbS: 1 mol% Ce^{3+} (d) PbS: 1 mol% Tb^{3+}: 0.3 mol% Ce^{3+} and (e) PbS: 1 mol% Tb^{3+}: 2 mol% Ce^{3+} illustrating the effect of dopant and co-dopant molar concentrations on PbS.

Figure 10.3 (a), (b), (c) and (d) show SEM micrographs of the undoped, Tb^{3+}-doped, Ce^{3+}-doped and Ce^{3+} co-doped PbS nanostructures. The surface aspects of undoped PbS is composed of nearly spherical nanoparticles. It is clear that all nanostructures are clustered and non-homogeneous. When the PbS was doped with 1 mol% of Tb^{3+} or Ce^{3+}, the morphology changed to mixture of spherical nanoparticles and nanorods as shown in Figure 10.3 (b) and (c). By co-doping Tb^{3+}-doped PbS nanostructures with 0.3 mol% and 2 mol% Ce^{3+}, the spherical nanoparticles changed to the nanorods surrounded by the spherical

nanoparticle. It is clear that the nanorods size increases with an increase in the molar concentration of Ce^{3+} ions.

A representative TEM image of undoped PbS, Tb^{3+}-doped and Ce^{3+} co-doped PbS are displayed in Figure 10.4. The image shows that the undoped crystallites have almost agglomerated spherical (marked red arrows) morphology, with the average diameters of 40 ± 1 nm, which is consistent with the results calculated using Scerrer's formula. In the TEM images (PbS: 1 mol% Tb^{3+}: 2 mol% Ce^{3+}) in Figure 10.4(d), lattice fringes (marked with blue arrows) can be clearly observed, which indicate that the particles are crystalline.

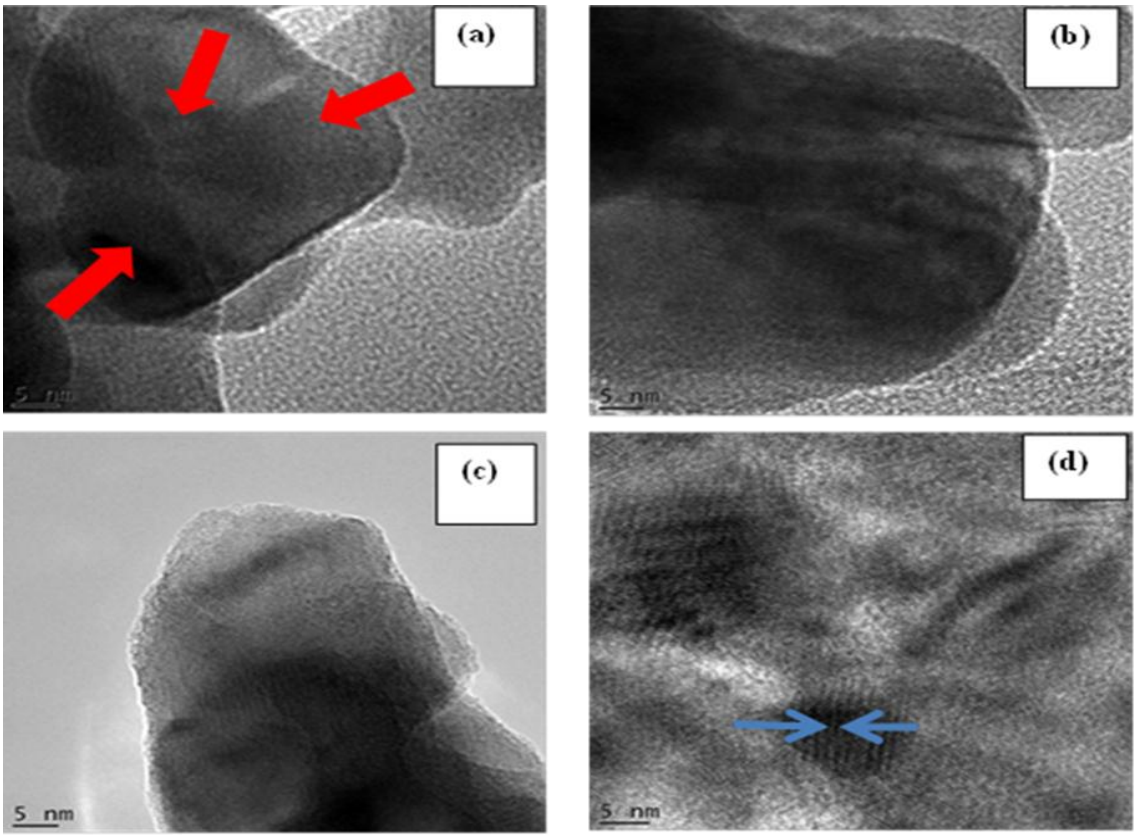

Figure 10.4: TEM images of (a) PbS, (b) PbS: 1 mol% Tb^{3+} (c) PbS: 1 mol% Tb^{3+}: 0.3 mol% Ce^{3+} and PbS: 1 mol% Tb^{3+}: 2 mol% Ce^{3+} illustrating the effect of dopant and co-dopant molar concentrations on PbS.

TEM-EDX spectrum of the nanostructures suggests the existence of Pb, S, Ce,Tb, O and C in addition to the copper signal from a TEM Cu grid (see Figure 10.5). From the spectra it is clear that the Tb and Ce became visible for the higher Tb doped concentration of PbS. No Ce^{3+} was measured for the lower (0.5 mol% Ce^{3+}) concentration of Tb doped. From spectra there is no clear evidence of S except for a small shoulder to the right of the Pb peak.

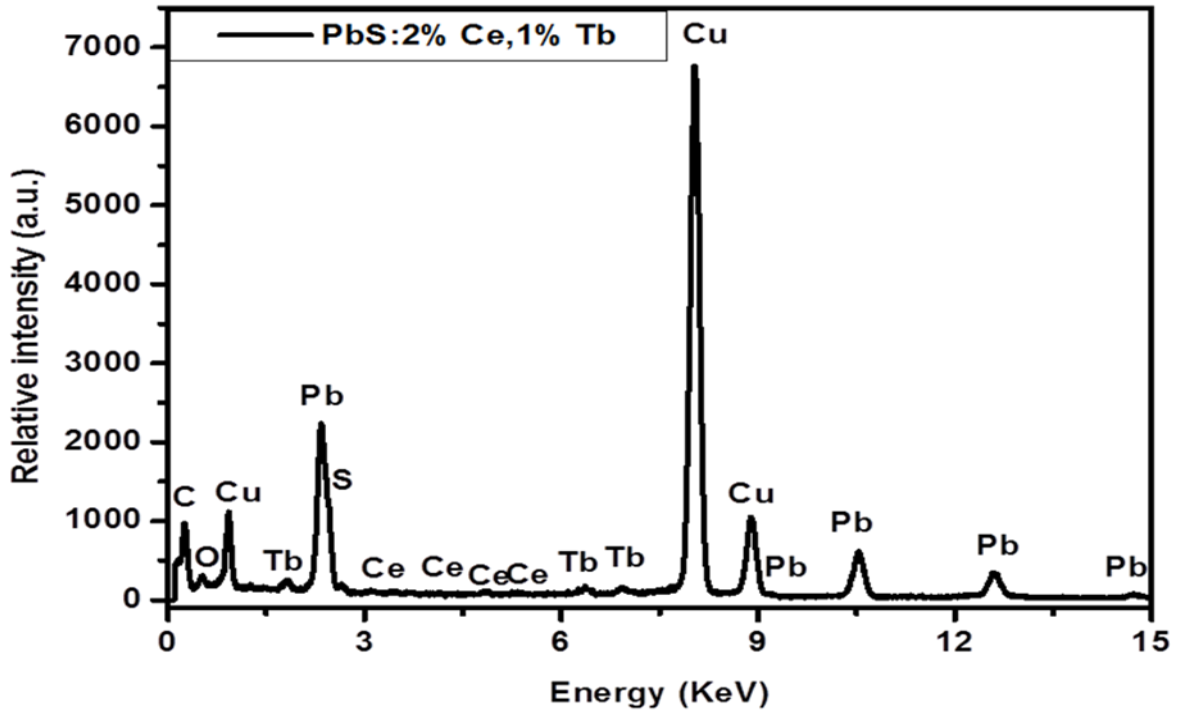

Figure 10.5: A representative EDX spectrum of the PbS: 1 mol% Tb^{3+}: 2 mol% Ce^{3+} doped PbS nanoparticles prepared by the CBD method.

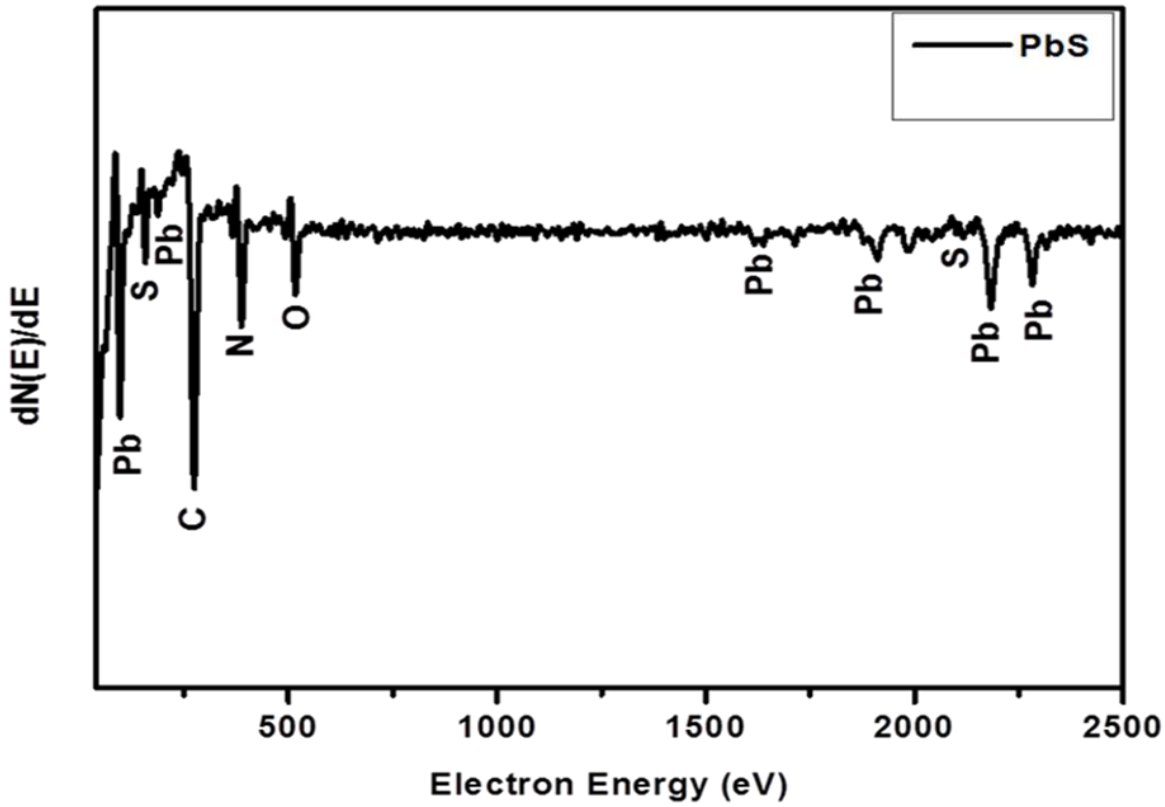

Figure 10.6: Auger spectra of the undoped PbS nanoparticles prepared by the CBD method.

Due to the overlapping between the Pb and the S signal in the EDX spectra, AES measurements were carried out to double check the elements and to evaluate their purity. The Auger spectrum of the undoped PbS nanoparticles is shown in Figure 10.6. The typical spectrum of the spherical nanoparticles confirms the presence of Pb and S. The signals at kinetic energies of 517, 387 and 276 eV are ascribed to the presence of adventitious O, N and C, respectively, which come from atmospheric adsorbed gases. Moreover, no other impurities were found on the surface of the PbS nanoparticles.

10.3 Optical properties

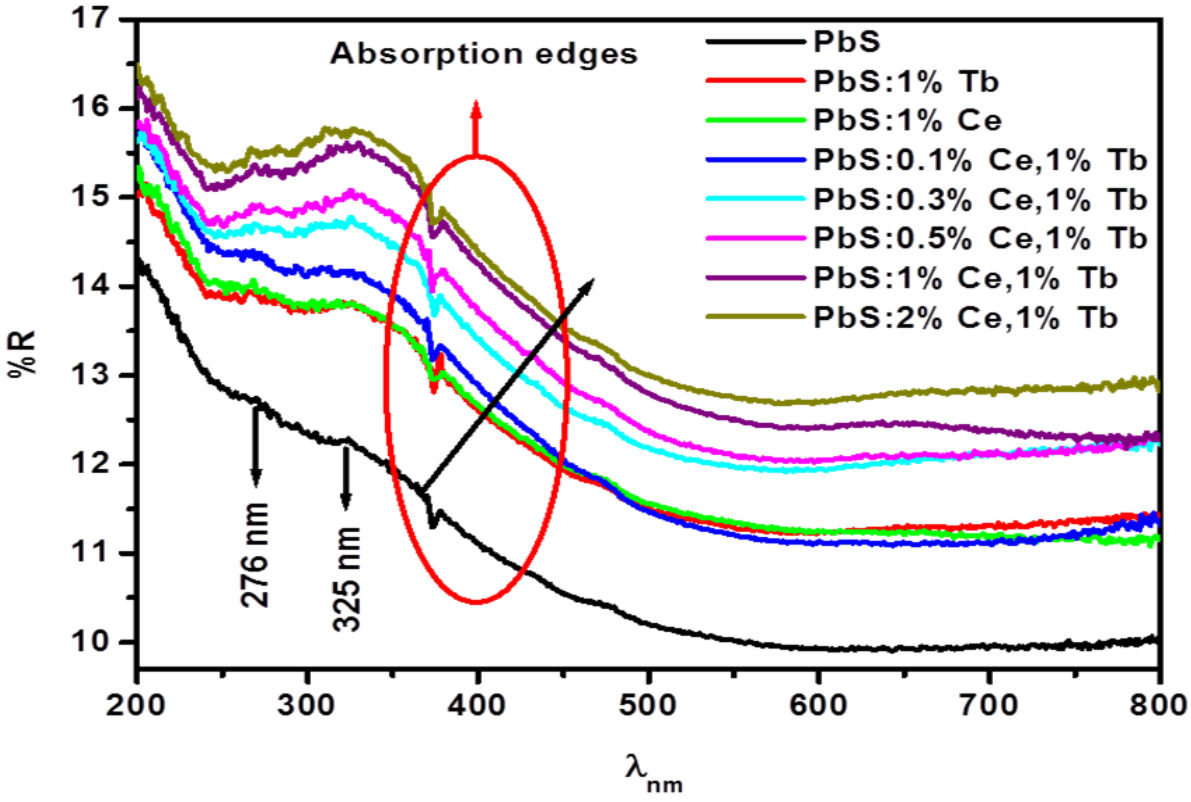

Figure 10.7: The reflectance spectra of of undoped, Tb-doped, Ce-doped and Tb-Ce co-doped PbS nanostructures at different molar concentrations of Ce acetate and holding Tb nitrate constant.

Figure 10.7 represents the diffuse reflectance (DR) spectra of the undoped, Tb^{3+}-doped, Ce^{3+}-doped and Tb^{3+}-Ce^{3+} co-doped PbS samples. It clearly indicates that as the molar concentration of Tb^{3+} dopant and Ce^{3+} co-dopant ions increases the optical absorption edges (the circled red part) by shifting to a higher wavelength while the total reflectance intensity increases. Although the percentage absorption changes, the absorption edge onset at around 580 nm did not change much. Again the inclusion of Tb and Ce as a dopant and Ce as co-

dopant improves the reflectance band at around 325 nm. The dependence of the absorption edges of the PbS: 1 mol% Tb^{3+}: x mol% Ce^{3+} where x is 0.1, 0.3, 0.5, 1 and 2 mol% of Ce^{3+} is illustrated in Figure 10.8. It can be seen clearly that the absorption edges of the PbS decay exponentially with the Ce content. Optical spectra of the undoped and Tb-doped PbS powders exhibit reflectance peaks at around 335 and 276 nm nm. The peaks are attributed to the electronic transitions between the split energy levels of PbS nanoparticles: $1s_h \rightarrow 1s_e$ and $1d_h \rightarrow 1d_e$, respectively **[20-22]**.

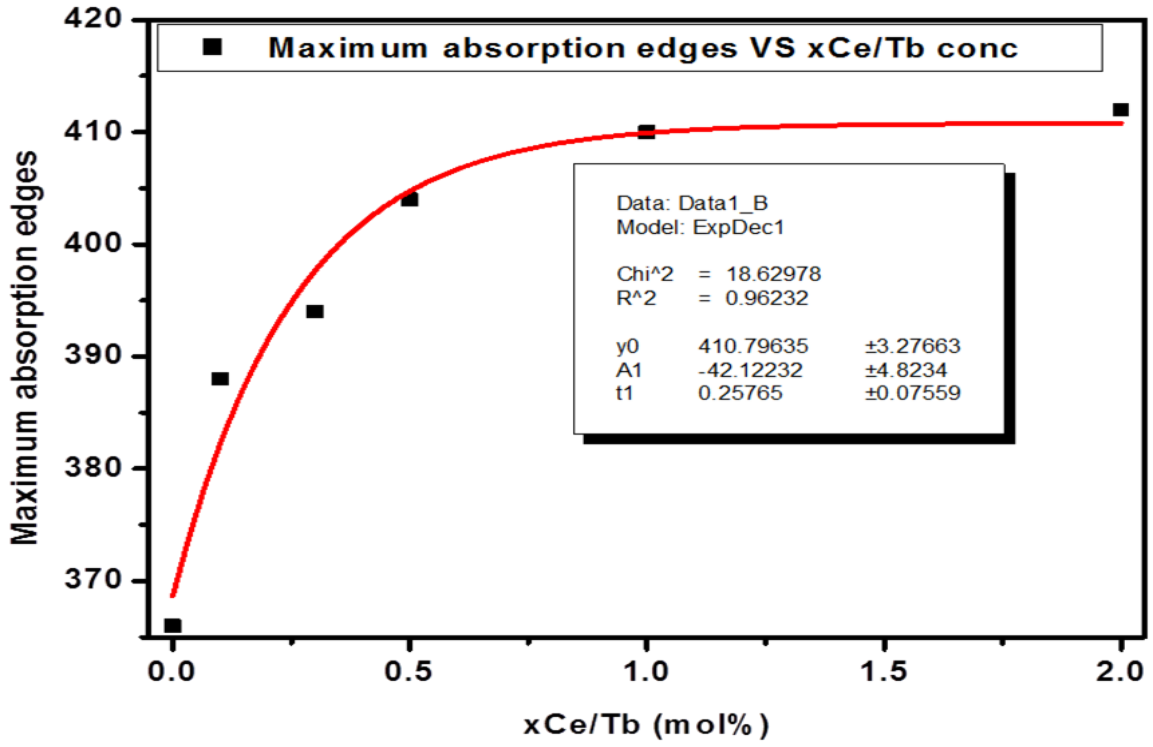

Figure 10.8: The dependence of maximum absorption edges of the PbS on the amount of Ce ion dopants.

Firstly the shift of the absorption band edges to higher wavelengths may be due to the increase in the carrier concentration by the inclusion of dopants and co-dopant ions and creation of defect levels in the band gap. This can be attributed to an increase in the doping and co-doping concentration, which may induce the lattice disorder in the nanocrystals **[16, 23, and 24]**.

10.4 Photoluminescence

The PL emission spectra of the samples when excited at 276 nm are shown in Figure 10.9. The excitation wavelength which correspond to the $1d_h \rightarrow 1d_e$ transition of PbS was confirmed

by UV analysis. Deconvolution of the undoped PbS emission spectra reveals two bands in the visible region. The bands are associated with the electronic transitions from the $1p_e \rightarrow 1p_h$ (338 nm) and $1s_e \rightarrow 1p_h$ (376 nm) energy levels **[20]**. The emissions in the UV region (338 and 376 nm) arise from the recombination of excitons and/or shallowly trapped electron-hole pairs **[18, 25, 26]**. The PL peak at around 433 nm is usually related to the transition of electrons from conduction band edge to holes, trapped at interstitial Pb^{2+} sites **[20-22].** An extra PL emission is observed in the infrared region (with inset), with a maximum of broad emission at 725 nm and a shoulder at 825 nm.

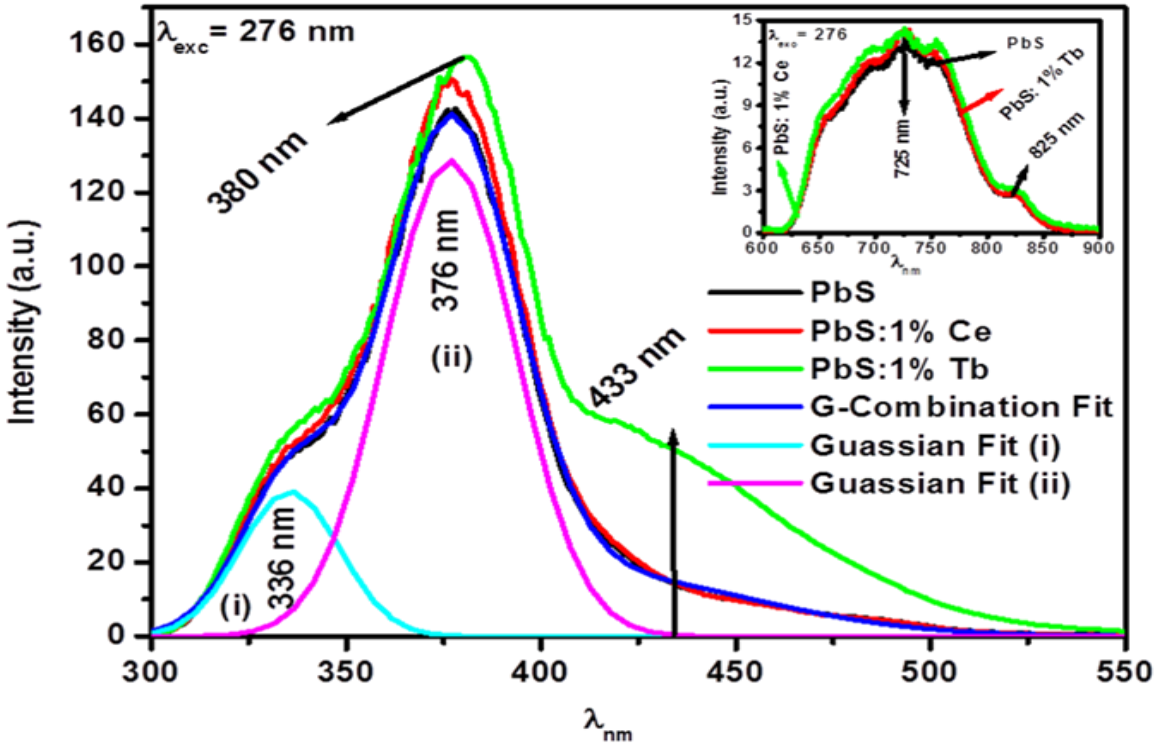

Figure 10.9: PL spectra of of undoped, Tb-doped and Ce-doped PbS nanostructures showing visible and with the inset IR (as an inset) emissions prepared by the CBD method and with the deconvolution of the luminescence spectra taken from undoped PbS.

These emissions are due to deep level defects. In Figure 10.9, firstly, it was observed that the emission bands of the Tb^{3+}-doped and Ce^{3+}-doped PbS at around 336, and 726 nm did not change, only the emission band of undoped PbS shifted to 380 nm with the addition of Tb^{3+} content. This shift may be due to non-homogeneous morphology as confirmed by SEM analysis. Secondly, the presence of Tb^{3+} and Ce^{3+} ions, respectively, enhances the luminescence intensity in the UV and IR region slightly. The maximum luminescence

intensity was found at PbS: 1 mol% Tb^{3+}. The luminescence band at around 433 nm attributed to lattice defects emerges with an addition in Tb^{3+} content. An enhancement in luminescence intensity implies that there is a possibility of dopants (Ce^{3+} and Tb^{3+}) transferring energy to the host (PbS). Figure 10.10 and 10.11 shows the PL emission spectra of undoped, Tb-doped and Ce co-doped PbS nanostructures excited at 276 nm, respectively. From both spectra's it is clear that the highest luminescence intensity is obtained at PbS:1 mol%Tb^{3+}: 0.1mol% Ce^{3+} for the luminescence bands at around 337, 376 and 726 nm. The effects of Ce^{3+} ions concentrations on Tb-doped PbS nanostructures for the maximum peaks intensities of the emissions are clear in Figure 10.12.

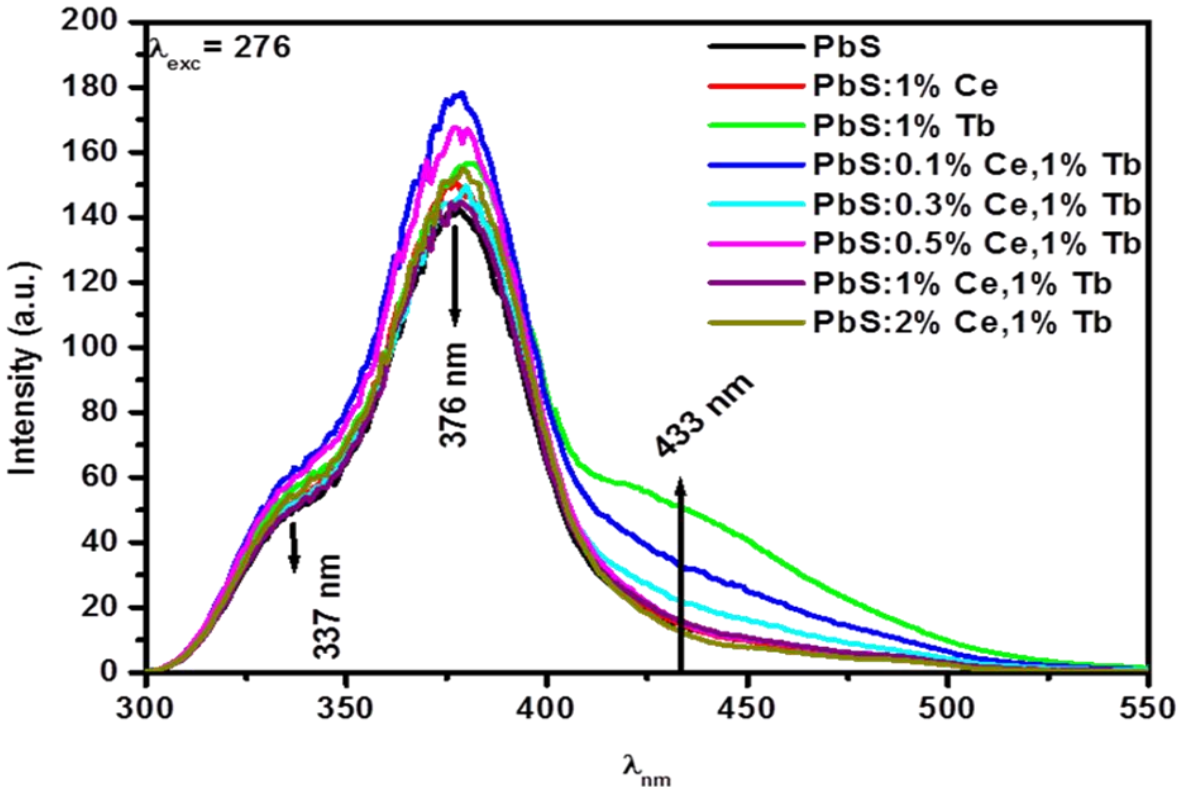

Figure 10.10: PL emission spectra for undoped, Tb-doped, Ce-doped and Tb-Ce co-doped PbS nanostructures at different molar concentrations of Ce acetate and holding Tb nitrate constant excited at wavelength of 276 nm using Xenon lamp.

The emission intensity for the luminescence bands at around 338, 376 and 725 nm increases with increasing Tb dopant concentration up to 0.1 mol% Tb and then it decreases thereafter as shown in Figure 10.13. It was observed that as the molar concentration of co-dopant (Ce^{3+}) increases the luminescence band at around 433 nm diminishes. This decrease may be due to Ce^{3+} decreasing the defects of Pb^{2+}. The increases in luminous intensity up to ratio of 1:10

Ce:Tb may be due to the different in valences between Ce^{3+} and Pb^{2+} which produced defects, because of charge compensation requirements, resulting in change of energy transfer with the presence of the Ce^{3+} ions. The excitation energy was absorbed by Ce^{3+} ions (donor) and transferred non-radiatively to the PbS nanoparticles (acceptor). This implies that there is a possibility of co-dopant (Ce^{3+}) transferring energy to the host (PbS) just like in ZnO-SiO_2:Ce system, in which ZnO transfer energy to SiO_2:Ce **[27]**.

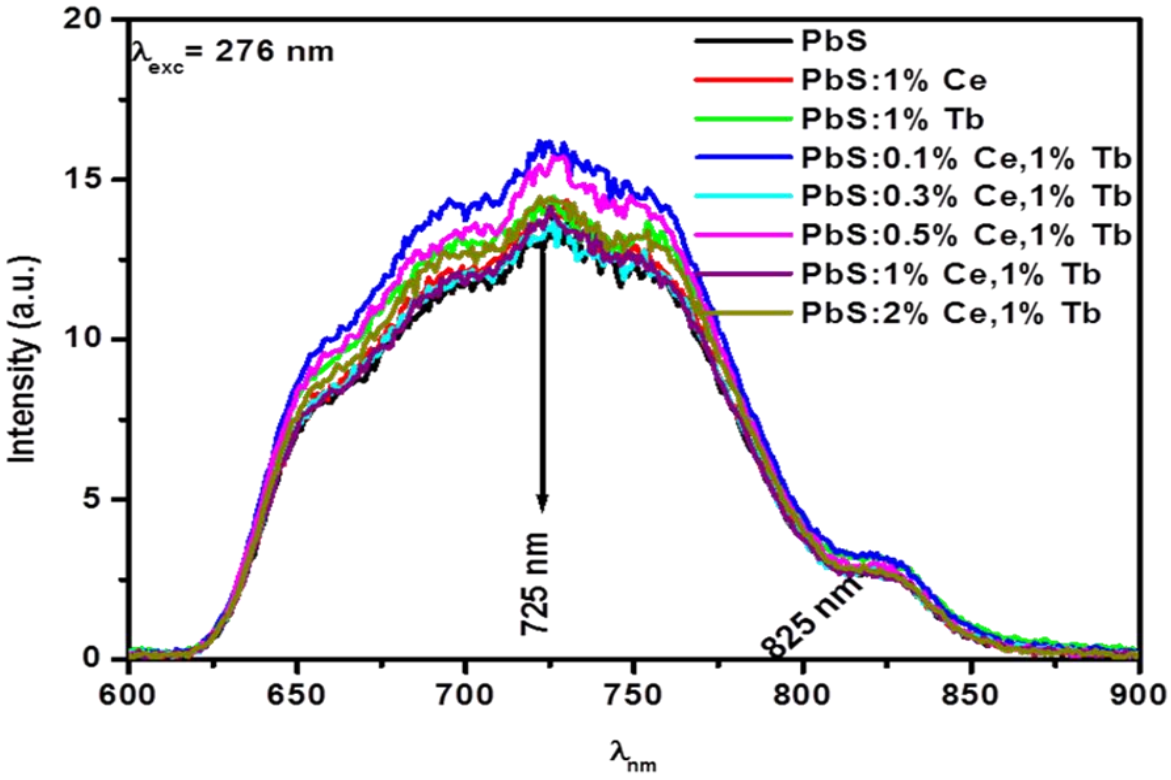

Figure 10.11: PL emission spectra for of undoped, Tb-doped, Ce-doped and Tb-Ce co-doped PbS nanostructures at different molar concentrations of Ce acetate and holding Tb nitrate constant showing emissions in the IR region.

A further increase in the Tb^{3+} ions above PbS:1 Mol% Tb^{3+}: 0.1 mol% Ce^{3+} resulted in luminescence quenching. The decrease in luminescence intensity might be due to a slightly increase in the nanorods sizes with an increase in the Ce^{3+} ion molar concentration, as confirmed by the SEM analysis. It is well understood that the non-radiative recombination increased with increasing particle size which resulted in the luminescence intensity decrease **[28, 29].** The luminescence quenching might also be due to the Ce^{3+} ions either tending to locate on the crystal surface, causing an undesired Ce^{3+}-Ce^{3+} interaction, or forming cerium acetates aggregates, which act as a quenching site, resulting in a drastic decrease in the luminescent intensity **[26]**.

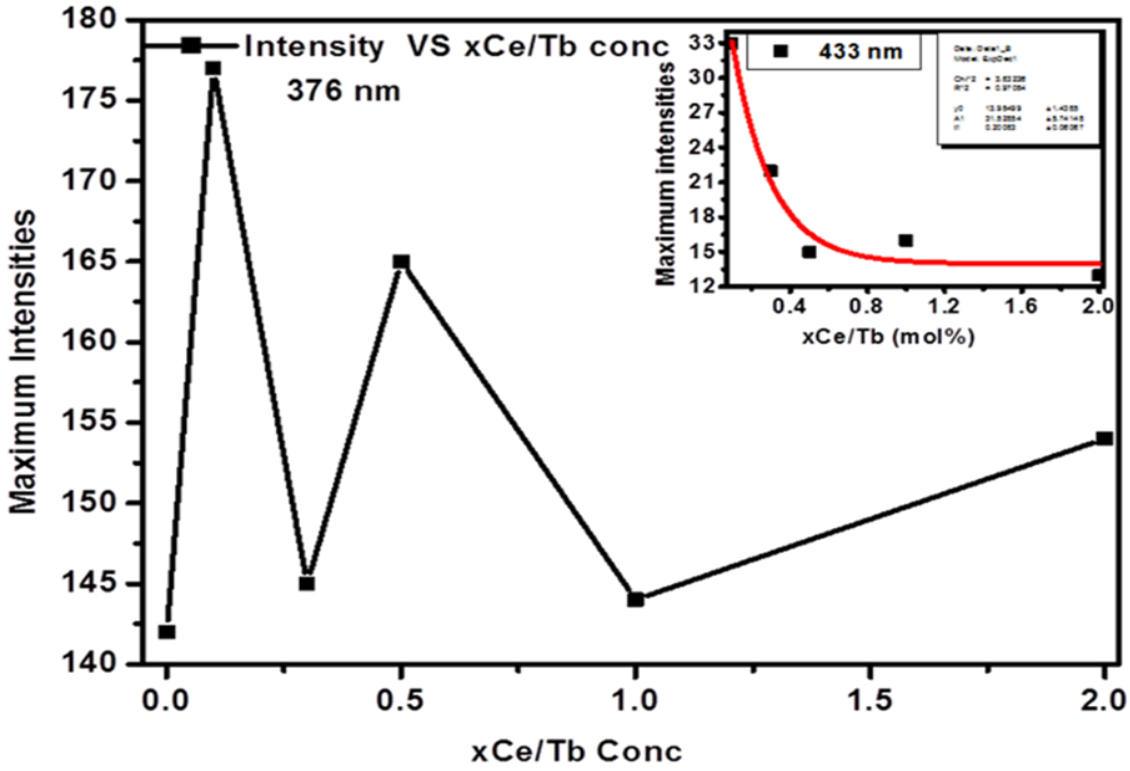

Figure 10.12: Maximum PL intensity of PbS nanoparticles at 376 nm and 433 nm (inset) prepared by the CBD method as function of Xmol% Ce/Tb (1 mol%).

References

[1]. W. C. W. Chan, S. Nie, *Scie*, **281 (**1998) 2016-2018.

[2]. H. Q. Cao, Y. Xu, J. M. Hong, H. B. Liu, G. Yin, B. L. Li, C. Y. Tie, Z. Xu, *Advanc. Mater*, **13 (**2001) 1393-1394.

[3]. A. L. Rogach, A. Eychmuller, S. G. Hickey, S. V. Kershaw, *Small*, **3(4)** (2007) 536-557.

[4]. D. M. N. M. Dissanayake, R. A. Hatton, T. Lutz, C. E. Giusca, R. J. Curry, and S. R. P. Silva, *App. Phys. Lett*, **91 (**2007) 133506:1-133506:3.

[5]. B. R. Hyun, H. Chen, D. A. Rey, F. W. Wise, C. A. Batt, *J. Phys. Chem B*, **111 (20)** (2007) 5726-5730.

[6]. V. Popescu, D. Raducanu, C. L. Popescu, *Chalcogenide. Lett.* **9(5)** (2012) 175-183.

[7]. Z. Wang, B. Zhao, F. Zhang, W. Mao, G. Qian, X. Fan, *Mater. Lett*, **61 (**2007) 3733-3735.

[8]. J. Zhu, S. Liu, O. Palchik, Y. Koltypin, A. Gedanken, *J. Solid. State. Chem*, **153 (**2000) 342-348.

[9]. Y. Yang, S. Xue, S. Liu, J. Huang, J. Shen, *App. Phys. Lett*, **69(3)** (1996) 377-378.

[10]. C. R. Kagan, C. B. Murray, M. Nirmal, M. G. Bawendi, *Phys. Rev. Lett*, **76 (**1996) 1517-1520.

[11]. Y. Wang, N. J. Herron, *J. Phys. Chem*, **91(2)** (1987) 257-260.

[12]. S. B. Qadri, J. Yang, B. R. Ratna, E. F. Skelton, J. Z. Hu, *App. Phys. Lett*, **69 (**1996) 2205-2207.

[13]. S. Sadhu, P. Saha Chowdhury, A. Patra, *J. Lumin*, **126 (**2007) 387-392.

[14]. J. Lang, Q. Han, J. Yang, C. Li, X. Li, L. Yang, Y. Zhang, M. Gao, D. Wang, J. Cao, *J. App. Phys*, **107 (**2010) 074302:1-074302:4.

[15]. P. P. Partha, J. Manam, *Nanosystems: Phys. Chem. Mathem*, **4(3)** (2013) 395-404.

[16]. L. Saravanan, A .Pandurangan, R. Jayavel, *J. Nanopa. Research*, **13 (**2011) 1621-1628.

[17]. S. N. Sahu, K. K. Nanda, *PINSA*, **67A (1)** (2001) 103-130.

[18]. M. Pal, U. Pal, J. M. G. Y. Jiménez, F. Pérez-Rodriguez, *Nano. Research. Lett*, **7 (**2012) 1-12.

[19]. B. D. Cullity, *Elements of X-ray Diffraction*, second ed, Addison Wesley, 1978. 284-285.

[20]. X. Ai, L. Guo, Y. Zou, Q. Li, H. Zhu, *Mater. Lett*, **38 (**1999) 131-135.

[21]. K. S. Babu, C. Vijayan, P. Haridoss, *Mater. Scie. Engin C*, **27 (**2007) 922-927.

[22]. S. Lu, U. Sohling, T. Krajewski, M. Menning, H. Schmidt, *J. Mater. Scie. Lett*, **17 (**1998) 2071-2073.

[23]. M. Saleem, L. Fang, H. B. Ruan, F. Wu, Q. L. Huang, C. L. Xu, C. Y. Kong, *Intern. J. Phys. Scie*, 2012, **7(23)**: 2971-2979.

[24]. A. Douayar, P. Prieto, G. Schmerber, K. Nouneh, R. Diaz, I. Chaki, S. Colis, A. El Fakir, N. Hassanain,A. Belayachi, Z. Sekkat, A. Slaoui, A. Dinia, and M. Abd-Lefdil, *Eur. Phys. J. Appl. Phys.* **61** (2013) 10304:1-10304:5.

[25]. M. Cheraghizade, R. Yousefi, F. Jamali-Sheini, A. Sa'aedi, *J. Telecomm. Devices*, **1(3)** (2012) 79-82.

[26]. M. Navaneethan, K. D. Nisha, S. Ponnusamy, C. Muthamizhchelvan, *Rev. Advan. Mater. Scie*, **21 (**2009) 217-224.

[27]. L. F. Koao, F. B. Dejene, H. C. Swart, J. R. Botha, *J. Lumin*, **143 (**2013) 463-468.

[28]. S. Kaci, A. Keffous, L. Guerbous, M. Trari, *Thin. Solid. Film*, **520 (**2011) 79-82.

[29]. J. Lang, Q. Han, J. Yang, C. Li, X. Li, L. Yang, Y. Zhang, M. Gao, D. Wang, J. Cao, *J. App. Phys*, **107 (**2010) 074302:1-074302:4.

Chapter 11

Conclusion and Future work

Conclusions

The CBD process is a promising industrial process to produce large area semiconductors for applications in solar cell and electronic devices. The CBD which is designed in the present work is an accurate method that can be used to prepare stoichiometric semiconducting nanopowders. The aim of the present work was to synthesis undoped and doped ZnO (PbS) semiconducting nanostructures using CBD method by varying the growth parameters (synthesis temperature, synthesis time, precursors concentration, etc.) and to study the effect of the rare earth (Ce^{3+}, Tb^{3+} and Eu^{3+}) and transition metal (Cu^{2+}) doping on the material properties of the semiconducting nanostructures. The important conclusions drawn from the present investigation are given as below:

- ZnO nanostructures are found to have a hexagonal crystal structure with the diffraction peaks coming from (100), (002), (101), (102), (110), (112) and (201) planes. An increase in the synthesis time and the zinc acetate molar concentration in of the precursor results in to more intense and sharp diffraction peaks, showing an increase in the crystallinity.

- The mean calculated crystallite size of the ZnO nanoparticles was in the order of 45 ± 1 nm which is slightly larger than the Bohr`s exciton radius for ZnO, 7 nm. Moreover, the grain size increased with an increase in synthesis time and the zinc acetate molar concentration in the precursors.

- SEM observations of ZnO particles showed the presence of microcrystallites forming microflower-like aggregates. The use of higher molar concentration of zinc acetate in the precursor results in large sized particles without any change in shape.

- Energy dispersive X-ray (EDS) analysis showed all expected elements. It was observed that the Zn and O increased with an increase in the amount of zinc acetate.

- In the measurements of the optical properties it was found that the reflectance spectra depict a red shift of the absorption edge and the band gap energies of ZnO

nanostructures decreased with an increase in the molar concentration of zinc acetate and the synthesizing time.

- In PL results the maximum luminescence intensity was reached at the ZnO synthesized for 5 minutes, any further increase in the synthesizing time resulted into the luminescence intensity decrease. An increase in zinc acetate mol% in the precursor resulted only in a decrease in luminescence intensity.

- The XRD spectra of the ZnO:Ce^{3+} (Eu^{3+} and Cu^{2+}) nanostructures correspond to the various planes of a single hexagonal ZnO phase for the lower Ce (Eu and Cu) concentration samples. At high dopant concentration, the powders were no longer single phase. The estimated grain sizes calculated using the XRD spectra were found to be in order of 42 ± 2, 47 ± 5 and 46 ± 1 nm for ZnO samples doped with Ce, Eu and Cu, respectively. The estimated grain size is independent on the Ce and Eu ion doping concentration up to 3 and 4 mol%. The estimated grain size of the Cu doped samples was found not to dependent on the concentration of the Cu used at all.

- SEM micrographs indicate that the addition of Ce, Eu and Cu influence the morphology of the samples. The flower-like structures obtained for the undoped and low concentration Ce and Eu doped ZnO changed into a mixed structure with the emergence of pyramid and block shapes for higher concentration Ce and Eu doped samples. With the incorporation of the Cu^{2+} ions into the ZnO, the flower-like structure changed to a mixed structure with the emergence of irregular shapes. When the Cu concentration was increased to 2 mol%, the morphology of the ZnO:Cu has totally changed to clustered irregular shapes with small quantities of other material attached to the main structures.

- AES spectrum of the undoped and Ce^{3+}-doped ZnO of the nano flowers confirms the presence of Zn and O. The Ce peaks were clearly visible for the low mol% samples as indicated by the example of the ZnO:0.5 mol % Ce^{3+} sample. A high concentration of Ce was detected on the material adsorbed on the surface of the ZnO:10 mol % Ce^{3+} sample. The Zn concentration was relatively very low compared to the bulk sample. Moreover, no other impurities were found on the surface of the ZnO, suggesting that

the as-synthesized ZnO are relatively pure with agglomerated Ce enrich adsorbed material on the surface thereof.

- UV-vis spectroscopy showed that as the molar concentration of Ce^{3+} and Eu^{3+} ions increased the optical absorption edge shifted to a higher wavelength while band gap energy of the doped ZnO decreased with an increase in the concentration of Ce and Eu. In Cu-doped samples no effects on the absorption edges with increasing the molar concentration of Cu, was observed. The highest band gap energy was obtained for undoped ZnO with its estimated band gap energy of 3.26 ± 0.12 eV. Optical properties show a significant change in band gap value on doping.

- PL showed that the undoped and low concentration Ce doped ZnO flower-like rods exhibited a green emission, peaking at about 559 nm. The higher Ce concentration (0.3 mol % and above) emitted at 436 and 503 nm due to the Ce transitions. The intensity of these emission spectra of the ZnO:Ce^{3+} decreased with the addition of more Ce^{3+} ions.

- The PL spectrum for undoped ZnO nanostructures is broad and asymmetric, whereas on doping the nanoparticles with Eu ions, the spectra have become sharp. This shows that the Eu doping has removed the number of surface defects leading to radiative transitions. The PL intensity was found to be a maximum for ZnO:3 mol% Eu^{3+} with excitation wavelengths of 300 and 395 nm. The best excitation wavelength was found to be 395 nm giving the highest Eu^{3+} luminescence intensity without any noticeable ZnO defect emissions. The PL analyses for Cu doped samples revealed that the highest luminescence intensity was obtained for the undoped ZnO.

- The XRD spectra of the PbS showed a cubic structure for all samples grown with variation in synthesis temperature and lead acetate content, with the diffraction peaks coming from (111), (200), (220), (311) and (222) ZnO surfaces. Extra peaks were observed for PbS powders prepared at low synthesis temperature (55 ºC) which are due to unreacted lead acetate oxide hydrate. However, as the bath temperature was increased from 65 to 80 ºC the extra peaks disappear. It was found that the estimated average size increased slightly with an increase in the synthesis temperature. The

improved intensity with well-defined sharper peaks indicates a higher crystallinity of the prepared material.

- For the PbS samples synthesized by varying the molar concentration of lead acetate in the precursor it was observed that the best crystallite structure was obtained for PbS samples synthesized at 0.13 M of lead acetate. The estimated grain sizes were 30 ± 1, 35 ± 1 and 31 ± 1 nm for 0.12, 0.13 and 0.14 mol% of lead acetate, respectively. No clear trend in the estimated crystallite sizes was observed in this case. The estimated grain sizes are of the order of the Bohr`s exciton radius for PbS, 18 nm, which shows that the synthesized nanoparticles are in quantum confinement regime.

- The surface aspects of the SEM images of the PbS powders were composed of uniform nanorods structures for the synthesis temperature of 55 to 70 ºC, however, the nanorods size increased slightly with an increase in the synthesis temperature. With a further increase in the synthesis temperature to 80 ºC, the nanorods structure broke up in mixed structures with the emergence of spherical nanoparticle and plate-like shapes. It was also observed that an increase in the molar concentration of lead acetate has no significant influence on the morphology of the PbS nanorods and the crystallite sizes.

- The reflectance spectra showed a partially shift of the absorption edge to a higher wavelength with an increase in the synthesis temperature and molar concentration of Pb acetate in the precursor. An additional absorption band in the visible region (647 nm) emerged with an increase in the synthesis temperature.

- The maximum luminescence intensity was obtained for samples synthesized at 55 ºC and at a 0.12M of Pb acetate concentration and further increase in synthesis temperature resulted into luminescence quenching.

- The XRD spectra of the undoped, Tb-doped and Ce co-doped nanostructures correspond to the single cubic phase PbS for the lower and higher dopants and co-dopants. When Ce^{3+} co-doped is higher than 1 mol% the additional peaks appear which are associated with the Ce acetate. The estimated grain size are 34 ± 2, 36 ± 2, 37 ± 2, 33 ± 1 and 32 ± 1 nm for undoped, 1 mol% Tb^{3+}-doped, 1 mol% Ce^{3+}-doped,

0.3 mol% Ce: 1 mol% Tb co-doped and 2 mol% Ce: 1 mol% Tb co-doped PbS samples. It was observed that the estimated grain size increases for doped PbS samples but decreases for Ce co-dopant when compared to undoped PbS.

- SEM micrographs of undoped PbS depict spherical nanoparticles while Tb^{3+}-doped PbS samples displayed mixed spherical and rod-like nanostructures. By Ce co-doping PbS nanostructures the spherical nanoparticles changed to the nanorods surrounded by the spherical nanoparticle. It was observed that the nanorods size increases with an increase in the molar concentration of Ce^{3+} ions.

- UV-vis showed that the absorption edged of undoped PbS shifted to the higher wavelength with addition of dopants and co-dopant.

- At a Tb^{3+} concentration of 0.3 mol%, the PL intensity was found to be a maximum. Above that Tb^{3+} concentration, the luminescence intensity at 376 nm decreased due to the concentration quenching but the 433 nm intensity increased. The photoluminescence results displayed an optimum luminescence intensity when the ratio of Ce:Tb was 1:10 and further increase in cerium content quenched the luminous intensity.

Future Work

- Research should be done on comparison of material properties of the samples synthesized using various other methods.
- In this study the samples were annealed at ambient conditions only. Further work can include the annealing of samples at higher temperatures and in different enviroment (e.g. Nitrogen, oxygen and hydrogen). Studies can include an investigation to see at what temperature the modified ZnO is converted into hexagonal ZnO.
- Absorption and photoluminescence were only measured for powder samples. Further studies can be done on samples that are still in solution before and after washing of the impurities to see if washing and drying of the samples will affect the structure, morphology, optical and luminescence properties.
- It is reported that the band gap of materials will increase with decrease in particle size. This blue shift in the band gap is due to quantum confinement effects. A study can be conducted to see what effect of various morphologies can have on quantum confinement or band gap increase.
- It would be ideal to prepare a phosphor semiconductor that can emit from 400 nm to 600 nm. This can be achieved by using various dopants. By co-doping semiconductor nanostructures with Al, Mg, Cl, Au, Mn, Cd, and Cu different emission peaks may be obtained ranging from 400 nm to 600 nm. By doing this a phosphor can be created that is emitting in blue, green and red region resulting in a white light.
- Since the surface morphology of most of our samples appear agglomerated. A study could be done on effects of surfactants (e.g. PVP, PVA).

Appendix A

Publications

- F. V. Molefe, **L. F. Koao**, J. J. Dolo, and B. F. Dejene, Effect of synthesizing time on structural, morphological and optical properties of ZnO nanoflakes prepared by chemical bath deposition method. Physica B 439 (2014) 185-188.

- **L. F. Koao**, F. B. Dejene, H. C. Swart, Synthesis of PbS nanostructures by chemical bath deposition method. Int. J. Electrochem. Sci. 9 (2014) 1747-1757.

- **L. F. Koao**, F. B. Dejene, and H.C. Swart, The effect of Cu^{2+} on structure, morphology and optical properties of flower-like ZnO synthesized using the chemical bath deposition method. Physica B 439 (2014) 173-179.

- **L.F. Koao**, F. B. Dejene, H.C. Swart and R.E. Kroon, Effect of Eu^{3+} on structure, morphology and optical properties of flower-like ZnO synthesized using the chemical bath method. J. of Lumin 147 (2014) 85-89.
- **L. F. Koao**, F. B. Dejene, H.C. Swart and J.R. Botha, The effect of Ce^{3+} on structure, morphology and optical properties of flower-like ZnO synthesized using the chemical bath method. J. of Lumin 143 (2013) 463-468.
- R. E. Kroon, H. A. A. Seed Ahmed, O. M. Ntwaeaborwa, **L. F. Koao**, I. M. Nagpure, M. A. Gusowski, J. R. Botha and H. C. Swart, Luminescence from Ce in sol-gel SiO_2, Physica B, Condensed matter: **407** (2012) 1595–1598.1.
- O. Onani, P. Mushonga, **L. F. Koao** and F. B. Dejene, Luminescence properties of Eu, Mg co-doped sol–gel SiO_2 glasses, Nanotechnology (2012), Article ID 298698, page 5.
- **L. F. Koao**, H .C. Swart, R. I. Obed, F. B. Dejene, Synthesis and Characterization of Ce^{3+} doped SiO_2 nanoparticles, J. of Lumin **131** (2011) 1249–1254**.**

- **L. F. Koao**, F. B. Dejene, H. C. Swart, SAIP'2011 Proceedings, the 56th Annual Conference of the South African Institute of Physics, edited by I. Basson and A.E. Botha (University of South Africa, Pretoria), ISBN: 978-1-86888-688-3 (2011) 151-155.
- **L. F. Koao**, H. C. Swart and F. B. Dejene, Synthesis and characterization of PbS nanostructures using the chemical bath deposition method, S.A. Institude of Physics 2011. ISBN: 978-1-86888-688-3.
- **L. F. Koao**, H. C. Swart, and F. B. Dejene, The effects of the Al^{3+} ions on the photoluminescence intensity and wavelength of Ce^{3+} with SiO_2, J. of Rare Earth Elements accepted **28** (2010) 206-210.
- **L. F. Koao**, H. C. Swart, E. Coetsee, M. M. Biggs and F. B. Dejene, The effect of Mg^{2+} ions on the Photoluminescence of Ce^{3+} doped SiO_2, Physica B **404** (2009) 4499–4503.

Submitted papers

- T. M. Sithole, B. F. Dejene, **L. F. Koao**, Synthesis and Characterization of SrB6O10:Eu^{2+} nano-phosphors Prepared Using Solution - Combustion Method. Submitted physica B.

- **L. F. Koao**, H. C. Swart and F. B. Dejene, Synthesis and characterization of ZnO flower-like microstructures using the chemical bath deposition method. Submitted Material Science in Semiconductor Processing.

- **L. F. Koao**, F. B. Dejene and H.C. Swart, Effect of terbium molar concentration on optical properties of lead sulphide nanoparticles. Submitted to Rare Earth.

- **L. F. Koao**, F. B. Dejene and H.C. Swart, Optical properties of Ce^{3+} co-doped PbS:Tb^{3+} nanoparticles synthesized using chemical bath. Submitted to Rare Earth.

- **L. F. Koao**, F. B. Dejene and H. C. Swart, Effect of synthesis temperature on the structure, morphology and optical properties of PbS nanostructures prepared by chemical bath deposition method. Submitted at SAIP at UKZN July 2013.

- F. B. Dejene and **L.F. Koao**, Energy transfer and photoluminescence properties of Ce^{3+} or/ and Tb^{3+}-doped PbS nanorods. Submitted at SAIP at UKZN July 2013.

- F. V. Molefe, **L. F. Koao,** J. J. Dolo**,** B. F. Dejene, Structural and luminescent properties of ZnO flake-like nanostructures synthesized using the chemical bath deposition method. Submitted at SAIP at UKZN July 2013.

- T. M. Sithole, B. F. Dejene, **L. F. Koao**, Synthesis and Characterization of $CaB_4O_7:Eu^{3+}$ nano-phosphors Prepared Using Solution - Combustion Method. Submitted at SAIP at UKZN July 2013.

In preparation papers

- **L. F. Koao**, H. C. Swart and F. B. Dejene, Structural and luminescent properties of ZnO flower-like microstructures synthesized using the chemical bath deposition method. In preparation.
- **L. F. Koao**, H. C. Swart and F. B. Dejene, Synthesis and characterization of MnO nanostructures using the chemical bath deposition method. In preparation.
- F. B. Dejene, S. V. Motloung, **L. F. Koao**, K. E. Foka, T. L. Lotha, M. A. Tshabalala, A. G. Ali, A. H. Wako, J. J. Dolo and H. C. Swart, Solution-combution synthesis and photoluminescence property of $(Gd,Y)BO_3:Tb^{3+}$ phosphor powders. In preparation.
- T. M. Sithole, B. F. Dejene, **L. F. Koao**, Synthesis and characterization of BaB_8BO_{13}:Eu nanophosphors prepared using solution-combution method. In preparation.
- T. L. Lotha, B. F. Dejene, **L. F. Koao**, Morphological, structural and photoluminescence properties of sol-gel synthesized strontium titanate ($SrTiO_3$:Pr:Al) nanophophors. In preparation.
- F. B. Dejene, **L. F. Koao**, J. J. Dolo and H. C. Swart, Structural, morphological, and luminescence properties of hexagonal ZnO particles by wet chemical process. In preparation.

- F. B. Dejene, R. Kittesa and **L. F. Koao**, Structural and luminescence properties of yellow $Y_3Al_5O_2:Ce^{3+}$ thin film phosphors prepared by Pulsed Laser Deposition. In preparation.
- **L. F. Koao**, H. C. Swart and F. B. Dejene, Synthesis and characterization of CuS nanoparticles using the chemical bath deposition method. In preparation.
- **L. F. Koao**, HC Swart and FB Dejene Synthesis and characterization of CdS nanoparticles using the chemical bath deposition method. In preparation.

International Conferences

- **L. F. Koao**, F. B. Dejene, and H. C. Swart, Effect of Tb^{3+} on the structure, morphology and optical properties of spherical PbS synthesized using chemical bath deposition, presented at 7th International conference on rare-earth development and application, August 2013.
- **L. F. Koao**, F. B. Dejene, and H. C. Swart, The effects of Ce^{3+} co-doping on the structure, optical and luminescence properties of Tb^{3+} doped PbS nanoparticles synthesized using the chemical bath deposition method, presented at 7th International conference on rare-earth development and application, August 2013.
- **L. F. Koao**, F. B. Dejene, and H. C. Swart, The effect of Cu^{2+} on structure, morphology and optical properties of flower-like ZnO synthesized using the chemical bath deposition method, 5th Conference on Photo-Responsive Materials, Kariega Game Reserve, South Africa, May 2013.
- T. M. Sithole, B. F. Dejene, **L. F. Koao**, Synthesis and Characterization of $SrB_6O_{10}:Eu^{2+}$ nano-phosphors Prepared Using Solution - Combustion Method, 5th Conference on Photo-Responsive Materials, Kariega Game Reserve, South Africa, May 2013.
- F. V. Molefe, **L. F. Koao,** J. J. Dolo**,** B. F. Dejene , Effect of reaction time on structural, morphological and optical properties of ZnO nanoflakes prepared by chemical bath deposition method, 5th Conference on Photo-Responsive Materials, Kariega Game Reserve, South Africa, May 2013.

- **L. F. Koao**, F. B. Dejene, and H. C. Swart, Synthesis and characterization of PbS nanorods doped with Tb^{3+} ions using the chemical bath deposition method, presented at 4th International Workshop on Photoluminescence in rare earths: Photonic materials and devices (PRE'12). March 28-30, 2012, Kyoto, Japan.
- **L. F. Koao**, F. B. Dejene, and H. C. Swart, Synthesis and characterization of ZnO nanoflakes doped with Tb^{3+} ions using the chemical bath deposition method, presented at 4th International Workshop on Photoluminescence in rare earths: Photonic materials and devices (PRE'12). March 28-30, 2012, Kyoto, Japan.
- R. E. Kroon, H. A. A. Seed Ahmed, O. M. Ntwaeaborwa, **L. F. Koao**, I. M. Nagpure, M. A. Gusowski, J. R. Botha and H. C. Swart, Luminescence from Ce in sol-gel SiO2, 4th Conference on Photo-Responsive Materials, Kariega Game Reserve, South Africa, May 2011.
- **L. F. Koao**, H. C. Swart and F. B. Dejene, Synthesis and characterization of Ce^{3+} doped SiO_2 nanoparticles, International Conference On Nanotechnology and Advanced Materials At University of Bahrain (4/7 May 2009).

National Conferences

- **L. F. Koao**, F. B. Dejene and H. C. Swart, Effect of synthesis temperature on the structure, morphology and optical properties of PbS nanostructures prepared by chemical bath deposition method. SAIP at UKZN July 2013.
- F.B. Dejene and **L.F. Koao**, Energy transfer and photoluminescence properties of Ce^{3+} or/ and Tb^{3+}-doped PbS nanorods. SAIP at UKZN July 2013.
- F. V. Molefe, **L. F. Koao,** J. J. Dolo**,** B. F. Dejene , Structural and luminescent properties of ZnO flake-like nanostructures synthesized using the chemical bath deposition method. SAIP at UKZN July 2013.
- T. M. Sithole, B. F. Dejene, **L. F. Koao**, Synthesis and Characterization of $CaB_4O_7:Eu^{3+}$ nano-phosphors Prepared Using Solution - Combustion Method. SAIP at UKZN July 2013.
- **L. F. Koao**, F. B. Dejene, and H. C. Swart, Synthesis and characterization of ZnO flower-like microstructures using the chemical bath deposition method. SAIP at UP July 2012.

- **L. F. Koao**, F. B. Dejene, and H. C. Swart, Synthesis and characterization of MnO nanostructures using the chemical bath deposition method. SAIP at UP July 2012.
- F. B. Dejene, **L. F. Koao**, J. J. Dolo and H. C. Swart, Structural, morphological, and luminescence properties of hexagonal ZnO particles by wet chemical process. SAIP at UP July 2012.
- F. B. Dejene, R. Kittesa and **L. F. Koao**, Structural and luminescence properties of yellow $Y_3Al_5O_2:Ce^{3+}$ thin film phosphors prepared by Pulsed Laser Deposition. SAIP at UP July 2012.
- F. B. Dejene, S. V. Motloung, **L. F. Koao**, K. E. Foka, T. L. Lotha, M. A. Tshabalala, A. G. Ali, A. H. Wako, J. J. Dolo and H. C. Swart, Solution-combution synthesis and photoluminescence property of $(Gd,Y)BO_3:Tb^{3+}$ phosphor powders. SAIP at UP July 2012.
- T. M. Sithole, B. F. Dejene, **L. F. Koao**, Synthesis and characterization of BaB_8BO_{13}:Eu nanophosphors prepared using solution-combution method. SAIP at UP July 2012.
- T. L. Lotha, B. F. Dejene, **L. F. Koao**, Morphological, structural and photoluminescence properties of sol-gel synthesized strontium titanate ($SrTiO_3$:Pr:Al) nanophophors. SAIP at UP July 2012.
- **L. F. Koao**, F. B. Dejene and H C. Swart, Synthesis and characterization of PbS nanostructures using the chemical bath deposition method. SAIP at UP July 2012.
- **L. F. Koao**, H. C. Swart and F. B. Dejene, Synthesis and characterization of SiO_2 doped with Rare-Earth metal (e.g.Ce^{3+}) and co-doped with Al^{3+} ions**.** SAIP Durban July 2009.
- **L. F. Koao**, H. C. Swart and F. B. Dejene, The effect of Mg^{2+} ions on the Photoluminescence of Ce^{3+} doped SiO_2, 3rd International Conference on Photonic Materials, Mabula, Limpopo (23-27 March 2009).
- **L. F. Koao**, H. C. Swart and F. B. Dejene, Synthesis and characterization of rare-earth metal doped SiO_2 nanoparticles. SAIP Limpopo July 2008.